Photospheric Albedo and the Measurement of Energy and Angular Electron Distributions in Solar Flares

Ewan Cameron Mackenzie Dickson

MSci

School of Physics and Astronomy

College of Science and Engineering

University of Glasgow

Submitted in fulfilment of the requirements for the degree of

Doctor of Philosophy

September 2012

To my parents, Alexandra and David, and my siblings Kirsty, Eilidh and Alasdair.

Abstract

In this thesis I examine the role of Compton back-scatter of solar flare Hard X-rays, also known as albedo, in the inference of the parent electron spectrum. I consider how albedo affects measurements of the energy and angular distributions when the mean electron flux spectrum in a solar flare is inferred using regularised inversion techniques.

The angular distribution of the accelerated electron spectrum is a key parameter in the understanding of the acceleration and propagation mechanisms that occur in solar flares. However, the anisotropy of energetic electrons is still a poorly known quantity, with observational studies producing evidence for an isotropic distribution and theoretical models mainly considering the strongly beamed case. First we investigate the effect of albedo on the observed spectrum for a variety of commonly considered analytic forms of the pitch angle distribution. As albedo is the result of the scattering of X-ray photons emitted downwards towards the photosphere different angular distributions are likely to exhibit a varying amount of albedo reflection, in particular, downward directed beams of electrons are likely to produce spectra which are strongly influenced by albedo.

The low-energy cut-off of the non-thermal electron spectrum is another significant parameter which it is important to understand, as its value can have strong implications for the total energy contained in the flare. However, both albedo and a low energy cut-off will cause a flattening of the observed X-ray spectrum at low energies. The Ramaty High Energy Solar Spectroscopic Imager (RHESSI) X-ray data

base has been searched to find solar flares with weak thermal components and flat photon spectra in the $15 - 20$ keV energy range. Using the method of Tikhonov Regularisation, we determine the mean electron flux distribution from count spectra of a selection of these events. We have found 18 cases which exhibit a statistically significant local minimum (a dip) in the range of $10 - 20$ keV. The positions and spectral indices of events with low-energy cut-off indicate that such features are likely to be the result of photospheric albedo. It is shown that if the isotropic albedo correction was applied, all low-energy cut-offs in the mean electron spectrum were removed.

The effect of photospheric albedo on the observed X-ray spectrum suggest RHESSI observations can be used to infer the anisotropy in the angular distribution of X-ray emitting electrons. A bi-directional approximation is applied and regularized inversion is performed for eight large flare events viewed by RHESSI to deduce the electron spectra in both downward (towards the photosphere) and upward (away form the photosphere) directions. The electron spectra and the electron anisotropy ratios are calculated for broad energy range from about 10 and up to ~ 300 keV near the peak of the flares. The variation of electron anisotropy over short periods of time intervals lasting 4, 8 and 16 seconds near the impulsive peak has been examined. The results show little evidence for strong anisotropy and the mean electron flux spectra are consistent with the isotropic electron distribution.

The inferred X-ray emitting electron spectrum is likely to have been modified from the accelerated or injected distribution by transport effects thus models of electron transport are necessary to connect the observations. We use the method of stochastic simulations to investigate the effect of Coulomb collisions on an electron beam propagating through a coronal loop. These simulations suggest that the effect of Coulomb collisions on a uniformly downward directed beam as envisaged in the collisional thick target model is not strong enough to sufficiently scatter the pitch angle distribution to be consistent with

the measurements made in the previous chapter. Furthermore these simulations suggest that for the conditions studied the constraints inferred in Chapter 4 are only consistent with a low level of anisotropy in the injected electron distribution.

Declaration

I declare that, except where explicit reference has been made to the contribution of others, this thesis is my own composition.

Signature: _____

Printed name: Ewan Cameron Mackenzie Dickson

Acknowledgements

I would like firstly to thank my supervisor, Dr Eduard Kontar, who has helped and supported me with this research. A summer project with Eduard on solar flares was my first introduction to this fascinating field. Thanks also to my second supervisor, Dr Alec MacKinnon, for his help with the stochastic simulations and his insightful comments, thus improving my thesis.

Thanks to all the members of the Astronomy and Astrophysics Group for generously sharing their knowledge and acumen. To all of my officemates over the years, thanks for good company, good conversation and good coffee!

I am grateful to the STFC for providing the funding for my PhD.

Finally, thanks to my family who provided a supportive background to this work, and especially my grandparents, Margaret and Donald Mackenzie, who first introduced me to the wonders of the skies.

Contents

List of Figures

List of Tables

1

Introduction

1.1 The Sun

The Sun, our closest star, is the ultimate source of almost all the energy on Earth, making it one of the most significant objects to study. The mean distance between the Earth and the Sun, with a value of $1.5 \times 10^{13}\,\mathrm{cm}$, defines the Astronomical Unit (AU), one of the standard measurements of astronomical distance. The luminosity of the Sun has a value $L_{\odot} = 3.83 \times 10^{33}\,\mathrm{ergs\,s^{-1}}$. This results in a solar irradiance at Earth of $1.36 \times 10^{6}\,\mathrm{ergs\,cm^{-2}\,s^{-1}}$ (Cox, 2000), this value being known historically as the solar constant, although it is now known that it varies by $\sim 0.1\%$ over the solar cycle. The Sun is a typical main sequence star with a radius of $1R_{\odot} = 6.96 \times 10^{10}\,\mathrm{cm}$ and a mass of $1M_{\odot} = 1.99 \times 10^{33}\,\mathrm{g}$; it is about 4.5 billion years old, putting it close to half way through its life-cycle. The Sun is mainly composed of Hydrogen (70% by mass), the second most abundant element is Helium ($\sim 28\%$) and all other elements, often referred to as metals by astronomers, make up only a small fraction ($\sim 2\%$).

The Sun has a surface temperature of roughly 5800K and is classified in the Harvard system as a G2V spectral type. G-type stars are yellow in colour and have a surface temperature of between 5200 and 6000 K; spectral types are each subdivided into 10 classes running from the hottest to the coolest, denoted by the numbers 0 to 9, G2 is thus the third hottest class of G-type. The V represents

the luminosity class. Here stars are classified with roman numerals from the most luminous hyper-giants classed 0 to the least luminous white dwarfs classed VII, with V class main sequence stars sometimes referred to as yellow dwarfs.

As the closest star, the Sun is our prototype for understanding all stars as well as astrophysical plasmas which cannot be reproduced in the lab. The Sun is the only star that it is possible for us to study in detail, and until the 90s the only stellar disk which we could directly image (Gilliland and Dupree, 1996). Fortunately, as the Sun is a fairly average main sequence star, our understanding can be applied to many other stars. This does not mean that the Sun is uninteresting, the Sun is magnetically active, exhibiting sunspots on its surface and producing flares and Coronal Mass Ejections (CMEs) which can have a direct effect on Earth.

There are still many unanswered questions about the physics of the Sun such as the "Coronal Heating Problem" which seeks to explain why the outer layers of the Sun's atmosphere are much hotter than expected; the creation of the Sun's dipole magnetic field by the solar dynamo and the origin of solar flares also still have open questions. Another significant contribution of solar studies to recent advances in physics is the "Solar neutrino problem" - the measured flux of neutrinos at Earth being lower than theoretically predicted. The solution to this problem required changes to the Standard Model of particle physics, namely that neutrinos, which previously were believed to be massless, must have mass.

1.1.1 The Solar Interior

In order to understand the physics of the Sun it is useful to first consider its structure. The Sun is usually divided into concentric shells with the inner layers below the visible surface being considered part of the solar interior and the outer layers being considered the Sun's atmosphere.

The structure of the interior of the Sun is usually considered to consist of three regions, from the centre up to $0.3R_\odot$ which is the core where the energy that drives the Sun is generated by nuclear fusion; between $0.3R_\odot$ and $0.7R_\odot$ is the radiative zone where radiation is the main form of energy transport; and thirdly

between $0.7R_\odot$ and $1R_\odot$ is the convective zone where convective cells are the dominant transport mechanism moving energy out to the solar surface.

The core of the Sun, with a central temperature of 15 million K and a density of $\sim 150\,\mathrm{g\,cm^{-3}}$ (an electron density $n_e \approx 10^{26}\,\mathrm{cm^{-3}}$), is the source of its nuclear energy. The process responsible for most (99%) of the energy release is the p-p chain where hydrogen is fused into helium (Hansen and Kawaler, 1994). This is a highly temperature sensitive process. There are several other nuclear burning processes which occur on the Sun including the CNO-cycle where four Hydrogen nuclei undergo fusion in a cyclical process involving interactions the heavier elements of Carbon, Nitrogen and Oxygen.

The Radiative zone is characterised by electromagnetic radiation energy transport. Here the density is high so that the high energy photons which are emitted in the nuclear fusion processes scatter off many particles. The number of interactions is such that it can take thousands of years for a photon to travel the distance between the centre and the upper boundary of the Radiative zone.

Between the radiative and convective zones is the tachocline (from the Greek *tachos* meaning speed) where there is a sharp change in the angular velocity of the plasma. Here the rigid body rotation of the core can no longer be supported so that the outer layers rotate differentially, with the equator moving $\sim 30\%$ faster than the polar regions; this differential rotation can be clearly seen on the surface when tracking solar features. The tachocline is believed to be the source of the solar dynamo responsible for the Sun's strong toroidal magnetic fields.

Recently the study of helioseismology has allowed us to probe the solar interior. Helioseismology works by studying the resonant vibrations on the solar surface and comparing these observations with what would be expected from different models of temperature and density.

1.1.2 The Photosphere

The photosphere is a thin ($\sim 100\,\mathrm{km}$) shell where the the opacity for visible light drops to zero and is generally considered to be the surface of the Sun. The

name photosphere comes from *photos* the Greek for light. The photosphere has a temperature of roughly 5700 K and is close to being a Black Body radiator. The plasma number density here is roughly $10^{13}\,\mathrm{cm}^{-3}$. As the visible surface of the Sun the photosphere is one of the most studied aspects of the Sun, particularly historically: ancient Chinese and Greek astronomers describe observations of sunspots and telescopic observations of the solar surface were performed by Galileo.

One of the most noticeable features on the photosphere are sunspots. These appear as dark regions on the solar surface, which can usually be divided into a dark umbra (*umbra* is Latin for shadow) in the centre surrounded by a lighter penumbra (*pen-* comes from the Latin *paene* meaning almost). Sunspots appear dark because they are cooler than the surrounding area; the strong magnetic fields inhibit plasma flows and so the temperature drops.

Sunspots are one of the most obvious features of Active Regions; these are regions of high magnetic flux passing through the solar surface into the solar atmosphere. The magnetic field at the Photosphere is usually measured by Zeeman splitting of emission lines. Solar flares almost invariably occur within active regions with larger flares often occurring within large and complex active regions. Variations in the visible number of sunspots was the first evidence for the activity cycle of the Sun, roughly every eleven years magnetic activity reaches a maximum with high numbers of phenomena such as flares and sunspots being observed.

Another slightly less distinct feature of the solar surface is granulation, When viewed with a telescope the surface of the Sun appears mottled with bright and dark patches roughly 1000 km ($\sim 1''$) in diameter (Zirin, 1988). This is the result of convective cells which transport plasma through the solar interior reaching the photosphere. The bright patches correspond to the hot rising material, this is surrounded by a darker ring where the cooled material is beginning to flow down. Larger scale convective motion is also seen as super-granular cells ~ 300 times bigger.

1.1.3 The Chromosphere and Transition Region

Above the photosphere is the chromosphere named for *chromos* the Greek for colour, due to the bright red glow caused by Hydrogen alpha emission, although this is typically only visible if the disk of the Sun is covered. The chromosphere is notable for its temperature profile, several hundred metres above the photosphere the temperature reaches a minimum of around 4000 K and then starts to rise. The density continues to fall as height increases $n_e \approx 10^{11}\,\mathrm{cm}^{-3}$ at a height of 1000 km above the photosphere.

The chromosphere is usually viewed in narrow wavelength bands corresponding to the energies of atomic transitions. These are usually emission lines, when an excited electron makes a transition to a lower energy state it emits a photon, with energy equal to the difference between the two states.

The chromosphere exhibits structural features. The most notable of these are known as filaments or prominences, regions of cool dense plasma suspended by strong magnetic fields. When viewed against the disk these appear as long dark filaments but when seen on the limb these appear as bright structures extending out of the Sun.

The chromosphere and the next layer, the corona, are separated by a thin layer called the transition region. Here the temperature increases rapidly from 20000 K to $\sim 10^6$ K in several hundred km. This results in the Hydrogen rapidly becoming ionised. This region is usually viewed in emission lines in the extreme-ultraviolet (EUV).

1.1.4 The Corona

The corona, named after the Latin for crown, is generally considered to be the highest layer of the solar atmosphere. The corona, with an electron density of $n_e = 10^9\,\mathrm{cm}^{-3}$ at its base, is far more tenuous than the inner layers of the Sun and as a result coronal emission is much weaker than photospheric emission, the corona can usually only be seen if the disk of the Sun is blocked either naturally

during a solar eclipse or artificially using a corona graph. In optical light the corona can be seen as uneven streaks of light often structured into semi-circular loops, cusp-like helmet structures and radial streamers; these can be seen due to the Thompson scattering of light from the photosphere off the magnetically dominated coronal gas. This emission is known as the K-corona. There are two other origins of coronal light which are referred to as the the F-corona and the E-corona (Golub and Pasachoff, 2009). The F-corona is characterised by Fraunhofer absorption lines which are caused by the scattering of solar light by small dust particles.

Coronal emission lines (which comprise the E-corona), on the other hand, tend to be in the UV to soft X-ray range. When solar spectroscopy was beginning several emission lines were detected which did not correspond to any transitions observed in the laboratory. It was proposed that these lines were from a new element, coronium, and this was a popular idea at the time as Helium had first been detected on the Sun before subsequently being discovered on Earth. It was eventually determined that this line was due to highly ionised iron and calcium Grotian (1939) suggesting that the Corona was far hotter ($\sim 1\,\mathrm{MK}$) than was previously assumed. One of the major unanswered questions in Solar Physics is the coronal heating problem: the temperature of the corona is far higher than would be expected.

The corona is highly dynamic with structures being formed and dissipating on several different timescales. The corona is magnetically dominated and generally believed to be the main site for magnetic reconnection and the acceleration of particles in solar flares.

Beyond the corona (from roughly $3R_{\odot}$) lies the solar wind, a flow of charged particles which streams out from the corona. Interactions between these solar wind particles and the Earth's atmosphere cause the polar aurorae.

1.2 Solar Flares

A flare in the solar atmosphere is generally characterised by a sudden large emission of electromagnetic radiation. A solar flare generally lasts for tens of minutes though the profile varies significantly in different wavelength ranges, often appearing as a sharp spike in the hard X-ray regime (that is X-rays with energy of roughly > 10 keV) but as a broad slowly varying hump in soft (lower energy) X-rays (Figure 1.1). The occurrence of solar flares tends to follow a power law distribution with the most energetic being the least common (Crosby, Aschwanden, and Dennis, 1993). Related phenomena are microflares, which are believed to be simply less energetic versions of solar flares and nanoflares which are linked to small, currently undetectable, energy release events. Large flares may occur up to 100s of times a day at solar maximum. A typical flare is visible in all bands of the electromagnetic spectrum but at optical wavelengths is greatly dominated by the ambient thermal emission of the photosphere. Flares can most clearly be seen in the Radio, EUV, X-rays and γ-ray regimes. Solar flares can have energy budgets of up to 10^{33} ergs with typical flares releasing 10^{29} ergs of energy (Hannah *et al.*, 2011) making them some of the most energetic events in the solar system.

The temporal evolution of flares is typically divided into three stages: the preflare, impulsive and gradual phases. In the preflare stage the levels of soft X-rays gradually increase. This stage usually lasts several minutes. This is followed by the impulsive phase which might last ~ 20 seconds and is characterised by a sharp peak in hard (higher energy) X-rays and sometimes γ-rays. Finally the flare enters the gradual phase where the hard X-rays have died away and the soft X-rays reach a maximum value then slowly decrease over several tens of minutes.

1.2.1 Flare observations

Flare observations have been made in almost every band of the EM spectrum from radio waves to γ-rays.

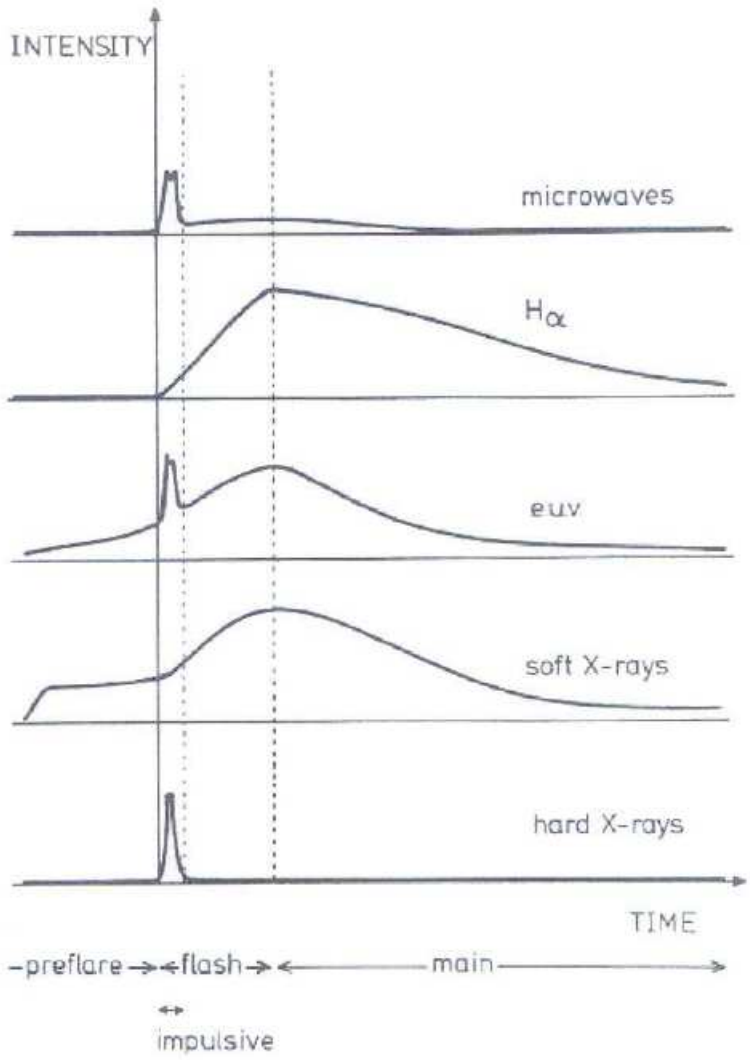

Figure 1.1: Flare temporal profile in different energy bands (Priest, 1984)

Flares were first witnessed by Richard Carrington and Richard Hodgson on September 1 1859, when using telescopes to project an image of a sunspot group onto a screen; they witnessed a localised increase in the brightness of the Sun lasting only a few minutes (Carrington, 1859; Hodgson, 1859). This was a comparatively rare white light flare. The potential effect solar flares could have on the Earth were almost immediately clear as the magnetometer at Kew Observatory

recorded a magnetic crochet at roughly the same time as the flare; 17 hours later there was a large geomagnetic storm which saturated the magnetometer readings and caused numerous aurorae throughout the world (Stewart, 1861). It has been suggested that this flare could be one of the most energetic events in the last 150 years (Cliver and Svalgaard, 2004).

White light flares (flares which have enough energy to change the visible brightness of the Sun) are sometimes viewed as rare compared with flares seen in other energy ranges such as X-rays; this is because for electron beam models, it requires a large proportion of the flare energy to be transported to the photosphere. However, detailed high sensitivity studies have suggested that all flares could have an optical component (Hudson, Wolfson, and Metcalf, 2006; Jess *et al.*, 2008). Measurements in this regime are difficult as the contrast is low against the bright photosphere; a typical flare lasting an hour has an energy release rate $\sim$ 300 times lower than the adjacent photosphere (Ambastha, 2003). It is likely that other factors also play a role in the production of white light flares.

Optical observations of the Sun are still a significant source of information about solar flares, both for observations of white light flares and for contextual information about the state of the photosphere, particularly for extrapolation of the coronal magnetic field structure and for measurements of line emission.

The H-α (656.3 nm) line of the Balmer series is of particular significance to solar flare studies. The line is caused by the transition of an electron between the $n = 3$ and $n = 2$ energy states in atomic hydrogen. A flare can increase the intensity in this line by several orders of magnitude compared with the adjacent continuum emission. Historically, as this line is part of the visible spectrum a large amount of solar flare measurements were made solely in H-α; thus , flaring in this line was considered the most significant type of impulsive solar emission. A commonly used method for classifying flares was based on the brightness and apparent area of the flare in H-α (Zirin, 1988). Observations at this wavelength are still frequently performed by ground-based telescopes as they tend to have better angular and temporal resolution.

Historically, radio is the second regime used to study solar flares, as radio wavelengths can penetrate the Earth's atmosphere. Technology for studying the Sun at these wavelengths first became available in the 1940s as a result of improvements to radio receivers during World War 2 (Hey, Parsons, and Phillips, 1948). The primary emission mechanisms in this regime are gyrosynchrotron and coherent plasma emission. Radio emission is of particular interest as a complement to X-ray studies as the keV electrons which emit in X-ray via bremsstrahlung also emit gyrosynchrotron radiation in the GHz regime.

A significant fraction of coronal emission, both as part of the quiet corona and from flares, is observed in the ultraviolet energy range, this is sometimes separated into UV (Ultraviolet) at $\sim 3 - 10\,\mathrm{eV}$ and EUV (Extreme Ultraviolet) at $\sim 10 - 100\,\mathrm{eV}$. This is predominantly line emission from the hot plasma which can be greatly increased as the energy from the flare heats the ambient plasma in the corona. As the plasma temperature is so high, for the most part hydrogen and helium are completely ionised, so that many of these lines are ionised states of heavy metals , most notably iron (Doschek and Feldman, 2010).

Flare Soft X-rays are commonly understood to be photons with energy in the range $\sim 0.1 - 10\,\mathrm{keV}$ though the division between SXR and Hard X-rays (HXR) is somewhat ambiguous. As SXR are commonly defined to be the X-rays emitted by electrons in a thermal distribution, and HXR are considered to arise from an accelerated non-thermal distribution , the exact cutoff can depend on the characteristics of the individual spectra. The range is generally considered to be between 10 and 40 keV. SXR photons are predominantly produced by bremsstrahlung emission from hot thermal plasma and so tend to follow a similar time profile to the EUV emission (Benz, 2008). High temperature emission lines are also apparent at SXR energies.

Flares are typically characterised by their soft X-ray flux. GOES (Geostationary Operational Environmental Satellite) measures X-rays in the $0.1 - 0.8\,\mathrm{nm}$ wavelength range. Flares are then classified by letter: A, B, C, M and X, each representing a decade in flux, they are then subdivided by number so for example GOES A1 class is equivalent to $1 \times 10^{-5}\,\mathrm{ergs\,cm^{-2}\,s^{-1}}$ and a C3 class flare would

have a measured flux of $3 \times 10^{-3}\,\mathrm{ergs\,cm^{-2}\,s^{-1}}$. The highest X-ray flux flare detected by GOES was on 4 November 2003; however, this saturated the detectors which are not reliable at such high fluxes, other estimates suggest that its true flux could be in the range from X24 to as high as X40 (Brodrick, Tingay, and Wieringa, 2005).

Gamma rays are typically considered to be photons with energy greater than several hundred keV. Emission from the Sun in this regime is observed in some, often particularly strong, solar flares. Gamma ray emission is often associated with energetic protons and ions accelerated in the solar flare process (see Vilmer, MacKinnon, and Hurford 2011 for a recent review). There are several processes which can create gamma-ray energy photons, producing both continuum and line emission.

Continuum emission is generally considered to be produced by bremsstrahlung emission from highly relativistic electrons, these can either be primarily accelerated electrons similar to those considered to produce the X-ray emission or electrons produced in secondary decay processes by accelerated protons and ions. At very high energies ($\geq 300\,\mathrm{MeV\,nucleon^{-1}}$), proton-ion collisions can produce pions which decay into photons of a very wide range in energies (centred on 67 MeV, half the neutral pion rest-mass). As this spectrum is relatively flat it is usually only able to be detected at gamma-ray energies of ≥ 10 MeV.

Line emission is also visible in gamma-rays, this is created by nuclear de-excitations when accelerated ions and protons interact with thermal ions. At 511 keV the electron-positron line is visible. Positrons can be created by nuclear processes; when these encounter ambient electrons, they annihilate, releasing a pair of photons each with energy 511 keV. Another significant gamma-ray line is the 2.23 MeV neutron capture line. Accelerated protons can interact with ambient ions releasing neutrons, which are then captured by ambient thermal protons producing deuterium and emitting a gamma ray photon with an energy equal to the binding energy of deuterium (2.223 MeV).

The fact that the gamma rays and hard X-rays follow similar spectral evolution suggests that the ions and electrons are accelerated in the same process; however,

Hurford *et al.* (2003, 2006) used RHESSI spectral imaging to determine the centroid positions of the gamma ray footpoints and determined that for some flares (3 out of the 5 examined) (Vilmer, MacKinnon, and Hurford, 2011) they were not consistent with the positions of the HXR footpoints, suggesting that either the transport mechanisms or the acceleration process differs between protons and electrons.

1.2.2 Flare Theory

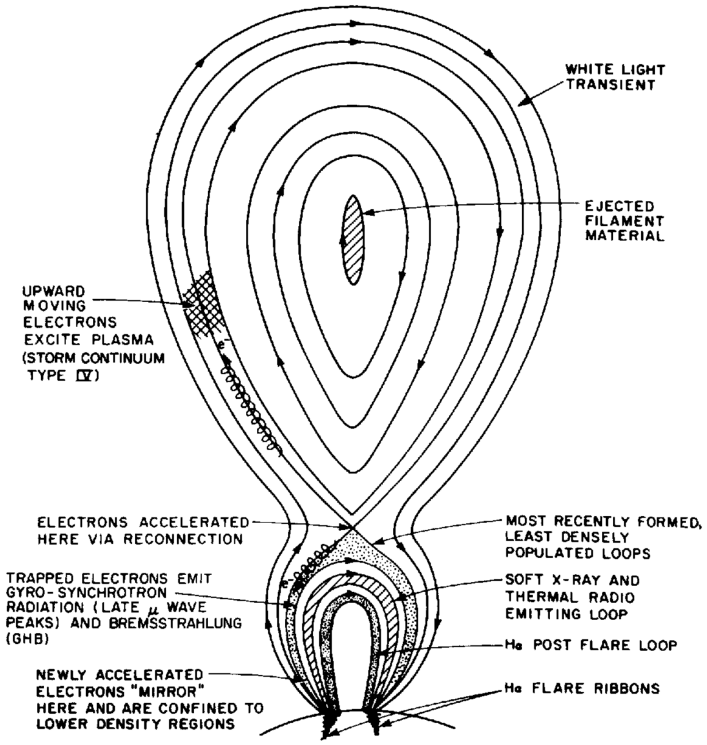

Figure 1.2: Flare loop during magnetic reconnection (Cliver *et al.*, 1986)

In the simplest interpretation of the standard picture solar flares occur in 2D magnetic loops anchored at the photosphere extending into the corona (Figure 1.2). Magnetic reconnection occurs in the corona, releasing energy which accelerates particles and heats the ambient plasma. Many of these accelerated particles stream along the field lines of the loop reaching the denser layers of the solar

atmosphere, emitting radiation and heating the plasma. The hot plasma from the lower atmosphere then "evaporates" filling the loop with hot dense plasma. This then radiates in EUV and SXR, cooling down to preflare levels after several tens of minutes.

This simplistic cartoon has been developed into many more detailed physical theories. While there is no single simple model which fits the characteristics of all flares one of the most popular 2D models has been the CSHPK model named after the main initial contributors. It was initially developed by Carmichael (1964), Sturrock (1966), Hirayama (1974), Kopp and Pneuman (1976). In this model a prominence above an active region rises in between two regions of oppositely directed open field-lines. The resulting magnetic collapse forms an X-point geometry where reconnection can occur.

The clearest features of a solar flare in X-ray images are the looptop and footpoints. The looptop is usually seen in soft X-rays. The footpoints are much lower down in the solar atmosphere and represent the location where the density of plasma is great enough to stop the high energy electrons, thus causing a large emission of X-ray radiation by collisional bremsstrahlung. Footpoints are generally seen in the hard X-ray regime, that is X-rays with energy of order tens of keV. Flare HXR foot-points generally occur at a height of around 1000 km above the solar photosphere (Battaglia and Kontar, 2011).

One feature of solar flare morphology which has had a significant amount of interest recently is above-the-looptop hard X-ray sources. These were first noted by Masuda *et al.* (1994): they appear as bright HXR sources above the SXR loop which are simultaneous with the HXR footpoint sources. As the corona is usually significantly less dense at these heights ($n \approx 10^9\,\mathrm{cm}^{-3}$), strong HXR sources are not expected here. Several theories have been put forward to explain these observations, for example, particle trapping could hold accelerated electrons for longer at these heights. Originally they were believed to be thermal emission from very hot ~ 100 MK plasma (Tsuneta *et al.*, 1997) but RHESSI measurements suggest they have a non-thermal component.

It is almost universally accepted that the Sun's magnetic field is the source of the energy for solar flares. In the prevalent model of solar flares, the motion of plasma in the solar atmosphere causes a constantly changing magnetic field. This will cause the magnetic field lines will become stressed, at some point they will reconfigure to a lower energy state, this can cause a substantial amount of energy to be released explosively. It is believed that in solar flares magnetic field lines perpendicular to the photosphere connect, forming a loop, as shown in Figure 1.2. As this is often a lower energy configuration, by conservation, the remainder of this energy must be released in some form. This energy causes the acceleration of ions, protons and electrons.

The relationship between the plasma and the magnetic field here is "frozen-in": this means that, depending on the dominant type of pressure, either the plasma follows the magnetic field or vice versa. However, when this frozen-in condition is broken reconnection may occur. The plasma conditions are usually encapsulated in the ratio between gas pressure and magnetic pressure known as the plasma-β i.e.

$$\beta = \frac{p_g}{p_m} = \frac{2\mu_0 n k_B T}{B^2} \tag{1.1}$$

In the photosphere, β is high and surface flows move the magnetic field lines, shifting the footpoints of the magnetic loop. In the corona, on the other hand, β is low and the plasma follows the magnetic fields.

A popular early mechanism for magnetic reconnection is Sweet-Parker reconnection (Parker, 1957; Sweet, 1958), named after Peter Sweet and Eugene Parker. Sweet-Parker reconnection is a 2D steady state model where two sets of oppositely directed field lines come into contact. This creates a long narrow diffusion region where reconnection can occur. However, this type of reconnection is too slow to account for the rapid energy release seen in solar flares. Petschek reconnection (Petschek, 1964) addresses this problem by allowing a smaller diffusion region.

Many reconnection models are now calculated numerically using dynamic 3D codes in the framework of Magnetohydrodynamics (MHD); however, these are

far more computationally intensive than the simple 2D steady state pictures historically considered. Detail can be found on the theory of MHD in the solar context in Priest (1984). The magnetic field in the corona is harder to determine than that of the photosphere or chromosphere so that computational extrapolations are usually used to estimate the magnetic flux in the corona.

The Hard X-ray emission is usually associated with an accelerated non-thermal distribution of electrons. There are several proposed mechanisms by which coronal electrons in a reconnection region might be accelerated: Direct acceleration by electric fields, stochastic acceleration and shock acceleration (Miller *et al.*, 1997). Each proposed mechanism needs to account for the relativistic energies needed to explain the hard X-ray emission. Direct acceleration can either be sub or super Dreicer, where the Dreicer field is given by (Dreicer, 1959)

$$\mathcal{E}_D = 4\pi n_e \left(\frac{e^3}{m_e v_{th}}\right) \ln\Lambda = e\frac{\ln\Lambda}{\lambda_D^2}\,, \tag{1.2}$$

where v_{th} is the thermal velocity, as the particles are initially assumed to be part of a thermal distribution, and λ_D is the Debye length. This represents the minimum level of electric field needed to freely accelerate particles out of a thermal distribution, without being stopped by collisions. For electric field $\mathcal{E}$ a particle with speed greater than

$$v = v_{th}\sqrt{\frac{\mathcal{E}_D}{\mathcal{E}}} \tag{1.3}$$

will be accelerated out of the thermal distribution. Super-Dreicer acceleration requires stronger electric fields but shorter distances than Sub-Dreicer acceleration.

The accelerated electrons will tend to stream along the magnetic field lines of the loop; thus many will travel downwards against the density gradient of the Sun, and in solar flare physics it is therefore often useful to consider the electrons as a beam propagating through the ambient plasma of the solar atmosphere. In doing so they will lose energy by a variety of processes such as radiation, but the most significant is energy loss by binary Coulomb collisions with ambient electrons and protons. As they propagate they will emit radiation, the most notable being

X-ray bremsstrahlung and synchrotron radiation. Collective plasma effects will also affect transport.

A significant question in the study of solar flare physics is what is the total energy budget for flares and how is it distributed among particle acceleration, particle heating, and Cornal Mass Ejection (CME) acceleration.

There are several methods used to estimate the total energy of the flare and one is to consider the amount of free magnetic energy in the corona. Free magnetic energy is the difference between the total magnetic energy in a volume and the energy associated with the potential field. This free energy can then be compared to the observed emitted energy either given by measurements of the total solar irradiance (TSI) or estimated by combining the total power in various wavebands (e.g. Emslie *et al.* 2004, 2005). A method often used to estimate the total energy in solar flare accelerated electrons is to consider the power in Hard X-ray emission given by the thick target model. These calculations are consistent, with a large fraction of the total flare energy going into the acceleration of electrons. If there is a CME associated with the flare this may also comprise a significant fraction of the flare energy budget.

1.3 Hard X-rays

1.3.1 HXR production

The dominant mechanism for X-ray production in solar flares is the process of bremsstrahlung, or braking radiation, as the accelerated electrons interact with denser plasma lower in the solar atmosphere where they are slowed down (Korchak, 1967). This deceleration in the electric field of the ambient plasma causes the electrons to radiate.

The electron will predominantly be involved in binary collisions with significantly heavier ions. The majority of these collisions will be long distance, resulting in only small angle deflections to the trajectory of the electron so that the resulting photons will be low energy. However some of the collisions will be close and cause

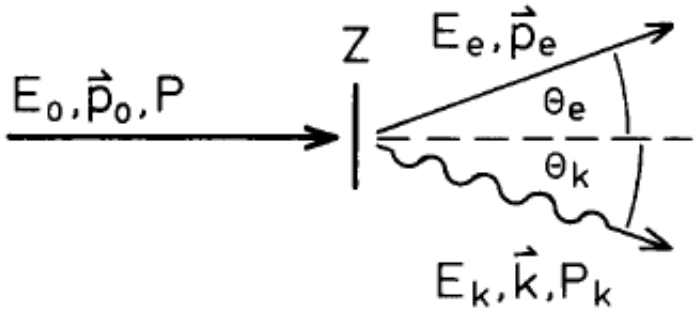

Figure 1.3: Schematic diagram of bremsstrahlung interaction (Nakel, 1994). An incident electron of energy, E_0, momentum, $\mathbf{p_0}$, and polarisation, P, scatters off a target nucleus of atomic number, Z, emitting a photon of energy, E_k, and momentum, $\mathbf{k}$, at an angle, θ_k, from its initial direction of travel. The scattered electron has energy, E_e, and momentum, $\mathbf{p_e}$, at an angle, θ_e, from the initial momentum of the electron.

large angle deflections, these can result in photons comparable in energy to the kinetic energy of the incident electron (Figure 1.3). For electrons accelerated to very high energies by the flare, the emitted photons can be in the X-ray or γ-ray regimes.

The theory of light emission by an electron undergoing deflection in a Coulomb field can be understood using classical physics, but for higher energy electrons relativistic corrections are necessary and the quantum nature of light becomes more significant. The process of an incoming electron with a given velocity vector interacting with a heavier particle and emitting an X-ray photon is encapsulated in a differential cross-section. A range of relativistic cross-sections have been calculated using the Born approximation, many of these are tabulated in Koch and Motz (1959). As in astrophysics the trajectory of the electron is unknown and the X-ray source is only viewed from one position, the direction of the incoming and outgoing electron and the outgoing photon are commonly averaged over, leaving a cross-section differential only in photon energy.

The simplest form of the bremsstrahlung cross-section, Kramers approximation

(Kramers, 1923), is given by

$$Q_{Kramers}(\epsilon, E) = \frac{Q_0 m_e c^2}{\epsilon E} \quad , \tag{1.4}$$

where E is the electron energy, ϵ is the photon energy, m_e is the mass of the electron and, $Q_0 = \bar{Z}^2 \alpha r_e^2 \approx 1.54 \times 10^{-31}$ cm^2, where α is the fine structure constant r_e, is the classical radius of the electron and $\bar{Z}^2$ is a factor which takes account of the contribution of elements heavier than Hydrogen. This form is non-relativistic and so can be substantially different from the true cross section thus it is mostly only applicable for analytic calculations.

While the simplicity of the Kramer's Cross-section makes it useful for analytic studies it is too inaccurate for most practical applications. A better approximation commonly used in solar flare studies is the non-relativistic Bethe-Heitler cross-section (Heitler, 1954).

$$Q_{NRBH}(\epsilon, E) = \frac{Q_0 m_e c^2}{\epsilon E} \ln \frac{1 + \sqrt{1 - \epsilon/E}}{1 - \sqrt{1 - \epsilon/E}} \quad , \tag{1.5}$$

This cross section still has a fairly simple form and so can be used analytically and requires very little computation. As a result of this it has been frequently used in solar physics literature (e.g. Brown 1971, Piana 1994). However the Bethe-Heitler cross-section is not relativistic so it becomes highly inaccurate at high energies and thus is not sufficiently accurate for contemporary data analysis (Haug, 1997).

The bremsstrahlung photon flux, differential in energy $I(\epsilon)$, can then be calculated by integrating over the distribution of electrons passing through the plasma volume (Tandberg-Hanssen and Emslie, 1988).

$$I(\epsilon) = \frac{1}{4\pi R^2} \int_V n(r) \int_\epsilon^E Q(\epsilon, E) F(E) dE dV \quad , \tag{1.6}$$

where $F(E)$ is the electron flux differential in energy; R is the distance to the observer; V is the volume of the source, and $n(r)$ is the density at position r. This can be simplified by replacing the integral of density over the volume with the

average density multiplied by the total volume $\overline{n}V = \int_V n(r)dV$. Substituting in the Kramers cross-section this has the form:

$$I(\epsilon) = \frac{\overline{n}V}{4\pi R^2}\frac{Q_0 m_e c^2}{\epsilon}\int_\epsilon^E \frac{F(E)}{E}dE \quad . \tag{1.7}$$

The electron flux at arbitrary height can be calculated from a given initial electron flux by assuming a model for the interaction between the ambient plasma and the electron beam, the two most common which consider purely collisional energy losses are thin and thick targets. These models are named by analogy to early scattering experiments, where beams of electrons were fired at metal targets of various thicknesses.

The assumption that the electrons are fully stopped, releasing all of their kinetic energy is known as the thick target model. Collisional energy loss can be characterised by assuming an equation of motion; as we are considering the Kramers cross-section we will consider the non-relativistic form (Brown, 1971)

$$\frac{dE}{dx} = \frac{-Kn(x)}{E} \quad , \tag{1.8}$$

where $K = 2\pi e^4 \ln\Lambda = 2\times10^{-18}$ cm^2 is constant and Λ is the Coulomb logarithm (Emslie, 1978).

The initial injected electron spectrum is usually taken to be a power law of spectral index δ

$$F_0(E_0) = aE_0^{-\delta} \quad , \tag{1.9}$$

where a is a scaling constant. This results in a power law form for $I(\epsilon)$ of spectral index $\gamma = \delta - 1$.

Thus the total power in accelerated electrons will be given by

$$P_{beam} = \int F_0(E_0)E_0 dE_0 = \int_{E_c}^\infty aE_0^{-\delta}E_0 dE_0 = \frac{a}{\delta-2}E_c^{2-\delta} \tag{1.10}$$

where E_c is the low energy cutoff, the minimum particle energy in the non-thermal distribution. To determine the total energy in the flare, knowledge of the low energy cutoff is critical.

The number flux of non-thermal electrons can be calculated in a similar manner

$$N_{beam} = \int F_0(E_0)dE_0 = \int_{E_c}^{\infty} aE_0^{-\delta}dE_0 = \frac{a}{\delta - 1}E_c^{1-\delta}\,. \tag{1.11}$$

However, this results in estimates of 10^{37} electrons s^{-1} for large flares suggesting a coronal loop with average density $\bar{n} \approx 10^{11}\,cm^{-3}$ and volume $V \approx 10^{27}\,cm^3$ would be depleted in tens of seconds. This is known as the "electron number problem". A beam of electrons this large would carry a current of $\sim 10^{18}$ A. This sets up an electric field which drives a return current moving in the opposite direction (Knight and Sturrock, 1977) from the background electrons. While this alleviates the number problem it represents an additional energy requirement. As with the total energy to determine the total number of accelerated electrons it is necessary to have an accurate value for E_c.

Bremsstrahlung is also known as free-free emission, as the electron is unbound both before and after interaction with the ion, and is widely thought to be the primary mechanism of X-ray emission in solar flares. However, recent studies (Brown and Mallik, 2008, 2009; Brown, Mallik, and Badnell, 2010) have suggested that free-bound or recombination radiation ought to be accounted for when analysing solar flare X-ray emission. In this case, the initially unbound electron interacts with an ion and is captured by it, this releases a photon. While free-bound emission is unlikely to be a major contribution to the X-ray spectrum, the presence of sharp lines can have a significant influence on inferred electron spectra if they are not properly taken into account.

Hard X-rays can also be produced by Inverse Compton Scattering (Korchak, 1967). The scattering of light from massive particles is often split into three regimes - Thomson scattering, Compton scattering and Inverse Compton scattering. At low energies it is known as Thomson scattering and the photon experiences no change in wavelength. Compton scattering is generally considered when a high energy photon interacts with a low energy particle, the electron gains some kinetic energy from the photon which is scattered to a lower energy. Inverse Compton scattering is similar but the particle imparts energy to the photon. As Compton scattering is responsible for the phenomena of Photospheric Albedo

the details shall be considered extensively in Section 1.4. The inverse mechanism occurs when a low energy photon interacts with a high energy electron and the electron imparts some of its energy to the photon. As in a solar flare there are likely to be high numbers of electrons accelerated to relativistic energies and the photon flux of the Sun from the photosphere is predominately at eV energies (500 nm $\approx$ 2.5 eV), some component of the observed spectrum could be due to inverse Compton scattering.

As well as from free electrons, X-rays are also produced in the form of spectral emission lines (Phillips, 2004). The solar flare can heat the corona to several tens of MK producing even more highly ionised atomic species than those that produce the EUV lines seen in the quiet corona. The most notable line features at high energies are the Fe feature at 6.7 keV and Fe-Ni feature at 8 keV, these are the result of the contributions of many lines including a large number from Fe XXV and Fe XXIV (i.e iron atoms which have lost all but 2 and 3 electrons respectively).

Hard X-ray bremsstrahlung emission can be produced by the interaction of many sufficiently energetic pairs of charged particles. Alternative explanations proposed to explain solar flare HXR observations include "inverse" bremsstrahlung from proton (Emslie and Brown, 1985) or neutral (Karlický *et al.*, 2000) beams interacting with electrons in the solar atmosphere. However measurements of γ-ray lines and timing of X-ray pulses (Aschwanden, 1996) suggests that deka-keV electrons are the most likely production mechanism for solar flare hard X-rays.

1.3.2 HXR Observations

As the Earth's atmosphere is opaque to X-ray emission, the first solar X-ray measurements did not occur until the start of the space age. The first detection of solar flare X-rays was made in 1958 from a balloon borne detector (Peterson and Winckler, 1958), several balloons and rockets with X-ray instruments followed. As interest in high energy solar physics grew, more long term satellite missions were launched dedicated to measuring solar HXR. To test new technologies, balloon

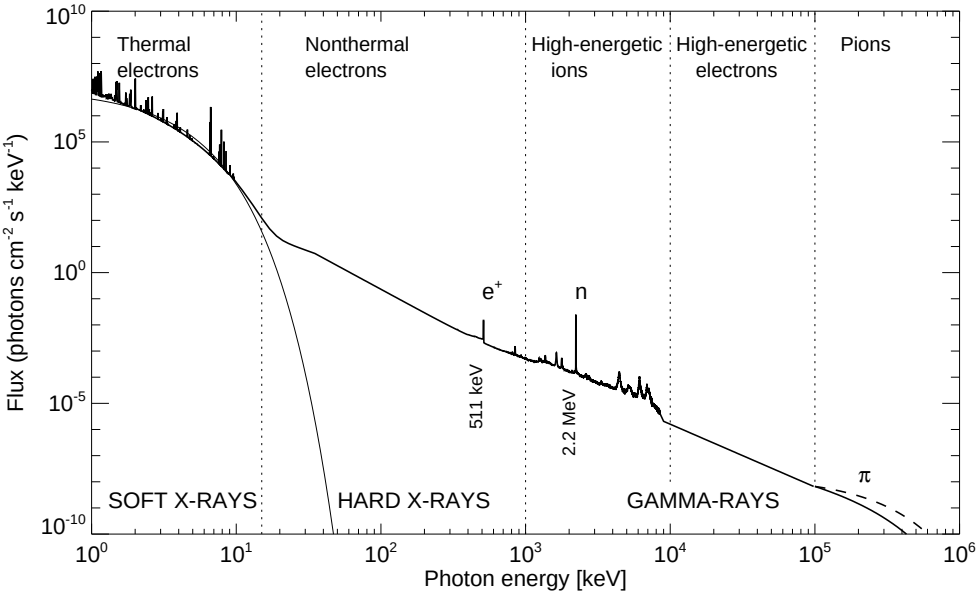

Figure 1.4: Spectrum of high energy flare emission from soft X-rays to gamma rays (Aschwanden, 2004)

and rocket based X-ray detectors are still flown today, such as the proposed FOXSI (Krucker *et al.*, 2009) and GRIPS (Shih *et al.*, 2009) missions.

The first satellites taking solar flare X-ray measurements were part of the Orbiting Solar Observatory (OSO) program which lasted between 1962 and 1978, sending a total of 8 satellites into low earth orbit aiming to study the Sun over an entire 11-year cycle. Each satellite had a slightly different design but most included some form of hard X-ray detector.

In the 1980s several spacecraft were launched to study high energy aspects of solar flares during the maximum of cycle 21, the most notable of these were: the International Sun-Earth Explorer (ISEE-3) in 1978 (Anderson *et al.*, 1978), Solar Maximum Mission (SMM) in 1980 and the Japanese ASTRO-A (later renamed Hinotori meaning firebird) in 1981 (Tanaka, 1983). The HXIS (Hard X-ray Imaging Spectrometer) (van Beek *et al.*, 1980) onboard SMM was the first instrument to provide hard X-ray imaging of solar flares, though it was only sensitive up to 30 keV.

During the next decade, the most significant satellites studying hard X-rays were

the Compton Gamma-Ray Observatory (CRGO) and Yohkoh (Kosugi *et al.*, 1991). The Burst and Transient Source Experiment (BATSE) (Fishman *et al.*, 1989) was a highly sensitive instrument designed to study gamma-ray bursts but capable of detecting solar flares. Yohkoh (meaning sunbeam) used Fourier imaging to produce flare images up to 100 keV.

1.3.3 RHESSI

The Ramaty High Energy Solar Spectroscopic Imager (RHESSI) satellite was launched in 2002 by NASA with the primary aim of studying electron acceleration in solar flares (Lin *et al.*, 2002). RHESSI uses germanium detectors to perform high precision spectroscopy. RHESSI can observe solar flares in the X-ray and gamma ray regimes in the energy range 3 keV up to 17 MeV with a resolution of up to 1 keV, an unprecedentedly high level. Due to the high photon fluxes measured by RHESSI during a solar flare, the satellite is equipped with aluminium attenuators which limit the X-ray flux to the detectors and thus the total counts measured. Another method used by RHESSI to limit the amount of information which must be committed to the onboard memory is count decimation: here, only 1 in every N measured counts are recorded, where N is a known number between 2 and 16. Throughout this project, flares in which the attenuator status or the decimation status changes during the impulsive phase were discounted. RHESSI uses a Solar Aspect System (SAS) to ensure that the spacecraft pointing with regards to the solar centre is always known. The SAS uses three linear CCDs to measure the position of three points on the solar limb and can thus be used to determine the solar radius (Fivian *et al.*, 2002).

For imaging RHESSI uses 9 collimators (Figure 1.5) with a grid at either end of varying spacing. These grids rotate along with the satellite and provide a modulated time profile depending on the angle of the incoming X-ray photon (Hurford *et al.*, 2002). A variety of algorithms are available to infer the positional information from this modulated time profile and thus create images of solar flares in HXR.

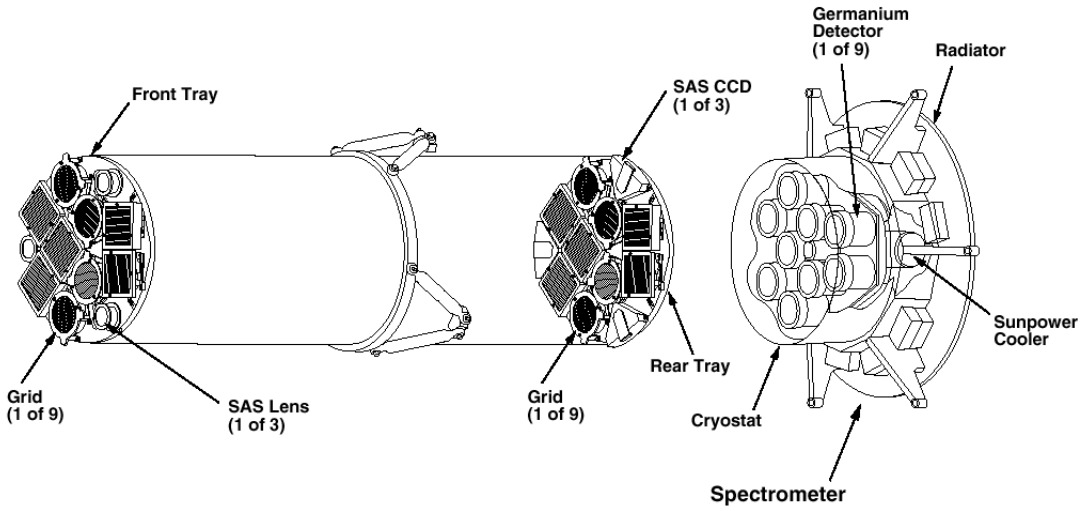

Figure 1.5: Schematic diagram of RHESSI telescope (Hurford *et al.*, 2002)

1.4 Compton Scattering of X-rays

The classical theory of light scattering by charged particles is known as Thomson scattering and was proposed by J.J. Thomson in 1903. In this case the incident light is viewed as a wave of oscillating electric and magnetic fields. The simplest case is light incident on a free particle, such as an electron. The changing electric field causes the electron to accelerate in that direction. This then results in dipole radiation, mostly in the plane perpendicular to the motion of the electron, that is the direction of the initial electric field. This process can clearly be viewed as the electron changing the direction of the electromagnetic wave without altering the frequency. The key parameter for Thomson scattering is the Thomson cross-section which is a measure of the effective area over which the electron interacts with the electromagnetic wave:

$$\sigma_T = \frac{8\pi}{3} r_e^2 = 6.65 \times 10^{-25} \text{ cm}^2 \ , \tag{1.12}$$

where

$$r_e = \frac{e^2}{c^2 m_e^2} \ , \tag{1.13}$$

is the classical electron radius.

The Thomson model works well for light of low energies, but once the energy of the incident light is of the hard X-ray regime, or greater, experimental results show significant digression from Thomson's predictions. In particular, a shift in the wavelength of the X-rays and directional beaming of the scattered X-rays are observed. These effects were accounted for by Arthur H. Compton (Compton, 1923). Compton's theory accounted for these discrepancies by considering the X-ray as particles, that is X-ray photons, and by considering the relativistic effects of the motion of the electron. Compton predicted an energy dependent cross-section of

$$\sigma_c = \sigma_T \frac{(1+\alpha)}{(1+2\alpha)^2} \quad , \tag{1.14}$$

where

$$\alpha = \frac{\epsilon_0}{m_e c^2} \quad , \tag{1.15}$$

$\epsilon_0 = h\nu_0$ being the energy of the incident X-ray photon.

The significant difference in Compton scattering is the change in energy, to the scattered photon

$$\frac{1}{\epsilon} - \frac{1}{\epsilon_0} = \frac{1}{m_e c^2}(1 - \cos\theta) \quad , \tag{1.16}$$

where ϵ is the energy of the scattered photon, ϵ_0 is the energy of the initial photon, and θ is the scattering angle. As momentum must be conserved overall, the photon must impart energy to the electron, changing its energy.

The full cross-section was calculated by Klein and Nishina (Bai and Ramaty, 1978) using the framework of quantum electrodynamics (QED) and is thus the expression used in all accurate calculations for the scattering cross-section of light

$$\sigma_{KN} = \frac{2\pi r_e^2}{\alpha}\left\{1 - \left[\frac{2(\alpha+1)}{\alpha^2}\right]\ln(2\alpha+1) + \frac{1}{2} + \frac{4}{\alpha} - \frac{1}{2(2\alpha+1)^2}\right\} \quad . \tag{1.17}$$

This tends to the constant Thomson cross-section in the low energy limit. When dealing with photons of energy $h\nu_0 \ll m_e c^2$ the full Klein-Nishina formula is generally not used.

Also, the Thomson cross-section can be compared to the collisional cross-section. The collisional cross-section is given by

$$\sigma_{collisional} \cong \frac{K}{E^2} \quad , \tag{1.18}$$

where K is defined in the same way as for Equation 1.8. For 10 keV electrons this gives $\sigma_{collisional} = 2 \times 10^{-20}\,\mathrm{cm}^2$. Clearly this is much larger than the Thomson cross-section implying that the X-rays are produced far higher in the solar atmosphere than where any Compton scattering is likely to occur. Thus outward emitted photons can be considered to escape the solar atmosphere unscattered. On the other hand X-rays emitted downwards towards the Sun will encounter an increasing density of electrons and are likely to be Compton scattered. There is a probability that these photons will be scattered back in the direction of the observer.

1.4.1 Effect of Compton Scattering on photon spectrum

When a solar flare is observed the recorded spectrum will likely be a mix of both the primary spectrum produced by collisional bremsstrahlung and the Compton scattered X-ray photons directed back towards the observer.

The reflectivity, which is defined as the ratio of scattered photons to incident photons of the Compton scattering, is energy dependent, therefore the influence of Compton backscattering can severely distort the observed photon spectrum (Bai and Ramaty, 1978).

The drop off in reflectivity at low energies, as seen in Figure 1.6, is caused by photoelectric absorption. The temperature in the solar atmosphere where Compton scattering is likely to occur is low enough that it is mostly made up of neutral hydrogen. Thus photons can promote electrons to higher energy levels or photoionise. For higher energies other elements become significant. This effect tends to drop off as $\sim \epsilon^{-3}$ (Fireman, 1974).

At low energies the Compton cross-section is thus roughly constant whereas at high energies the Compton cross-section drops off roughly as $\sim \epsilon^{-1}$ so higher

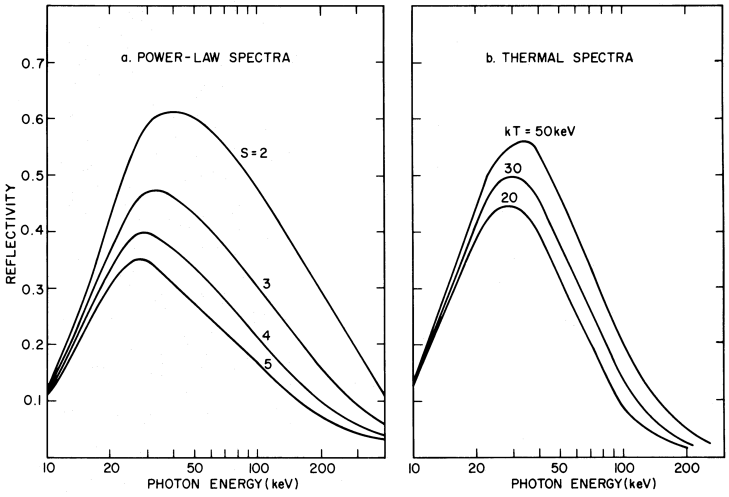

Figure 1.6: Variation of integral reflectivity with incident photon energy for power-law and thermal spectra (Bai and Ramaty, 1978)

energy photons penetrate more deeply into the Sun. In accordance with Equation 1.16 these higher energy X-rays will lose more energy when they are Compton scattered. This loss of energy results in the photons now seeing a much higher cross-section and becoming unable to escape the solar atmosphere. Thus for energies of several hundred keV, photons are not significantly backscattered. This results in the broad hump in reflectivity with a peak at 30 – 40 keV as seen in Figure 1.6. Thus the expected effect of Compton scattering on a primary photon spectrum produced by bremsstrahlung emission can be calculated (Tomblin, 1972). The net effect is for the spectral index of the X-ray spectrum, γ, to be greater at lower energies and smaller at higher energies (Santangelo, Horstman, and Horstman-Moretti, 1973). This can therefore have an influence on the characteristics of the electron spectra inferred from solar flare observations and thus implications for our understanding of flare energetics.

2

Forward Modelling of Anisotropic Electron Spectra to Determine the Effect of Albedo

To understand the effect of albedo on the observed X-ray spectra some simple forward modelling was performed. We will first consider the angle-averaged case and examine the commonly used theoretical energy-dependent electron distributions and their corresponding photon spectra. We will then consider the effect variation in the angular distribution of the electrons has on the emitted photon spectrum. Finally we will include the effect of photospheric albedo and how it can distort the photon spectrum.

2.1 Energy Variation

When studying solar flare physics, it is important to understand the distribution of accelerated electrons. These are often modelled using several simple analytic functional forms. These forms are then fitted to observed spectra and used in the modelling and simulation of the processes which occur during solar flares.

An important distinction has to be made between the accelerated or injected

electron spectrum $F_0(E)$ and the mean electron flux spectrum $\overline{F}(E)$ (Brown, Emslie, and Kontar, 2003). This is the density weighted volumetric average, given by:

$$\overline{F}(E) = \frac{1}{\overline{n}V} \int_V F(E, \mathbf{r}) n(\mathbf{r}) d^3 r \,, \tag{2.1}$$

where the average target proton density is given by $\overline{n} = V^{-1} \int_V n(\mathbf{r}) dV$. The product $\overline{n} V \overline{F}$ is the maximum amount of information which can be inferred from $I(\epsilon)$ without further assumptions.

X-ray emission from solar flares is often separated into two categories: Soft X-rays (SXR), which are in the energy range 1-20 keV and are often associated with a thermal distribution; and Hard X-rays (HXR) in the energy range 20-500 keV, mostly emitted by a non-thermal accelerated electron distribution, which tends to follow a power-law.

2.1.1 Thermal Distribution

A significant component, particularly at low ($\lesssim 20$ keV) energies, of observed solar flare X-rays, is believed to come from thermal emission from high temperature plasma ($T \sim 10^7$ K) in the corona. It is characterised by an exponential decrease of the X-ray flux with energy by $I(\epsilon) \propto \exp(-\epsilon / k_B T)$. This is often modelled as a single isothermal component which usually provides a good fit to the observational data, though there have been some suggestions that a multi-thermal model might be more suitable.

The thermal distribution of electrons is generally taken to have a classical Maxwellian form:

$$\overline{F}_{Thermal}(E) = \frac{2^{3/2}}{\sqrt{\pi m_e}} \frac{EM \cdot E}{(k_B T)^{3/2}} \exp\left(-\frac{E}{k_B T}\right) ,$$

where T is the temperature, k_B is Boltzmann's constant (1.38×10^{-16} erg/deg(K)) and EM is the emission measure defined as

$$EM = \int_V n_e^2 dV \,,$$

where n_e is the electron density in volume element dV and the integration is performed over the entire source volume.

The efficiency of bremsstrahlung photon production for a thermal distribution is generally seen as higher than for the non-thermal case. For a non-thermal distribution fast electrons quickly lose the majority of their energy collisionally, whereas, for a thermal distribution the electrons are in a state of equilibrium, with electrons tending to exchange energy in collisions, thus, the electron population can continue to emit high energy photons.

2.1.2 Single Power-law

Observations of solar flare X-rays frequently show evidence for a non-thermal component. The most common way of modelling this is a single power-law dependence of flux on electron energy:

$$\overline{F}(E) = AE^{-\delta} \tag{2.2}$$

where A is an arbitrary scaling constant.

The total power in the non-thermal part can be found simply by integration

$$P_{non-thermal} = \int_0^\infty AE^{-\delta} E dE. \tag{2.3}$$

However this equation is divergent at the lower limit for indices $\delta \geq 2$. As this is the case for the observed spectra (Dennis, 1985) a low energy cut-off, E_c, must be imposed. The exact value of this cut-off is significant, as most of the non-thermal energy is situated in the low energy part of the non-thermal distribution, thus this has a significant influence on the value of $P_{non-thermal}$ and therefore the total energy budget of the flare. It is also sometimes assumed that there is a maximum energy to which electrons are accelerated and thus a high energy cutoff, E_h, is assumed; in practice, when performing forward fits to HXR data, computational limitations require a maximum energy to be specified. The general form used when fitting a single power law therefore has the form:

$$\overline{F}(E) = \begin{cases} 0 & \text{if } E < E_c \\ AE^{-\delta} & E_c < E < E_h \\ 0 & E > E_h \,, \end{cases}$$

The low and high energy cutoffs can have a significant effect on the shape of the emitted photon spectrum. This was studied in detail by Holman (2003).

2.1.3 Broken power-law

Often when studying X-ray spectral data a single power law is too restrictive and does not provide a good fit to the data. This can be improved by allowing a double power law (Dulk, Kiplinger, and Winglee, 1992) with break energy E_c, which is generally taken with the form (Brown *et al.*, 2008) :

$$\overline{F}(E) = \begin{cases} 0 & \text{if } E < 0 \\ AE^{-\delta_1} & E_c < E < E_b \\ BE^{-\delta_2} & E_b < E < E_h \\ 0 & E > E_h \end{cases}$$

where $B = AE_b^{-\delta_1+\delta_2}$. There are several possible explanations for this broken power-law behaviour including a high-energy limit to particle acceleration. Other explanations suggest that the initial distribution is a single power-law and that the break is due to transport effects, such as non-uniform ionisation of the ambient solar plasma (Kontar, Brown, and McArthur, 2002) or the effect of return-current (Zharkova and Gordovskyy, 2006).

2.1.4 Resultant Photon Spectra

The spectral variation of emitted X-rays in solar flares is one of the most studied aspects in solar flare physics.

While in general both the bremsstrahlung cross-section and the electron distribution will be angularly dependent, for simplicity we will first consider the angle averaged case. This is equivalent to averaging the angular dependent cross-section over all solid-angles

$$Q(\epsilon, E) = \int_{\phi=0}^{2\pi} \int_{\theta=0}^{\pi} Q(\epsilon, E, \theta) \sin\theta d\theta d\phi \quad . \tag{2.4}$$

and assuming that the electron distribution is isotropic in pitch angle.

A more accurate, fully-relativistic, solid-angle-averaged cross-section commonly used when studying solar flares is the 3BN cross-section of Koch and Motz (1959).

The terminology 3BN denotes twice integrated (over the outgoing electron directions and emitted photon direction), where B stands for Born approximation and N for non-screening. An approximate version was calculated by Haug (1997) using an expansion in terms of the squares of initial and final momenta in order to be more computationally efficient.

The Born approximation is applicable when $\frac{2\pi Z}{137\beta'}, \frac{2\pi Z}{137\beta} \ll 1$. To compensate for cases where this assumption starts to break down a Coulomb correction as a function of initial and final electron velocities (v and v' respectively) is included as devised by (Elwert, 1939), is often applied to the cross-section. This has the form:

$$C = \frac{\beta(1 - e^{-2\pi Z\alpha/\beta})}{\beta'(1 - e^{-2\pi Z\alpha/\beta'})} \qquad \beta = \frac{v}{c} \qquad \beta' = \frac{v'}{c} \tag{2.5}$$

As was calculated in Chapter 1, with a single power law and the Kramer's cross-section, the relation between the electron spectral index, δ, and the photon spectral index, γ is given by $\gamma = \delta - 1$ in the thick target case and $\gamma = \delta + 1$ for the thin target case. For more accurate cross sections and more complex energy distributions the relationship between γ and δ does not follow these simple thin and thick target relationships and in general will be dependent on energy. $\gamma(\epsilon)$ is commonly defined as (Brown and Emslie 1988, Conway *et al.* 2003)

$$\gamma(\epsilon) = -\frac{\epsilon}{I}\frac{dI}{d\epsilon} = -\frac{d\,log\,I}{d\,log\,\epsilon} \quad , \tag{2.6}$$

This may be further complicated by additional distortions to the photon spectrum such as photospheric albedo.

2.2 Angular Variation

As well as a distribution in kinetic energy, electrons will also have a distribution in angle. The motion of the particle can be described by two angles: the pitch angle with respect to the magnetic field, η, and the azimuthal angle around, ϕ. For simplicity, we assume here that the variations in energy and angle are separable i.e. that the distribution has the form $\overline{F}(E, \eta) \propto G(E)H(\eta)$.

As the ion-electron bremsstrahlung cross-section is dependent on θ, the angle between the initial electron velocity vector and the direction of the emitted photon, both the energy and angular distributions of the electron spectrum will affect the distribution of emitted X-rays and hence the observed spectrum at Earth.

The most commonly used angular-dependent cross-section in solar flare studies is given by formula 2BN (Figure 2.2) from Koch and Motz (1959) with Coulomb correction by Elwert (1939) included and is the form used here:

$$\begin{aligned} Q_{2BN}(\epsilon, E, \theta) \;=\; & Z^2 \frac{\alpha}{2} \frac{r_0^2}{mc^2} \left(\frac{1}{k}\right) \frac{p'}{p} \left(8 \sin^2\theta \frac{2\Gamma^2+1}{p^2\Delta^4} - 2\frac{5\Gamma^2 + 2\Gamma\Gamma' + 3}{p^2\Delta^2} \right. \\ & -2\frac{p^2-k^2}{T^2\Delta^2} + \frac{L}{p'p} \left\{ \frac{4\Gamma^2(\Gamma^2+\Gamma'^2) - 2(7\Gamma^2 - 3\Gamma\Gamma' + \Gamma'^2) + 2}{p^2\Delta^2} \right. \\ & \left. + \frac{2k(\Gamma^2 + \Gamma'\Gamma - 1)}{p^2\Delta} + \frac{4\Gamma \sin^2\theta (3k - p^2\Gamma')}{p^2\Delta^4} \right\} + 4\frac{\Gamma'}{p^2\Delta} \\ & \left. + \frac{\xi_T}{p'T} \left[\frac{4}{\Delta^2} - \frac{6k}{\Delta} - \frac{2k(p^2-k^2)}{T^2\Delta} \right] - \frac{4\xi}{p\Delta} \right) C \,. \end{aligned} \tag{2.7}$$

Here, the normalised photon energy k, initial and final electron kinetic energies (Γ and Γ' respectively) and corresponding initial and final electron momenta (p and p' respectively) are defined as:

$$\begin{gathered} k = \frac{\epsilon}{mc^2}\,, \quad \Gamma = \frac{E}{mc^2} + 1\,, \quad \Gamma' = \Gamma - k\,, \\ p = \sqrt{\Gamma^2 - 1}\,, \quad p' = \sqrt{\Gamma'^2 - 1}\,. \end{gathered}$$

Other intermediate quantities Δ, T, L, ξ and ξ_T are defined as

$$\begin{gathered} \Delta = \Gamma - p\cos\theta\,, \quad T = \sqrt{p^2 + k^2 - 2pk\cos\theta}\,, \quad L = \log\left(\frac{\Gamma'\Gamma + p'p - 1}{\Gamma'\Gamma - p'p - 1}\right)\,, \\ \xi = \log\left(\frac{\Gamma' + p'}{\Gamma' - p'}\right)\,, \quad \xi_T = \log\left(\frac{T + p'}{T - p'}\right)\,. \end{gathered}$$

The Coulomb correction C (Equation 2.5) as a function of initial and final electron velocities (β and β' respectively) is included.

The relation between the angles η, θ_0, ϕ and θ is given by

$$\cos\theta = \cos\eta\,\cos\theta_0 + \sin\eta\,\sin\theta_0\,\cos\phi \quad , \tag{2.8}$$

where θ_0 is the angle between the emitted photon and the upwards direction (see Figure 2.1).

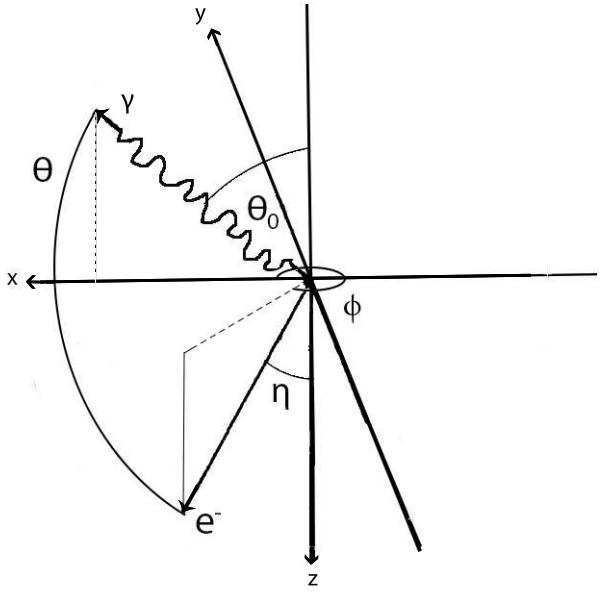

Figure 2.1: Diagram showing the relevant angles. An electron, e^-, emits a photon, γ, by bremsstrahlung. The axes are defined such that the z-direction points down towards the solar centre and the photon is emitted in the xz-plane. The electron has pitch angle with respect to the z-azis, η, and azimuthal angle, ϕ, measured from the x axis. The angle between the initial electron velocity vector and the direction of the emitted photon is θ and the angle between the emitted photon and the negative z-axis is θ_0.

2.2.1 Downward Directed Beam of Electrons

One of the most common forms of pitch angle distribution is a beamed distribution. In general a beam is any distribution satisfying $\langle v_\parallel \rangle >> \langle v_\perp \rangle$ where $v_\parallel$

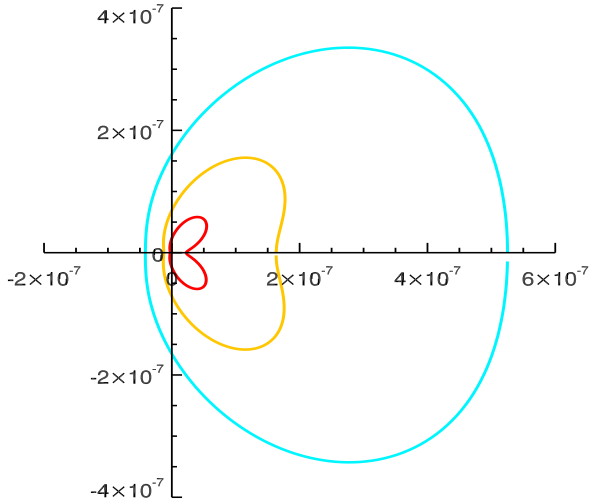

Figure 2.2: Polar diagrams of the 2BN ion-electron bremsstrahlung cross-section (Equation 2.7). The angle made with the x-axis represents the angle between the velocity vector of the incoming electron and the emitted photon and the radial extent represents the size of the cross-section. For an electron with initial energy 100 keV emitting a photon of 30 keV (blue) 50 keV (yellow) and 80 keV (red). After Massone *et al.* (2004).

and $v_\perp$ are the particle velocity components perpendicular and parallel to the magnetic field and $\langle .. \rangle$ denotes averaged over the distribution. Strongly directed distributions are popular because the electrons will tend to stream along the strong magnetic fields common in solar flares. Another advantage in strongly downward directed distributions is that they allow efficient transport from high in the solar corona, where particle acceleration is often assumed to take place, to lower in the solar atmosphere the where the X-ray footpoints are observed. Strong beaming is one of the main components of the Collisional Thick Target Model (Brown, 1972).

A common functional form for a beam is (Leach and Petrosian, 1983)

$$H(\eta) = \exp\left(-\frac{(1-\mu)^2}{\Delta\mu^2}\right) , \tag{2.9}$$

where $\mu = \cos(\eta)$. The strength of beaming is determined by the parameter $\Delta\mu$ (Figure 2.3). This form is used because it has useful analytic properties.

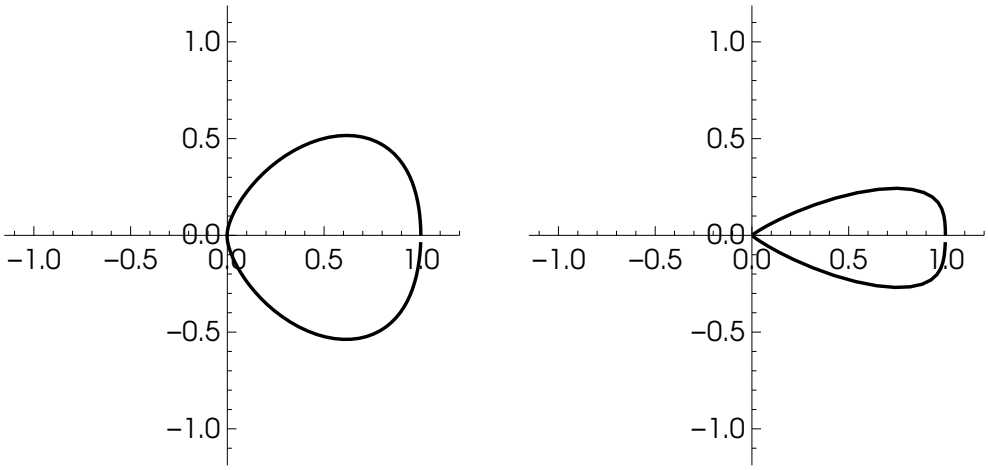

Figure 2.3: Polar diagrams of the assumed electron distribution $H(\eta)$. The angle made with the x-axis corresponds to the pitch angle η and the radial extent corresponds to the magnitude of the electron distribution. Left: intermediate anisotropic case $\Delta\mu = 0.4$. Right: Highly beamed case $\Delta\mu = 0.1$.

2.2.2 X-Rays from an Isotropic Electron Distribution

As the assumed electron distribution has azimuthal symmetry, an average cross-section integrated over ϕ can immediately be defined, leaving only the angles θ_0 and η needed to characterise the angular distribution (c.f. Massone *et al.* (2004))

$$Q'(\epsilon, E, \theta_0, \eta) = \int_{\phi=0}^{2\pi} Q(\epsilon, E, \theta(\phi))d\phi \quad . \tag{2.10}$$

The angular distribution of the emitted X-rays with respect to the downward direction can now be found by applying this cross-section to the assumed electron spectrum and integrating over electron energy and pitch angle

$$I(\epsilon, \theta_0) = \frac{\bar{n}V}{4\pi R^2} \int_0^{\pi} \int_{\epsilon}^{\infty} F(E, \eta) Q'(\epsilon, E, \eta, \theta_0) sin(\eta) dE d\eta \quad . \tag{2.11}$$

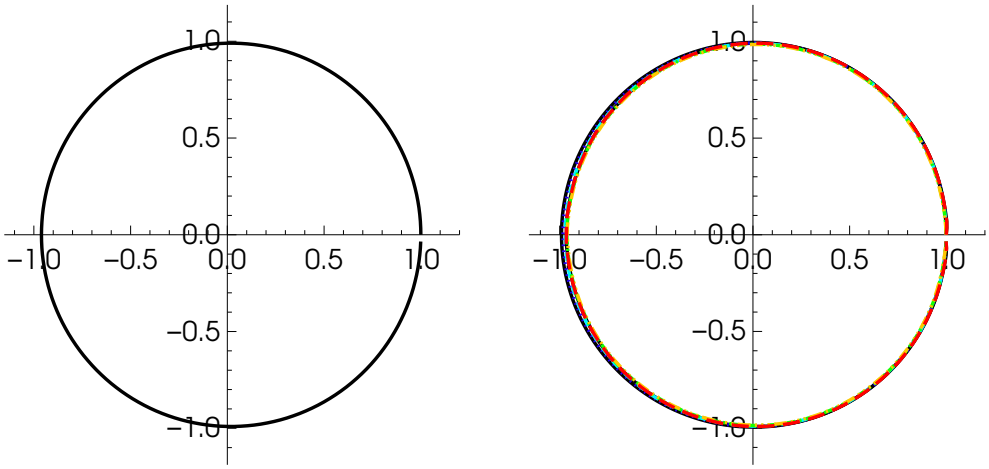

Figure 2.4: Left: Polar diagrams of the assumed electron pitch-angle distribution $H(\eta)$ for the isotropic case ($\Delta\mu = 100$). The angle made with the x-axis corresponds to the pitch angle η of the electron and the radial extent corresponds to the magnitude of the distribution. The electron flux with $\mu = 1$ is normalised to 1. Right: Polar diagrams of the emitted photon distribution $I(\epsilon, \theta_0)$ for the isotropic case. The angle made with the x-axis corresponds to the angle θ_0 and the radial extent corresponds to the magnitude of the photon distribution. The energy distribution is plotted for several energies: 10 keV (solid black), 40 keV (dotted purple), 150 kev (dashed green), 600 (dashed yellow) and 5 MeV (solid red). The photon flux with $\cos\theta_0 = 1$ is normalised to 1. As an isotropic electron distribution results in an isotropic photon distribution at all energies, these lines are all the same, with a slight discrepancy at higher energies due to the discretisation of the integral.

As a first test of this, the emitted photon spectrum from an approximately isotropic electron distribution was calculated numerically by approximating the integrals as sums

$$I(\epsilon_i, \theta_{0j}) = \sum_k \sum_l F(E_k, \eta_l) Q'(\epsilon_i, E_k, \eta_l, \theta_{0j}) sin(\eta_l) \Delta E_k \Delta\eta_l \quad . \tag{2.12}$$

As we are interested here in the shape of the electron spectrum and the angular distribution of the emitted photons, the normalisation is not important; thus, the term $\frac{\bar{n}V}{4\pi R^2}$ is omitted. The energy dependence of the electron spectrum is taken to be a single power-law as solar flare x-ray observations are often well

fit by power laws, implying close to power-law electron spectra. For energy, a pseudo-logarithmic binning scheme with 100 bins starting at 10 keV and going up to 5 MeV is used for both electrons and photons. Due to the highly-anisotropic nature of the cross-section at high energies, fine resolution in angle was needed. Angles η and θ_0 were binned in 90 evenly spaced bins between 0 and π whereas ϕ was binned in 180 evenly spaced bins between 0 and 2π. The results show, as expected, that an isotropic electron distribution produces an isotropic photon distribution (Figures 2.4 and 2.5). As expected, the photon spectrum is the same for all viewing angles, so that the lines of Figure 2.5 are identical.

The spectral index, as defined in Equation 2.6 was also calculated. This can be seen to be close to a value of 3, which is expected in the thin target case with $\delta = 2$ for the Kramers approximation. The discrepancy is due to the difference between the relativistic 3BN cross-section and the simplified Kramers cross-section.

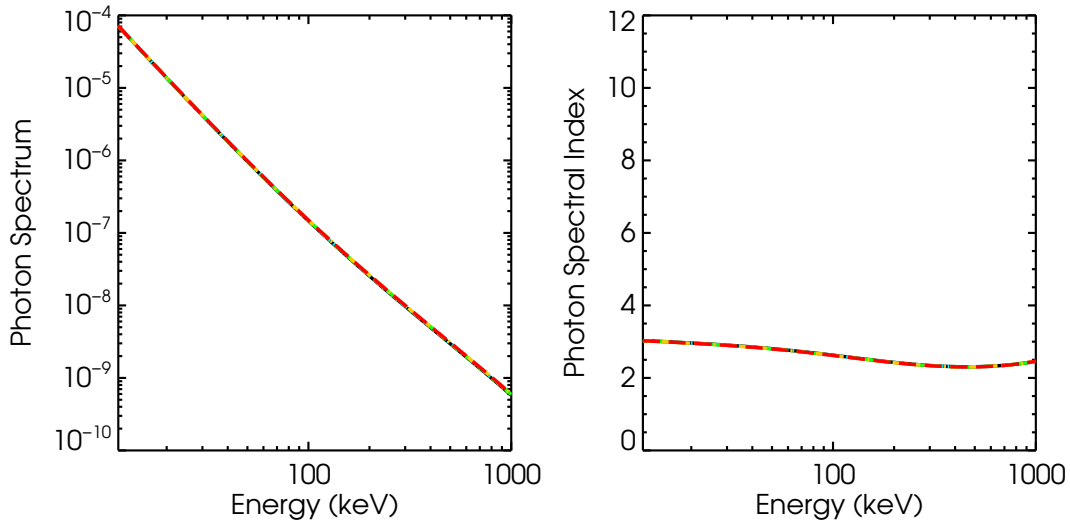

Figure 2.5: Left: Photon flux for several selected values of θ_0 - red 0°, yellow 45°, green 90°, blue 135° and black 180°. Right: Photon spectral index for several selected values of θ_0

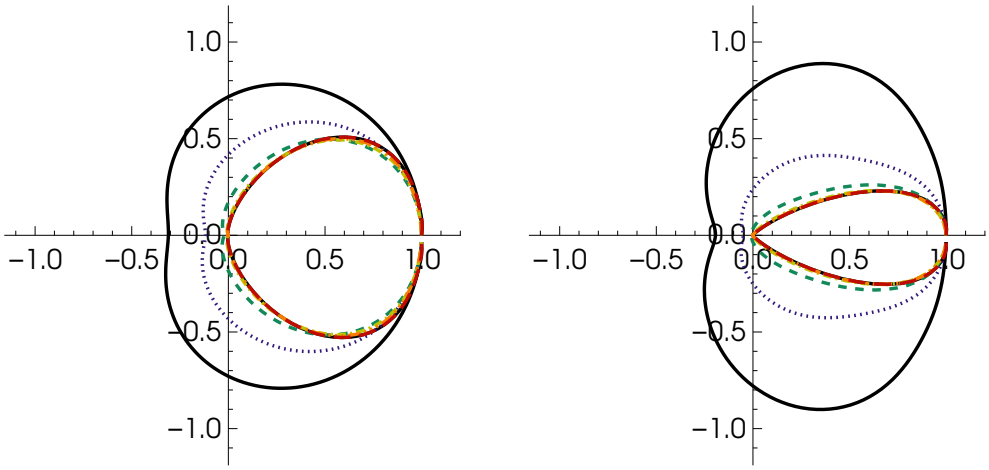

Figure 2.6: Polar diagrams of the emitted photon distribution $I(\epsilon, \theta_0)$. The angle made with the x-axis corresponds to the angle θ_0 and the radial extent corresponds to the magnitude of the photon distribution. The energy distribution is plotted for several energies: 10 keV (solid black), 40 keV (dotted purple), 150 kev (dashed green), 600 (dashed yellow) and 5 MeV (solid red). The photon flux with $\cos\theta_0 = 1$ is normalised to 1. Left: intermediate anisotropic case ($\Delta\mu = 0.4$). Right: Highly beamed case ($\Delta\mu = 0.1$).

2.2.3 X-Rays from a Beamed Electron Distribution

The angular distribution of emitted photons from a beamed distribution can be calculated in the same manner. The emitted photon distribution is close to isotropic at low energies as the cross-section is fairly broad, however at high energies it can be highly anisotropic.

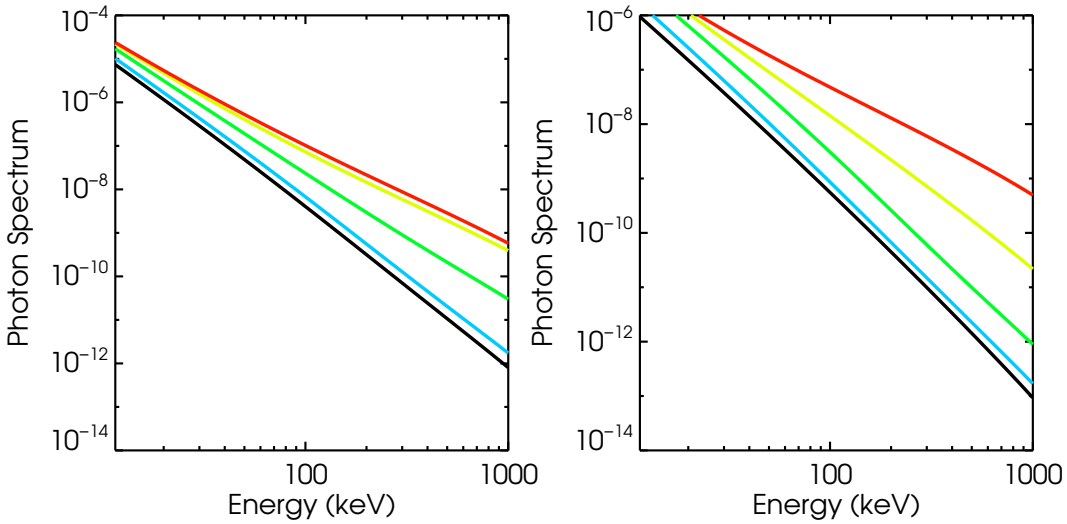

Figure 2.7: Photon flux for several selected values of θ_0 - red 0°, yellow 45°, green 90°, blue 135° and black 180°. Left: intermediate anisotropic case. Right: highly beamed case.

This method was performed for the cases of strong ($\Delta\mu = 0.1$) and intermediate ($\Delta\mu = 0.4$) Gaussian beam centred downwards, over an energy range 10 keV to 5 MeV (Figure 2.3). After applying this assumed electron spectrum to the bremsstrahlung cross-section the angular dependent X-ray emission is found, for lower energies this tends towards being closer to isotropic than the electron distribution, but for high energies it is reasonably similar to the input electron spectrum (Figure 2.6). The observed flux density (Figure 2.7) and spectral index (Figure 2.8) for a range of angles of observation are then calculated.

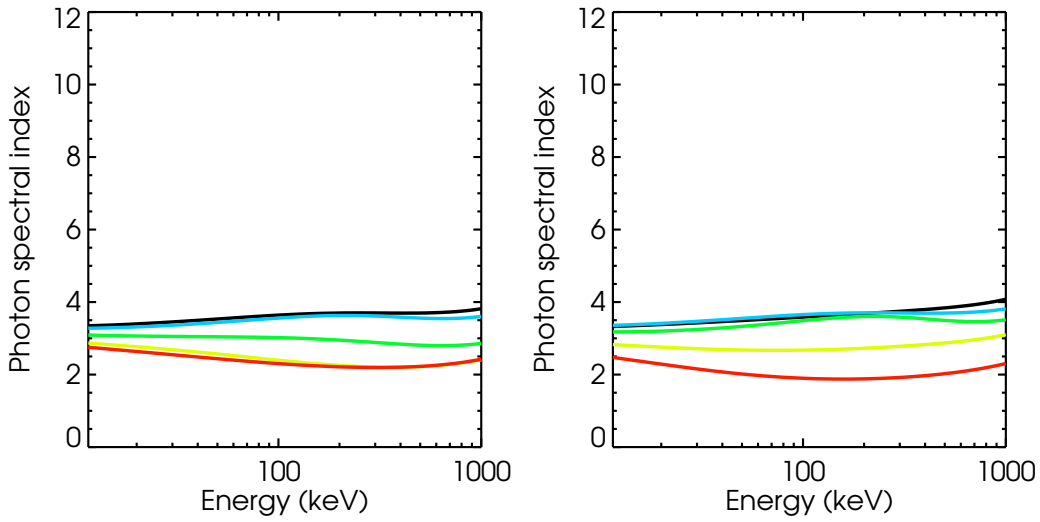

Figure 2.8: Photon spectral index for several selected values of θ_0 - red 0°, yellow 45°, green 90°, blue 135° and black 180°. Left: intermediate anisotropic case. Right: highly beamed case.

2.3 How albedo affects observations

As the albedo reflection contribution is energy dependent it can significantly distort the photon spectrum, and this distortion depends on the details of the primary photon spectrum. To accurately determine the effect of albedo, modelling of Compton scattering in the solar atmosphere is needed. The most detailed approach is to include the effects of radiative transfer as was done by Poutanen, Nagendra, and Svensson (1996).

A more straightforward approach is to use Monte Carlo simulations as was done by Bai and Ramaty (1978). These allow the Compton reflection from a variety of assumed X-ray sources to be calculated. However, these calculations assumed power-law electron spectra, and even if the initial accelerated electron spectrum was a power-law, transport effects in the solar atmosphere are likely to cause deviation in the emitting spectra.

A method for determining the albedo contribution from an arbitrary primary photon spectrum is to use a Green's function method. Magdziarz and Zdziarski

(1995) calculated an analytic angular dependent Green's function (Figure 2.9), which gives the probability a photon with energy ϵ' will be Compton scattered to energy ϵ and angle θ'. The calculations were performed assuming a cold plane-stratified atmosphere and that the initial angular distribution was isotropic in the downwards direction. The Green's functions were calculated by performing Monte Carlo simulations and fitting the results with functional forms based on previous analytic results. This allows the reflected albedo spectrum to be calculated from any given primary spectrum. The Green's functions used here are calculated using the analytic forms tabulated in Magdziarz and Zdziarski (1995).

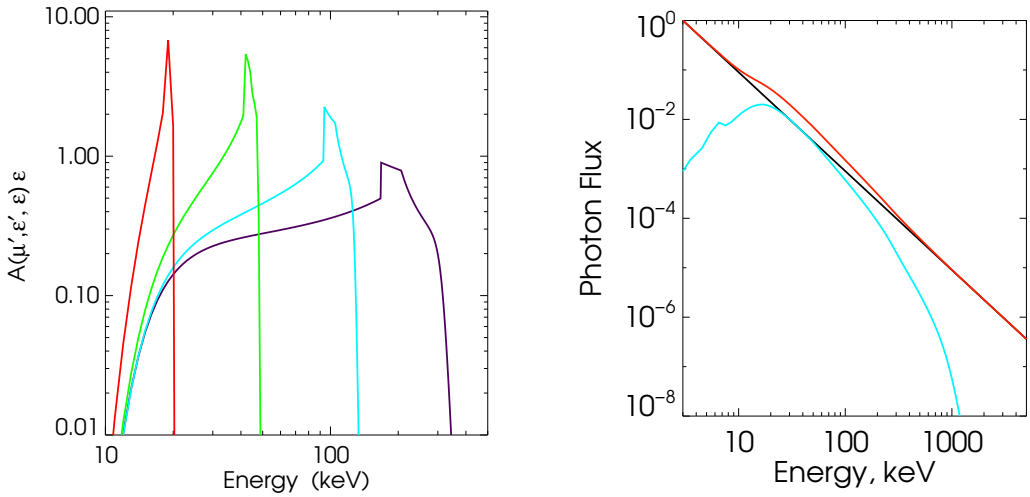

Figure 2.9: Albedo contribution to the X-ray spectrum for a source located at $\mu' = 0.9$. Left: Green's Matrix $A(\mu, \epsilon', \epsilon)\epsilon$, for incident photons of energy $\epsilon' =$ 20 (red), 50 (green), 150 (blue) and 500 (purple) keV. Right: Reflected (blue) and total (red) spectra for a primary spectrum $I_P(\epsilon) \propto \epsilon^{-2}$ normalised such that $I_P(\epsilon = 3\,\mathrm{keV}) = 1$. The spiked feature between 6 and 8 keV is due to the Ni and Fe absorption edges (after Kontar *et al.* (2006)).

The Compton scattered spectrum $I_C(\epsilon)$ resulting from primary spectrum a $I_P(\epsilon)$ is given by

$$I_C(\epsilon, \mu') = \int_{\epsilon}^{\infty} I_P(\epsilon') A(\mu', \epsilon, \epsilon') d\epsilon' \tag{2.13}$$

where $A(\mu', \epsilon, \epsilon')$ is the Green's function representing the Compton scattering dependence on the variable $\mu' = \cos\theta'$, the cosine of the heliocentric angle of the flare.

The total observed spectrum is found by summing the primary spectrum in the direction of the observer and the albedo reflection for the heliocentric angle where the flare occurred.

$$I(\epsilon) = I_P(\epsilon) + \int_{\epsilon}^{\infty} I_P(\epsilon') A(\mu', \epsilon, \epsilon') d\epsilon' \tag{2.14}$$

As well as Compton scattering, photoelectric absorption will also have a large effect on the reflected spectrum (more detail of this effect is given in Section 1.4.1). Below $\sim 10\,\mathrm{keV}$ the absorption cross-section, σ_A, is greater that the scattering cross section σ_C, and so must be correctly incorporated into the albedo Green's matrix. As the level of photoelectric absorption is atomic species dependent, for solar flare spectra accurate elemental abundances for the photosphere are needed.

2.4 Effect of anisotropic electron distribution

To examine the effect of albedo the reflection from power-law distributions are considered from several viewing angles.

The primary emission observed for a flare at heliocentric angle θ' is expected to come from a small range in angle in the direction of the observed. Considering the geometry it is clear that the upward directed photon distribution can be approximated as

$$I_U(\epsilon) = I(\epsilon, \theta_0 = 180^\circ - \theta') \quad . \tag{2.15}$$

The albedo reflected component, on the other hand, results from the photons directed down towards the photosphere. This is likely to be a broader distribution so that an average is taken over a downwards directed cone concentric with the

mean direction of the electron distribution and with half angle α. The downward directed flux can then be defined as

$$I_D(\epsilon) = \frac{\int_{\theta_0=0}^{\alpha} I(\epsilon, \theta_0) \sin\theta_0 d\theta_0}{\int_{\theta_0=0}^{\alpha} \sin\theta_0 d\theta_0} \quad . \tag{2.16}$$

The reflected component, due to albedo, of a given X-ray spectrum incident on the photosphere can then be characterised by using the Green's function A dependent on observation angle θ', described in Section 2.3. Thus, the total observed X-ray spectrum will be given by the sum of the directly observed and reflected components (c.f. Equation 2.14):

$$I_O = I_U + AI_D \tag{2.17}$$

where I_O is the total and I_U, I_D are upward and downward directed components.

The upward and downward components of the photon flux are now given by vectors. The observer directed component is defined as

$$\mathbf{I_U} = \{I_U(\epsilon_i), ..., I_U(\epsilon_n)\}, \qquad i = 1, .., n \tag{2.18}$$

where ϵ_i corresponds to the centre energy of the photon bin and n is the number of bins in photons space. The photosphere directed component is given by $\mathbf{I_D}$ defined in the same way. Similarly the angle dependent Green's function is here calculated in the form of a $n \times n$ Green's matrix $\mathbf{A}$. The vector representing the total observed flux is simply given by

$$\mathbf{I_O} = \mathbf{I_U} + \mathbf{AI_D} \tag{2.19}$$

where A is the albedo matrix constructed from Green's functions. This is defined by

$$\mathbf{A}_{ij}(\epsilon_i, \mu') = \int_{\epsilon_j}^{\epsilon_{j+1}} A(\mu', \epsilon_i, \epsilon') d\epsilon' \, . \tag{2.20}$$

The integral is calculated in the wavelength domain due to the sharp features of the Green's function.

The albedo reflection for flares at a range of heliocentric angles (Kontar *et al.*, 2006) was then calculated (Figures 2.10 and 2.11). Emission close to the solar limb shows very little influence from albedo as expected, and the expected power-law in photon energy is recovered, however emission closer to the disk centre shows a distinctive hump over the entire energy range due to the albedo reflection. For the case of beamed electron spectrum at low energies, the primary photon flux directed towards the observer for limb events is several times greater than that for events on the disk centre as the albedo contribution is low at these energies. This results in the total observed flux being greater for limb events.

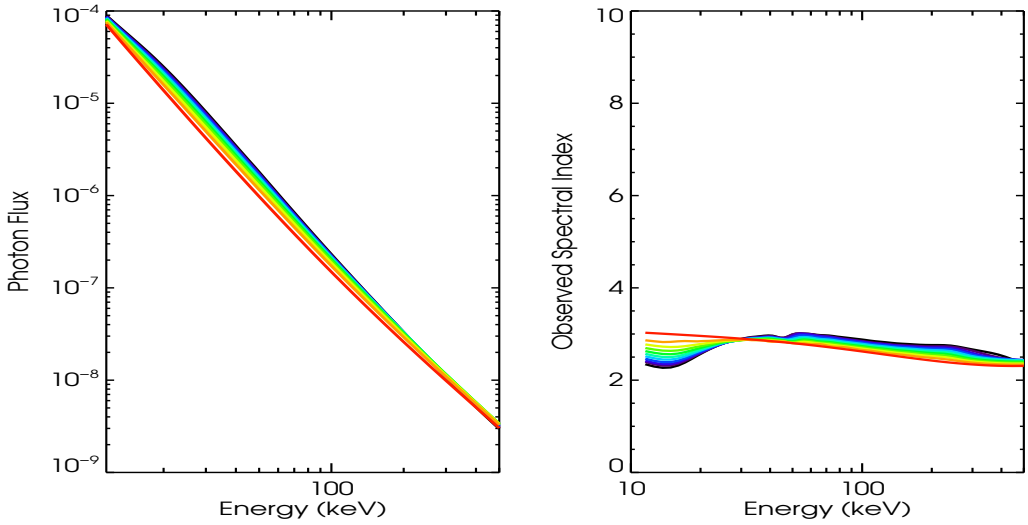

Figure 2.10: Left: Total observed photon flux for the isotropic case including reflected albedo component for flares located at different places on the disk - disk centre ($\cos\theta' = \mu' = 1$) - black, $\mu' = 0.9$ - purple, $\mu' = 0.8$ - dark blue, $\mu' = 0.7$ - blue, $\mu' = 0.6$ - bright blue, $\mu' = 0.5$ - dark green, $\mu' = 0.4$ - green, $\mu' = 0.3$ - bright green, $\mu' = 0.2$ - yellow, $\mu' = 0.1$ - orange, and limb ($\cos\theta' = 0.01$) - red. Right: Photon spectral index for the total observed spectrum against photon energy

Due to the effect of albedo one of the most notable variations with changing anisotropy is in the photon spectral index, calculated as in Equation 2.6. This was calculated for both the primary photon spectrum for a range of viewing angles and for the total observed spectrum, including albedo component, for a range of positions on the solar disk. The influence of albedo can be seen more clearly in

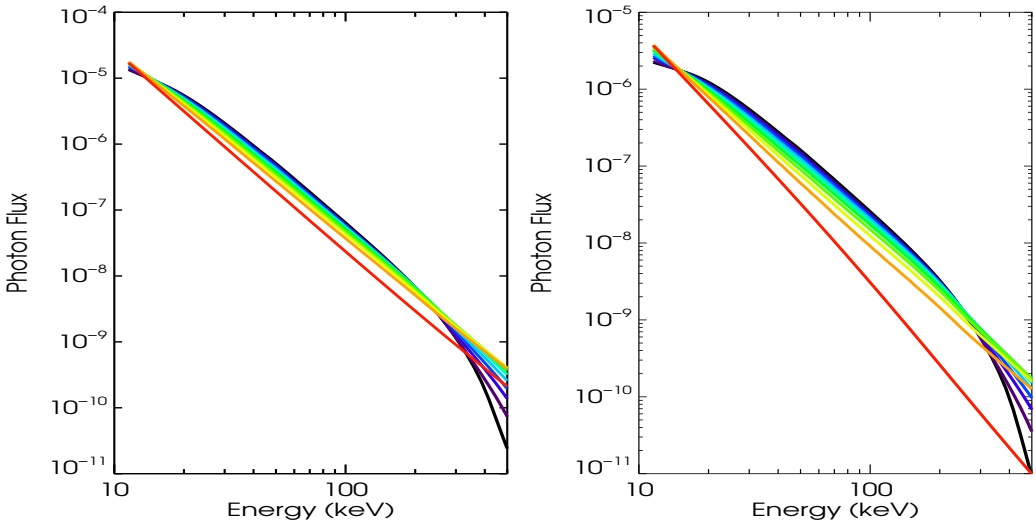

Figure 2.11: Total observed photon flux including reflected albedo component for flares located at different places on the disk, ranging from disk centre to limb Left: intermediate anisotropic case. Right: Highly beamed case. Colours as in Figure 2.10

flares close to the disk centre which show a large increase in γ above 200 keV, and this is more pronounced in the strong beaming case (Figure 2.12).

2.5 Other distributions

While beamed distributions are the most popular model for the electron angular distribution there are many other potential angular distributions. Several commonly considered distributions were assumed and the full photon spectra including albedo reflection was calculated for a range of source heliocentric angles.

2.5.1 Pancake

The pancake distribution is the opposite extreme to the beam; here, the majority of the velocity distribution is perpendicular to the magnetic field i.e. $\langle v_{\parallel} \rangle <<$

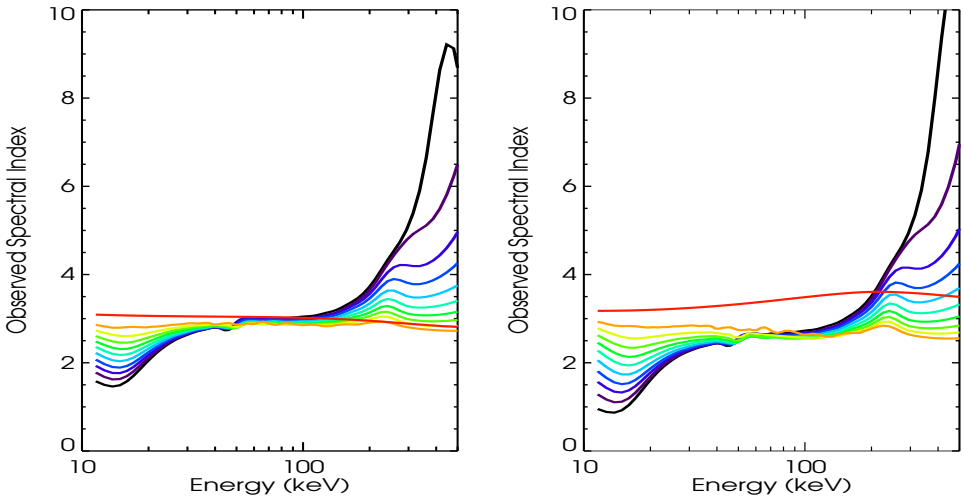

Figure 2.12: Photon spectral index for the total observed spectrum against photon energy for flares located at different places on the disk, ranging from disk centre to limb. Left: intermediate anisotropic case. Right: highly beamed case. Colours as in Figure 2.10

$\langle v_\perp \rangle$. This distribution can be used to describe the behaviour of electrons at magnetic mirror points. One common form for this distribution is:

$$H(\eta) = \exp\left(\frac{-(\eta - \pi/2)^2}{\eta_0^2}\right) \tag{2.21}$$

Similar to the beamed case the strength of the pancake distribution is controlled by the parameter η_0 for $\eta_0 << 1$ the electrons form a narrow distribution around $\pi/2$, as η_0 increases the distribution becomes much broader (Figure 2.13). Pancake distributions have been suggested as an explanation for the looptop hard X-ray sources first viewed by Yohkoh (Petrosian and Donaghy, 1999).

It has been suggested this distribution can be produced by betatron acceleration in a collapsing magnetic trap (Karlický and Kosugi, 2004).

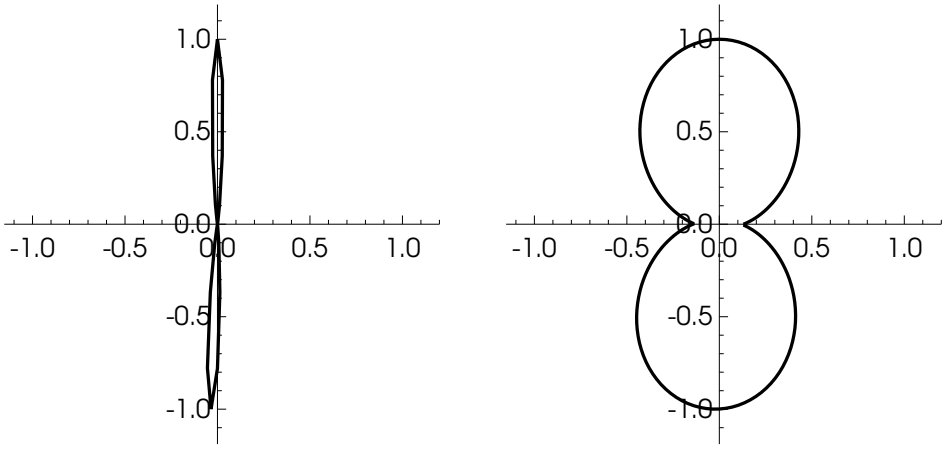

Figure 2.13: Polar diagram of the normalised angular variation of the assumed electron distribution $F(E, \eta)$. The angle made with the x-axis corresponds to the pitch angle η of the electron distribution and the radial extent corresponds to the magnitude of the electron distribution. Left: $\eta_0 = 0.07$ Right: $\eta_0 = 1.1$

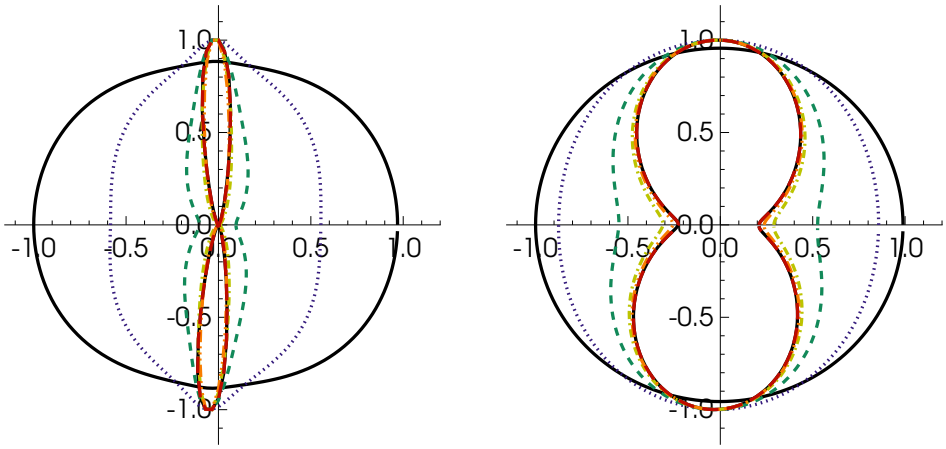

Figure 2.14: Polar diagram of the normalised angular variation of the assumed emitted photon distribution $I(\epsilon, \theta_0)$. The angle made with the x-axis corresponds to the angle θ_0 and the radial extent corresponds to the magnitude of the photon distribution. The energy distribution is plotted for a range in energies ranging from 10 keV (black) to 5 MeV (light blue). Left: $\eta_0 = 0.07$, Right: $\eta_0 = 1.1$. Colour scheme as in Figure 2.6.

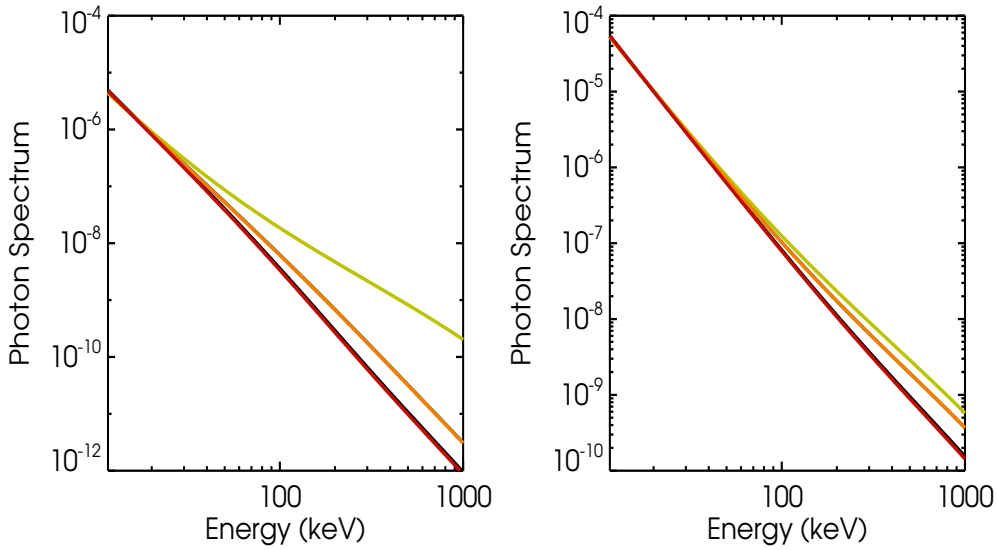

Figure 2.15: Photon spectra I against ϵ for several selected values of θ_0 - red 0°, orange 45°, yellow 90°, green 135° and black 180°. Left: $\eta_0 = 0.07$ Right: $\eta_0 = 1.1$

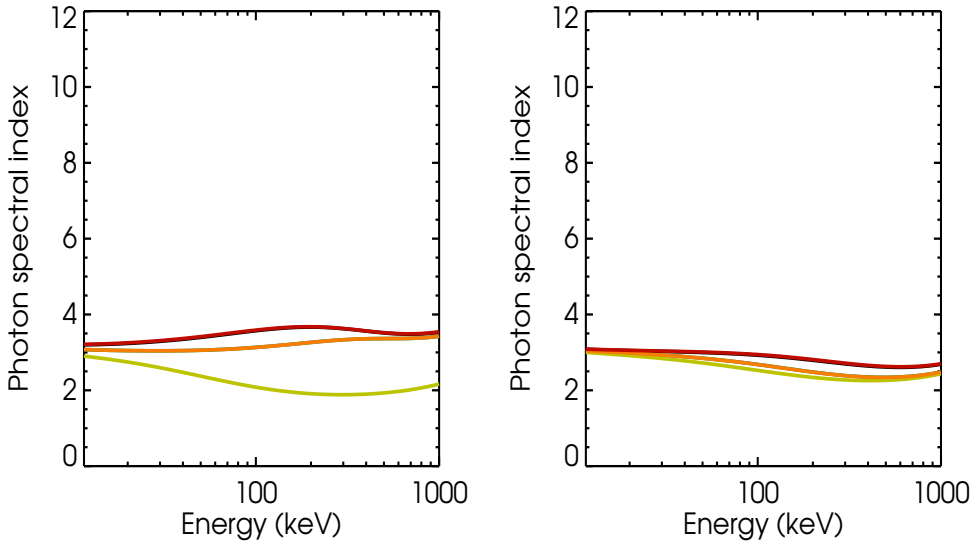

Figure 2.16: Photon spectral index γ against energy ϵ for several selected values of θ_0 - red 0°, orange 45°, yellow 90°, green 135° and black 180°. Left: $\eta_0 = 0.07$ Right: $\eta_0 = 1.1$

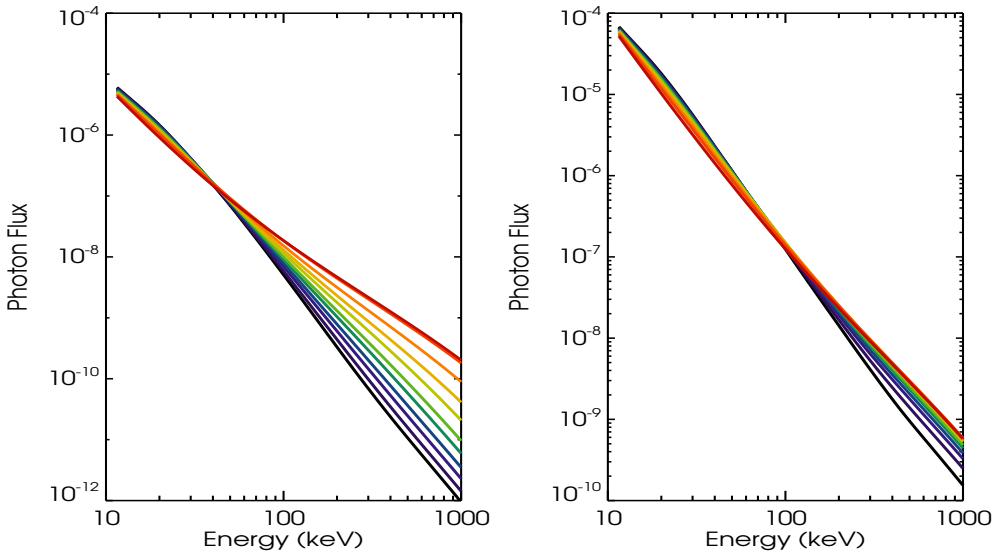

Figure 2.17: Total observed electron spectrum including reflected albedo component against photon energy for flares located at different places on the disk: disk centre $\cos\theta' = 1$ black, $\mu' = 0.9$ - indigo, $\mu' = 0.8$ - purple, $\mu' = 0.7$ - blue, $\mu' = 0.6$ - teal, $\mu' = 0.5$ - lime green, $\mu' = 0.4$ - yellow, $\mu' = 0.3$ -light orange, $\mu' = 0.2$ - orange, $\mu' = 0.1$ - brick red, and limb ($\cos\theta' = 0.01$) - red. Left: $\eta_0 = 0.07$ Right: $\eta_0 = 1.1$

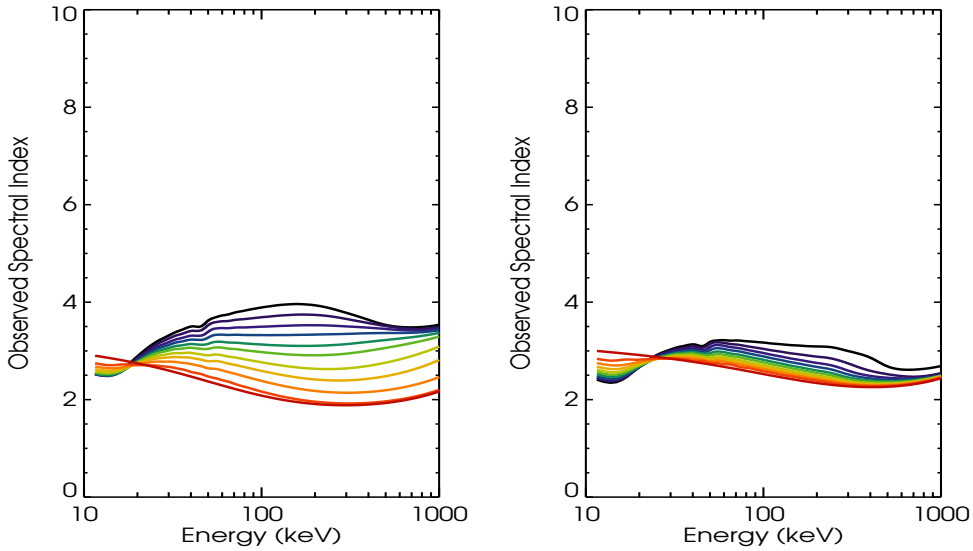

Figure 2.18: Photon spectral index γ for the total observed electron spectrum including reflected albedo component against photon energy for flares located at different places on the disk, ranging from disk centre $\cos\theta' = 1$ (black) to limb $\cos\theta' = 0.01$. Left: $\eta_0 = 0.07$ Right: $\eta_0 = 1.1$. Colour scheme as in Figure 2.17

2.5.2 Gaussian Loss-cone

Another commonly studied form of the electron angular distribution is the Gaussian loss-cone (e.g. Fleishman and Kuznetsov 2010)

$$H(\mu) = \begin{cases} \exp\left(\frac{-(\mu-\mu_c)^2}{\Delta\mu^2}\right) & \text{if } \mu > \mu_c \\ 1 & -\mu_c < \mu < \mu_c \\ \exp\left(\frac{(\mu+\mu_c)^2}{\Delta\mu^2}\right) & \text{if } \mu < -\mu_c \end{cases}$$

This distribution can occur when the electrons are magnetically trapped in a coronal loop. Electrons with pitch angle $\mu < \mu_c$ are trapped in the less dense region whereas electrons with $\mu > \mu_c$ precipitate down to the higher density

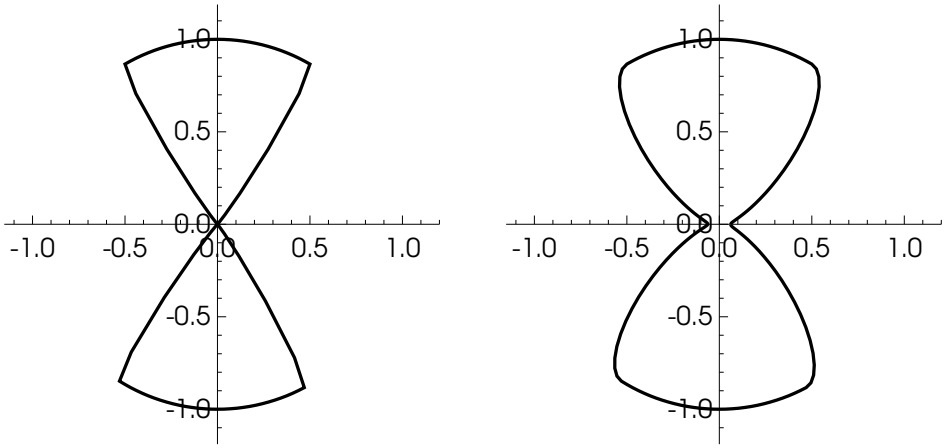

Figure 2.19: Polar diagram of the normalised angular variation of the assumed electron distribution $F(E, \eta)$. The angle made with the x-axis corresponds to the pitch angle η of the electron distribution and the radial extent corresponds to the magnitude of the electron distribution. Left: $\Delta\mu = 0.07$ Right: $\Delta\mu = 0.3$.

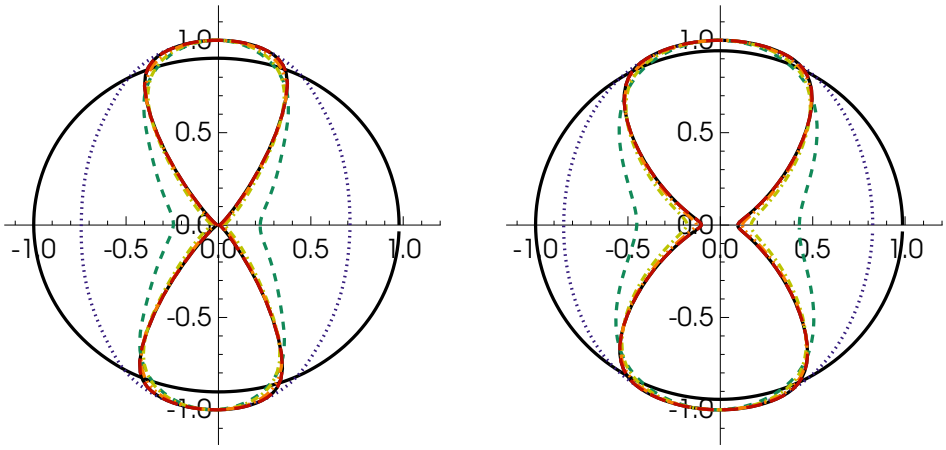

Figure 2.20: Polar diagram of the normalised angular variation of the assumed emitted photon distribution $I(\epsilon, \theta_0)$. The angle made with the x-axis corresponds to the angle θ_0 and the radial extent corresponds to the magnitude of the photon distribution. The energy distribution is plotted for a range in energies ranging from 10 keV (black) to 5 MeV (light blue) Left: $\Delta\mu = 0.07$ Right: $\Delta\mu = 0.3$. Colour scheme as in Figure 2.6.

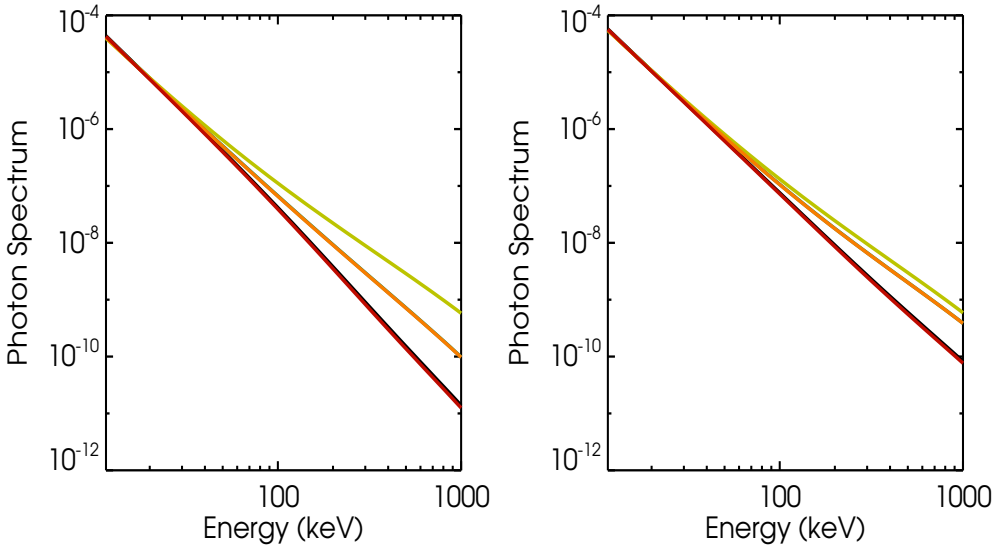

Figure 2.21: Photon spectra I against ϵ for several selected values of θ_0 - red 0°, orange 45°, yellow 90°, green 135° and black 180°. Left: $\Delta\mu = 0.07$ Right: $\Delta\mu = 0.3$

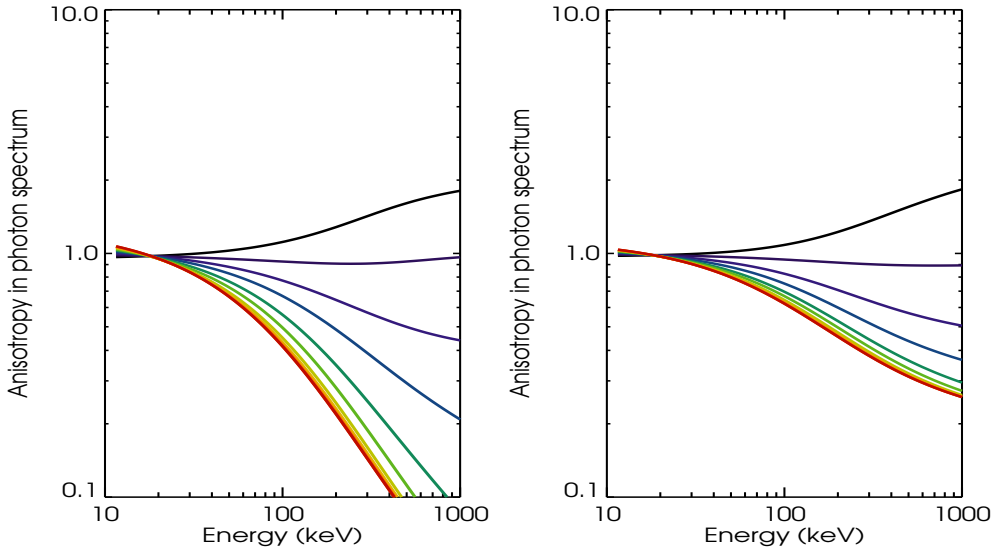

Figure 2.22: Anisotropy (defined here as I_D/I_U) against photon energy for flares located at different places on the disk ranging from disk centre $\cos\theta' = 1$ (black) to limb $\cos\theta' = 0.01$. Left: $\Delta\mu = 0.07$ Right: $\Delta\mu = 0.3$. Colour scheme as in Figure 2.17.

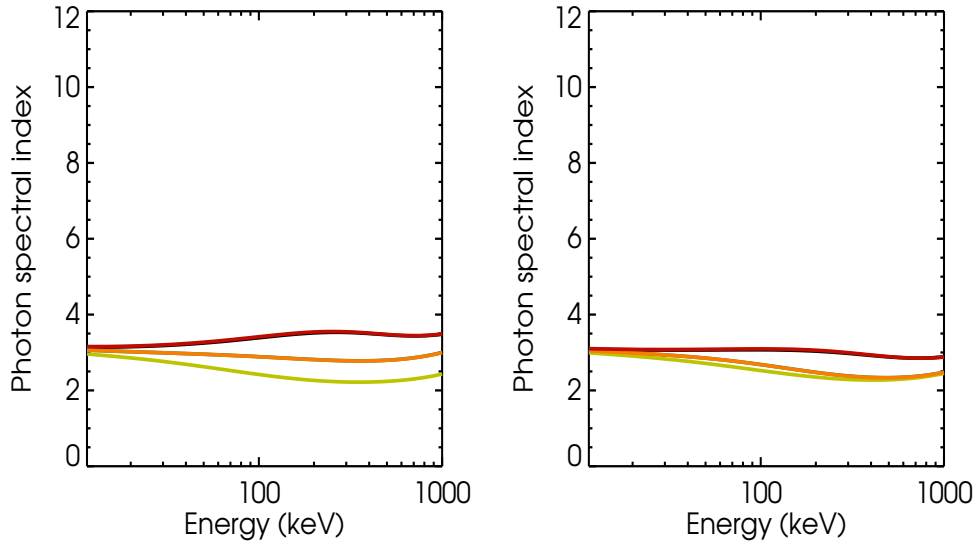

Figure 2.23: Photon spectral index γ against energy ϵ for several selected values of θ_0 - red 0°, orange 45°, yellow 90°, green 135° and black 180°.

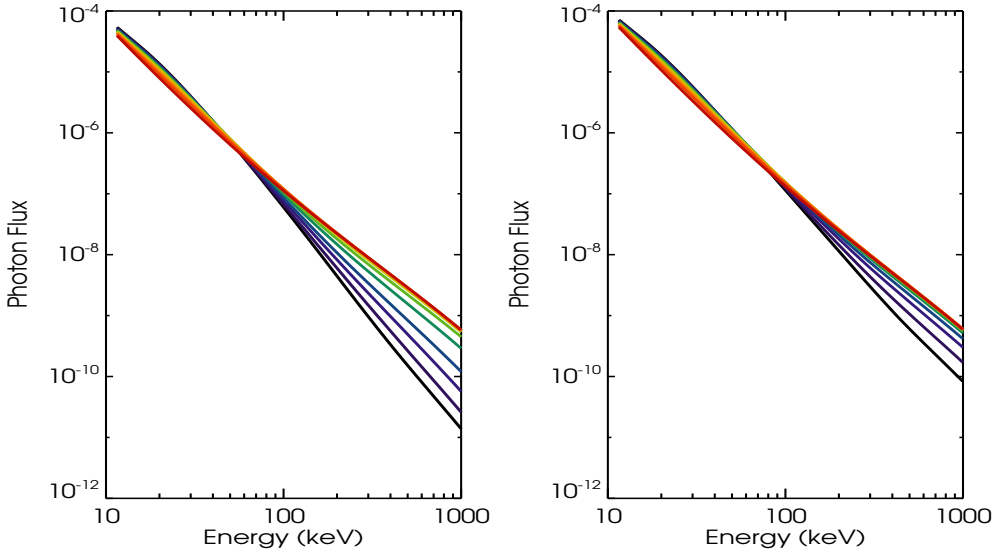

Figure 2.24: Total observed electron spectrum including reflected albedo component against photon energy for flares located at different places on the disk ranging from disk centre $\cos\theta' = 1$ (black) to limb $\cos\theta' = 0.01$. Left: $\Delta\mu = 0.07$ Right: $\Delta\mu = 0.3$.Colour scheme as in Figure 2.17.

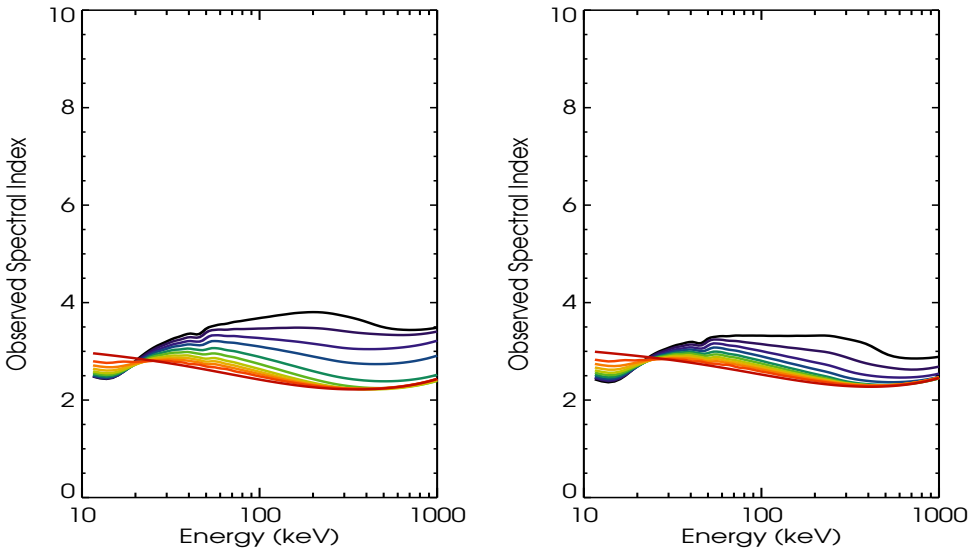

Figure 2.25: Photon spectral index γ for the total observed electron spectrum including reflected albedo component against photon energy for flares located at different places on the disk ranging from disk centre $\cos\theta' = 1$ (black) to limb $\cos\theta' = 0.01$. Left: $\Delta\mu = 0.07$ Right: $\Delta\mu = 0.3$. Colour scheme as in Figure 2.17.

2.5.3 Sin-n

Another way of modelling a loss cone is a distribution of the form $\sin^n$ (e.g. Fleishman and Melnikov 2003)

$$H(\mu) = \begin{cases} \sin^n\left(\frac{\pi\eta}{2\eta_c}\right) & \text{if } 0 < \eta < \eta_c \\ 1 & \eta_c < \eta < \pi - \eta_c \\ \sin^n\left(\frac{\pi(\eta-\pi)}{2\eta_c}\right) & \text{if } \pi - \eta_c < \eta < \pi \end{cases}$$

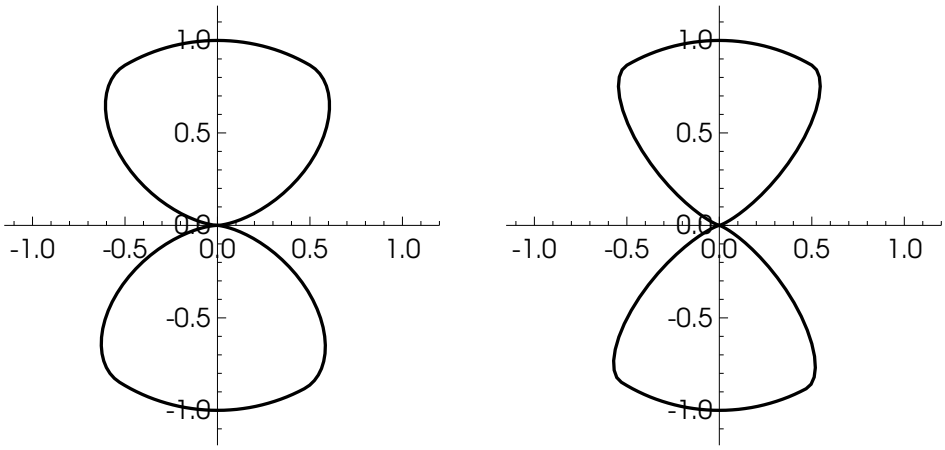

Figure 2.26: Polar diagram of the normalised angular variation of the assumed electron distribution $F(E, \eta)$. The angle made with the x-axis corresponds to the pitch angle η of the electron distribution and the radial extent corresponds to the magnitude of the electron distribution Left: $n = 2$ Right: $n = 6$

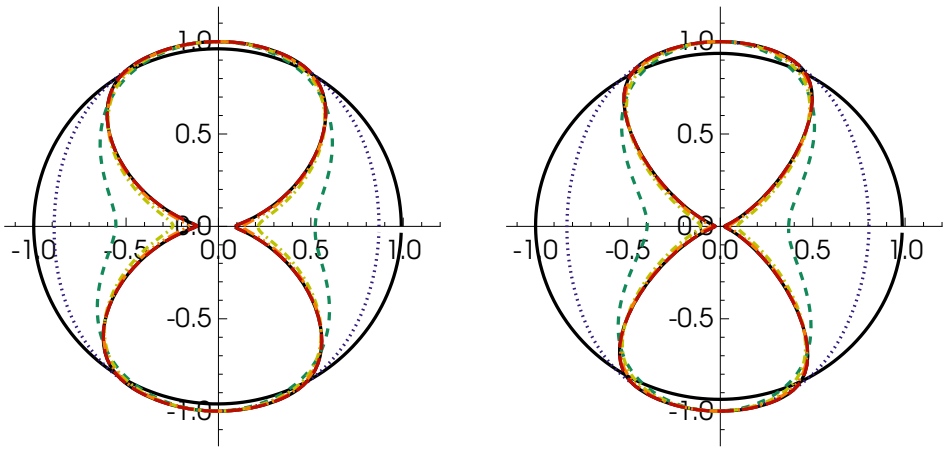

Figure 2.27: Polar diagram of the normalised angular variation of the assumed emitted photon distribution $I(\epsilon, \theta_0)$. The angle made with the x-axis corresponds to the angle θ_0 and the radial extent corresponds to the magnitude of the photon distribution. The energy distribution is plotted for a range in energies ranging from 10 keV (black) to 5 MeV (light blue). Left: $n = 2$ Right: $n = 6$. Colour scheme as in Figure 2.6.

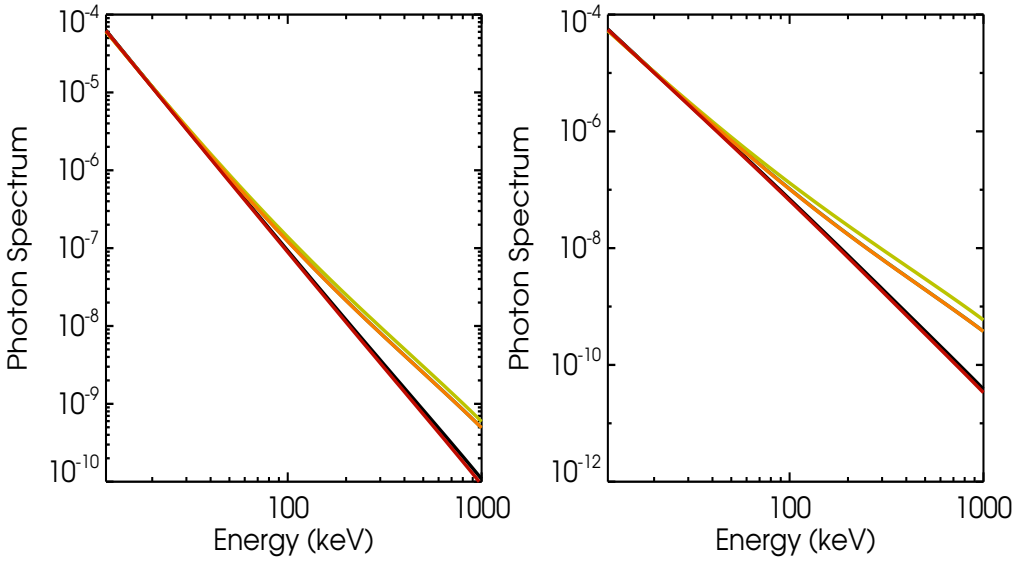

Figure 2.28: Photon spectra I against ϵ for several selected values of θ_0 - red 0°, orange 45°, yellow 90°, green 135° and black 180°. Left: $n = 2$ Right: $n = 6$

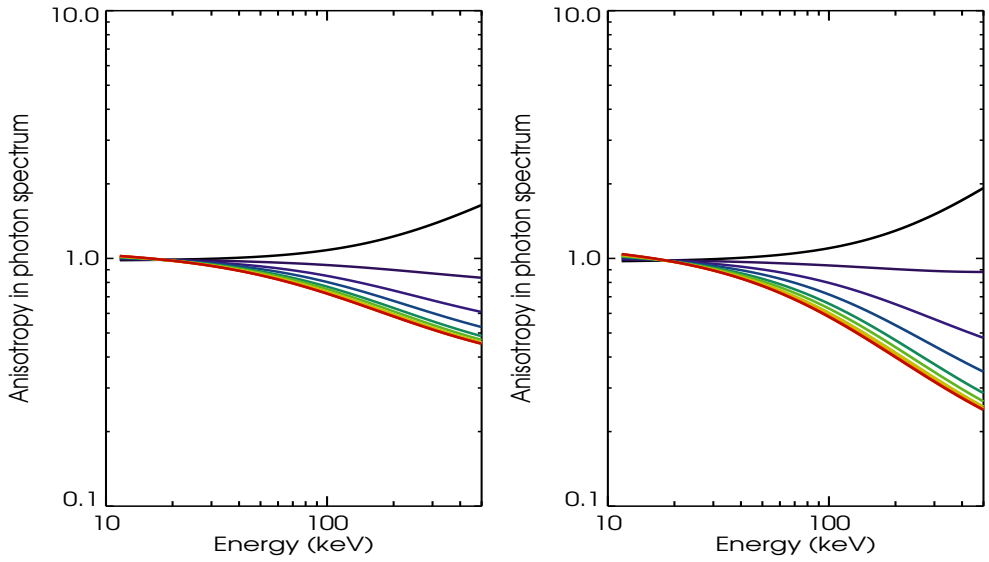

Figure 2.29: Anisotropy (defined here as I_D/I_U) against photon energy for flares located at different places on the disk ranging from disk centre $\cos\theta' = 1$ (black) to limb $\cos\theta' = 0.01$. Left: $n = 2$ Right: $n = 6$. Colour scheme as in Figure 2.17.

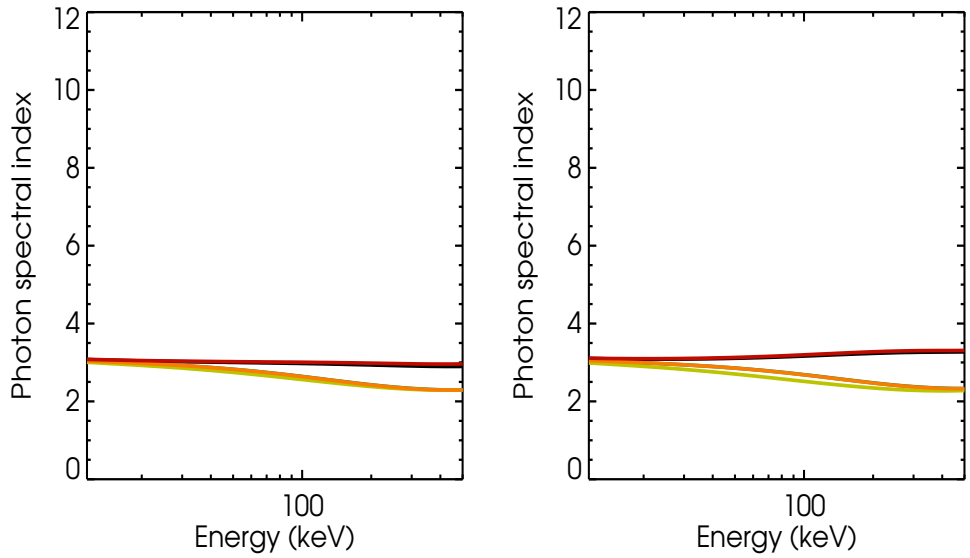

Figure 2.30: Photon spectral index γ against energy ϵ for several selected values of θ_0 - red 0°, orange 45°, yellow 90°, green 135° and black 180°. Left: $n = 2$ Right: $n = 6$

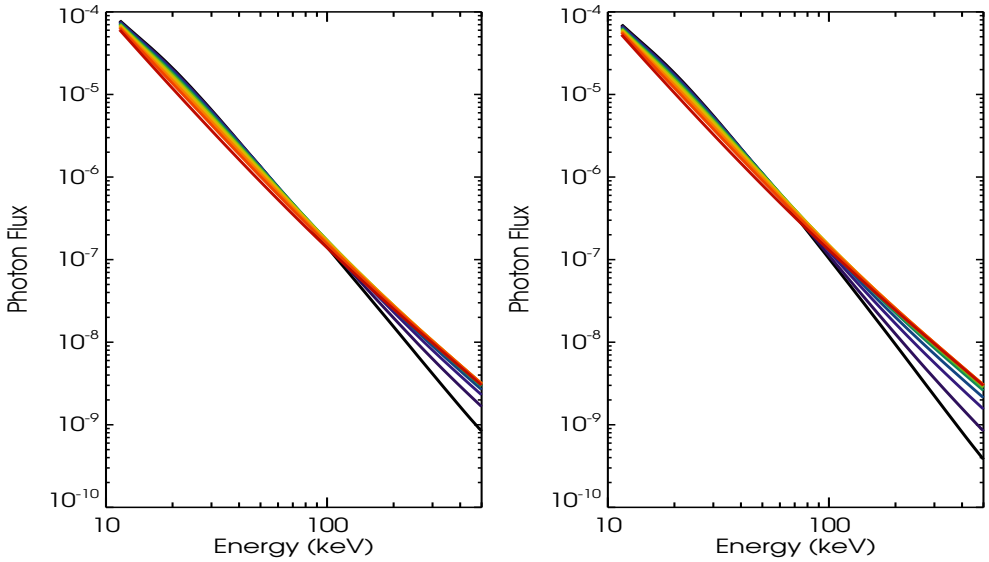

Figure 2.31: Total observed electron spectrum including reflected albedo component against photon energy for flares located at different places on the disk ranging from disk centre $\cos\theta' = 1$ (black) to limb $\cos\theta' = 0.01$. Left: $n = 2$ Right: $n = 6$. Colour scheme as in Figure 2.17.

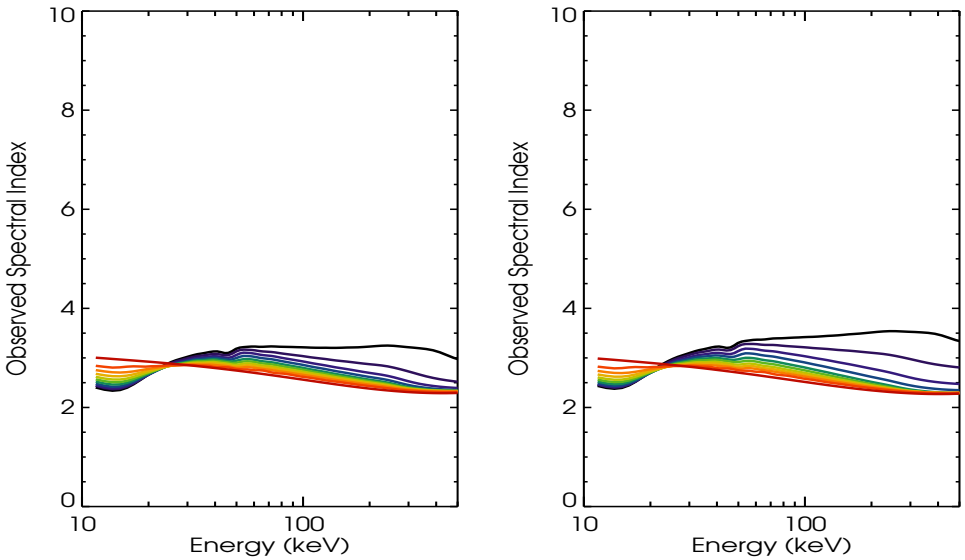

Figure 2.32: Photon spectral index γ for the total observed electron spectrum including reflected albedo component against photon energy for flares located at different places on the disk ranging from disk centre $\cos\theta' = 1$ (black) to limb $\cos\theta' = 0.01$. Left: $n = 2$ Right: $n = 6$. Colour scheme as in Figure 2.17.

2.5.4 Hemispheric average

Unrealistic simple two component distributions were also considered as these are the most directly analogous to the bi-directional inversions performed in Chapter 4.

The simplest two component distribution takes averages over hemispheres in both the downward ($0 < \eta < \pi/2$) and upward ($\pi/2 < \eta < \pi$) directions. This is similar to bi-directional inversions where the bremsstrahlung cross section is averaged over $\alpha = 90°$. This distribution is taken to have the form:

$$F(E,\mu) = \begin{cases} C_D E^{-\delta} & \text{if } 0 < \eta < \pi/2 \\ C_U E^{-\delta} & \text{if } \pi/2 < \eta < \pi \end{cases}$$

The ratio of the scaling constants C_D and C_U gives the anisotropy of this distribution

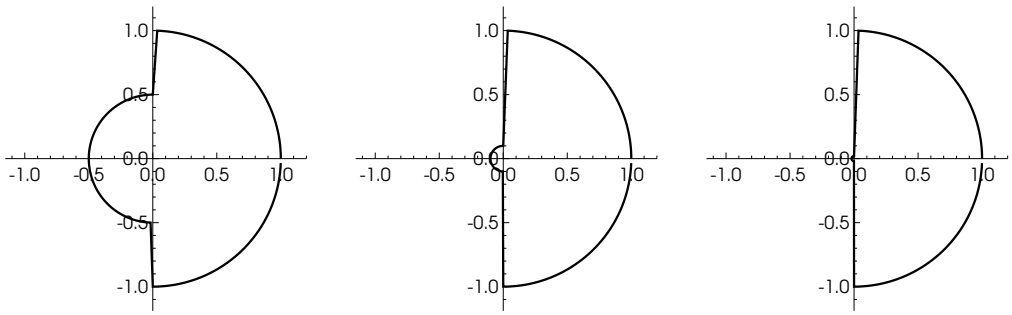

Figure 2.33: Polar diagram of the normalised angular variation of the assumed electron distribution $F(E,\eta)$. The angle made with the x-axis corresponds to the pitch angle η of the electron distribution and the radial extent corresponds to the magnitude of the electron distribution. Left: ratio of 2:1 Middle: ratio of 10:1 Right: ratio of 50:1 .

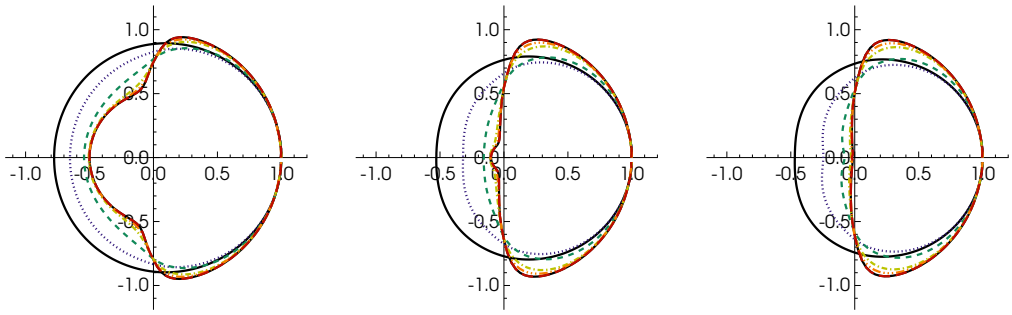

Figure 2.34: Polar diagram of the normalised angular variation of the assumed emitted photon distribution $I(\epsilon, \theta_0)$. Left: ratio of 2:1 Middle: ratio of 10:1 Right: ratio of 50:1. Colour scheme as in Figure 2.6.

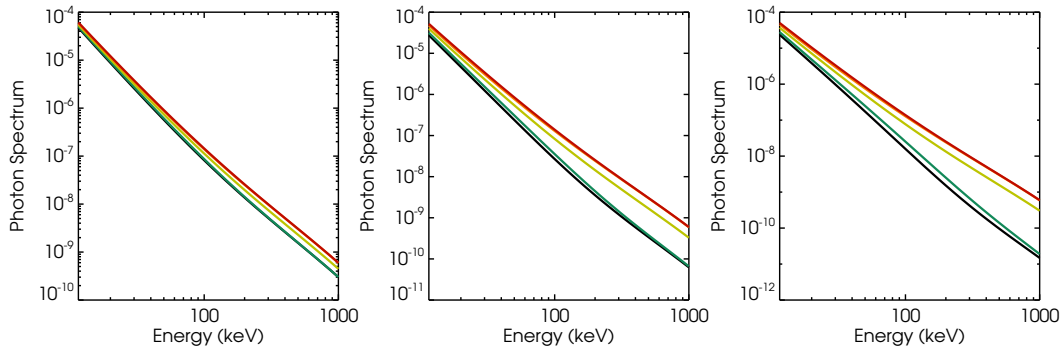

Figure 2.35: Photon spectra I against ϵ for several selected values of θ_0 - red 0°, orange 45°, yellow 90°, green 135° and black 180°. Left: ratio of 2:1 Middle: ratio of 10:1 Right: ratio of 50:1.

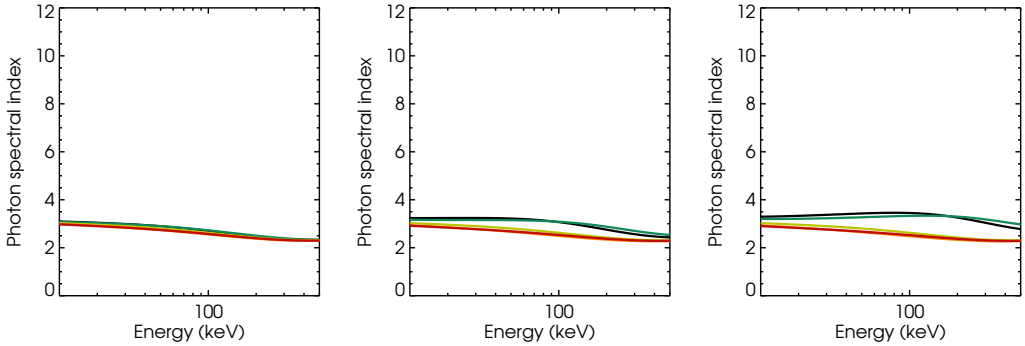

Figure 2.36: Photon spectral index γ against energy ϵ for several selected values of θ_0 - red 0°, orange 45°, yellow 90°, green 135° and black 180°. Left: ratio of 2:1 Middle: ratio of 10:1 Right: ratio of 50:1.

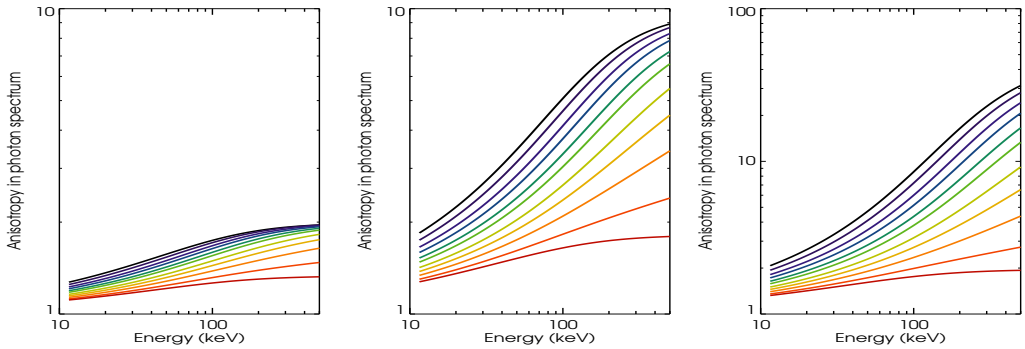

Figure 2.37: Anisotropy (I_D/I_U) against photon energy. Left: ratio of 2:1 Middle: ratio of 10:1 Right: ratio of 50:1. Colour scheme as in Figure 2.17.

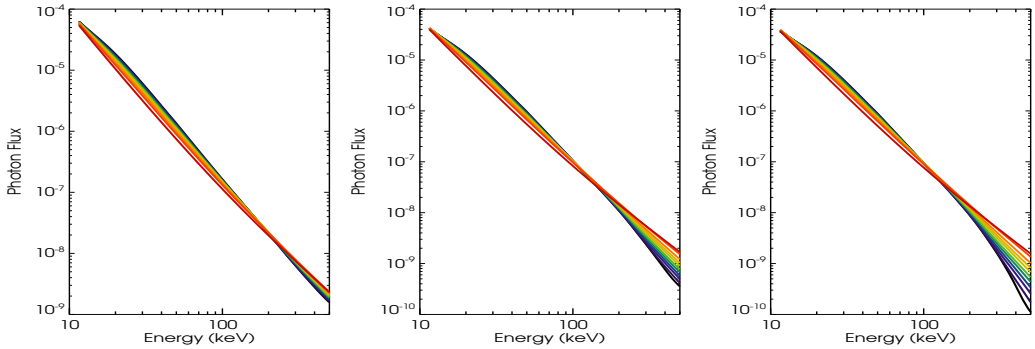

Figure 2.38: Total observed electron spectrum including reflected albedo component against photon energy. Left: ratio of 2:1 Middle: ratio of 10:1 Right: ratio of 50:1. Colour scheme as in Figure 2.17.

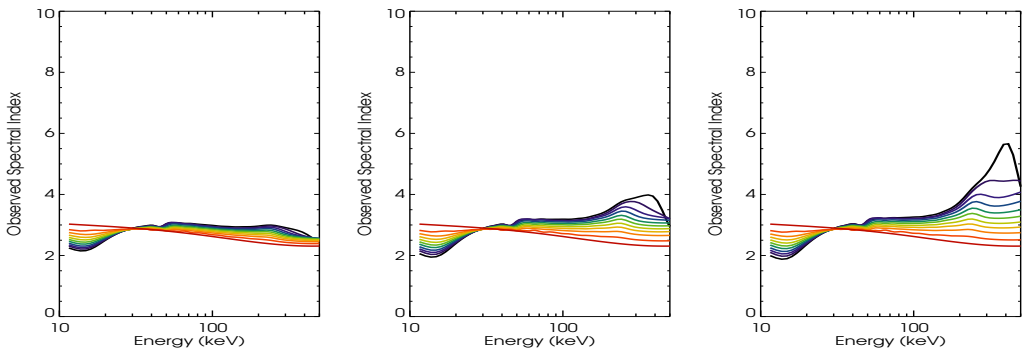

Figure 2.39: Photon spectral index γ for the total observed electron spectrum including reflected albedo component against photon energy. Left: ratio of 2:1 Middle: ratio of 10:1 Right: ratio of 50:1. Colour scheme as in Figure 2.17.

2.6 Conclusions

These examples show the effect of albedo can be a very significant influence on the observed photon spectrum, particularly for hard spectra from flares located close to the disk centre. It is also important to note, similar to the presence of a low energy cutoff in the electron spectrum, that albedo can cause a flattening of the observed photon spectrum at low energies. For an initial electron spectral index $\delta = 2$ the non-relativistic isotropic approximation gives an expected observed photon spectral index of $\gamma = 3$, when albedo is not included. The inclusion of albedo can lead to a reduction in spectral index of ~ 1 at low energies and an increase in spectral index of ~ 0.5 at high energies for flares at disk center (Figure 2.10).

The forward modelling shows very clearly that when there is significant beaming in the emitting electron population it will result in a very strong albedo emission. The effects of albedo are most pronounced near the disk centre where a greater proportion of the scattered X-ray photons will be observed. For many cases with substantial beaming, particularly close to the disk centre, the albedo component can dominate over the primary component resulting in a spectrum with very different characteristics to the assumed emitted power-law-like x-ray spectrum (Figure 2.11). The effect of anisotropy can most clearly be seen via the energy dependence of the photon spectral index, γ, for a strong beam this should rapidly increase at high energies, for example, a strongly beamed flare with $\delta = 2$ shows an increase from $\gamma \approx 3$ at 100 keV to $\gamma \approx 10$ at 400 keV (Figure 2.12).

For non-beamed distributions (Figures 2.13 - 2.32) the influence of albedo on the observed X-ray spectrum was much less significant as expected, as fewer downward going electrons result in fewer downward emitted photons which can be backscattered. However, all perpendicular distributions do show a slight influence of albedo. For all of the transverse distributions the angular distribution at low energies is much closer to isotropic than from downward-directed distributions (Figures 2.14, 2.20 and 2.27).

For the strongly perpendicular distributions, such as the pancake distribution with $\Delta\mu = 0.07$, (Figure 2.13) the variation with viewing angle is greater (Fig-

ures 2.15 and 2.16). However, the influence of albedo on these distributions is slightly smaller, due to the smaller fraction of downward-going photons. As these emit photon distributions which are close to isotropic below 100 keV, where the strongest influence of albedo occurs, the effect of albedo is similar to the isotropic case at these energies, resulting in an increase in flux of ~ 2 and an overestimate of spectral index of ~ 0.5 for events on the disk centre (Figure 2.18).

On the other hand for high energies at high viewing angles there is a greater amount of upward going photon flux, so the effect of albedo is negligible, even compared to the isotropic case (for example Figure 2.22). As albedo affects even transverse distributions to a varying degree with position on the disk centre, it should be considered when performing centre-to-limb studies. As the broader Gaussian loss-cone distributions and the $\sin^n$ distributions are very similar to each other (Figures 2.19 and 2.26) they exhibit similar signatures (Figures 2.25 and 2.32). As with the beamed distributions the broader perpendicular distributions produce spectra which are similar to the isotropic distribution.

The hemispheric averaged cases (Figures 2.33 - 2.39) show a similar variation to the downward beam but with a smaller increase in γ at high energies as would be expected, as the most significant contribution to the albedo spectrum occurs close to $\mu = 1$ (Figure 2.39). The comparison between the anisotropy in the electron spectrum and the corresponding anisotropy in the photon spectrum can most clearly be seen in Figure 2.37, the ratio between I_D and I_U only approaches the ratio between the downward and upward going electron at high energies and for low heliocentric angles.

3

Effect of Albedo on Data Inversion

3.1 How Regularised Inversion works

In physics and mathematics there are many questions which are considered inverse problems. Generally solving a problem in physics involves applying input parameters to a model and determining the observable quantities, this is called the forward or direct problem; the reverse of this, the inverse problem, then attempts to determine which input parameters gave rise to a set of observations. These are problems involving a a set of measurements which are given by a convolution over the set of source quantities we would like to find. Historically, of these pairs of forward and inverse problems, the forward problem is often considered first as it tends to have been the one most straightforward to solve. The common feature of most of the problems considered inverse problems is that they are ill-posed in the sense of Hadamard, Kirsch (1996). Under this definition to be well posed a problem must have a solution which is extant, unique and stable.

Considering an operator A acting on variable x to produce data b, the forward problem corresponds to the equation $b = Ax$. To solve the inverse problem and

determine x naively we should be able to invert the equation to achieve

$$x = A^{-1}b\,; \tag{3.1}$$

however this in general may not meet any of the requirements for well-posedness. The equation may not have a solution and if it does it often will not be unique or stable.

There will also be uncertainty associated with the data, $b = Ax_{true} + \delta b$, and while these perturbations δb may be small, direct inversion will no longer produce the true solution and in many cases will be substantially different from x_{true}. For an ill-posed problem, small variations in the data are greatly magnified in the solution. This is particularly true in the case of experimental data which can contain significant uncertainties. In order to reliably solve this, further information in the form of constraints must be added. These are often constraints on the smoothness of the solution vector.

In practice, the data we are dealing with is never a continuous function but a vector of discrete measured points $\mathbf{b}$ so the linear problem must be approximated by the matrix equation $\mathbf{b} = \mathbf{A}\mathbf{x}$. This discretisation is likely to make determination of the solution vector, $\mathbf{x}$, more difficult and amplify errors due to noise.

The classical method of finding this inverse, particularly when the system of equations is overdetermined, is the least squares approach, which seeks to minimise a slightly reformulated version of the problem (e.g. Hansen 2010):

$$\|\mathbf{A}\mathbf{x} - \mathbf{b}\|^2 = \min\,. \tag{3.2}$$

Here $||\mathbf{x}||$ represents the Euclidean norm of the vector $\mathbf{x}$ a measure of its "length" defined as $||\mathbf{x}|| = \left(\sum_{i=0}^{N} x_i^2\right)^{1/2}$. If x and b are of the same dimension this is identical to Equation 3.1. However this direct least square approach generally produces a very unstable result when the problem is ill-posed. This can occur when the solution is unstable, that is, small changes in the data result in large changes to the solution, this is common when solving an integral equation.

One method of finding the solution is to solve the Lagrange multiplier problem

$$\mathcal{L}(\mathbf{b}) \equiv \|\mathbf{A}\mathbf{x} - \mathbf{b}\|^{\mathbf{2}} + \lambda\|\mathbf{x}\|^{\mathbf{2}} = \min\,, \tag{3.3}$$

where the constraint term $\|\mathbf{x}\|^2$ aims to reduce the large oscillations which are caused by noise amplification, λ is the regularisation parameter, a variable which determines the degree of smoothness imposed on the solution. This method is known as Tikhonov regularisation (Tikhonov, 1963)

The solution for a given value of λ can be analytically given by (Craig and Brown, 1986)

$$\mathbf{x}_\lambda = \mathbf{Rb} = (\mathbf{A^T A} + \lambda \mathbf{I})^{-1} \mathbf{A^T b} \tag{3.4}$$

However there are several practical problems in computing this (Hansen, 1992).

One way of efficiently computing the solution is to use the method of Singular Value Decomposition (SVD) (e.g. Craig and Brown 1986) or its extension Generalised Singular Value Decomposition (GSVD). The matrix $\mathbf{A}$ can be decomposed into the form

$$\mathbf{A} = \mathbf{USV^T}, \tag{3.5}$$

where $\mathbf{U}$ and $\mathbf{V^T}$ are orthogonal i.e. $\mathbf{UU^T} = \mathbf{U^T U} = \mathbf{1}$ and $\mathbf{VV^T} = \mathbf{V^T V} = \mathbf{1}$ and $\mathbf{S}$ is a diagonal matrix whose values are the singular values of $\mathbf{A}$, that is $\mathbf{S} = diag(\sigma_i)$. The singular values are the eigenvalues corresponding to the shifted eigenvalue problem $\mathbf{AU}_i = \sigma_i \mathbf{V}_i$, $\mathbf{A^T V}_i = \sigma_i \mathbf{U}_i$.

Substituting these into Equation 1.3 gives (Bertero, Demol, and Pike, 1985)

$$x_\lambda = \sum_{i=1}^{N} \frac{\sigma_i}{\sigma_i^2 + \lambda} (\mathbf{b} \cdot \mathbf{v_i}) \mathbf{u_i} \tag{3.6}$$

There are several methods available to select the regularisation parameter. The most straightforward is the discrepancy principle (Groetsch, 1984; Morozov, 1967). Here

$$\|(\mathbf{Ax}_\lambda - \mathbf{b})\|^2 = ||\delta \mathbf{b}|| \tag{3.7}$$

Often in practice the calculated value for λ will not provide the best balance between smoothing and the data, particularly if there are other physical constraints on the solution which are not accounted for by the method, such as positivity. For the optimum value for the regularisation parameter, the normalised residuals,

given by $r_k = ((\mathbf{Ax})_k - \mathbf{b}_k)/\delta b_k$, should be uncorrelated and have a distribution which is close to Gaussian.

A further parameter, α, tweaking the regularisation parameter can be implemented to manually adjust the solution. This gives additional freedom to obtain a solution with acceptable statistical properties.

$$\|(\mathbf{Ax}_\lambda - \mathbf{b})\|^2 = \alpha||\delta\mathbf{b}|| \tag{3.8}$$

However, Equations 3.7 and 3.8 consider only the total error, but it can be more instructive to consider the deviation weighted by the error, given by

$$\|(\mathbf{Ax}_\lambda - \mathbf{b})(\delta\mathbf{b})^{-1}\|^2 = \alpha \tag{3.9}$$

A complementary method is to consider the cumulative residuals, C_l, given by

$$C_l = \frac{1}{l}\sum_{k=1}^{l} r_k \tag{3.10}$$

This is close to the common concept of χ^2, which is calculated in a similar manner

$$\chi^2 = \frac{1}{N}\sum_{k=1}^{N} r_k^2 \tag{3.11}$$

For Gaussian errors the cumulative residuals should decay to zero faster than $\pm 1/\sqrt{k}$ and χ^2 should be close to 1.

Depending on the nature of the inverse problem, $\|\mathbf{x}\|$ may not be the most appropriate constraint, and a term of the form $\|\mathbf{Lx}\|$ is applied instead, where $\mathbf{L}$ is a linear matrix representing the constraint conditions. The choice of $\mathbf{L}$ is related to the constraint applied to the solution and when solving a physics-based inverse problem should be motivated by the underlying physics.

Often the constraint matrix, $\mathbf{L}$, is an approximation of a differential operator. For example, one finite difference approximation of the first derivative operator

has the form

$$D_1 = \begin{pmatrix} -1 & 0 & \cdots & 0 & 0 \\ 1 & -1 & \cdots & 0 & 0 \\ \vdots & \vdots & \ddots & \vdots & \vdots \\ 0 & 0 & \cdots & -1 & 0 \\ 0 & 0 & \cdots & 1 & -1 \end{pmatrix} \tag{3.12}$$

The Tikhonov functional now has the form

$$\mathcal{L}(\mathbf{b}) \equiv \|\mathbf{Ax} - \mathbf{b}\|^{\mathbf{2}} + \lambda \|\mathbf{Lx}\|^{\mathbf{2}} = \min \tag{3.13}$$

And consequently the solution for a given value of λ is now given by (Hansen, 1989)

$$\mathbf{x}_\lambda = (\mathbf{A^T A} + \lambda \mathbf{L^T L})^{-1} \mathbf{A^T b}\,. \tag{3.14}$$

The solution to this cannot be found in terms of a Singular Value Decomposition and its extension Generalised Singular Value Decomposition must now be used (Kontar *et al.*, 2004). This is similar to SVD but applies to the pair $(\mathbf{A}, \mathbf{L})$, when $\mathbf{L} = \mathbf{1}$ it reduces to SVD.

The decomposition now takes the form

$$\mathbf{A} = \mathbf{U} \begin{pmatrix} diag(\sigma_i^A) & 0 \\ 0 & (1)_{N-P} \\ 0 & 0 \end{pmatrix} \mathbf{W}^{-1} \qquad \mathbf{L} = \mathbf{V}(diag(\sigma_i^L)0)\mathbf{W}^{-1} \tag{3.15}$$

The solution, in terms of the singular values and vectors is now (Hansen, 1992)

$$x_\lambda = \sum_{i=1}^{M} \left(\frac{\sigma_i^2}{\sigma_i^2 + \lambda} \frac{(\mathbf{b} \cdot \mathbf{u_i})\mathbf{w_i}}{\sigma_i^A} \right) + \sum_{i=M+1}^{N} (\mathbf{b} \cdot \mathbf{u_i})\mathbf{w_i} \tag{3.16}$$

where $\sigma_i = \sigma_i^A / \sigma_i^L$

The error associated with Tikhonov Regularisation can be estimated in terms of the discrepancy between the regularised solution $\mathbf{x}_\lambda$ and the true solution $\mathbf{x}_{true}$ (Aki, 1980).

$$\begin{aligned} \delta\mathbf{x} &= \mathbf{x}_\lambda - \mathbf{x}_{true} \\ &= \mathbf{Rb} - \mathbf{x}_{true} \\ &= \mathbf{R}(\mathbf{Ax}_{true} + \delta\mathbf{b}) - \mathbf{x}_{true} \\ &= (\mathbf{RA} - \mathbf{1})\mathbf{x}_{true} + \mathbf{R}\delta\mathbf{b}\,, \end{aligned} \tag{3.17}$$

This error has two terms, the right hand side gives the magnification of the data error by the process inversion. The second term gives the spread in the solution due to the smoothing imposed by the regularisation, it can be thought of as a horizontal error.

In the case where the amount of additional smoothing is low $\mathbf{R}_{\lambda\to 0} \to \mathbf{A^{-1}}$ thus $\mathbf{RA}_{\lambda\to 0} \to \mathbf{1}$. The resolution of each point can be estimated by considering the matrix $\mathbf{RA}$, as a greater amount of smoothing is applied this matrix diverges from the identity, rows of the matrix tend to show peaks, centred on the diagonal, of increasing width with increasing λ (Hannah and Kontar, 2012). The Full Width at Half Maximum (FWHM) can then be used as an estimate of the horizontal resolution of the solution (Christensen-Dalsgaard, Hansen, and Thompson, 1993).

3.2 RHESSI Measurements

3.2.1 Photon measurements

The data which we consider here is taken from flare observations made by RHESSI which can measure X-rays in the range 3 keV up to gamma rays of 17 MeV with a resolution of up to 1 keV (FWHM) at the lowest energy and $\sim$ 10 keV at several MeV. RHESSI can achieve this resolution using 9 germanium detectors which are split into front and rear segments.

The telescope is the first to allow imaging in this energy range. This is possible as RHESSI uses a set of 9 rotating collimators which are spun as the spacecraft rotates. At either end of each collimator is a tungsten grid of parallel slats. As RHESSI rotates, the amount of X-rays blocked by each grid will vary, depending on the position of the sources in the telescope's field of vision. Thus the positional information of the hard X-ray source is converted into the temporal variation in the detector counts; this is analogous to a Fourier transform and so many mathematical methods exist for recovering the directional information and producing an image.

3.2.2 Spectral Response Matrix

In order to characterise the relationship between incident photons and measured counts detailed knowledge of the instrument response is needed (Smith *et al.*, 2002). This information is encapsulated in a matrix usually referred to as the SRM (Spectral Response Matrix) or the DRM (Detector Response Matrix). The SRM is M x N in size where M and N are the number of bins in photon and count space respectively (Figure 3.1). The SRM is calculated as the sum of 9 sub matrices reflecting the different contributions to instrument response for each detector used. The main contributions accounted for are: absorption in the grids mylar blankets and cryostat windows; noise and the low energy cutoff due to the spacecraft electronics; Compton scattering both into and out of the detectors; Compton scattering of X-rays off the Earth's atmosphere and radiation damage of the detectors. Some of these aspects are fairly constant, such as the absorption due to the imaging grids, however others have changed significantly since RHESSI was launched such as the degradation of the detectors due to radiation damage so the time interval of observation is needed when calculating the SRM.

3.2.3 Background

As RHESSI orbits in low Earth orbit (LEO), a significant component of the detected signal is due to charged particles in the Earth's atmosphere directly interacting with the detectors and giving false counts. Of particular concern is the SAA (South Atlantic Anomaly), this is a region where the geomagnetic field is weaker so the inner van Allen belt is closer to the surface of the Earth, resulting in a high number of energetic charged particles in this area. RHESSI frequently passes through this region in its orbit, and its detectors are usually shut off to avoid overloading the spacecraft memory with spurious counts. As RHESSI changes geomagnetic latitude during its orbit it encounters a varying flux of charged particles and secondary photons, produced in cosmic ray interactions with the Earth's atmosphere, which will also contribute to the background.

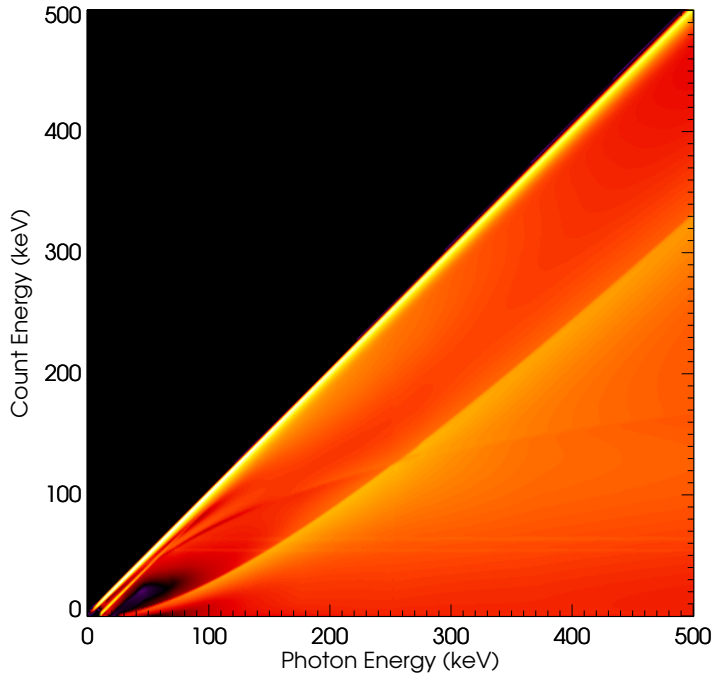

Figure 3.1: RHESSI Spectral Response Matrix for the combined front segments commonly used for analysis (all except 2 and 7). A logarithmic colour scale is used to highlight the non-diagonal components.

There is also background from solar sources during times of high solar activity. There may be several flares in a short period of time and the signals from each of these might overlap. These overlapping flares may be from different active regions in different parts of the solar disk. In this case imaging-spectroscopy techniques may be applicable to separate out the flare of interest; however, they are often from the same active region.

The standard method of background subtraction (Schwartz *et al.*, 2002) is to take the average of the count measurements just before and just after the flare. There are several more sophisticated approaches built into OSPEX (Object Spectral Executive), the standard RHESSI spectral analysis package[1], which allow multiple time intervals to be selected and linear, quadratic or cubic fits applied to estimate

[1] http://hesperia.gsfc.nasa.gov/ssw/packages/spex/doc/ospex_explanation.htm

the background, and this is particularly useful for long flares as the background is likely to change over the course of the flare. These background estimates can be the same over the full energy range, or different fits over different background intervals can be selected for different energy ranges. When the count measurements before and after the flare appear unlikely to produce a reliable estimate of the background, information from adjacent orbits may also be used.

3.2.4 Pulse Pileup

Another way in which the count spectrum can be distorted is pulse pileup. This occurs when two low-energy photons impact on a detector in-between detector readouts so that they are counted as one photon with the sum of their energies. This is a significant problem when the count rate is high, but there is always a finite probability of it happening. The general rule of thumb is that pileup becomes a significant when the count rate is $\sim 2 \times 10^4\,\mathrm{counts\,s^{-1}\,detector^{-1}}$. When count rate is very high, pulse pileup can also be the result of 3 photons arriving in a short period of time ($< 1\mu s$), this is known as second-order pileup. The effect this has on the detected count rate is to decrease the peak value at low energies and to add a "shoulder" at higher energies (roughly twice the peak energy value).

Software has been developed to attempt to characterise the level of pulse pileup for any given time interval of RHESSI observations and to correct for it during spectral analysis. However,it is a difficult effect to fully account for as it is an off-diagonal contribution and is non-linear, the number of pileup photons at a given energy depend strongly on the overall shape of the spectrum. Therefore it cannot be treated in the same way as the other distortions to the count spectrum which are accounted for in the SRM. The tool `hsi_pileup_check` uses parameters derived empirically from calibration tests to estimate the amount of pileup for any given time interval. When the spectrum for a given observation time interval is accumulated an attempt to correct for pileup can be made using the routine `hsi_correct_pileup` which removes the estimated value of pileup from the measured counts.

3.3 Regularised Inversion of RHESSI Data.

The general integral relating the electron spectrum to the photon spectrum is of the form of a Volterra integral of the first type:

$$g(x) = \int_a^x k(x,y)f(y)dy\,. \tag{3.18}$$

The properties of this equation are well known and solving it is an ill-posed problem (Bertero, Mol, and Pike, 1988), therefore regularised inversion techniques are appropriate for solving this equation to determine the electron flux (Craig and Brown, 1986).

While analytic methods of inverting hard X-ray data to determine the electron spectrum were first proposed in Brown (1971), these rely on having precise knowledge of the observed X-ray spectrum, and to solve this for arbitrary noisy discrete data regularised inversion methods are needed. However, regularised inversion of hard X-ray data was not routinely used until the launch of RHESSI; the reason for this is that previous hard X-ray telescopes did not have the resolution to justify using regularised inversion. Previous telescopes had $\delta\epsilon/\epsilon \sim 0.3$ whereas RHESSI has $\delta\epsilon/\epsilon \sim 0.01$ at 100 keV. The high resolution of RHESSI data compared with previous instruments allows a range of inversion techniques to be applied which were previously unused in the field solar flare physics, some of which are described in Craig and Brown (1986).

The method of Tikhonov regularisation was first applied to solar X-ray data by Piana (1994) who performed tests of the method using simulated count spectra and found it was robust at determining the electron spectrum. The method was then applied to RHESSI flare observations by Piana *et al.* (2003).

The problem of electrons to X-ray counts can be summarised in the matrix equation

$$\mathbf{C} = \mathbf{M}\overline{\mathbf{F}}\,, \tag{3.19}$$

where $\mathbf{M}$, $\overline{\mathbf{F}}$, and $\mathbf{C}$ are matrices which represent the cross-section, mean electron flux spectrum and observed count spectrum respectively. Here $\mathbf{M}$ is a matrix

defined by $\mathbf{M} = \mathbf{SQ}$ where $\mathbf{Q}$ is a matrix representing the bremsstrahlung cross-section, in this case the approximation to the 3BN cross-section calculated by Haug (1997) is used. To determine the emitting electron spectrum this must be solved for $\bar{\mathbf{F}}$.

In this case the Tikhonov regularisation equation now has the form

$$||\mathbf{M}\bar{\mathbf{F}} - \mathbf{C}||^2 + \lambda||\mathbf{L}\bar{\mathbf{F}}||^2 = minimum\,, \tag{3.20}$$

as the parameters being studied are physical variables these constraints must be defined by considering the physical properties of the electron spectrum. In particular, in the context of solar flare electron spectra both, zeroth and first order are physically defined parameters. Zeroth order corresponds to $||\mathbf{F}|| \leq \alpha$ that is $\mathbf{L} = \mathbf{1}$, this is physically equivalent to the statement that the total flux is finite, which in turn is limited by the total number of electrons accelerated during the solar flare.

Alternatively, first order regularisation corresponds to $\mathbf{L} = \mathbf{D_1}$ where $\mathbf{D_1}$ is the differential operator. That is, the mean electron flux should be a differentiable quantity. If it is assumed that the source averaged electron flux is the result of an initial injected electron spectrum and the transportation processes which occur in the solar atmosphere, then the injected and mean electron fluxes can be related by

$$F_0(E_0) \sim -\frac{d}{dE}\left[\frac{\overline{\mathbf{F}}(E)}{E}\right]_{E=E_0} \tag{3.21}$$

and therefore the mean flux should be differentiable (Brown and Emslie, 1988).

The robustness of the solution can be improved if the equation is first preconditioned (Kontar *et al.*, 2004). A forward fit performed on the data using a standard model of a thermal component plus a broken power law (Holman *et al.*, 2003). This estimated electron spectrum, $\mathbf{F}_{fit}$, is used as a starting point for the regularised inversion. The inversion is performed on the difference between the data, $\mathbf{C}$ and the fit, $\mathbf{MF}_{fit}$, This modified data vector and the cross-section matrix are also scaled by a factor of $(\mathbf{MF}_{fit})^{-\frac{1}{2}}$. These transforms both make the solution much flatter and so less prone to errors.

Thus the constraint matrix used here has the form

$$D_1' = \begin{pmatrix} -G_1 & 0 & \cdots & 0 & 0 \\ G_1 & -G_2 & \cdots & 0 & 0 \\ 0 & G_2 & \cdots & 0 & 0 \\ \vdots & \vdots & \ddots & \vdots & \vdots \\ 0 & 0 & \cdots & -G_{M-1} & 0 \\ 0 & 0 & \cdots & G_{M-1} & -G_M \end{pmatrix},$$

where $\mathbf{G} = (\mathbf{F}_{fit})^{-\frac{1}{2}}$.

Brown *et al.* (2006) performed a study on four inversion methods: forward fitting, zeroth order Tikhonov regularisation, first order Tikhonov regularisation, and matrix inversion using data adaptive binning (Johns and Lin, 1992). These tests were done blind: several count spectra were simulated from a range of electron spectra, some with features such as dips and thermal components. These were then supplied to different researchers who applied each of the regularisation techniques. The inverted electron spectra were then compared with the original input spectrum to ascertain the reliability of each method. All methods tested were able to reliably estimate the input electron spectrum (Figure 3.2). The implementations of Tikhonov regularisation fared well, particularly in recovering smaller features in the electron spectra.

The most popular approach to determining $\overline{F}(E)$ is forward fitting (Holman *et al.*, 2003). Here a functional form of the electron spectrum is assumed, as the parameters are adjusted until the best fit with the data is achieved. Usually an algorithm using a non-linear least squares method varies the parameters and analyses the resulting change in χ^2. Common functional forms include power-laws in electron energy and isothermal Maxwellian distributions, such as those described in Section 2.1, along with models based on the apparent shape of the spectra such as power laws in photon energy, and forms based on physical models such as thick and thin targets. Forward fitting of this type is available through OSPEX.

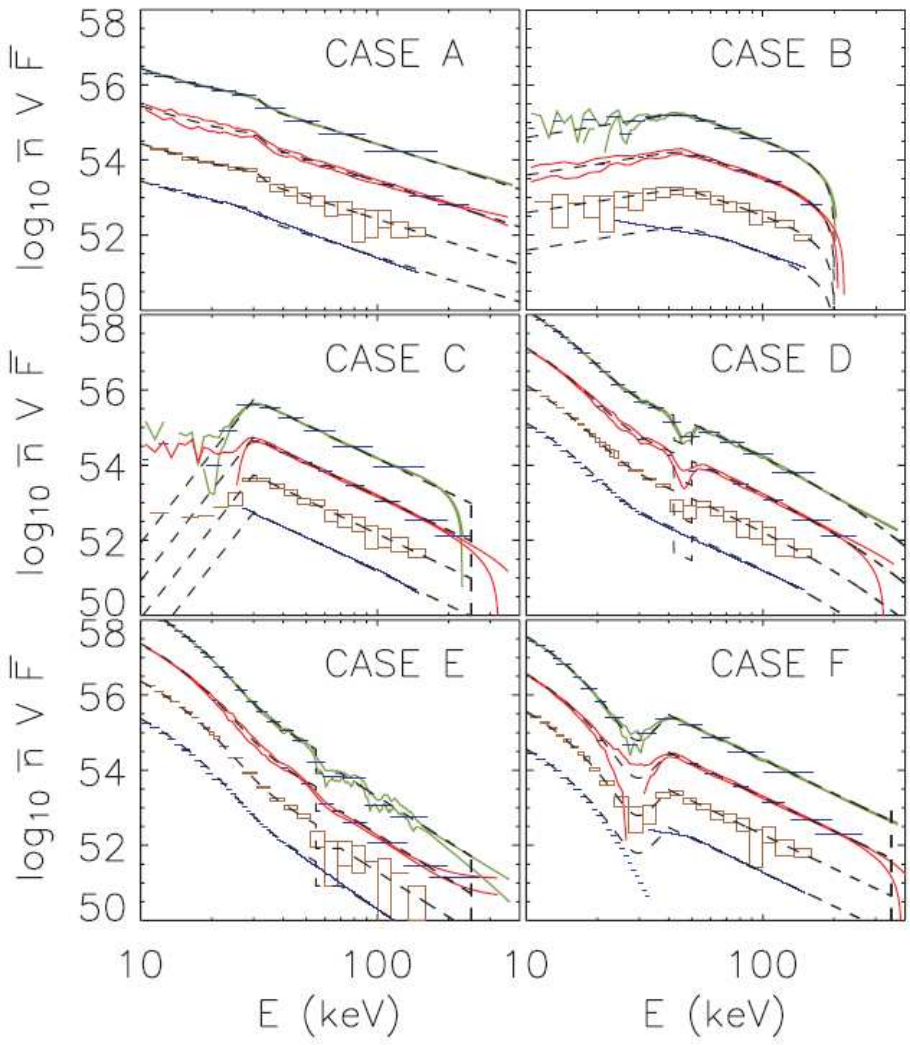

Figure 3.2: Comparison of different inversion methods - initial input electron spectra for 6 models (black dashed lines) were inverted using zeroth order Tikhonov regularisation (green lines), first order Tikhonov regularisation (red lines), and matrix inversion using data adaptive binning (brown boxes) and forward fitting (blue lines). For the Tikhonov regularisation results the upper and lower lines show the 3 σ confidence intervals. Similarly the size of the boxes for the binned-matrix-inversion method denotes the 3 σ confidence interval. From Brown *et al.* (2006)

3.4 Low energy cutoffs and local minima

3.4.1 Effect of low energy cutoff on spectra

The spatially integrated spectrum of energetic electrons $\bar{n}V\bar{F}(E)$ is often approximated as a sum of a thermal Maxwellian distribution and a non-thermal power-law distribution. The thermal component often dominates the overall spectrum at low energies ≤ 20 keV, making determination of the characteristics of the low-energy end of non-thermal distribution difficult. However, this low-energy part of the non-thermal spectra plays a crucial role in solar flare diagnostics. As with any steeply decreasing function such as a power-law, most of the non-thermal electron energy is concentrated in this part, hence this can be used to define the energy in non-thermal electrons and hence estimate the total energy budget of the flare. Additionally, the low energy electrons are more heavily influenced by several significant electron propagation effects such as collisions (Brown, 1971) and beam-plasma interactions (Mel'Nik, Lapshin, and Kontar, 1999), thus playing an important role in the diagnostics of electron transport in the solar flares.

3.4.2 Evidence for features in data

High resolution spectra observed by RHESSI (Lin *et al.*, 2002) allow us to infer much greater detail in the structure of electron distribution than ever seen before. RHESSI studies, using Tikhonov regularisation to recover $\bar{F}(E)$, measured a significant dip in the mean electron flux spectrum in the range $\sim 17 - 31$ keV (Kontar and Brown, 2006a). This feature, if reliable, would put strong constraints on acceleration models and would be inconsistent with the collisional thick target model of Brown (1971). However, the photon spectra of these events will be influenced by albedo (see Section 2.3). Similarly, Kašparová *et al.* (2005) have shown that the spectrum of the August 20, 2002 event has a puzzlingly large value of the low-energy cutoff when forward fit methods are applied, but that this can be also understood in terms of the change in the photon spectrum due to the albedo component.

Table 3.1: Events with a dip larger than 1σ

Flare Date	Flare Time	x position	y position	μ	γ_0	GOES Class
11-Apr-2002	03:06:08.00	-155.35	-209.38	0.96	1.60	C3.2
25-Apr-2002	05:55:12.00	-108.37	243.69	0.96	1.76	C2.0
29-Jun-2002	09:29:40.00	-886.45	-283.9	0.16	2.67	C2.1
30-Jul-2002	17:37:36.00	140.58	-198.18	0.97	2.12	C2.4
17-Sep-2002	05:51:12.00	567.41	-300.55	0.74	1.65	C2.1
24-Oct-2002	00:09:24.00	53.22	334.72	0.94	2.22	B5.9
22-Nov-2002	13:29:36.00	126.69	-334.59	0.93	2.47	C1.5
10-Mar-2003	10:02:56.00	-619.7	244.46	0.72	2.94	C1.4
20-Nov-2003	05:10:36.00	122.76	-16.32	0.93	2.91	C1.2
1-Apr-2004	23:00:32.00	459.91	33.01	0.88	2.60	B4.3
20-May-2004	17:16:12.00	-896.31	-247.21	0.19	2.90	C3.8
19-Jul-2004	20:56:52.00	-643.29	-4.45	0.73	2.01	C1.9
14-Aug-2004	08:15:30.00	490.5	-241.44	0.82	1.63	C7.7
28-Oct-2004	12:13:32.00	-869.75	-301.96	0.30	3.11	B8.2
9-Nov-2004	15:10:08.00	723.25	45.65	0.66	3.61	C1.1
30-Nov-2004	03:56:12.00	-10.77	-227.6	0.97	2.65	B7.8
21-Jan-2005	06:32:20.00	891.03	269.14	0.29	2.49	C1.7
5-Apr-2006	22:45:28.00	742.09	-129.63	0.62	2.17	B.28

This analysis can be done either by assuming a functional form of the electron spectrum (e.g. Sui, Holman, and Dennis (2007)) or by using a regularised inversion technique (Kontar *et al.*, 2004). As a low-energy cutoff in the electron spectrum will produce a very hard photon spectrum below the cutoff energy of $\gamma \approx 1$ Holman (2003), flat X-ray spectra can require low-energy cutoffs in the power-law distributions when a functional form is assumed (Kašparová *et al.* 2005; Sui, Holman, and Dennis 2007). The model independent approach, via the regularised inversion technique, (Piana *et al.* 2003) on the other hand, may interpret the origin of this as a dip or a gap in the electron distribution (Kontar and Brown 2006b, Kašparová, Kontar, and Brown 2007).

3.4.3 Dips in the mean electron flux distribution

We conducted a systematic search for dips in the mean electron flux distribution using the RHESSI solar flare database for the period of February 2002 - May 2006 (Kontar, Dickson, and Kašparová, 2008). The analysis confirms previous suggestions that the isotropic albedo correction is capable of removing all statistically significant dips in the mean electron flux distribution.

Table 3.2: Characteristics of dips larger than 1σ

Flare Date	Flare Time	depth (σ)	Energy at Minimum (keV)
11-Apr-2002	03:06:08.00	1.65	15.5
25-Apr-2002	05:55:12.00	2.49	16.5
29-Jun-2002	09:29:40.00	2.04	15.5
30-Jul-2002	17:37:36.00	1.87	18.5
17-Sep-2002	05:51:12.00	2.73	16.5
24-Oct-2002	00:09:24.00	2.03	15.5
22-Nov-2002	13:29:36.00	2.83	17.5
10-Mar-2003	10:02:56.00	1.16	13.5
20-Nov-2003	05:10:36.00	1.33	12.5
1-Apr-2004	23:00:32.00	2.90	15.5
20-May-2004	17:16:12.00	1.36	15.5
19-Jul-2004	20:56:52.00	1.89	16.5
14-Aug-2004	08:15:30.00	1.85	18.5
28-Oct-2004	12:13:32.00	1.48	16.5
9-Nov-2004	15:10:08.00	1.07	15.5
30-Nov-2004	03:56:12.00	1.22	14.5
21-Jan-2005	06:32:20.00	1.04	15.5
5-Apr-2006	22:45:28.00	2.51	17.5

As a basis, we used the list of 398 flares with weak thermal component previously determined by Kašparová, Kontar, and Brown (2007). Although this has limited the total number events for our analysis, it has helped us to avoid various effects, such as pulse pile-up and particle contamination, which would complicate the

spectral analysis. Next, we chose the 177 events with the smallest values of spectral index $1.6 \leq \gamma_0 \leq 4.0$ where γ_0 is the average spectral index of the photon spectrum, measured in the range between 15 and 20 keV - see Kašparová, Kontar, and Brown (2007).

For each flare, the spectra were accumulated over the duration of the impulsive phase, i.e. in the interval when counts at energies above 50 keV were sufficiently above background (Figure 3.3). The spectra were generated in the energy range from 3 to 100 keV with 1 keV energy resolution, avoiding detectors 2 and 7 due to their low resolution (Smith *et al.*, 2002). The background counts were removed in a standard way (Schwartz *et al.*, 2002).

To obtain a starting point for the regularised inversion, spectra were forward fitted assuming an isothermal plus a non-thermal double power-law distribution of $\bar{F}(E)$ for example Holman *et al.* (2003). Spectra were then inverted within OSPEX using the regularised inversion routines described in Section 3.1.

With the mean electron flux determined, the spectrum was examined for local minima or dips. These dips were analysed to infer the most important dip parameters: the energy $E_{\rm d}$ at which the dip minima occurs and the depth of the dip in terms of σ where σ is the statistical uncertainty on the inferred mean electron spectrum $nVF(E)$. This depth was calculated by dividing the difference between the minimum and the following maximum above the dip in units of electron spectra uncertainty at the minimum (Figure 3.4). We have found 18 events with dip-depth deeper than 1σ in the electron distribution function (Figure 3.5). The details of these events are presented in Table 3.1. Some of these events were also found using a thick target fit with a single power law and low energy cutoff Sui, Holman, and Dennis (2007).

The local minima in the mean electron spectrum tend to be 6-10 keV wide and hence cover several statistically independent points. For example, if a dip is three points wide at the 1σ level in each point then the probability of finding three consecutive points outside the 1σ intervals is $(1 - 0.68)^3 = 0.03$ and the corresponding statistical significance of the minimum is $1 - 0.03 = 0.97$. In general, given that errors have a normal distribution, the statistical significance

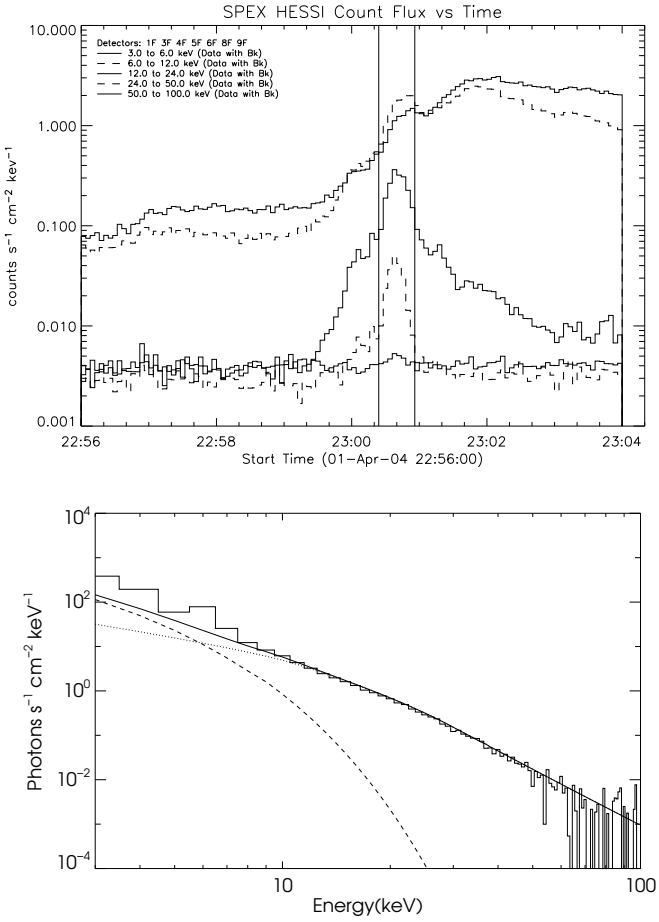

Figure 3.3: Example of a solar flare with flat electron spectrum. Thin lines show 1σ error bars. Upper panel: RHESSI Light curves; the vertical lines show the accumulation time interval for spectroscopic analysis. Lower panel: Photon spectrum and forward fit (solid line), isothermal component (dashed line), nonthermal component (dotted line).

of the local minimum is $1 - \prod_{i=1}^{N}(1 - \mathrm{erf}(d_i/\sqrt{2}))$, where N is the number of statistically independent points in the dip and d_i is the depth of each point in units of the corresponding σ_i uncertainties. The nature of the smoothing imposed by the regularisation method means that adjacent energy bins cannot be assumed to be statistically independent. The sizes of the statistically independent energy bins can be estimated from the horizontal errors. Thus the local minimum shown in Figure 3.4 has significance $\sim\ [1-\mathrm{erf}(2.9/\sqrt{2})][1-\mathrm{erf}(1.2/\sqrt{2})] \approx 99.9\%$

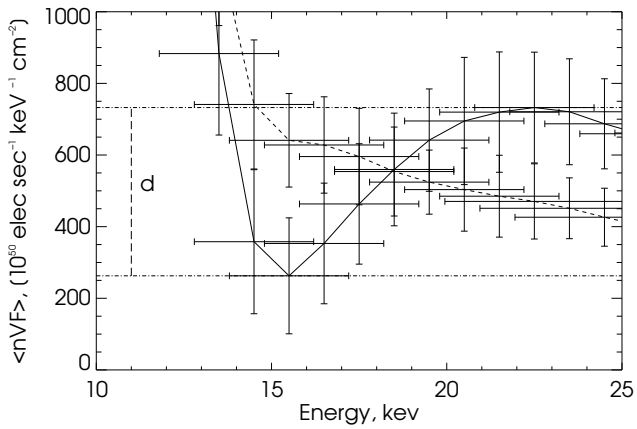

Figure 3.4: Mean electron distribution spectrum for April 1, 2004 $\sim 23:00$ UT solar flare. The observed electron spectrum (solid line) and electron spectrum after isotropic albedo correction (dashed line) are given with 1σ error bars. The dip depth, d, is shown.

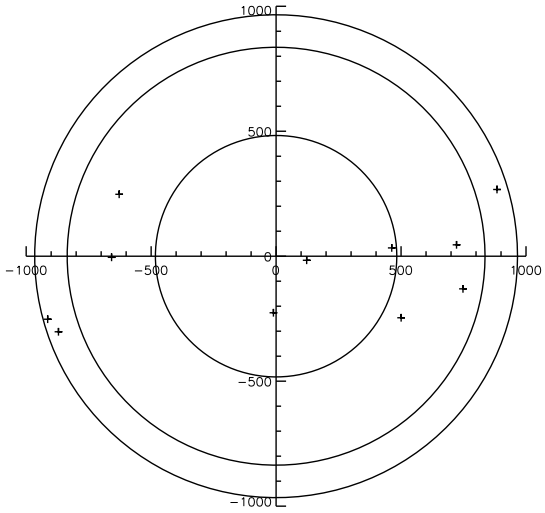

Figure 3.5: Positions on the solar disk of all flares with a statistically significant dip. The inner rings indicate heliocentric angles of 30° and 60°.

The dips are located between the thermal and non-thermal component and appear approximately at the same energy, in the range between 13 and 19 keV. The dip energies, E_d, are given in Table 3.2 as the bin centre energy. There is no

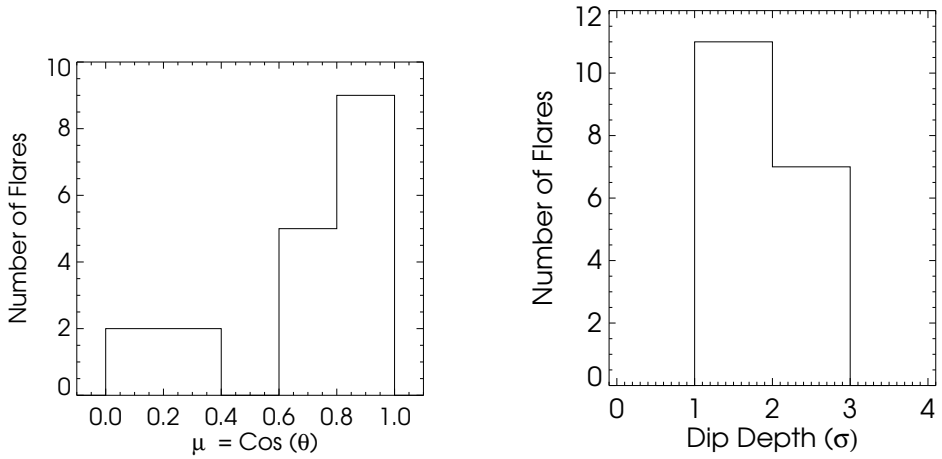

Figure 3.6: Left panel: Number of events as a function of cosine of heliocentric angle; Right panel: Number of events as a function of dip depth in σ.

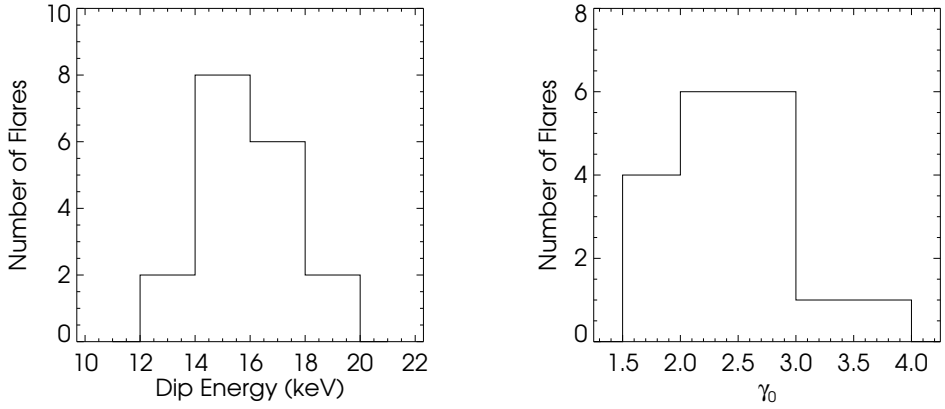

Figure 3.7: Histograms of 17 events with clear dip: Left panel: Number of events as a function of dip energy E_{d} in keV. Right panel: Histogram of spectral indices γ_0 for events with a dip.

preferential energy in this range (Figure 3.7 - left panel).

There is a clear pattern in the results: flares with dips tend to occur at locations with large $\mu = \cos\theta$, where θ denotes the heliocentric angle. Only 4 events are located close to the solar limb $\mu < 0.5$ while 14 are near the disk centre $\mu < 0.5$

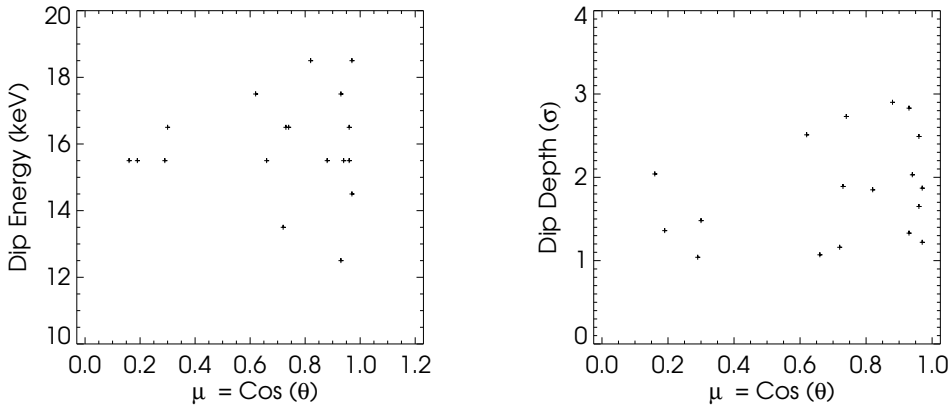

Figure 3.8: Left panel: Dip energy versus μ; Right panel: Dip depth versus μ.

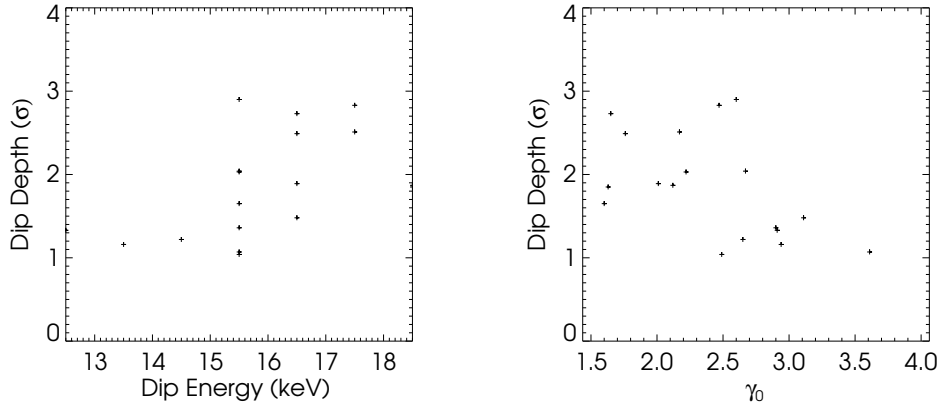

Figure 3.9: Left panel: Dip depth versus dip energy: Right panel: Dip depth versus γ_0.

see left panel in Figure 3.5. However, there is no strong evidence for the dip energy being dependent on the flare location or on the dip depth - see left panels in Figure 3.8 and Figure 3.9, respectively.

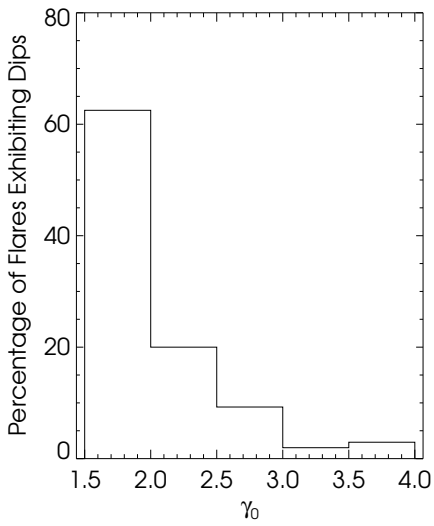

Figure 3.10: Percentage of flares exhibiting a dip for a given γ_0.

3.4.4 Effect of applying albedo correction

Previous works have shown (e.g. Kontar *et al.* (2004) and Kašparová, Kontar, and Brown (2007)) that a feature such as a dip can be a signature of distortion by albedo contribution. Figure 3.10 shows that larger dips appear for flatter X-ray spectra. Furthermore, events with large depths tend to appear close to the disc centre, see Figure 3.8 - Right panel. This is consistent with the albedo model which predicts larger albedo contribution for flat spectra and disc centre events (see e.g. Section 2.2.2).

To assess whether albedo is a feasible explanation for these observed dips a correction for albedo to determine the primary photon spectrum must be applied. The Green's matrices used in Section 2.3 can be applied as a modification to the to the SRM

$$\mathbf{C} = \mathbf{SI_O} = \mathbf{S}(\mathbf{1}+\alpha\mathbf{GI_P}) \tag{3.22}$$

Therefore, the isotropic albedo correction (Kontar *et al.*, 2006) was applied to all the events with a dip (Table 3.1) and new $\bar{n}V\bar{F}(E)$, i.e. corresponding to the primary photon spectra, were derived. Such albedo corrected mean electron spectra did not reveal any statistically significant dip, i.e. with depth $\geq 1\sigma$.

3.5 Conclusions

Our analysis shows that the clear dips are rare, less than 10 % (18 of 177) of events studied demonstrate a clear dip. The small number of events with a clear dip or low energy cutoff can be explained by a variety of reasons. Firstly, it suggests that the number of very flat primary spectra is rather small and that the vast majority of flares have primary spectral index larger than 2. Indeed, although the total number of events with a dip is small as a fraction of events, it could be as high as 60% for small spectral indices (Figures 3.7 (Right panel) and 3.10). This can be viewed as a lower limit on spectral indices of accelerated electrons in solar flares. In the case of a thick-target model, this corresponds to requiring a spectral index of accelerated electrons larger than 3. Secondly, the small number of events with a dip or low energy cutoff suggests that the thermal component substantially influences the spectrum in the range of above 10 keV for the majority of flares. This conclusion is partially supported by Kašparová, Kontar, and Brown (2007), who have found a large number of events with very soft spectra with spectral indices γ_0 which are larger than 5.

However, when dips do occur in the mean electron spectrum, the local minima in the electron flux spectrum are consistent with the albedo model (Kontar *et al.*, 2006). In the standard solar flare model, the electrons are believed to propagate downwards and hence the reflected flux from the photosphere should be larger (see e.g. Section 2.4). In this analysis an isotropic primary photon distribution was used when calculating the albedo contribution, so this should be viewed as a lower limit on the effect. It therefore seems unlikely that albedo might be overestimated for these flares. As can be seen in Figure 3.10 flares with a low value of γ_0 are very likely to exhibit a local minimum in the mean electron flux spectrum, therefore the small number of flares with flat spectra results in the low number of flares with dips. In addition, the energies of the dip minima are concentrated near 15 keV, the energy which is expected from isotropic albedo model (see Figure 1 in Kašparová, Kontar, and Brown 2007). In addition we note that earlier observations of flat X-ray spectra also appear to be consistent with the albedo model. The flares suggesting high value of low energy cutoff observed

by Nitta, Dennis, and Kiplinger (1990), Farnik, Hudson, and Watanabe (1997) had flat X-ray spectra and were disk centre events, the type of flares strongly influenced by albedo.

The low-energy cutoff is often introduced to limit the total number of non-thermal electrons in solar flares. Since all dips found in the electron spectra can be easily "removed" by applying albedo correction, our results allow us to conclude that if low-energy cutoff exists in solar flare spectra it should be below $\sim$ 12 keV. This upper limit on the low-energy cutoffs is somewhat less than the values published in the literature. In addition, since the total number of electrons accelerated in solar flares is dependent on the low-energy cutoff, the lower value of low-energy cutoff makes the electron number problem even more severe.

4

Bivariate Inversion of RHESSI Data

4.1 Introduction

Several techniques have been used to estimate the anisotropy in the pitch-angle distribution of X-ray emitting electrons in solar flares (Holman *et al.*, 2011; Kontar *et al.*, 2011). The most commonly used method is to look at the centre to limb variation of solar X-ray properties (Datlowe, Elcan, and Hudson, 1974; Vestrand *et al.*, 1987) that is comparing the characteristics, most commonly total X-ray flux (Pizzichini, Spizzichino, and Vespignani, 1974), or the spectral index of solar flares at the limb to disk centre events. Studies concentrating on lower energy emission (below 300 keV) tended to find no significant evidence of directivity. These studies have also been performed using SMM data (Dennis, 1988) studying flares with energies above 300 keV (Bai, 1988; Bogovalov *et al.*, 1985; Vilmer, 1994). Some evidence for directivity at high energies has been reported (McTiernan and Petrosian, 1991; Vestrand, Forrest, and Rieger, 1991). More recently RHESSI data (Lin *et al.*, 2002) has been used to determine the X-ray anisotropy (Kašparová, Kontar, and Brown, 2007) (Figure 4.1). An obvious disadvantage of the statistical method is that the variation can only be seen as an average

over a large number of solar flares, so little can be said about X-ray or electron anisotropy in a given flare.

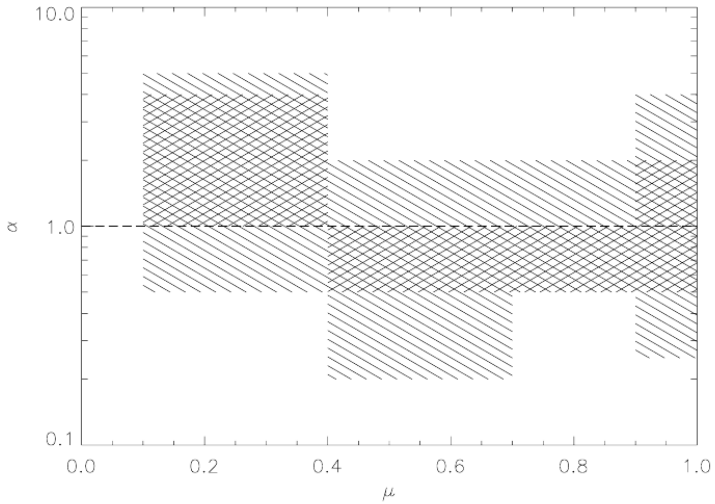

Figure 4.1: The directivity, α as a function of heliocentric angle μ calculated by Kašparová, Kontar, and Brown (2007), who performed a statistical survey of RHESSI flare measurements (α is the ratio of the X-ray flux towards the sun to the X-ray flux towards the observer i.e. $\alpha(\mu) = I_D/I_U(\mu)$). The amount of albedo reflection for flares at different μ was modelled and the results compared with RHESSI observations assuming that limb events showed no albedo and thus represented the true distribution. The hatched and crossed areas represent 95% and 99% confidence that the flares at that μ are drawn from the same distribution as the limb flares.

An approach which allows individual flares to be studied is the stereoscopic method (Catalano and van Allen, 1973). Here each individual flare is measured directly by two spacecraft at two different locations, ideally well separated in space. Studies that have been performed using this method do not show any clear evidence of directivity (Kane *et al.*, 1998; Li *et al.*, 1994). A disadvantage of this approach is the practicality, as there tends to be significant difficulty in cross calibrating pairs of different detectors which were not designed specifically to make stereoscopic measurements, which often leads to large errors. Another drawback is, as in the centre-to-limb method, this technique does not give direct

information about the downward electron distribution.

As an anisotropic electron distribution will produce polarised X-rays, measuring the polarisation can therefore give a measure of the anisotropy of the electron distribution (Leach and Petrosian, 1983). An isotropic source should show low polarisation, whereas a beam should produce significant polarisation (Bai and Ramaty, 1978; Emslie, Bradsher, and McConnell, 2008; Leach and Petrosian, 1983). Studies of polarisation have been performed using various X-ray satellites, recently using the Coronas-F satellite (Zhitnik *et al.*, 2006). The reported measurements vary substantially from observation to observation, adding to the scepticism of these measurements. A major drawback of this approach is the observational difficulty in measuring polarisation at HXR energies for transient events like solar flares. Several attempts have been made using RHESSI (McConnell *et al.*, 2002; Suarez-Garcia *et al.*, 2006), but so far there have been no conclusive measurements made. HXR polarisation has not yet been used to its full potential and future observations could provide a more definitive answer.

4.1.1 Albedo as a Probe of Anisotropy

Another important process which can be used to diagnose the angular distribution is photospheric albedo Kontar and Brown (2006b). As the spectral shapes of reflected and primary hard X-ray spectra are sufficiently distinct, these two components can be distinguished and the albedo reflected flux could be used as a measure of the downward going electrons (Figure 4.2). RHESSI provides sufficient energy resolution, broad energy coverage, and sensitivity to better constrain directivity of energetic electrons in individual solar flare events.

Here we use this albedo method to examine the directivity of energetic electrons in solar flares. The RHESSI flare catalogue has been searched for suitable flares between 2002 and 2008 and we use the spectral data from the impulsive phases of several well observed flares to perform a bi-directional inversion, estimating the fluxes of electrons travelling towards and away from the photosphere.

4.2 Bi-variate Inversion

The method of regularised inversion has been applied to the problem of inverting the angle averaged electron spectrum numerous times (e.g. Brown *et al.* (2006); Kontar *et al.* (2005)) but can be extended to determine an angular dependant electron flux. The cross-section matrix must be extended to take account of the angular dependence of the bremsstrahlung cross-section. The cross-section matrix can be split into two components Q^F representing the bremsstrahlung cross-section in the forward direction, that is the radiation beamed in the same direction as the electron was travelling and Q^B representing the cross-section for the radiation beamed in the opposite direction to the electron. These matrices are determined by taking the full angular dependant cross-section and averaging over a range of angles similar to the method applied to determine the upward and downward components of the photon flux in Section 2.4.

$$Q(\epsilon, E, \theta_0) = \frac{1}{2\pi(1-\cos(\alpha))} \int_{\eta=0}^{\alpha} Q'(\epsilon, E, \eta, \theta_0) \sin\eta d\eta \quad , \tag{4.1}$$

with $\alpha = 90^\circ$ $Q^B(\epsilon, E) = Q(\epsilon, E, \theta_0 = 180^\circ - \theta')$ and $Q^F(\epsilon, E) = Q(\epsilon, E, \theta_0 = 0^\circ)$ $\bar{F}_u$ Kontar and Brown (2006b). This results in a directly observed photon spectrum given by

$$I_u(\epsilon) = \frac{\bar{n}V}{4\pi R^2} \int_{\epsilon}^{\infty} (Q^F(\epsilon, E)\overline{F}_u(E) \; + \; Q^B(\epsilon, E)\overline{F}_d(E))dE \tag{4.2}$$

and a downward directed photon flux given by

$$I_d(\epsilon) = \frac{\bar{n}V}{4\pi R^2} \int_{\epsilon}^{\infty} (Q^B(\epsilon, E)\overline{F}_u(E) \; + \; Q^F(\epsilon, E)\overline{F}_d(E))dE \tag{4.3}$$

A solution can then be found for an electron flux matrix with two components, one directed down towards the photosphere, $\bar{F}_d$, and one directed towards the observer. The Green's function approach can be used to determine the fraction of this downward directed photon flux reflected back towards the observer by albedo Kontar *et al.* (2006).

The matrix relation between the observed count spectrum, $\mathbf{C}$, and the bi-directional electron spectra is now given by

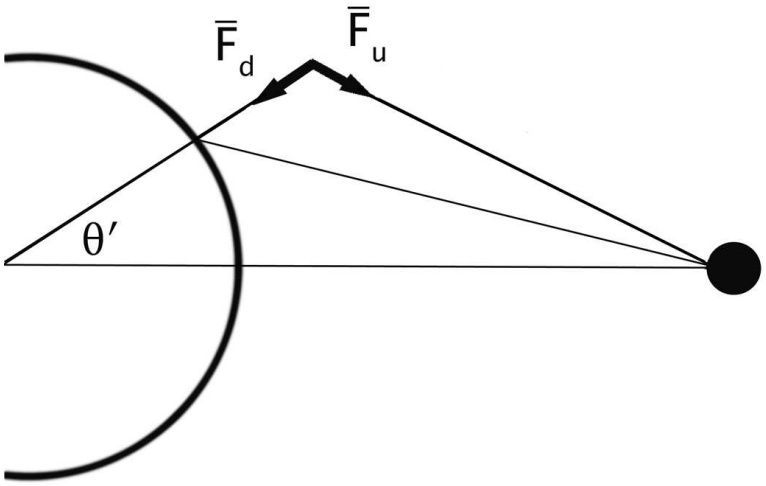

Figure 4.2: The geometry of the X-ray emitting source above the photosphere and bi-directional approximation. X-rays are emitted in all directions and observed directly at Earth or Compton back-scattered in the solar photosphere and then observed at Earth. The true angular distribution of electrons $\overline{F}(E,\eta)$ is approximated by downward $\overline{F}_d$ and upward $\overline{F}_u$ going electrons.

$$\mathbf{C} = \mathbf{S}\left(\mathbf{Q^F} + \mathbf{AQ^B}\ ,\ \mathbf{Q^B} + \mathbf{AQ^F}\right)\begin{pmatrix}\bar{\mathbf{F}}_\mathbf{u}\\ \bar{\mathbf{F}}_\mathbf{d}\end{pmatrix}\ , \tag{4.4}$$

where $\mathbf{A}$ is a discretised matrix representing the Green's function and $\mathbf{S}$ represents the photon to count spectral response of RHESSI.

Equation (4.4) must be simplified so that the array containing the cross-section and Green's functions is converted into a standard two dimensional matrix and the two component electron spectrum is represented as a one dimensional vector. A method of performing this transformation is described in Hubeny and Judge (1995). This can be done by defining a new matrix of the form $\mathbf{M}_{i\nu}$ where the indices of this new matrix are related to the previous 3 dimensional array by $\nu = \tau(j-1)+k$ where τ is the maximum value of k. The elements of the original array are then written into the appropriate elements of the new matrix. The equation can then be solved using the standard regularised inversion methods described in Section 3.1.

4.2.1 Determining anisotropy from count data

The inversion algorithm is applied to the selected time intervals of the flare and the upward, $\bar{n}V\bar{F}_u$, and downward, $\bar{n}V\bar{F}_d$, electron fluxes calculated. As with the angle averaged spectra considered in Chapter 3, a first estimate of a thermal plus double power-law fit is performed here assuming $\overline{F}_u = \overline{F}_d$. The fit is again used to precondition the matrices $\mathbf{M}$ and $\mathbf{L}$ and the data vector $\mathbf{C}$.

The errors on the electron flux components are calculated by combining the errors on the count flux and the errors on the background. Random perturbations are applied to the count flux based on the error and the electron flux is recalculated. The distribution of these realisations is then used to estimate the error on the electron flux. The regularised solution also has finite resolution. The resolution matrix is defined as $\mathbf{R} = \mathbf{M}_\lambda^{-1}\mathbf{M}_{true}$, where $\overline{\mathbf{F}}_{true}^{-1} = \mathbf{M}_{true}\mathbf{C}$ is the true solution to the inverse problem and $\overline{\mathbf{F}}_\lambda = \mathbf{M}_\lambda^{-1}\mathbf{C}$ is the regularised solution. The resolution matrix quantifies the horizontal errors of the solution, so the identity matrix (zero horizontal errors) correspond to the direct inverse $\mathbf{M}_\lambda^{-1}$. For any practical situations, the regularisation imposes a spread on the strong peaks centred on the main diagonal, this is an unavoidable occurrence in any inverse problem. The FWHM of each of the rows of this matrix is taken as the energy resolution for that energy bin and is considered here as the horizontal error in the electron flux (Figure 4.3).

The anisotropy was defined to be the ratio of $nV\overline{F}_d$ to $nV\overline{F}_u$. Confidence strips for the total anisotropy were calculated using the same method as the errors in the electron flux (Figure 4.4). Random perturbations were applied within the "confidence river" defined by both the horizontal and vertical error bars.

The binning scheme used is important to consider. Here pseudo-logarithmic binning was used in each case. It was found that the optimum scheme used the same bin size for count, photon and electron spectra but with different maximum energies for each. This was determined by applying the method to RHESSI observations for a variety of binning schemes, ranging from 20 to 800 bins in total and comparing the residuals and solution errors for each case. The count spectra was mostly constrained by the data, but a maximum value of 500 keV was also

imposed to avoid the positron annihilation line. The maximum energy considered in photon space was roughly half the maximum energy in electron space as photons are emitted up to a maximum value of the electron kinetic energy. Different values for the high energy cutoff in electron space were tested for each flare, ranging from 1 to 10 MeV, however this rarely had a significant effect on the result. If too many bins are used the error for each point increases this can be greatly magnified by inversion; however if there are too few bins, information about the spectra is lost. Therefore a range of values for the total number of bins used were also tested for each flare. The minimum energy was also constrained by the data, for most flares a value above 10 keV was used to avoid contamination with iron lines, however for some flares with high background at low energies higher values of up to 15 keV were used.

4.2.2 Inversion of Simulated Data

In order to test the method, we have applied it to simulated electron spectra. The electron spectra have been assumed to have simple functional forms and equivalent photon spectra calculated with reflected albedo component included. Random noise, at a similar level to the noise estimated from RHESSI observations, has been added to the resulting count spectrum. This simulated spectrum was then inverted using the same algorithm as the real data.

The input upward ($F_u(E)$) and downward ($F_d(E)$) electron fluxes were assumed with the functional forms

$$\overline{F}_d(E) = AE^{-2} \qquad \overline{F}_u(E) = \frac{\overline{F}_d}{\left(1+\frac{E-10}{50}\right)^a} \tag{4.5}$$

where the power-law parameter a sets the level of anisotropy and the scaling factor A is chosen such that the simulated count spectrum is of the same order of magnitude as the RHESSI observations.

Spectra from isotropic initial distributions generally give a result which is consistent with the input spectrum within errors and shows a reasonable distribution

of residuals (Figures 4.3 and 4.4 - left panels). For weak anisotropy the results generally show broader confidence intervals than for the isotropic case with the same level of noise, so that the solution is often consistent with the weakly anisotropic input spectrum and an isotropic input spectrum (Figures 4.3 and 4.4 - right panels). For stronger levels of anisotropy ($\overline{F}_d/\overline{F}_u > 10$ at 100 keV), the method tends to give unphysical negative values for the electron flux. This can be avoided by increasing the regularisation parameter to force the solution to be smoother and ensure the solution is positive everywhere. However, this approach leads to under-regularisation and unacceptably large residuals, suggesting that the method cannot converge on a physically meaningful solution which satisfies the data. It should be noted that there is an upper limit to the size of the maximum anisotropy detectable, as it is difficult to constrain an anisotropy that is greater than the fractional error in the larger component of electron flux.

The tests also confirm that this method works best for flares with high energy counts close to the disk centre and that the anisotropy cannot be reliably inferred for weak or limb events, as was expected from the forward modelling. All the inversions of RHESSI data show physically sound results with reasonable residuals.

4.3 Application to RHESSI Measurements

4.3.1 Flare Selection

The RHESSI data archive was examined for flares with emission above 300 keV with particular attention paid to flares close to the solar disk centre. The positions of the flares were verified by imaging in the $25 - 100$ keV energy range over the impulsive phase of each flare. These flares are selected because the forward modelling (Chapter 2) suggests that the variation due to beaming is strongest at high energies, and flares closest to the disk centre should have the strongest albedo reflection and should therefore also show the greatest change due to beaming. In total 8 suitable flares were found (Table 4.1) which were within 60° of

the solar centre (Figure 4.5) and showed significant $> 3\sigma$ counts above background (Figures 4.6 - 4.8); a number of other flares matching these criteria were found but they were discounted due to high levels of pulse pileup and particle contamination.

Table 4.1: Flares suitable for analysis

	Flare Date	Start Time (UT)	GOES Class	x position	y position	μ
A	20-Aug-2002	08:25:21	M3.4	562	-270	0.72
B	10-Sep-2002	14:52:47	M2.9	-622	-244	0.72
C	17-Jun-2003	22:52:42	M6.8	-783	-148	0.52
D	2-Nov-2003	17:16:00	X8.3	770	-343	0.51
E	10-Nov-2004	02:09:40	X2.5	738	116	0.69
F	15-Jan-2005	22:49:08	X2.6	117	325	0.93
G	17-Jan-2005	09:43:44	X3.8	441	301	0.86
H	10-Sep-2005	21:34:26	X2.1	-667	-255	0.69

For each of the flares found, the background was removed in the standard manner Schwartz *et al.* (2002). Counts were accumulated over the impulsive phase, as the differences in the spectra due to anisotropy in the electron spectra are greater at higher energies. The time intervals studied were selected ensuring a high number of high energy counts (Figures 4.10 and 4.11). A pseudo-logarithmic binning scheme between 10 keV and 500 keV was used to initially accumulate the spectra avoiding detectors 2 and 7 due to their poor resolution Smith *et al.* (2002). After background subtraction had been performed, the energy range was further reduced by discarding the energy bins with counts less than 3σ above the background.

4.3.2 20th August 2002

This flare was detected on 20th August 2002 around 08:20 UT with the impulsive peak starting about 08:25 UT. It was detected with a heliocentric angle of $\sim 43^\circ$ equivalent to $\mu = 0.73$. The flare also shows good count statistics up to

400 keV (see Figures 4.6 and 4.10). As this flare had attenuator status changes from A0 (open telescope) to A1 (thin shutter in) at 08:25:16 UT and to A3 (both shutters in) at 08:25:44 UT, the analysis was only performed over the 16 s period rather than the 64 s period studied for most flares. There is some particle contamination over the impulsive phase. This flare was extensively studied by Kašparová, Kontar, and Brown (2007) and the background subtraction used in this paper is similar to the subtraction described there. This flare was previously analysed using bi-directional inversion by Kontar *et al.* (2006). This is flare A in Table 4.1.

4.3.3 10th September 2002

This flare was detected on 10th September 2002 between 14:02 and 15:15 UT with the impulsive peak starting about 14:52 UT. It was detected with a heliocentric angle of $\sim 44°$ equivalent to $\mu = 0.72$. The flare also shows good count statistics up to 300 keV (see Figures 4.6 and 4.10). This flare also has an attenuator status change from A0 to A1 at 14:52:43 UT and to A3 at 14:54:16 UT, so the impulsive phase is taken to be a 32 s time interval between 14:52:47 and 14:53:19 UT. This is flare B in Table 4.1.

4.3.4 17th June 2003

This flare was detected on 17th June 2003 starting at approximately 22:30 UT. As RHESSI shows significant particle contamination during the early stages of this flare analysis was performed on a later impulsive peak with accumulation starting at 22:52:42 UT. It was detected with a heliocentric angle of 59° equivalent to $\mu = 0.51$. The flare also shows good count statistics up to 300 keV (see Figures 4.7 and 4.11). This is flare C in Table 4.1.

4.3.5 2nd November 2003

This flare was detected on 2nd November 2003. It was detected with a heliocentric angle of $\sim 59°$ equivalent to $\mu = 0.51$. The flare also shows good count statistics up to 300 keV (see Figures 4.7 and 4.11). RHESSI showed some elevated particle levels during the impulsive phase of the flare so analysis was confined to the earlier part of the impulsive phase. This is flare D in Table 4.1.

4.3.6 10th November 2004

This flare was detected on 10th November 2004. It was observed with a heliocentric angle of 46.5° equivalent to $\mu = 0.69$. The flare shows no significant particle measurements during the impulsive phase and low probability of pulse pileup. The flare also shows good count statistics up to 500 keV (see Figures 4.8 and 4.11). This is flare E in Table 4.1.

4.3.7 15th January 2005

This flare was detected on 15th January 2005. It was detected with a heliocentric angle of 20° equivalent to $\mu = 0.93$, the closest of all the flares selected to the disk centre and therefore the most likely to show evidence of strong downwards directivity. The flare also shows good count statistics up to 400 keV (see Figures 4.8 and 4.11). This is flare F in Table 4.1.

4.3.8 17th January 2005

This flare was detected on 17th January 2005 between 09:30 and 15:15 UT with the impulsive peak starting about 09:42 UT. It was detected with a heliocentric angle of $\sim 31°$ equivalent to $\mu = 0.86$. The flare also shows good count statistics up to 300 keV (see Figures 4.9 and 4.11). As this flare occurs in the tail of a previous flare it is has very high background at low energies. Counts below 18 keV

were not accumulated for this flare. This flare was also previously analysed using bi-directional inversion Kontar *et al.* (2006). This is flare G in Table 4.1.

4.3.9 10th September 2005

This flare was detected on 10th September 2005. It was detected with a heliocentric angle of $\sim 46°$ equivalent to $\mu = 0.69$. This flare showed negligible particle contamination and a low probability of pulse pileup. The flare also shows good count statistics up to 300 keV (see Figures 4.9 and 4.11). Due to changes in the attenuator status during the impulsive phase from A1 to A3 at 21:34:12 UT and the maximum time interval studied for this flare is 32 s starting at 21:34:26 UT. This is flare H in Table 4.1.

4.4 Anisotropy results

The bi-directional algorithm was applied to the impulsive phase of each of the flares studied. For most of the flares a 64 second time interval beginning when the counts above 100 keV are detected was considered. This is not possible for all flares as the period where the high energy counts are measured is shorter for some flares. Attenuator status changes can also introduce large discrepancies into spectral analysis so these were all avoided.

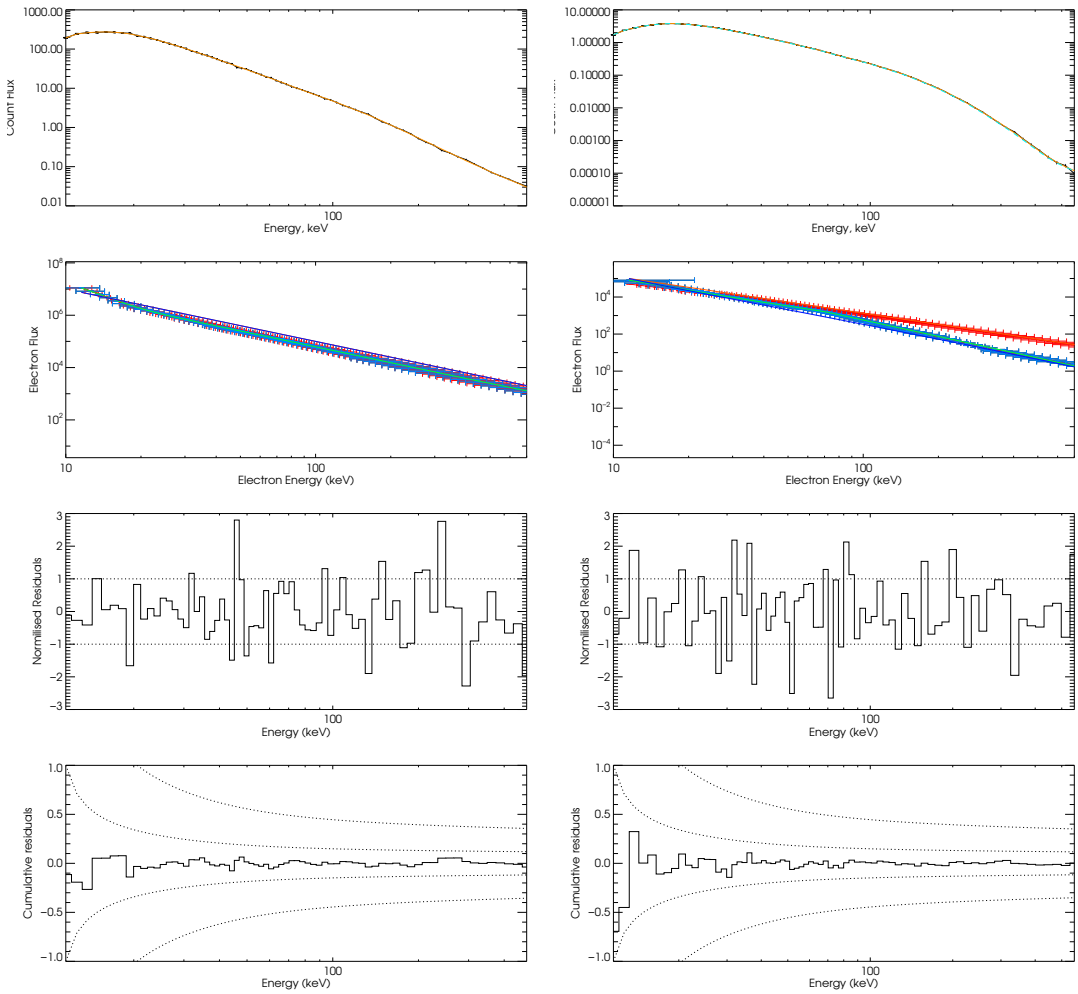

Figure 4.3: Results from the test on the bi-directional inversion algorithm assuming a disk centre event. The top panel shows the simulated observed count spectrum (orange) with associated errors and the count spectrum corresponding to the bi-directional solution (blue dashed line). The second panel shows the recovered upward (light blue) and downward (red) regularised electron spectrum with associated 1-σ vertical and horizontal error bars for each point. Overplotted are the input upward (dark blue) and downward electron spectra (orange) and the results of the initial forward fit used to precondition the data (green). The third panel shows the normalised residuals for each time interval and the bottom panel shows the cumulative residuals. Left: the case of weak beaming $a = 1$ Right: an intermediate beaming case $a = 3$.

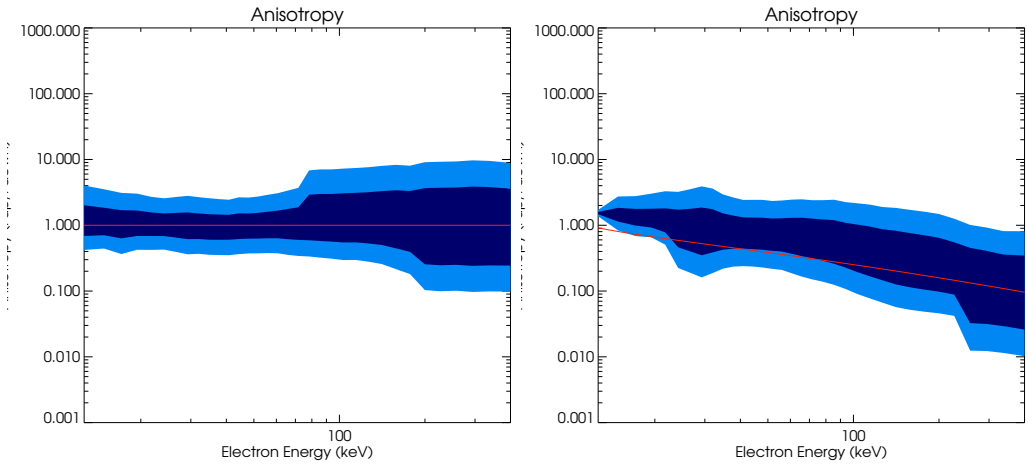

Figure 4.4: The anisotropy of the electron spectrum (defined as $\overline{F}_d/\overline{F}_u$) for the two cases in figure 4.3 Left: weak beaming ($a = 1$) Right: intermediate beaming ($a = 3$). The red line shows the anisotropy of the input electron spectrum, the dark blue area represents the 1σ confidence interval and the light blue the 3σ confidence interval.

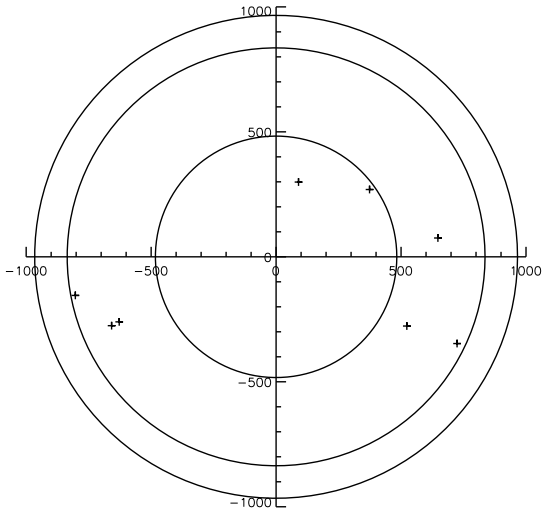

Figure 4.5: Positions of all 8 flares studied on the solar disk. The inner rings indicate heliocentric angles of 30° and 60°.

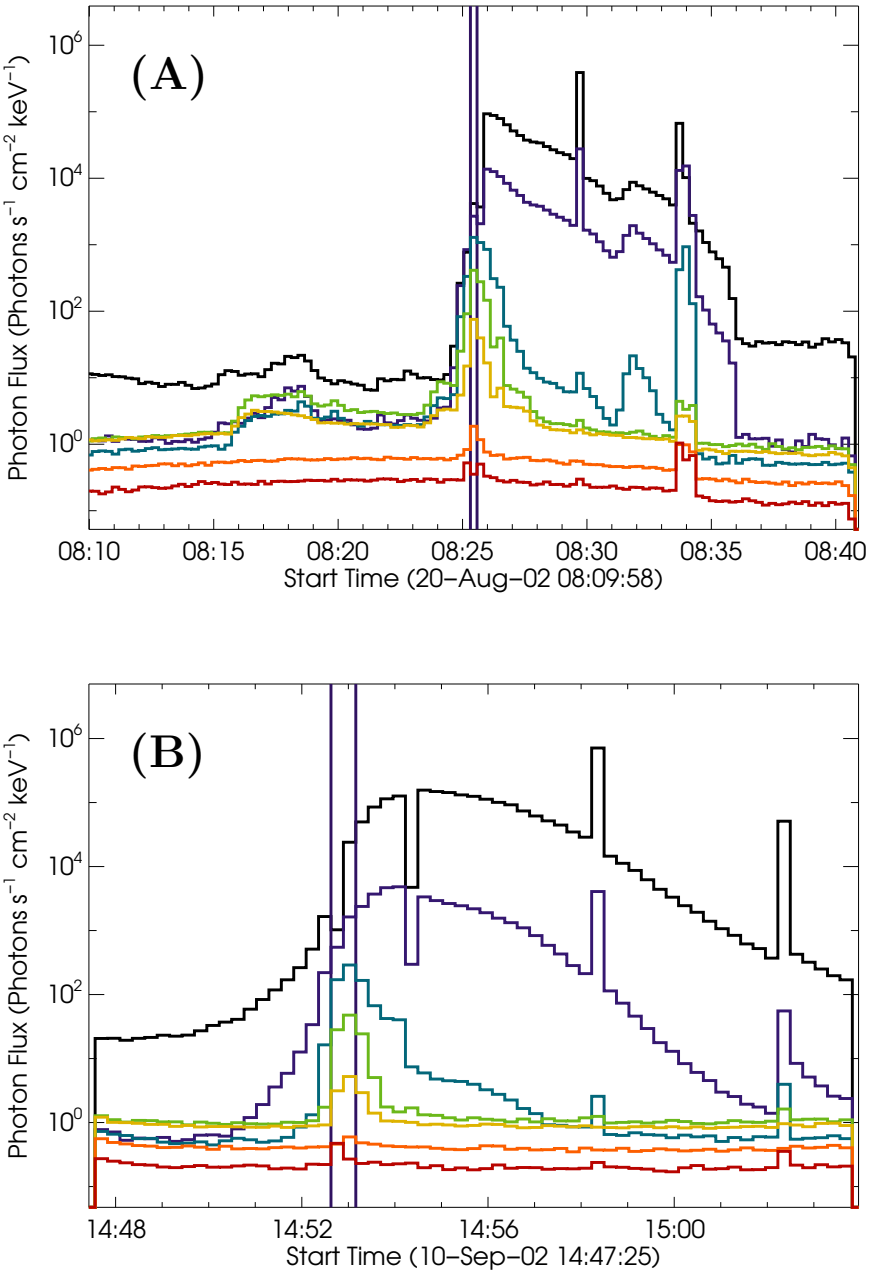

Figure 4.6: RHESSI lightcurves of the flares observed on 20th August 2002 (A) and 10th September 2002 (B) accumulated in 7 energy bands - black 7-12 keV, purple 12-25 keV, blue 25-50 keV, green 50-100 keV, yellow 100-300 keV, orange 300-800 keV, red 800-5000 keV. The vertical lines show the accumulation time interval used. The plots are semi-calibrated, a diagonal approximation of the RHESSI response is used to estimate the photon flux from the measured counts. There are still instrumental artefacts present with the very sharp spikes and dips being the result of attenuator status changes. All times are in UT.

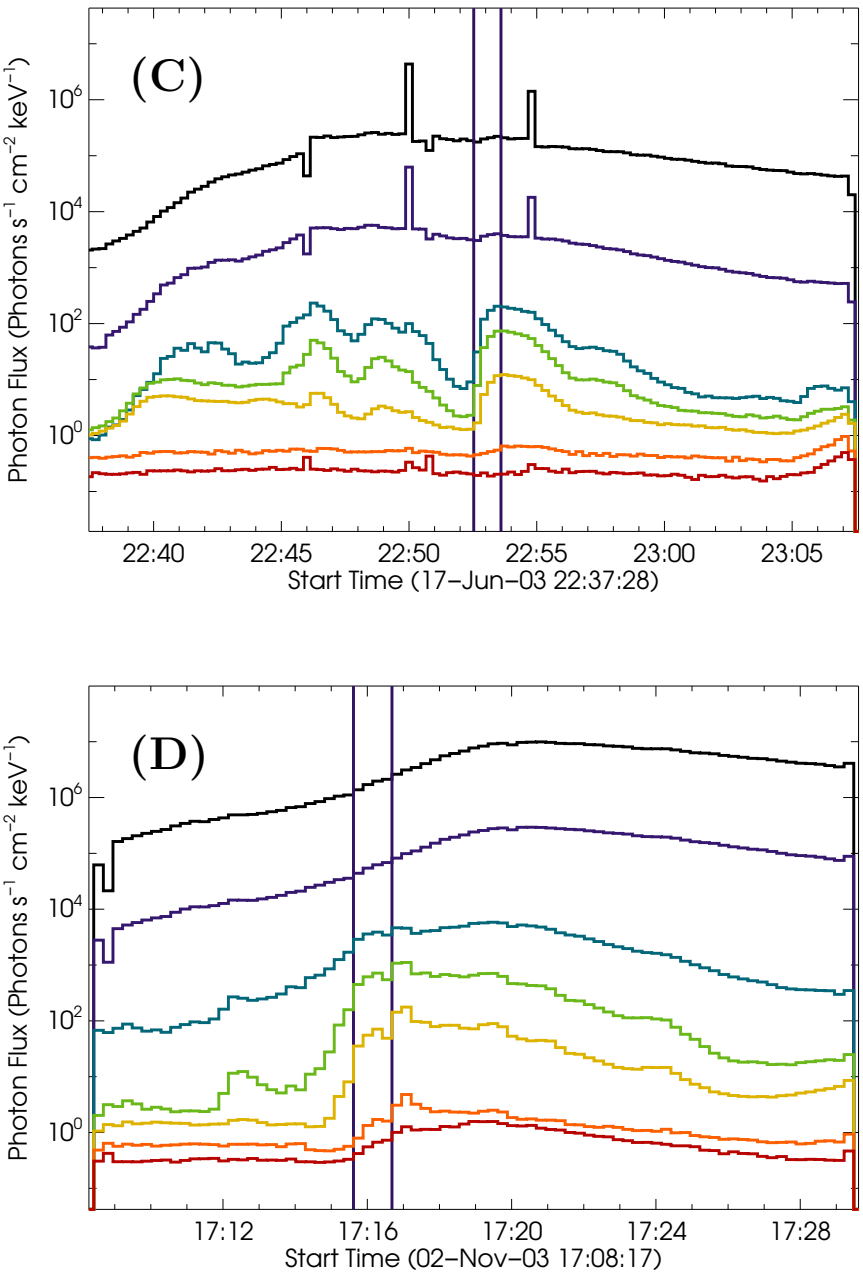

Figure 4.7: As Figure 4.6 for flares on 17th June 2003 (C), 2nd November 2003 (D) and 10th November 2004 (E). Colour key - black 7-12 keV, purple 12-25 keV, blue 25-50 keV, green 50-100 keV, yellow 100-300 keV, orange 300-800 keV, red 800-5000 keV.

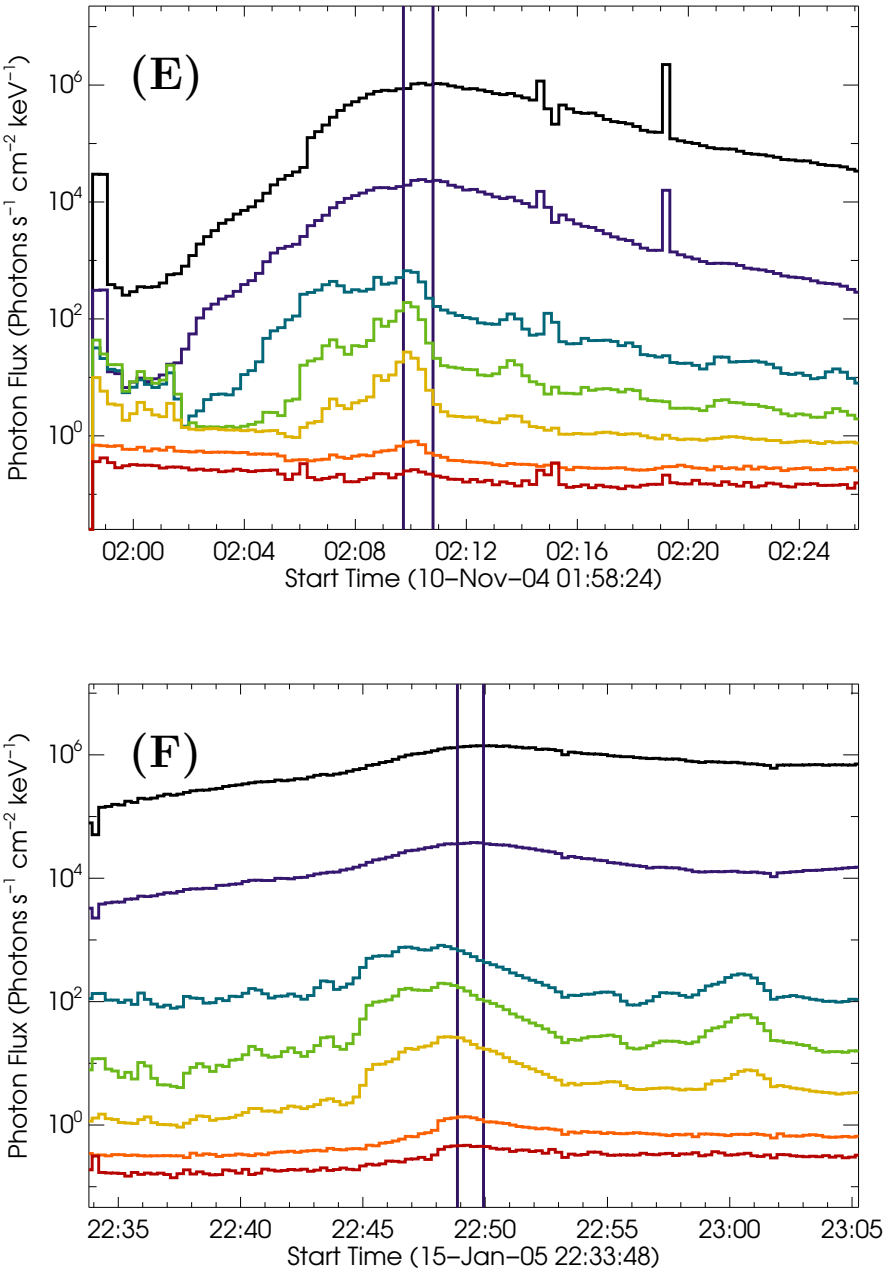

Figure 4.8: As Figure 4.6 for flares on 15th January 2005 (F), 17th January 2005 (G) and 10th September 2005 (H). Colour key - black 7-12 keV, purple 12-25 keV, blue 25-50 keV, green 50-100 keV, yellow 100-300 keV, orange 300-800 keV, red 800-5000 keV.

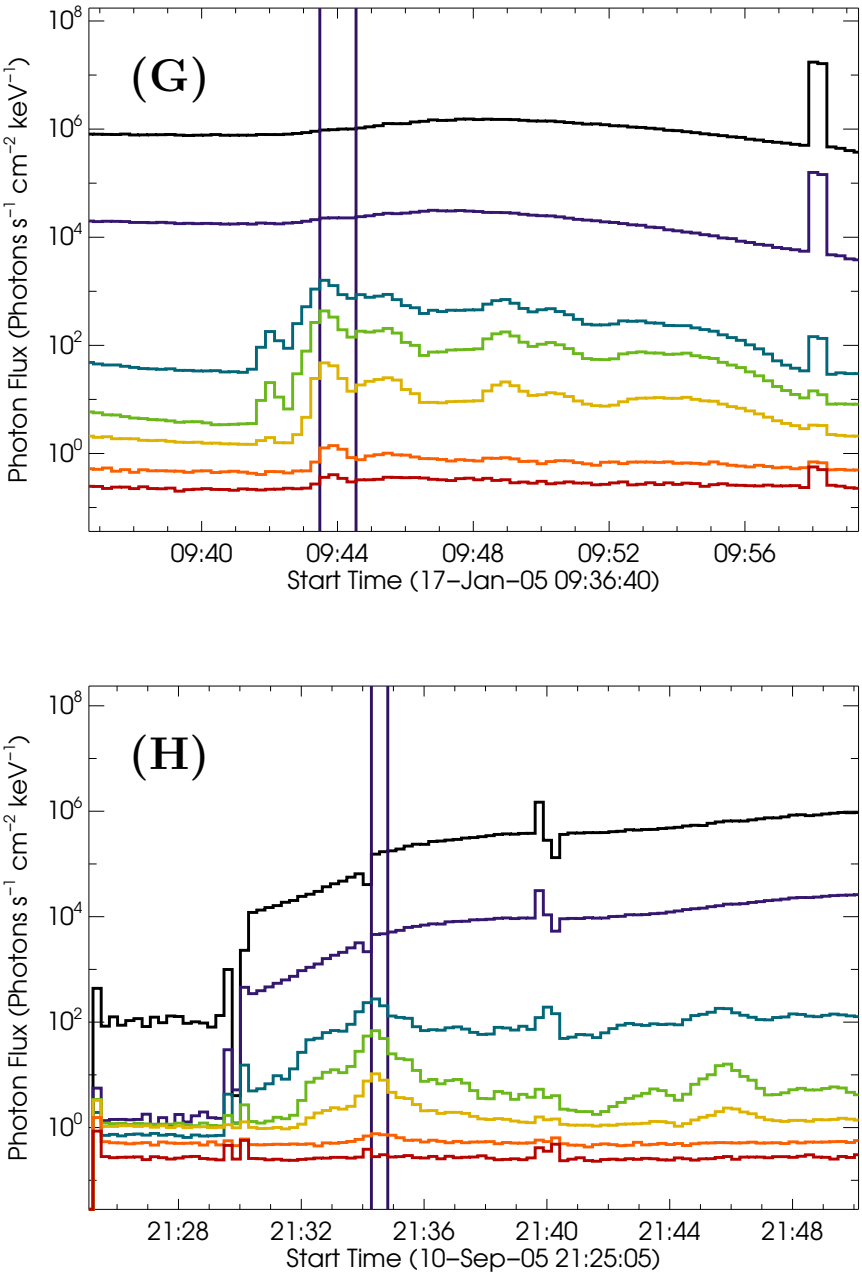

Figure 4.9: As Figure 4.6 for flares on 15th January 2005 (F), 17th January 2005 (G) and 10th September 2005 (H). Colour key - black 7-12 keV, purple 12-25 keV, blue 25-50 keV, green 50-100 keV, yellow 100-300 keV, orange 300-800 keV, red 800-5000 keV.

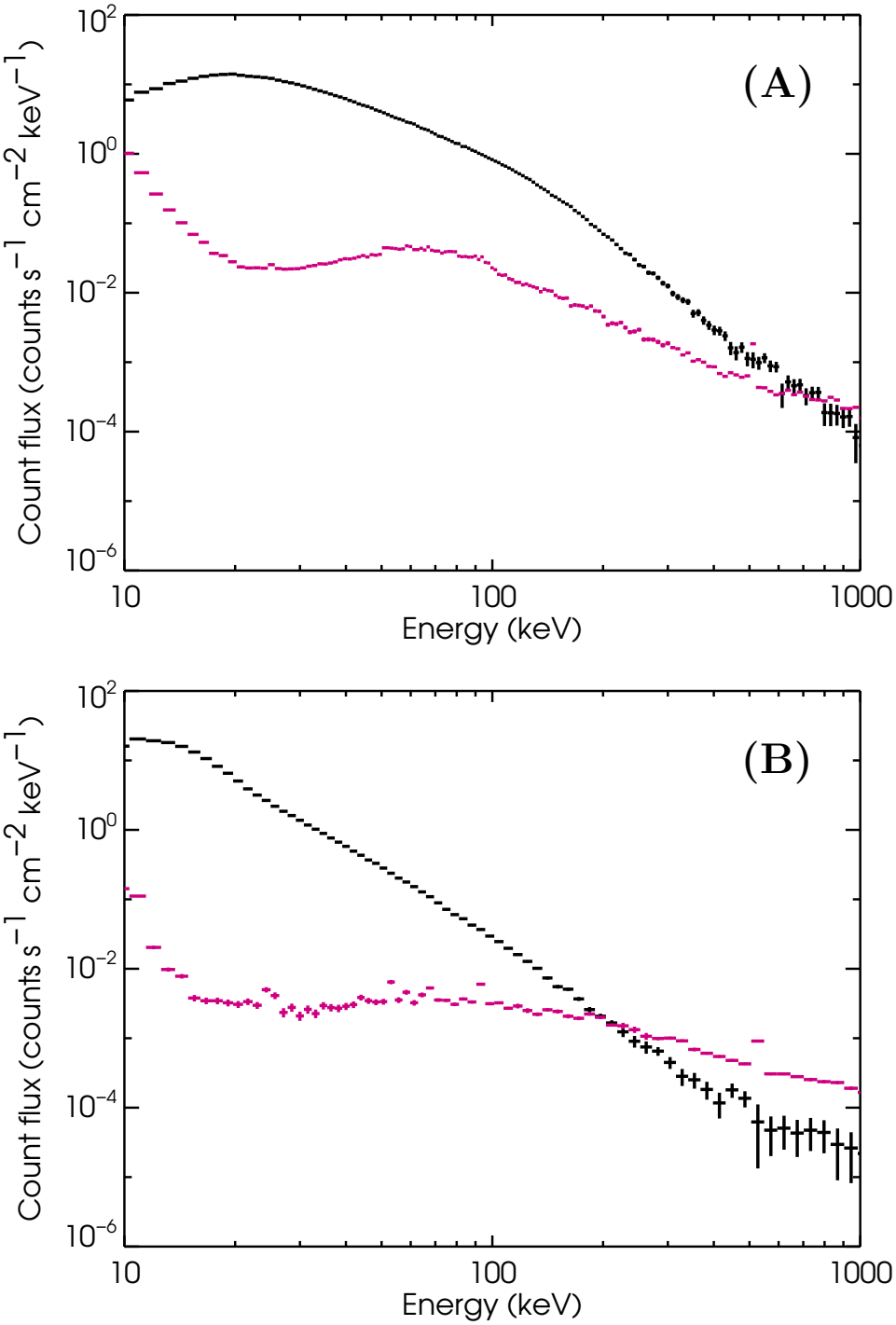

Figure 4.10: Impulsive phase count spectra accumulated by RHESSI flare observed on 20th August 2002 (A) and 10th September 2002 (B). The black line shows the background subtracted counts and the magenta line the background counts.

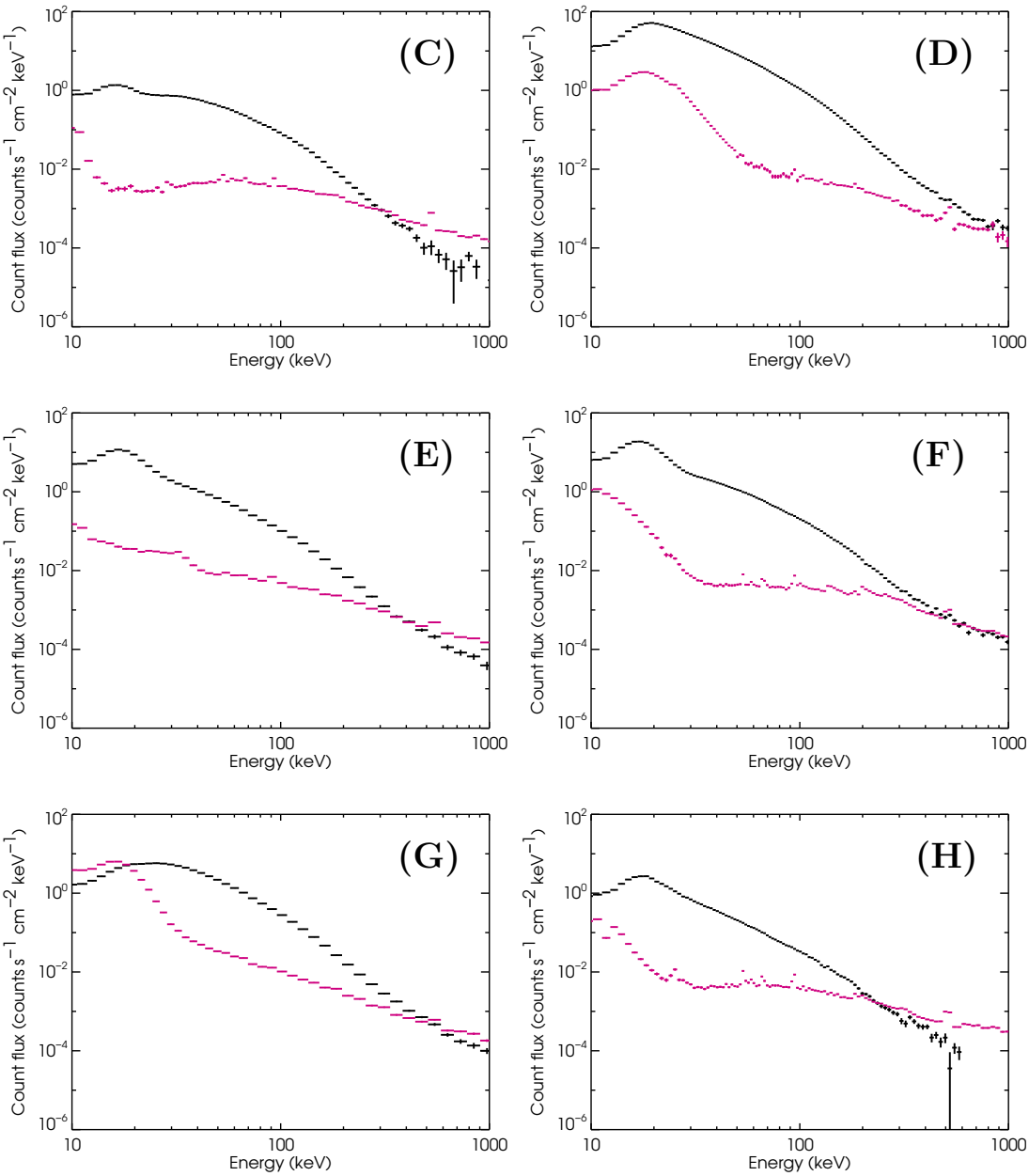

Figure 4.11: As Figure 4.10 for flares on 17th June 2003 (left), 2nd November 2003 (right), 10th November 2004 (E), 15th January 2005 (F), 17th January 2005 (G) and 10th September 2005 (H).

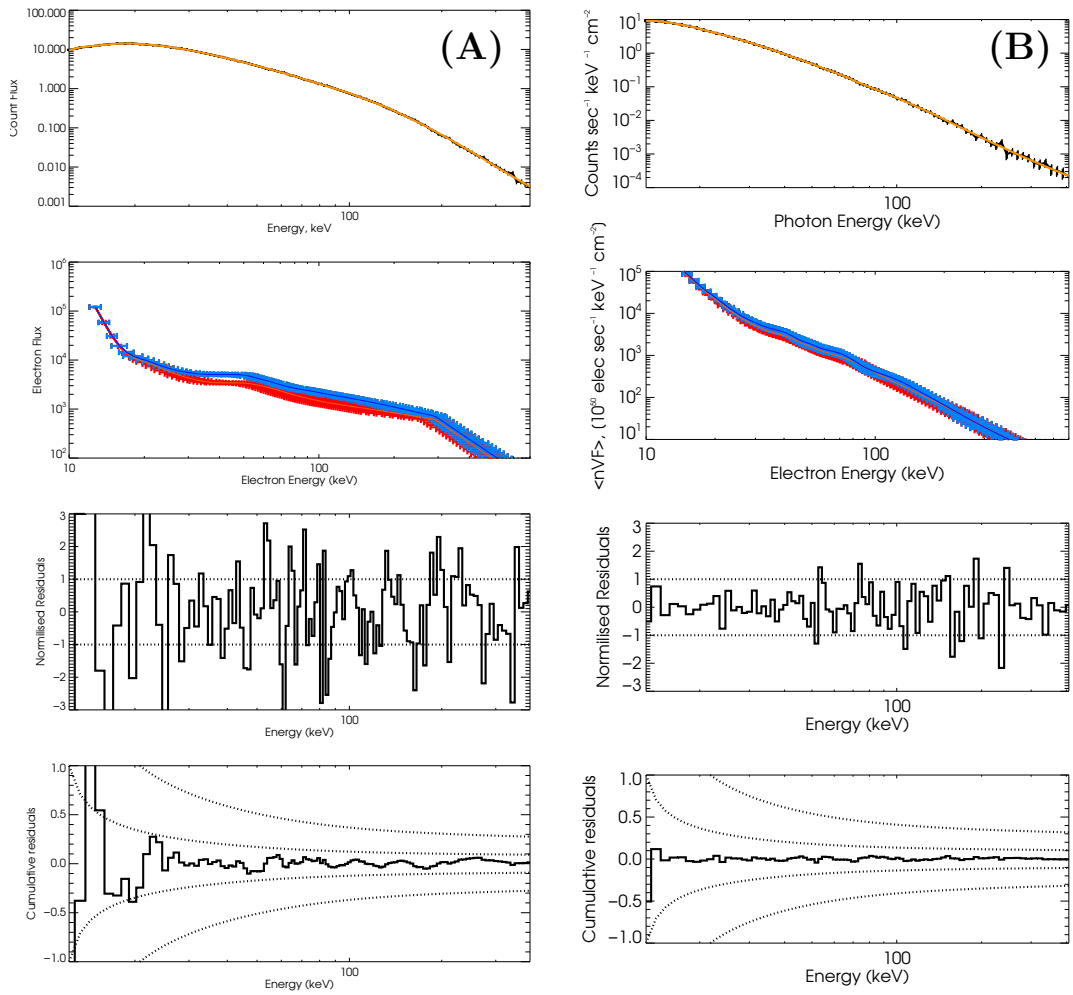

Figure 4.12: Results of the inversion procedure for full impulsive phase for flares observed on 20th August 2002 (left) and 10th September 2002 (right). Top panel shows the measured count spectrum (full line) overplotted with the count spectrum corresponding to the calculated regularised electron spectra (dashed line). The second panel shows the regularised electron spectrum with associated 1-σ vertical and horizontal error bars for each point, the blue line denotes the upward electron flux and the red line the downward electron flux. The third panel shows the normalised residuals for each time interval and the bottom panel shows the cumulative residuals.

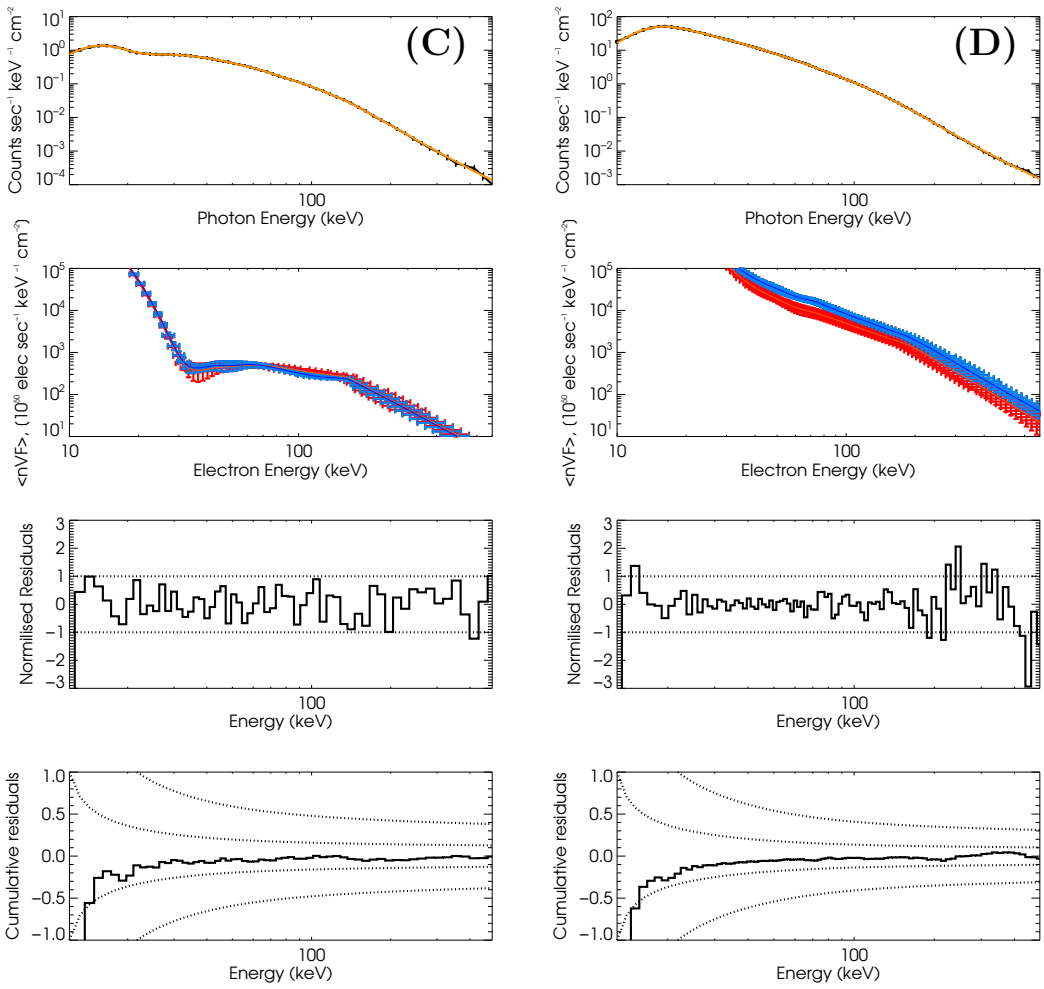

Figure 4.13: As Figure 4.12 for flares on 17th June 2003 (left) and 2nd November 2003 (right)

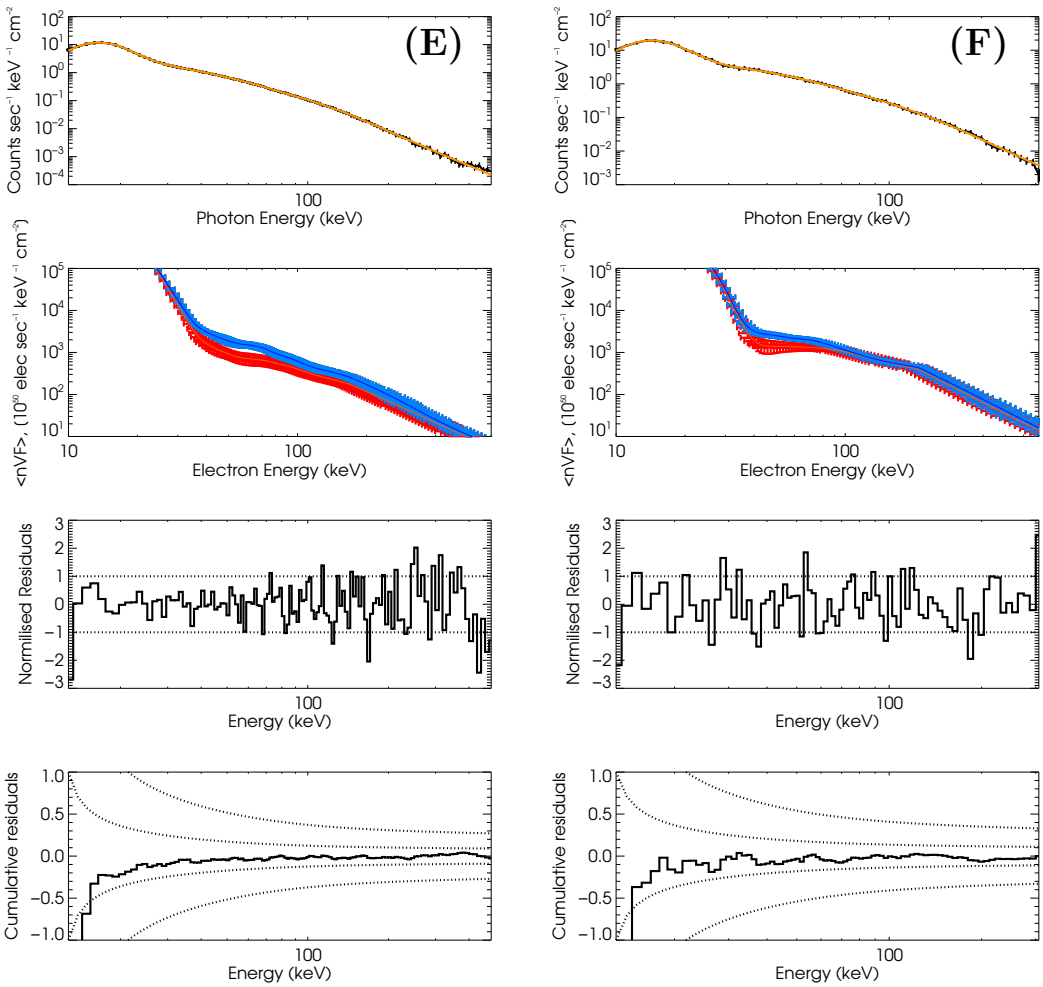

Figure 4.14: As Figure 4.12 for flares on 10th November 2004 (left) and 15th January 2005 (right).

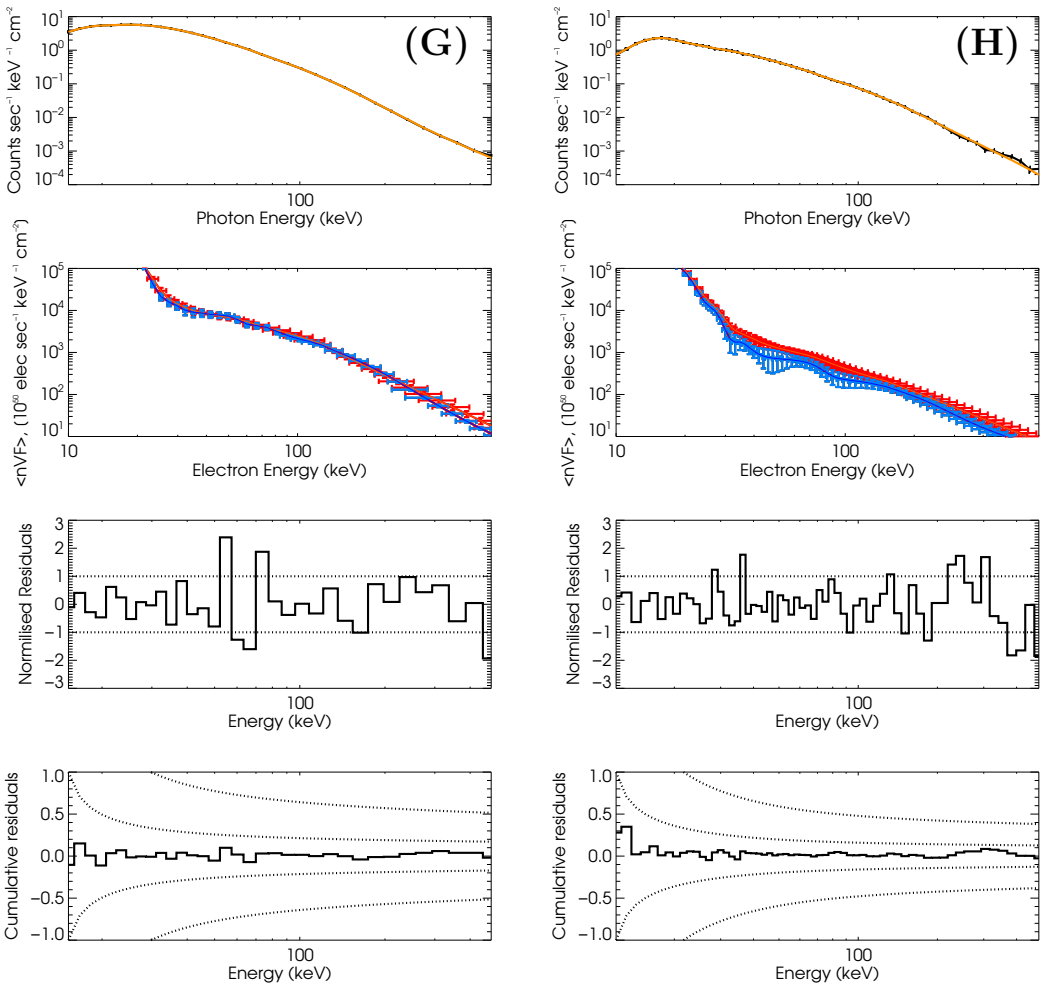

Figure 4.15: As Figure 4.12 for flares on 17th January 2005 (left) and 10th September 2005 (right).

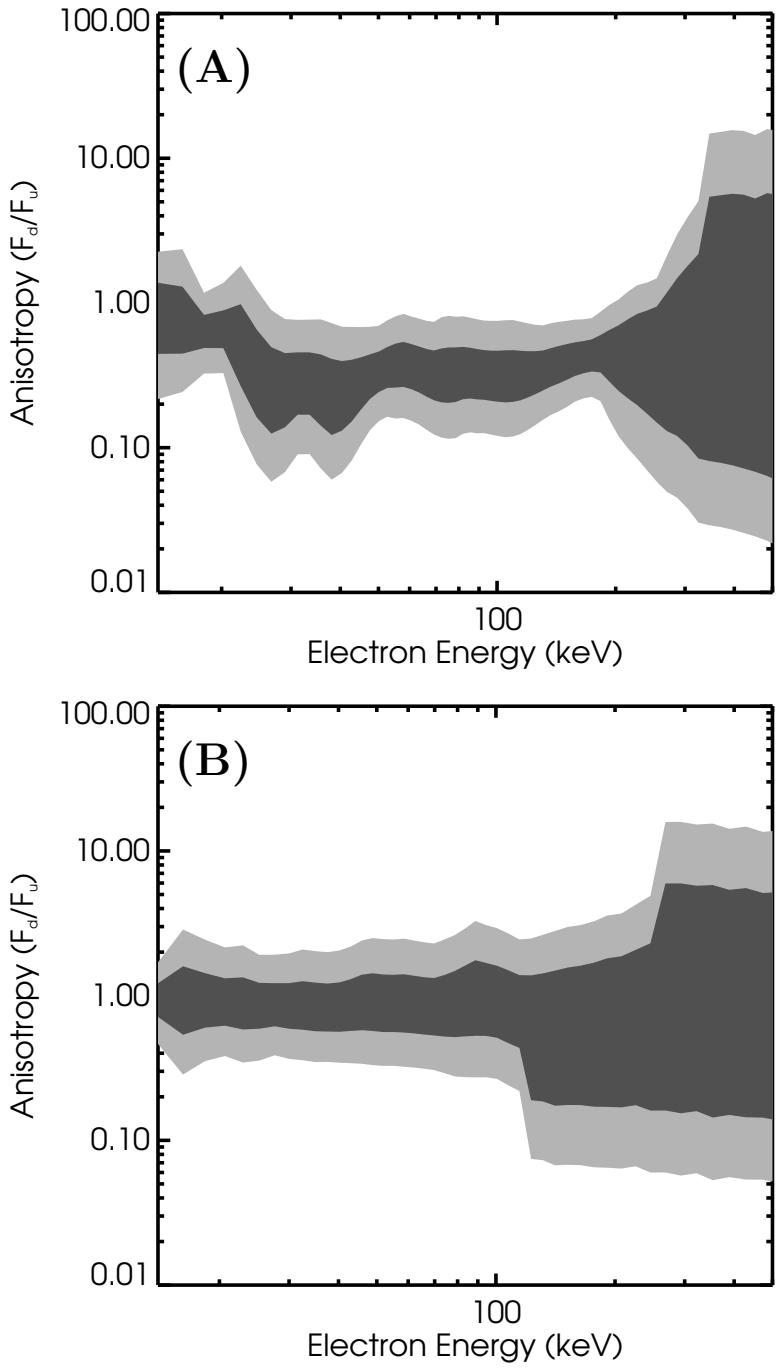

Figure 4.16: The anisotropy of the electron spectrum (defined as F_d/F_u) for flares observed on 20th August 2002 (A) and 10th September 2002 (B). The dark grey area represents the 1σ confidence interval and the light grey the 3σ confidence interval.

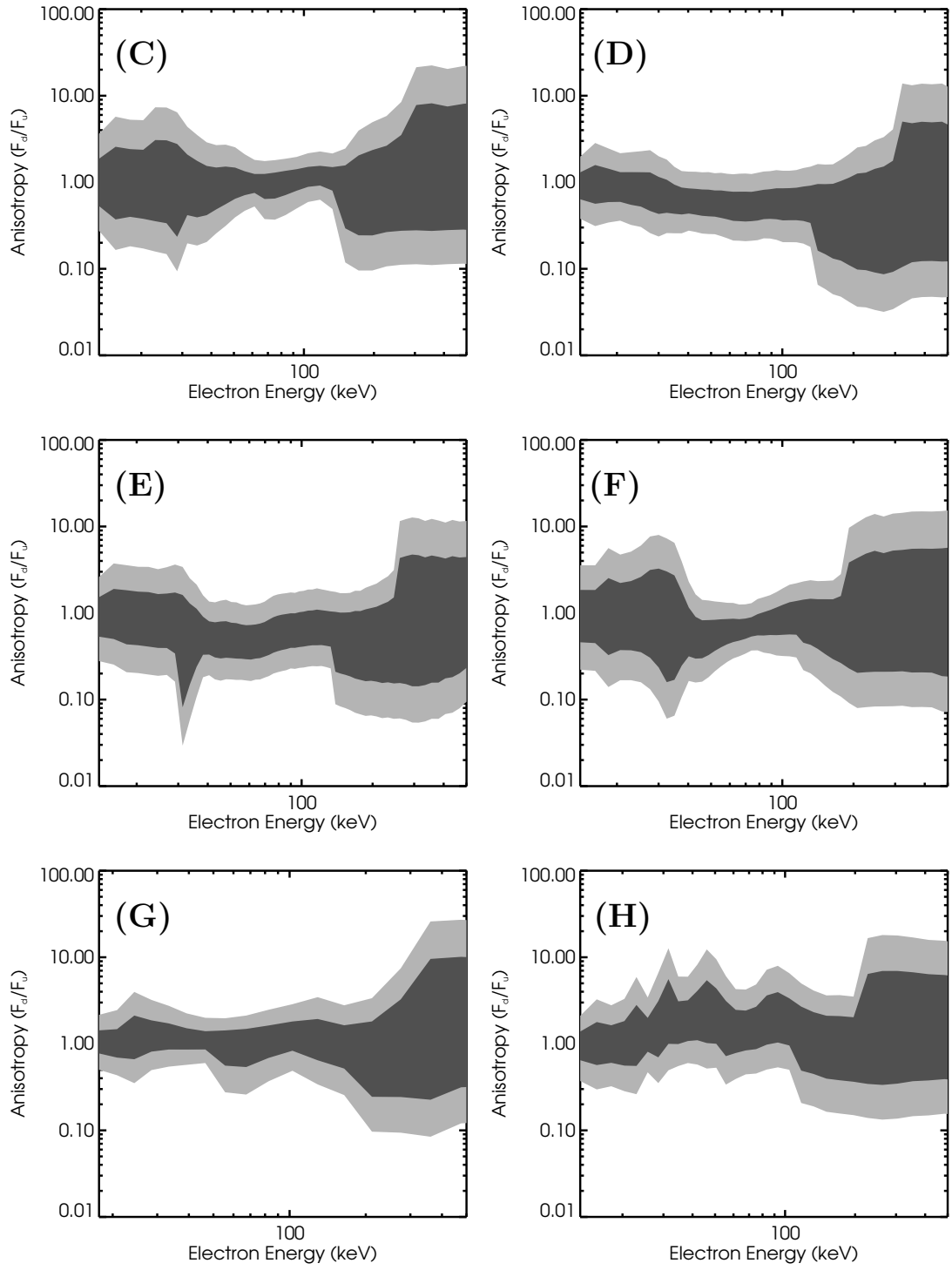

Figure 4.17: As Figure 4.16 for flares on 17th June 2003 (left), 2nd November 2003 (right), 10th November 2004 (E), 15th January 2005 (F), 17th January 2005 (G) and 10th September 2005 (H).

4.4.1 Temporal variation

Four seconds is roughly the rotation period of RHESSI and thus the shortest time interval studied here. Longer time intervals of 8, 16, and 32 seconds were also studied for some flares, depending on the length of the impulsive phase. The results for these time intervals are very similar to the results for the full impulsive phase. The inversions for short time intervals generally show confidence intervals around an anisotropy of 1 at the 1σ level extending to around 2 below 100 keV and sharply increasing above that. As the count statistics are lower for the shorter time intervals the confidence intervals are wider than for the full impulsive phase. There was no statistically significant variation in the level of anisotropy for the duration of the impulsive phase. As an example the recovered bi-directional electron spectra for each of the 4 second time intervals for the flare on 10th November 2004 are shown in Figures 4.19 to 4.24.

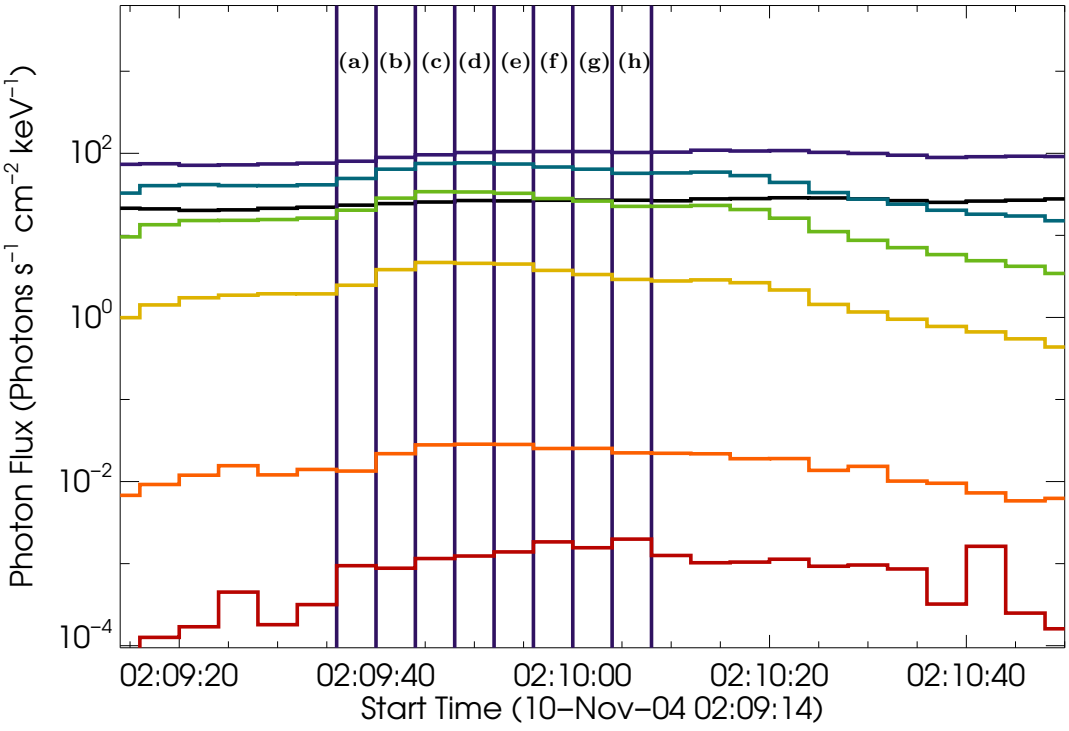

Figure 4.18: RHESSI lightcurves for the impulsive phase of the flare observed on 10th November 2004 (Flare E in Table 4.1) accumulated in 7 energy bands - black 7-12 keV, purple 12-25 keV, blue 25-50 keV, green 50-100 keV, yellow 100-300 keV, orange 300-800 keV, red 800-5000 keV. The vertical lines show the 4 second accumulation time intervals labelled a-h. The full extent between the first and last vertical bars is identical to the impulsive phase shown in Figure 4.7. The plot is semi-calibrated, a diagonal approximation of the RHESSI response is used to estimate the photon flux from the measured counts. Time is in UT.

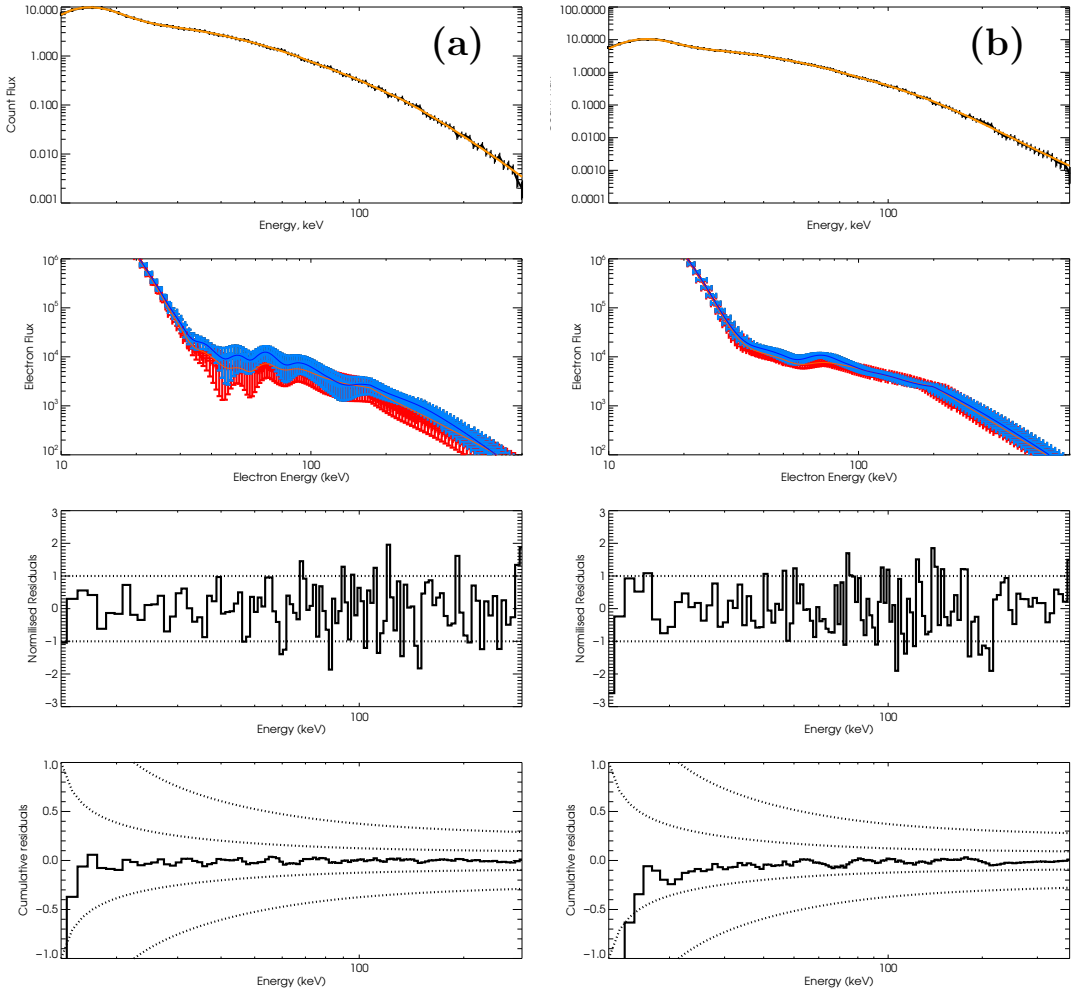

Figure 4.19: Results of the inversion procedure for full impulsive phase for flare time intervals a and b. Top panel shows the measured count spectrum (full line) overplotted with the count spectrum corresponding to the calculated regularised electron spectra (dashed line). The second panel shows the regularised electron spectrum with associated 1-σ vertical and horizontal error bars for each point, the light grey line denotes the upward electron flux and the dark grey line the downward electron flux. The third panel shows the normalised residuals for each time interval and the bottom panel shows the cumulative residuals.

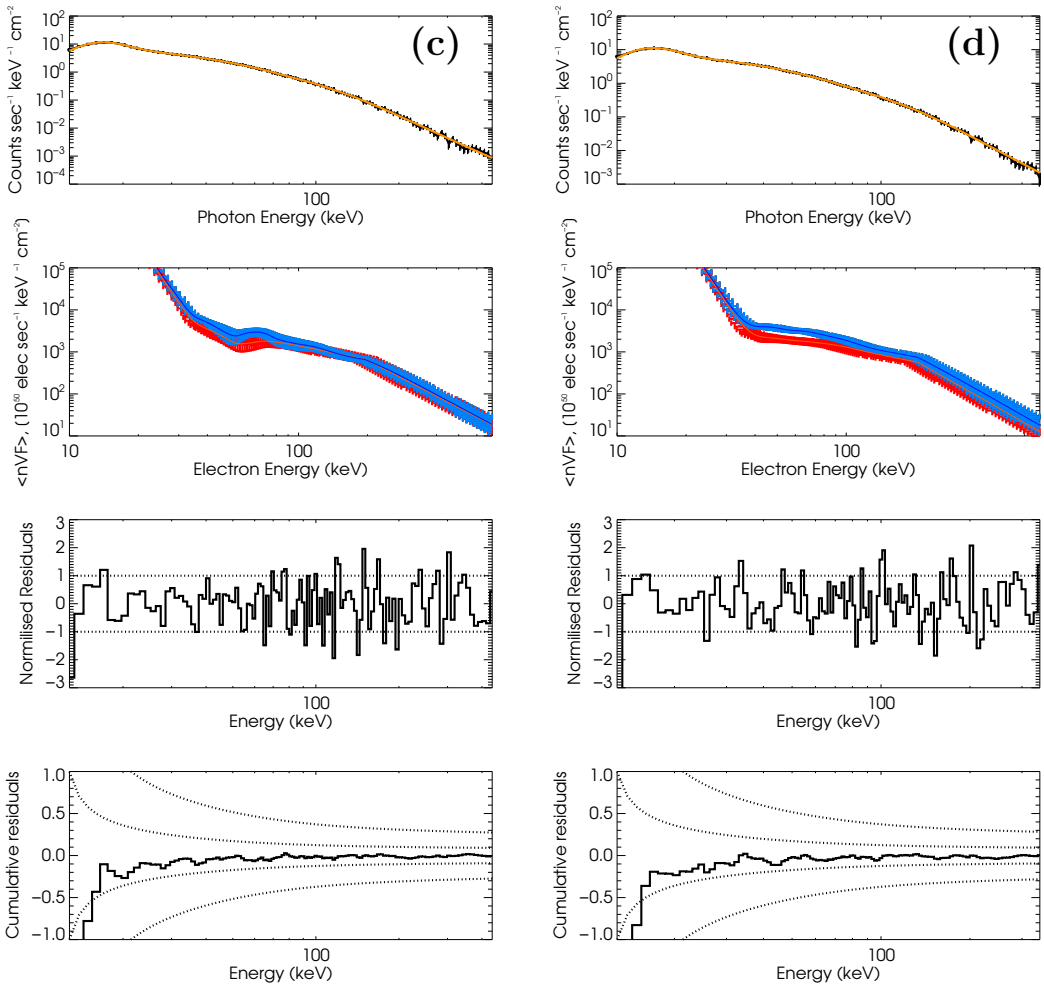

Figure 4.20: As Figure 4.19 for time intervals c and d.

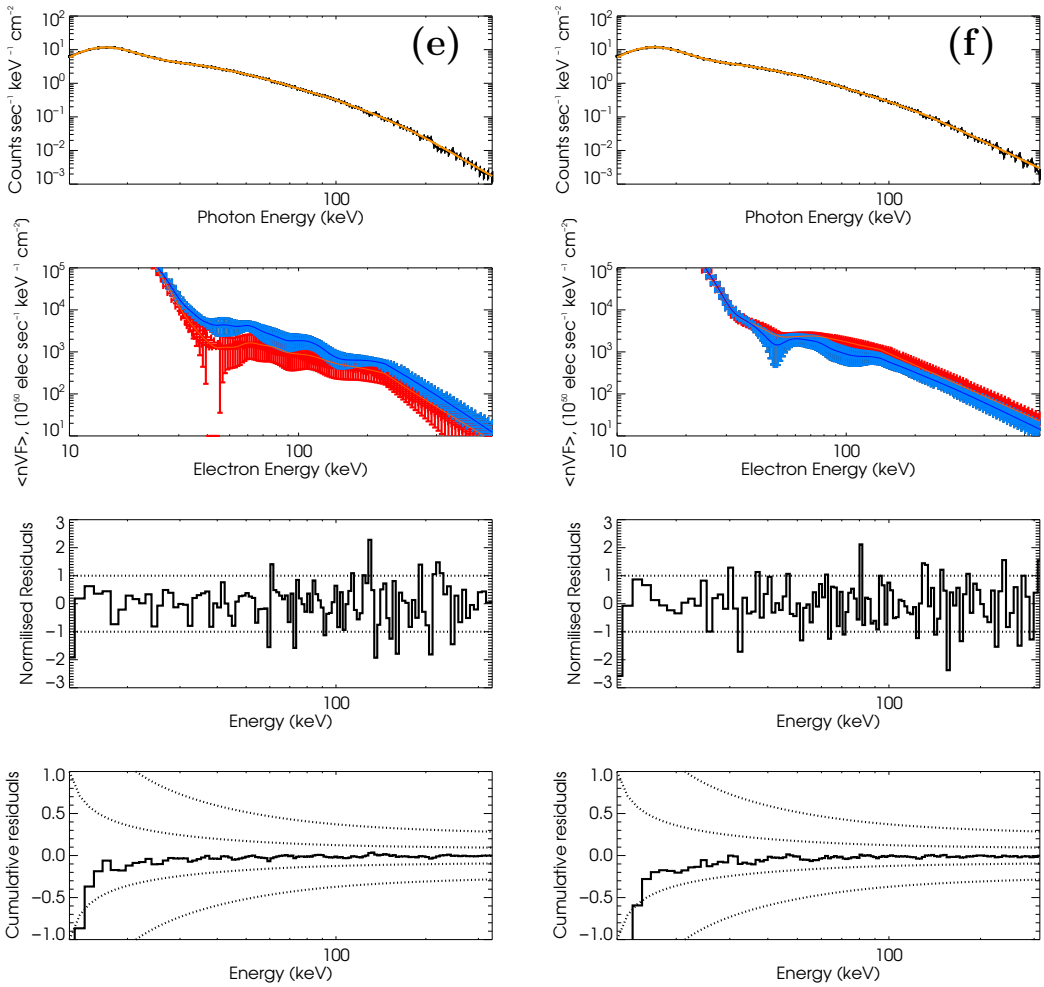

Figure 4.21: As Figure 4.19 for time intervals e and f.

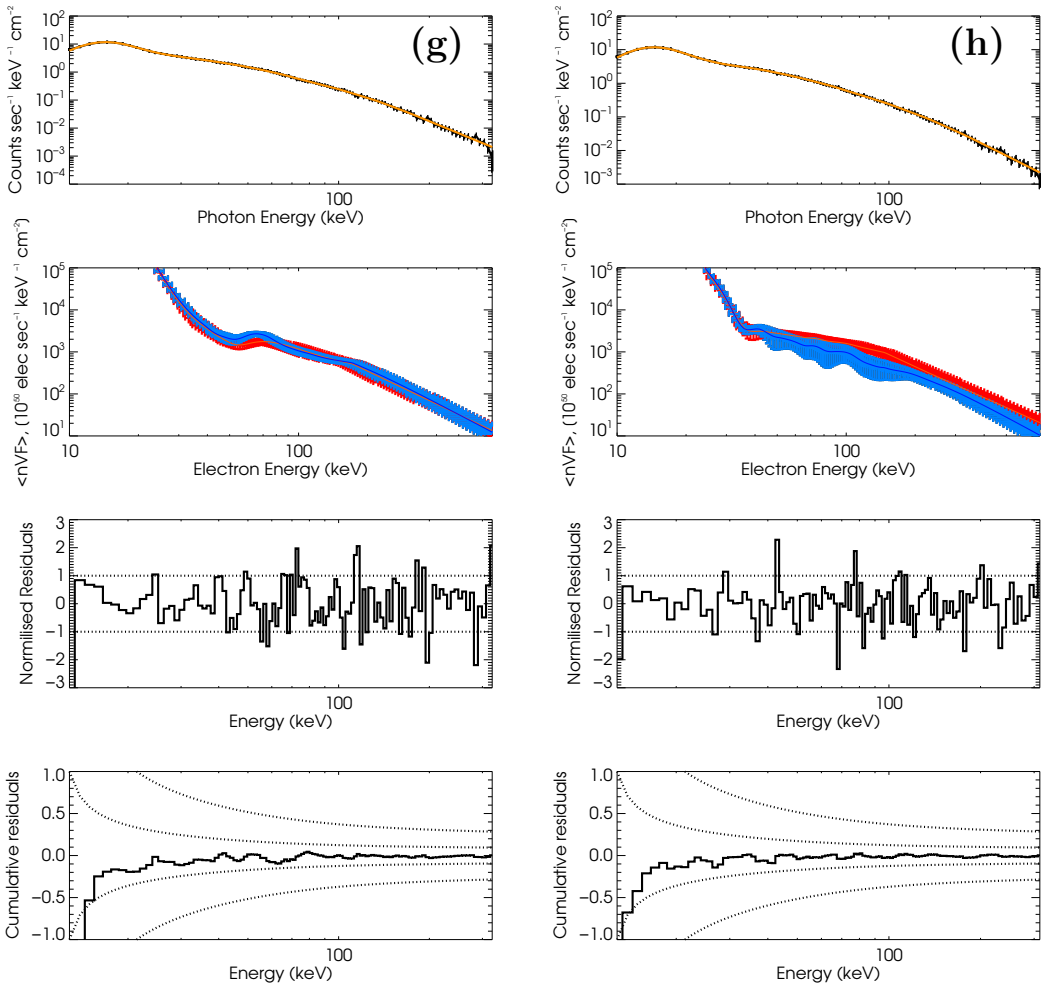

Figure 4.22: As Figure 4.19 for time intervals g and h.

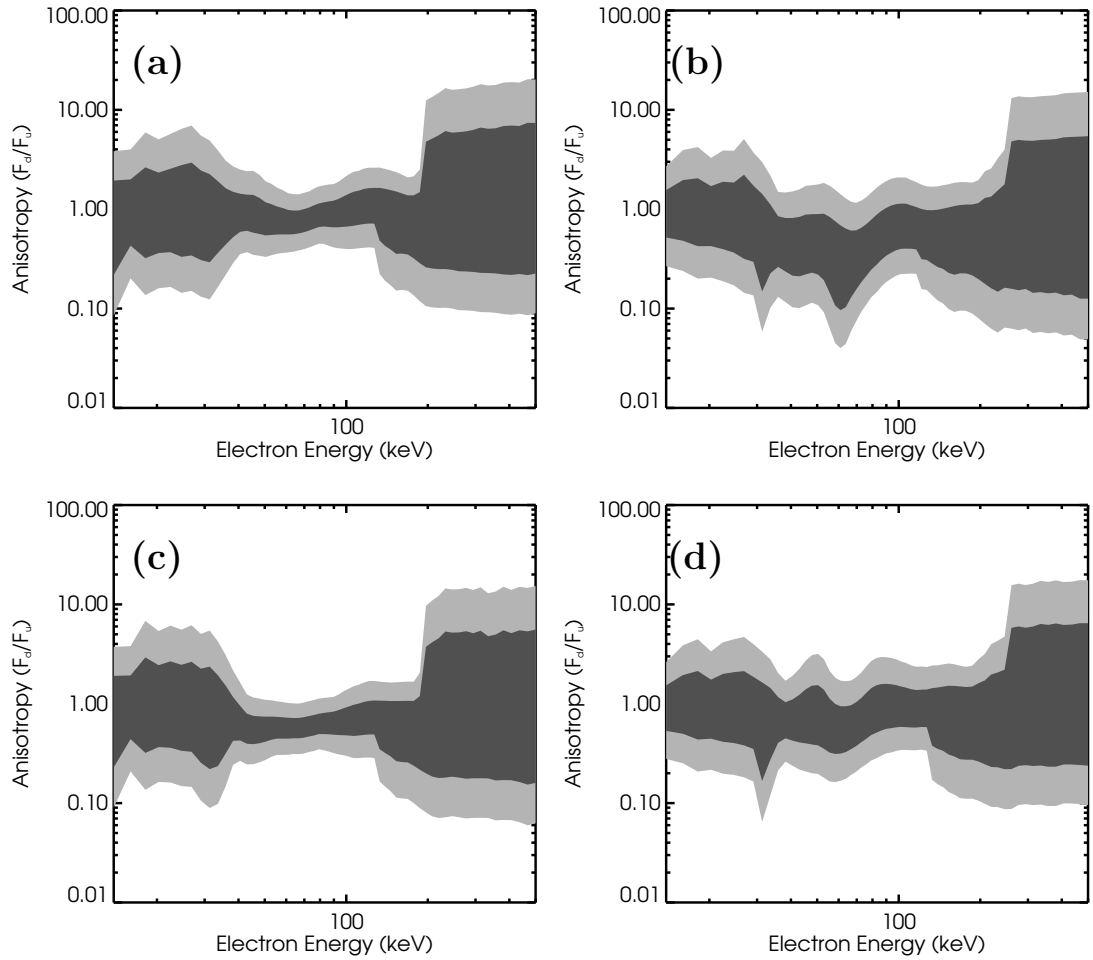

Figure 4.23: The anisotropy of the electron spectrum (defined as $\overline{F}_d/\overline{F}_u$) for the first four 4 (a-d) second time intervals for the flare that occurred on 10 November 2004. The first interval starts at 02:09:40 UT and the intervals shown here cover the most intense part of the impulsive peak. The dark grey area represents the 1σ confidence interval and the light grey the 3σ confidence interval.

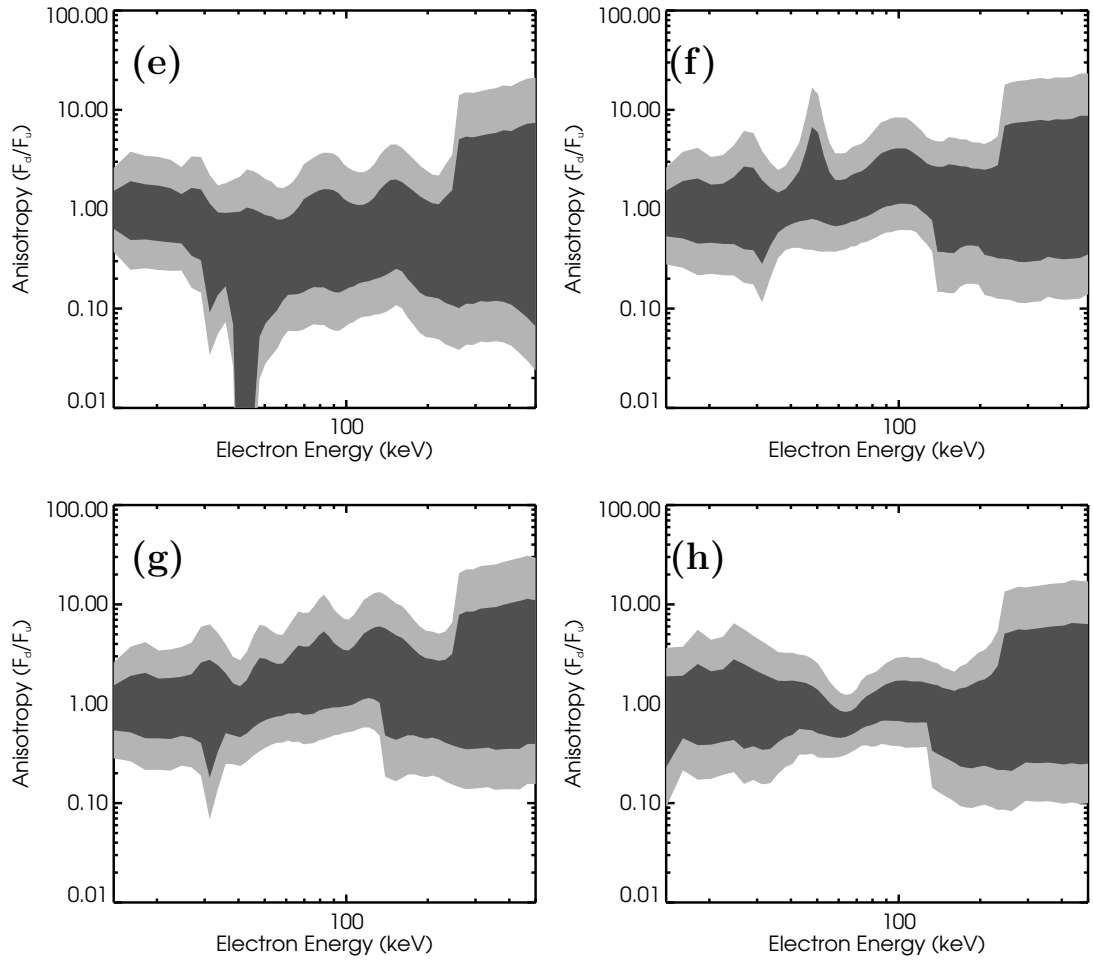

Figure 4.24: The anisotropy of the electron spectrum (defined as $\overline{F}_d/\overline{F}_u$) for the final four 4 second time (e - h) intervals for the flare that occurred on 10 November 2004. The first interval starts at 02:09:40 UT and the intervals shown here cover the most intense part of the impulsive peak. The dark grey area represents the 1σ confidence interval and the light grey the 3σ confidence interval.

4.5 Discussion and Conclusions

This analysis shows consistently that for almost all flares studied by RHESSI that the recovered $\overline{F}_d/\overline{F}_u$ is close to unity within the confidence intervals, being consistent with an isotropic pitch angle distribution. For almost every flare downward beaming of a ratio greater than $\sim 3:1$ is ruled out to 3σ confidence below ~ 150 keV. The size of the uncertainties could be reduced with better count statistics and better energy resolution, as each of these possible emitting distributions does show different spectral variation. The only clear exception to this is the flare on 20th August 2002 between 30 and 50 keV, where the recovered flux appears to be inconsistent with isotropic at the 3σ level and suggests a slightly greater $(1.5-2)$ upward flux. This flare is unusual in several respects. There is a high level of particle contamination throughout the impulsive phase. Several background subtractions were examined to attempt to account for this. This flare also has one of the flattest spectra of all the flares studied, which makes pileup correction more difficult to estimate. Also, this is one of only 2 flares studied where the attenuator status was A1 for the examined time interval.

These measurements appear to rule out any strong beaming such as would be expected in the basic collisional thick target model. While only two components are recovered and the confidence intervals can sometimes be fairly large using this method, these observations are only consistent with a limited range of possible pitch angle distributions for the emitting electron population. These include: fully isotropic distributions, pancake distributions and weak beaming below the measured confidence level. As the mean electron flux spectrum is density weighted, this suggests even an isotropic initial distribution should show some anisotropy in the mean electron flux spectrum (see Chapter 5). This appears to cast doubt on any solar flare model which relies on a large flux of electrons propagating down from high in the corona.

There are several suggested models which do not require beams of electrons precipitating from high in the corona down to the higher density regions, and therefore would be more likely to exhibit isotropic emitting electron populations. Two

examples of such mechanisms are energy transport by wave propagation and local re-acceleration.

An Alfvén wave energy transport model was proposed by Fletcher and Hudson (2008). Here reconnection in the corona causes contraction of the magnetic loops which produces Alfvén waves. These waves propagate towards the chromosphere where they can produce strong electric fields and thus accelerate particles. Calculations suggest that for a coronal field of 500G a perturbation of 50G could provide the Poynting flux for the necessary energies of observed solar flares.

The local re-acceleration thick target model (LRTT) of Brown *et al.* (2009) begins with a beam of electrons similar to the standard collisional thick target, but proposes that electrons, instead of simply losing energy in the dense chromosphere, may be reaccelerated there. One mechanism suggested which could achieve this is current sheet cascades. Here, the distribution accelerated in the corona is only needed as a seed, and so can be much weaker than the beams necessary in the standard CTT model. Modelling of this scenario appears to predict a distribution which has close to equal numbers of upward and downward going energetic electrons.

In order to directly compare the measured results to the forward model a plot of $\Delta\mu$ against anisotropy ($\overline{F}_d/\overline{F}_u$) is included (Figure 4.25) both for the functional form described by Equation 3 and for two commonly used forms $\overline{F} \propto \exp\left(\frac{-(1-\mu)^2}{\Delta\mu^2}\right)$ and $\overline{F} \propto \exp\left(\frac{-|1-\mu|}{\Delta\mu}\right)$. It should be stressed that the results in Figures 4.12 to 4.24 are model independent and can be interpreted in terms of a variety of models, including, but not limited to those considered in Figure 4.25.

These results are consistent with previous published results which showed little evidence of directivity below 300 keV. It should be noted that this study measures anisotropy in terms of the electron flux, whereas for other types of study the parametrisation of anisotropy is often in terms of the directivity of the X-ray emission for stereoscopic studies and the centre-to-limb variance for statistical studies. These are generally related to the electron anisotropy in a model dependant manner. As the X-ray emission can be quite broad, particularly for low

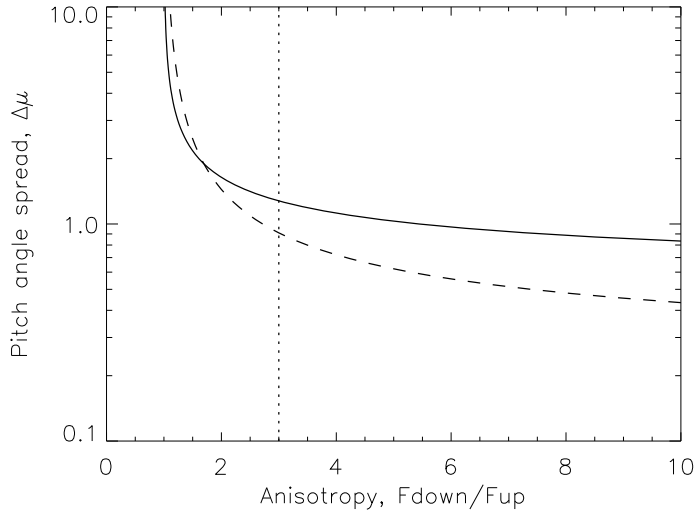

Figure 4.25: Pitch angle spread, $\Delta\mu$, for various anisotropies $\overline{F}_d/\overline{F}_u$ using $\overline{F}(\mu) \propto \exp\left(\frac{-(1-\mu)^2}{\Delta\mu^2}\right)$ (solid line) and $\overline{F}(\mu) \propto \exp\left(\frac{-|1-\mu|}{\Delta\mu}\right)$ (dashed line). The vertical dotted line shows an anisotropy of 3.

energies, a large anisotropy in the electron spectrum could result in a low photon spectrum directivity. Kašparová, Kontar, and Brown (2007) performed a centre-to-limb study using RHESSI data and inferred a directivity ratio between 0.2 and 5 in the range 15 - 20 keV. As the emission below $\sim$ 30 keV is expected to be predominantly produced by thermal electrons it is expected that the distribution in this energy range should be isotropic. This is particularly true for the flares on 17 June 2003 and 10 November 2004 which show strong thermal components; however this may not be the case for flares which show a weak thermal component such as the flare on 20 August 2002.

As this study measured X-rays in the energy range 10 - 500 keV the reliability of the inversion above approximately 250 keV is questionable. As can be seen from Figures 4.16 and 4.17 the confidence interval increases significantly at a few hundred keV. Thus it is difficult to make comparisons with the SMM studies which examined X-ray measurements above 300 keV. However the measurements in this study are for the most part in agreement with previous studies (McTiernan and Petrosian, 1991).

As electrons propagate through the corona and chromosphere, they will be pitch-angle scattered by Coulomb collisions (e.g. Leach and Petrosian (1981); MacKinnon and Craig (1991)), although it seems that collisions will be insufficient to isotropise an initially beamed distribution (Brown, 1972; Leach and Petrosian, 1981). These results, therefore, suggest that either the accelerated electron population is more isotropic, or other transport effects are more important than anticipated. Specifically, the electron scattering by various wave-particle interactions could increase the pitch angle spread of the energetic electrons. Further, if the distribution of energetic electrons is close to isotropic, the role of return current should be diminished. In addition we note, that although the return current itself does contribute to the formation of a backward going beam, it is likely to be more efficient at energies below ~ 50 keV, so that the higher energy electrons are expected to be weakly affected e.g. Holman *et al.* (2011).

5

Stochastic Simulations of Electron Transport

The results from Chapter 4 suggest that the mean electron flux spectrum, $\overline{F}(E, \mu)$, is consistent with an isotropic distribution and inconsistent with a strongly beamed distribution. However, to relate this to the accelerated electron distribution, the effects of particle transport between the dense regions where the bremsstrahlung x-rays are emitted and the more rarefied regions where the particle acceleration is thought to occur, the effects of particle transport must be considered. It is known that many of the transport effects will cause a diffusion in pitch angle of the distribution, thus a highly beamed accelerated or injected distribution, $F_0(E_0, \mu)$ will become broadened.

5.1 How Stochastic Simulations Work

The evolution of the distribution of accelerated electrons is the result of numerous interactions between particles in the distribution and in the ambient plasma of the solar atmosphere. One way of approaching this is to treat the distribution statistically. The time dependent evolution of the distribution can be described by a Fokker-Planck equation. As the particle gyro-radius about the field line is much smaller than the other length scales considered, it can be averaged over.

It is therefore useful to consider the distribution of the electrons in terms of two variables: particle kinetic energy, E and pitch angle μ (the cosine of the azimuthal angle, that is the angle between the downwards direction and the velocity vector of the electron).

The evolution of the distribution can then be described by combining the advection, D_i, and diffusion D_{ij} terms for these two variables (Hamilton, Lu, and Petrosian, 1990) to produce a Fokker-Plank equation,

$$\begin{aligned}\frac{\partial F}{\partial t} &= -\mu\beta c\frac{\partial F}{\partial s} - \frac{\partial}{\partial E}\left(D_E\right) - \frac{\partial}{\partial \mu}\left(D_\mu\right) + \frac{\partial}{\partial \mu}\left(D_{\mu\mu}\frac{\partial F}{\partial \mu}\right) + \frac{\partial}{\partial E}\left(D_{EE}\frac{\partial F}{\partial E}\right) \\ &\quad + \frac{\partial}{\partial \mu}\left(D_{E\mu}\frac{\partial F}{\partial E}\right) + \frac{\partial}{\partial E}\left(D_{E\mu}\frac{\partial F}{\partial \mu}\right) + S(E,\mu,s,t)\end{aligned} \tag{5.1}$$

where s is the path length travelled by the electron. As electrons are considered with initial energy up to several MeV, the relativistic forms are used so the speed of the electron, β, is measured in units of the speed of light ($c = 3\times10^{10}\,\mathrm{cm\,s^{-1}}$); the Lorentz factor $\gamma = \frac{1}{\sqrt{1-\beta^2}}$ is also used.

This method assumes the beam can be treated as test particles, that is, that the influence of the beam does not affect the underlying ambient particle distribution which determines the conditions, such as magnetic force and particle density, encountered by the test particle. Therefore in this scenario the effect of return current is not included.

For Coulomb collisions the advection and diffusion terms are given by (Leach and Petrosian, 1981)

$$D_E = -\frac{4\pi r_0^2 cn\ln\Lambda}{\beta} \qquad D_\mu = 0 \tag{5.2}$$

$$D_{\mu\mu} = -\frac{4\pi r_0^2 cn\ln\Lambda}{\beta^3\gamma^2}(1-\mu^2) \qquad D_{\mu E} \approx 0 \tag{5.3}$$

$$D_{EE} = -\frac{4\pi r_0^2 cn\ln\Lambda}{\beta}\left(\frac{k_BT}{m_ec^2}\right)\left[\mathrm{erf}\left(\sqrt{\frac{E}{k_BT}}\right) - 2\sqrt{\frac{E}{\pi k_BT}}\exp\left(-\frac{E}{k_BT}\right)\right] \tag{5.4}$$

The equations here defined in cgs, therefore s is measured in cm, density n in cm^{-3} and energy E in erg. The physical constants used are e, the charge on the electron (4.8×10^{-10} esu), m_e is the electron mass (9.1×10^{-28} g), the Boltzmann constant $k_B = 1.38 \times 10^{-16}\,\mathrm{erg\,K^{-1}}$. $\ln\Lambda$ is the Coulomb logarithm, for all cases here it is assumed that $\ln\Lambda = 20$ throughout the loop, thus we are neglecting the effects of partial ionisation (Emslie, 1978).

The term D_{EE} is proportional to the thermal velocity of the ambient plasma, as the dispersion in energy results from the spread in energies of the target particles, thus for high energy electrons encountering a thermal plasma it is negligible. The term $D_{\mu E}$ is also non-zero, but is smaller than $D_{\mu\mu}$ by a factor $\sim \ln\Lambda$ and therefore is omitted here.

The equation for a distribution influenced only by Coulomb collisions in the cold plasma limit has the form

$$\frac{\partial F}{\partial t} = -\mu\beta c\frac{\partial F}{\partial s} - \frac{\partial}{\partial E}\left(-\frac{4\pi e^4\, n\, ln\Lambda F}{\beta}\right) + \frac{\partial}{\partial \mu}\left(\frac{4\pi e^4\, n\, ln\Lambda\,(1-\mu^2)}{\beta^3\gamma^2}\frac{\partial F}{\partial \mu}\right) \quad (5.5)$$

This full equation cannot be solved analytically so numerical methods must be employed.

One method which can be used to solve Equation 5.5 is stochastic simulations. A Fokker-Plank equation of the form

$$\frac{\partial f}{\partial t} = -\frac{\partial}{\partial x_i}\left(A_i f\right) + \frac{1}{2}\frac{\partial^2}{\partial x_i \partial x_j}\left(B_{ij} f\right) \quad (5.6)$$

is equivalent to a set of stochastic differential equations (e.g. Gardiner 1985, MacKinnon and Craig 1991).

$$d\mathbf{x} = \mathbf{A}(x,t)dt + \sqrt{\mathbf{B}}(x,t)\mathbf{W}dt \quad (5.7)$$

where $\mathbf{W}$ represents a Wiener process and $\sqrt{\mathbf{B}}$ is defined such that $\sqrt{\mathbf{B}}\sqrt{\mathbf{B}}^T = \mathbf{B}$. When these equations are solved for a large number of test particles the statistical distribution of particles then gives the distribution function f. This method has previously been applied to the problem of electron transport in solar flares (Fletcher, 1996; Fletcher and Martens, 1998; MacKinnon and Craig, 1991).

As the time for electrons to propagate along the loop is much shorter than the time intervals used to accumulate RHESSI spectra (4 - 64 s), the steady-state approximation is appropriate here (Battaglia *et al.*, 2012). For example a 10 keV electron would take ~ 0.1 s to traverse a loop of 7×10^8 cm if collisions are ignored. The distribution evolves on the beam decay timescale, Zharkova and Gordovskyy (2005) calculated that 300 keV electrons in a corona with density $\sim 1 \times 10^{11}$ cm^{-3} would have a decay time of ~ 7 s and that most electrons are lower energy and so have shorter decay times while the high energy electrons are likely to precipitate down to higher densities more quickly so a realistic decay time is ~ 1 s. The term $\frac{\partial F}{\partial t}$ can therefore be dropped from Equation 5.5 and a steady state solution found. Thus Equation 5.5 is equivalent to the set of equations

$$dz = \mu ds\,, \tag{5.8}$$

$$dE = \frac{4\pi e^4\, n\, ln\Lambda}{m_e \beta^2 c^2} ds\,, \tag{5.9}$$

$$d\mu = \frac{4\pi e^4 \mu\, n\, ln\Lambda}{\gamma^2 m_e^2 \beta^4 c^4} ds + \sqrt{\frac{4\pi e^4\, n\, ln\Lambda\, (1-\mu^2)}{\gamma^2 m_e^2 \beta^4 c^4}} W \sqrt{ds}\,, \tag{5.10}$$

where z is the height above the photosphere, and W is a random number representing the Wiener process, chosen from a Gaussian distribution with mean 0 and variance 2.

This is a very versatile method as the advection and diffusion terms are all that is needed to describe the system, thus the influence of many processes can be incorporated straightforwardly by adding the relevant terms to Equations 5.8 - 5.10 . Another advantage is that the accuracy of the solution can be improved arbitrarily using small values of ds.

The density model takes the form of an exponentially decreasing density out from the photosphere plus a constant coronal (loop) density

$$n(z) = n_0 \exp\left(-\frac{z}{h}\right) + n_1 \tag{5.11}$$

where $n_0 = 1.16 \times 10^{17}$ cm^{-3} is the photospheric density, $n_1 = 5 \times 10^9$ cm^{-3} is the coronal density and $h = 1.44 \times 10^7$ cm is the scale height (Figure 5.1). This is very close to the model used by Battaglia and Kontar (2011) which based the values

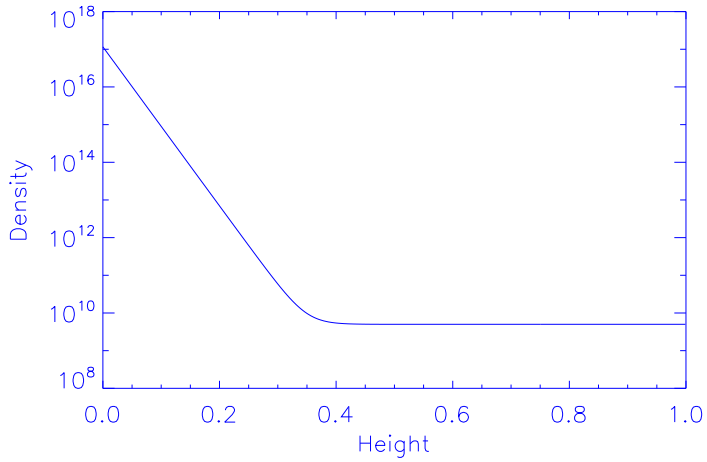

Figure 5.1: The one dimensional density model used: $n\,[\mathrm{cm}^{-3}]$ as a function of z/h_{loop}, where h_{loop} is the height of the coronal loop modelled (7×10^8cm)

for the photospheric density on the atmospheric models of Vernazza, Avrett, and Loeser (1981).

5.2 Testing the code

A one dimensional coronal loop model was used to test the effects of Coulomb collisions on a beamed electron distribution propagating down towards the photosphere. The test particles were injected at a range of heights near the loop top with a distribution in energy and pitch angle. They were then allowed to propagate by stepping forward in path length ds, the new height energy and pitch angle for each particle is then found by applying Equations 5.8 - 5.10.

In order to test that these simulations work as expected, reduced versions of the code for which analytic solutions are possible were first tested and compared with the expected values.

5.2.1 Spectral Index Change Due to Energy Loss

The first test of the stochastic simulation code considers energy loss in the absence of pitch angle scattering. Assuming electrons lose energy purely in Coulomb collisions with no pitch angle scattering for the non-relativistic case, this has the form $\frac{dE}{dz} = \frac{-Kn(z)}{E}$.

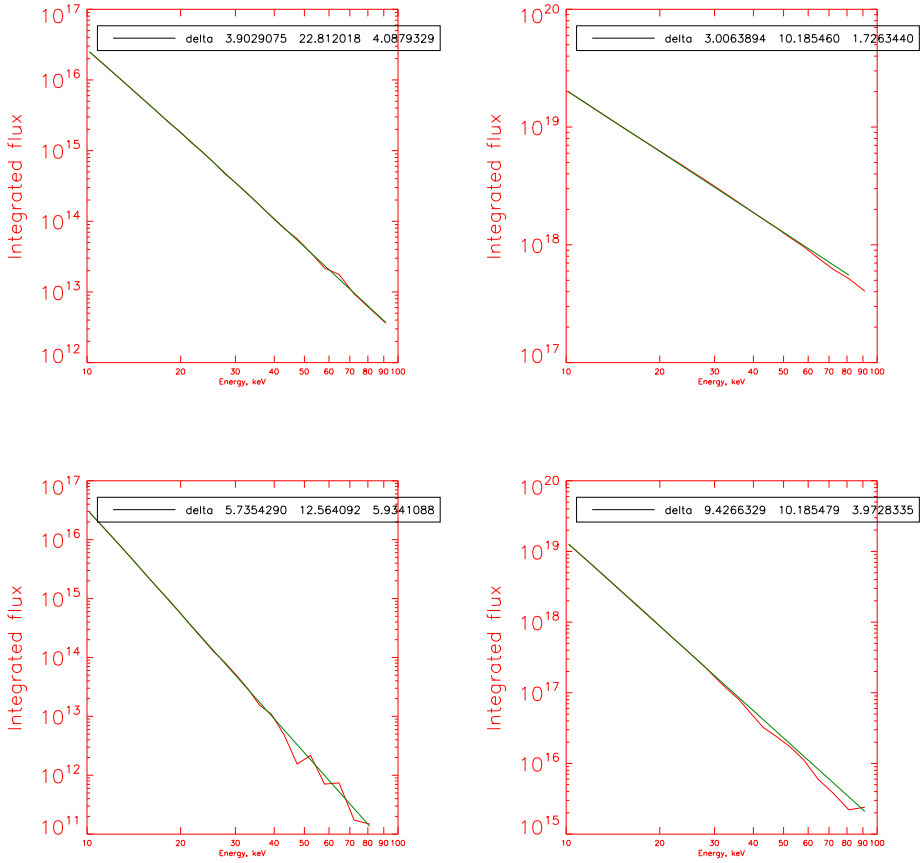

Figure 5.2: Power law spectra at start (left) and end (right) of the simulation for non-relativistic energy loss with no scattering. Flux is binned in log space and broken power law fit applied. Top: $\delta_0 = 4$ Bottom: $\delta_0 = 6$

We can assume electron flux continuity, which is to say that the total number of electrons in the flare volume remains constant: $F_0\left(E_0\right) dE_0 = F\left(E\right) dE$. The elec-

tron energy at height z where the electron now is given by $\int_{E_0}^{E} EdE = -KN(z)$ where $N(z) = \int_0^z n(z)dz$ is the column density experienced by the particle. The electron spectrum at height z therefore has the form

$$F(E,z) = F_0(\sqrt{E^2 + 2KN(z)})\frac{E}{\sqrt{E^2 + 2KN(z)}} \tag{5.12}$$

Assuming a power law form for the injected spectrum $F_0(E_0) \propto E_0^{-\delta}$ gives

$$F(E,z) \propto \frac{E}{(E^2 + 2KN(z))^{\frac{\delta+1}{2}}} \tag{5.13}$$

The mean electron flux spectrum, $\overline{F}(E)$, for the one dimensional case is given by

$$\overline{F}(E) = \int_0^\infty F(E,z)n(z)dz = \int_0^\infty F(E,N)dN \tag{5.14}$$

using the differential form $dN(z) = n(z)dz$, substituting Equation 5.13 gives

$$\begin{aligned} \overline{F}(E) &= \int_0^\infty \frac{E}{(E^2 + 2KN(z))^{\frac{\delta+1}{2}}} dN \\ &= \left[\frac{E(E^2 + 2KN)^{\frac{(1-\delta)}{2}}}{K(1-\delta)}\right]_0^\infty \\ &\approx \frac{E^{(2-\delta)}}{K(\delta - 1)} \end{aligned} \tag{5.15}$$

Thus the integrated mean electron spectrum has a spectral index two greater than the injected spectrum.

The stochastic simulation code was run using 10^5 particles with scattering turned off. Test particle energies were selected using the IDL `randomp` function which uses the inverse transform method (Bevington and Robinson, 1992) to produce an array of numbers drawn from a power law distribution. A low energy cutoff of 10 keV was assumed and a maximum energy of 2 MeV imposed. Below the low energy cutoff for the initial power law the electrons were not tracked and were assumed to be lost to the thermal distribution. The code was run until there were at most 200 particles left with energy above 10 keV.

A broken power law fit was applied to the electron flux. Single power laws were tried previously but they did not result in good fits. The graphs below show the

results of the fit at the start (100 iterations) and end (where there are roughly 100 particles left above 10 keV) and the power law spectral indices compared. The results are broadly in agreement with a change in spectral index of 2 (Figure 5.2). This was performed using both the fully relativistic and non-relativistic energy loss terms, though there is no real difference in the results between the two in the range of energies considered here.

5.2.2 Comparison With Analytic Solution

The rate of pitch angle scattering can be calculated analytically. Assuming a mono-energetic electron beam with all particles starting out with the same pitch angle (μ_0) the non-relativistic case the solution has the form MacKinnon and Craig (1991)

$$F(\mu,t) = \sum_{k=0}^{\infty}(1-3t)^{\frac{k(k+1)}{3}}(k+\frac{1}{2})P_k(\mu_0)P_k(\mu)\,, \tag{5.16}$$

where $P_k(x)$ is a Legendre polynomial of degree k. Here dimensionless units are used with speeds being divided by their initial speed, v_0, lengths being divided by $\frac{v_0^4 m_e^2}{4\pi e^4\, n\, ln\Lambda}$ and times being divided by $\frac{v_0^3 m_e^2}{4\pi e^4\, n\, ln\Lambda}$.

For the relativistic case under the same assumptions the solution has a similar form (Lu and Petrosian, 1988)

$$F(\mu,t) = \frac{\beta^2(\eta)}{\beta^2(\eta+y)}\sum_{k=0}^{\infty} e^{-k(k+1)[\rho(\eta+y)-\rho(\eta)]}(k+\frac{1}{2})P_k(\mu_0)P_k(\mu)\,, \tag{5.17}$$

where

$$y = \frac{ct}{\lambda_0} \tag{5.18}$$

is a dimensionless time variable and

$$\eta = \sqrt{E^2+2E} + \sin^{-1}\left(\frac{1}{E+1}\right) \tag{5.19}$$

$$\rho = \frac{1}{2}\ln\left(\frac{E}{E+2}\right) \tag{5.20}$$

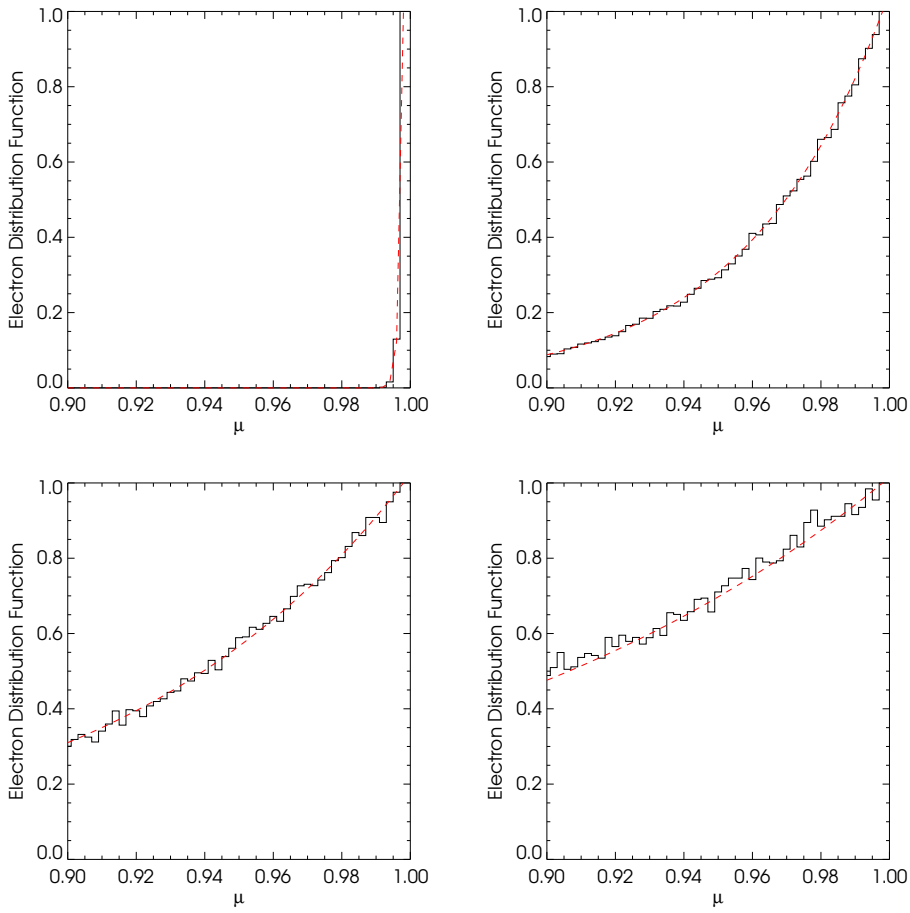

Figure 5.3: Pitch angle distribution comparison for the non-relativistic case, with initial conditions $\mu_0 = 1.0$ $E_0 = 64\,\mathrm{keV}$. Black histogram is result of Monte-Carlo simulation, red dotted line is analytic solution. Top left: after 100 iterations. Top right: after 4000 iterations. Bottom left: after 8000 iterations. Bottom left: after 12000 iterations.

These solutions were compared with the results of the Monte-Carlo simulations and for several values of μ_0 and initial energy. All simulations were performed with 10^7 electrons, a constant ambient density of $10^9\,\mathrm{cm}^{-3}$, and a step size equivalent to $0.001\,\mathrm{s}$ with the exception of the final simulation ($E_0 = 800\,\mathrm{keV}$, $\mu_0 = 1.0$) which used a step size equivalent to $0.01\,\mathrm{s}$. The solutions were found to be very close to the simulation results in all cases (Figures 5.3 - 5.4).

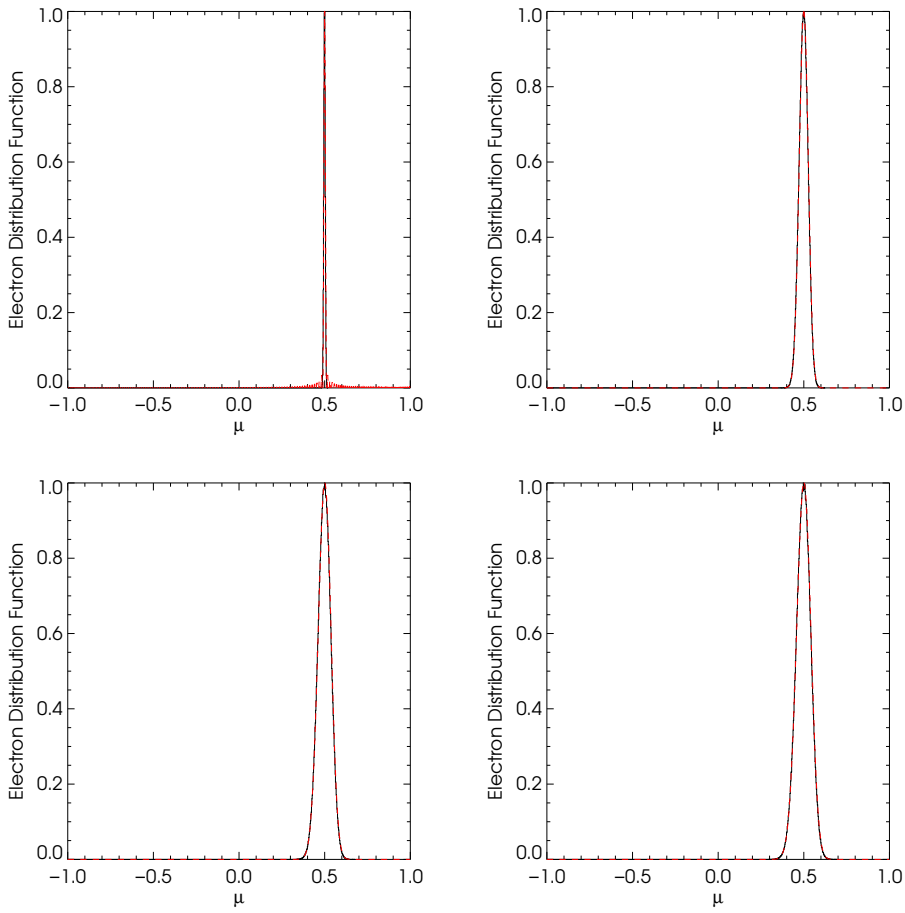

Figure 5.4: Pitch angle distribution comparison. Fully relativistic case. With initial conditions $\mu_0 = 0.5$ $E_0 = 800\,\mathrm{keV}$. Black histogram is result of Monte-Carlo simulation, red dotted line is analytic solution. Top left: after 100 iterations. Top right: after 10000 iterations. Bottom left: after 20000 iterations. Bottom left: after 30000 iterations.

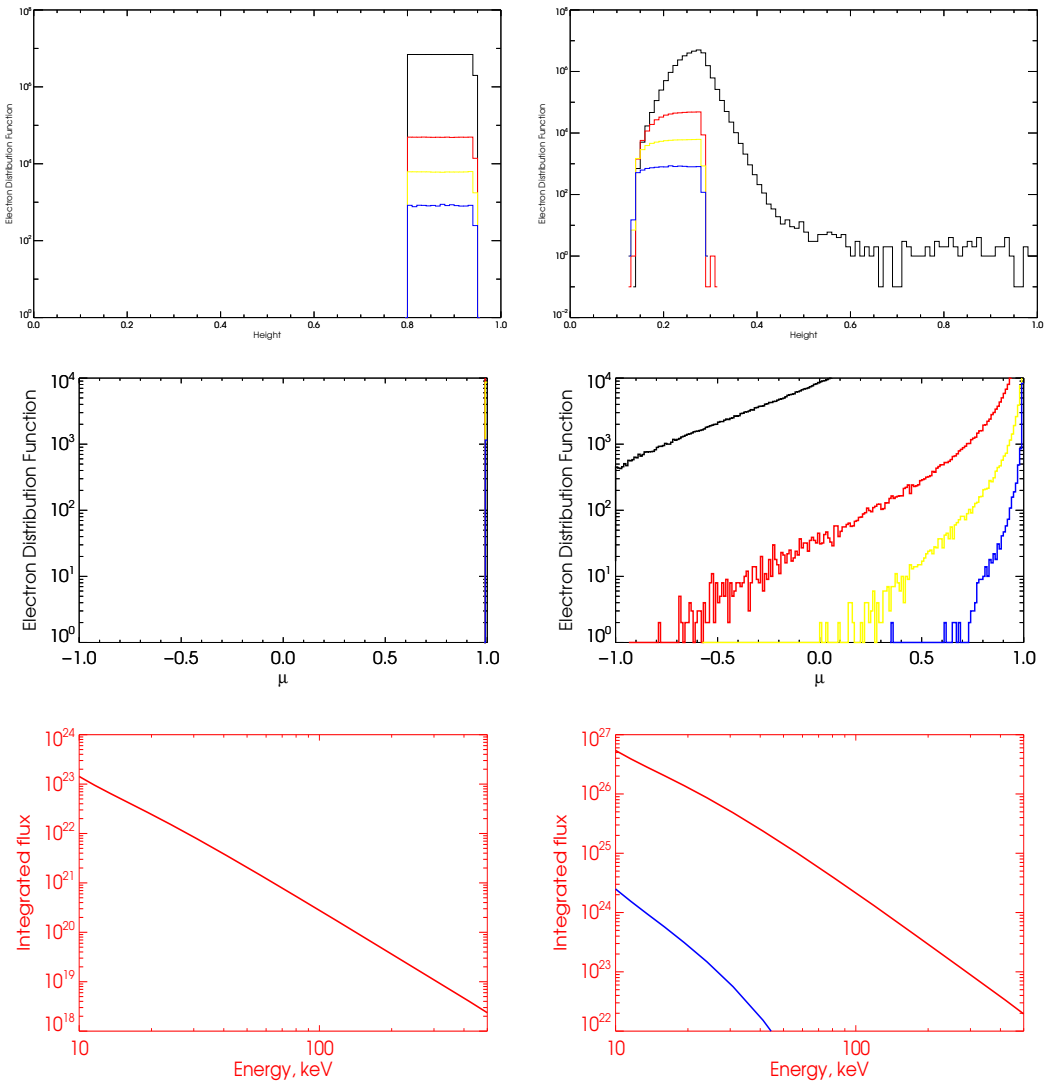

Figure 5.5: Distribution with all electrons having $\mu_0 = 1$. Top: distribution in height, for several energy bands 10-50 keV (black), 50 - 100 keV (red), 100- 200 keV (yellow), 200 - 500 keV (blue). Middle: distribution in pitch angle (μ) using the same colour codes. Bottom: electron flux spectrum $\overline{F}_d$ (red) $\overline{F}_u$ (blue) Left: initial distribution Right: distribution after 2000 iterations).

5.3 Results of Stochastic Simulation Code

5.3.1 Scattering Results from Pure Downwards Distribution

As with the power-law in energy, a beam of test particles were drawn from a power-law distribution of electrons and all given pitch angle $\mu_0 = 1$, that is, an

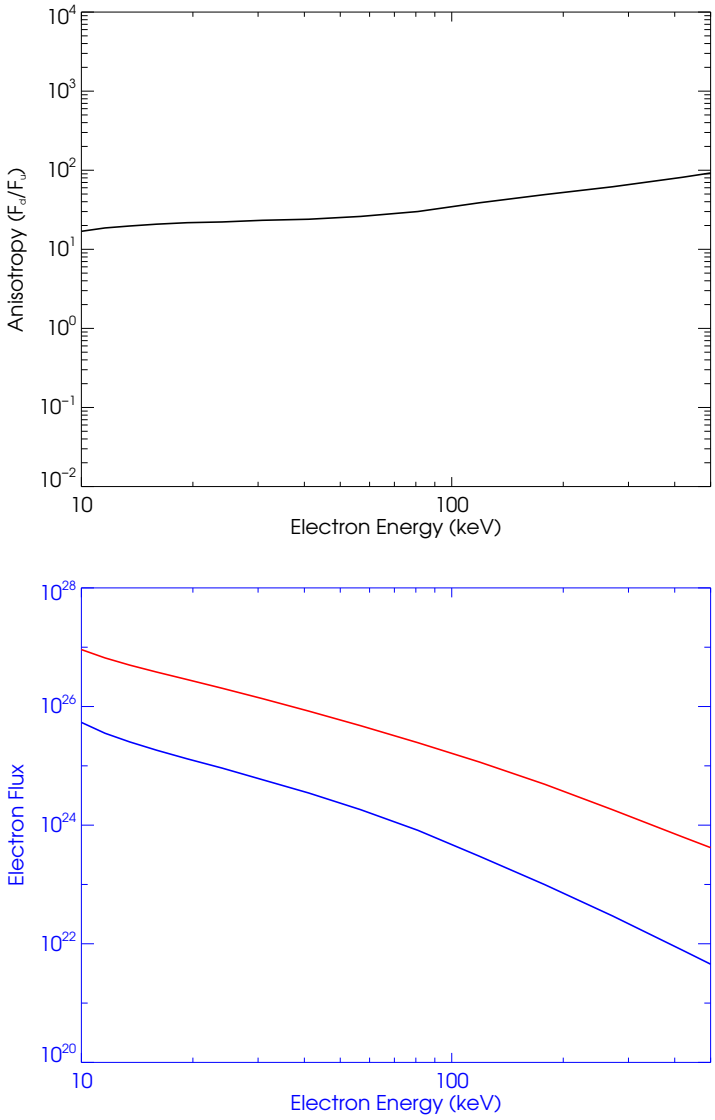

Figure 5.6: Results from stochastic simulation with $F_0(E_0) = E_0^{-2}\delta(\mu - 1)$. Top: anisotropy of mean electron flux spectrum ($\overline{F}_d/\overline{F}_u$). Bottom: electron flux spectrum $\overline{F}_d$ (red) $\overline{F}_u$ (blue).

initial distribution of the form $F_0(E_0, \mu) = E^{-d_0}\delta(\mu - \mu_0)$

However, this time both the scattering and energy loss terms were included to simulate the physical effect Coulomb collisions would have on this distribution. As anisotropy at several hundred keV is significant, a large number of particles

were needed to ensure that the high energy part of the distribution was not dominated by statistical noise: 10^8 particles were used in these simulations.

For each iteration the heights of the electrons above the photosphere, the distribution of particles throughout the loop, the pitch angle distribution in terms of μ and the energy of each particle are calculated by applying the stochastic equations. The instantaneous bi-directional electron flux is then computed, this is given by the sum of all electrons in either the upward or downward hemisphere for that iteration, binned in energy and multiplied by the average loop density that particles in that energy bin are encountering. As the coronal density is low there is not a significant change in the distribution until it has propagated down the loop.

At each step the total integrated electron flux is calculated for comparison with the measurements of $\overline{F}(E,\mu)$ made by inversion of RHESSI data. This is done by cumulatively summing the instantaneous distributions for each iteration. The final calculation is to determine the anisotropy ($\overline{F}_d/\overline{F}_u$) of the integrated flux and the the final integrated fluxes for the run. The code is run until there are at most 200 particles with energy greater than 10 keV.

5.3.2 Scattering Results from Beam Distribution

In order to compare the results to previous chapters the evolution of an initially beamed distribution was examined. The injected electrons were drawn from a distribution of the form

$$F_0(E,\eta) = E^{-\delta} \exp\left(-\frac{(1-\mu)^2}{\Delta\mu^2}\right) \tag{5.21}$$

As with the initial particle energies, the pitch angles were then selected using the integral transform method. This method allows random numbers from a uniform distribution to be transformed into a distribution with an arbitrary probability density function, $P(\mu)d\mu$, normalised such that $\int_{-\infty}^{\infty} P(\mu)d\mu = 1$, using the cumulative probability density C. For the case of a beam of electrons this is given

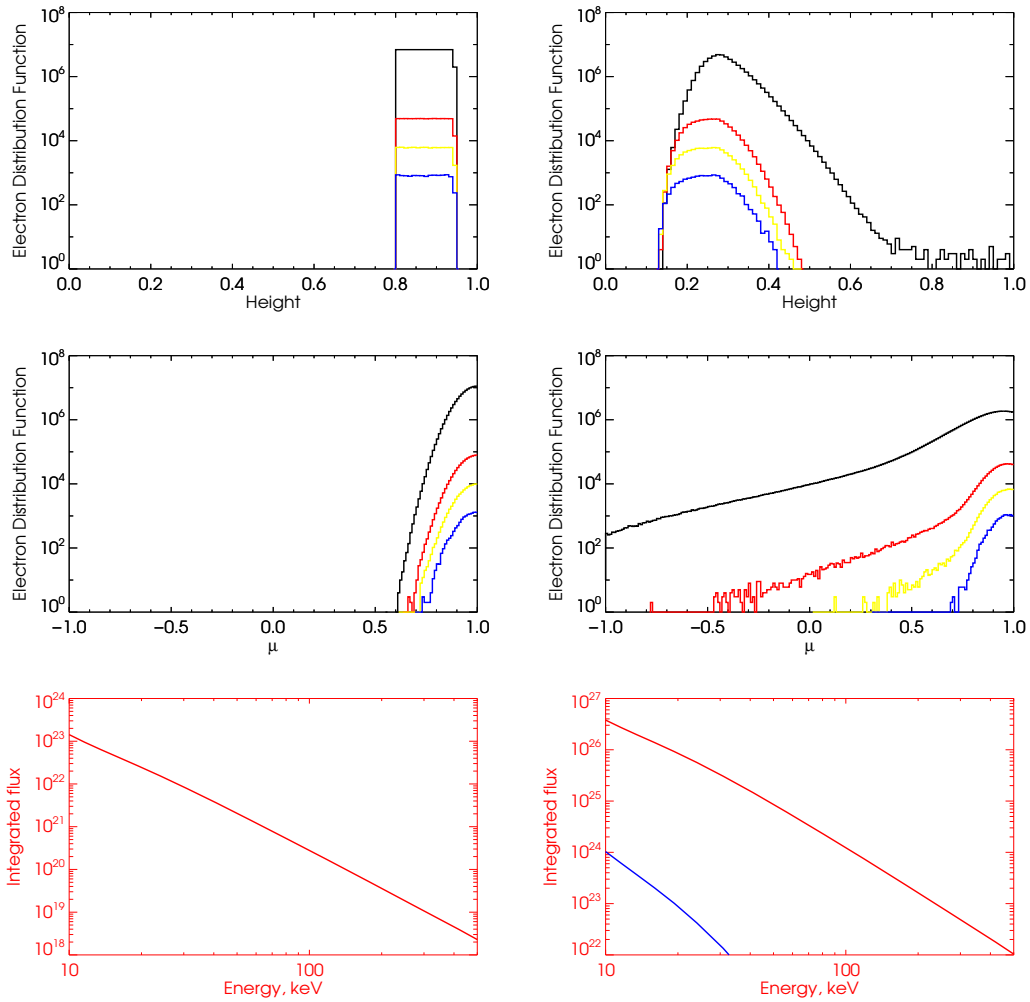

Figure 5.7: Electron distribution for an initial beamed distribution with $\Delta\mu = 0.1$. Top: Initial distribution in height, for several energy bands 10-50 keV (black), 50 - 100 keV (red), 100- 200 keV (yellow), 200 - 500 keV (blue). Middle: Initial distribution in pitch angle (μ) using the same colour codes. Bottom: electron flux spectrum $\overline{F}_d$ (red) $\overline{F}_u$ (blue) Left: initial distribution Right: distribution after 2000 iterations).

by

$$\begin{aligned} C &= \int_{-\infty}^{y} P(\mu)d\mu \\ &= \left[\frac{1}{\mathrm{erf}(2/\Delta\mu)}\,\mathrm{erf}\left(\frac{\mu-1}{\Delta\mu}\right)\right]_{-1}^{y} \\ &= \frac{1}{\mathrm{erf}(2/\Delta\mu)}\,\mathrm{erf}\left(\frac{y-1}{\Delta\mu}\right)+1 \end{aligned} \tag{5.22}$$

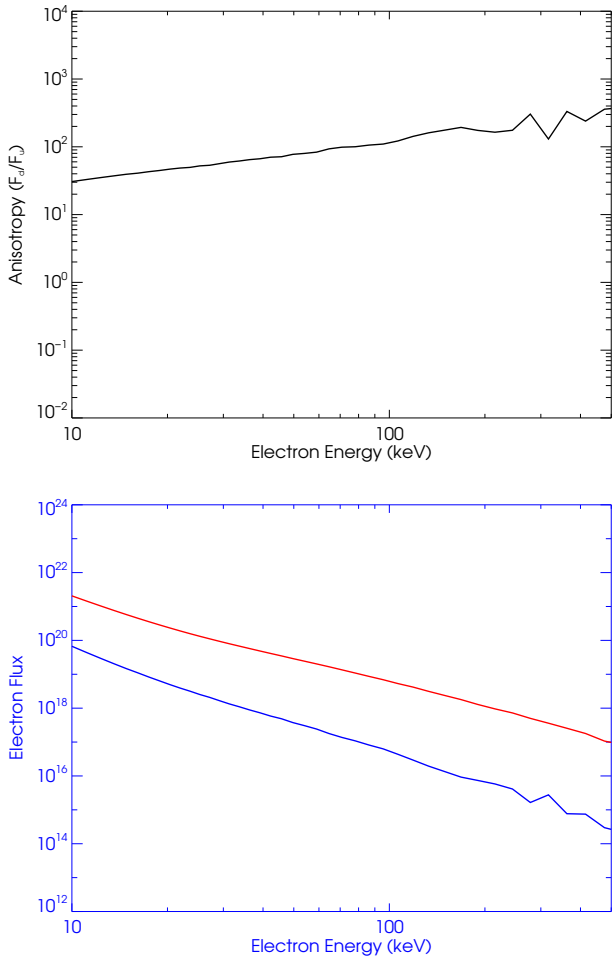

Figure 5.8: As Figure 5.6 for an initial beamed distribution with $\Delta\mu = 0.1$

This equation can be inverted to give y then if C is a random number drawn from a uniform distribution y is drawn from P

$$y = \Delta\mu \, \mathrm{erf}^{-1}\left((C-1)\,\mathrm{erf}\left(\frac{2}{\Delta\mu}\right)\right) \tag{5.23}$$

Several strengths of beaming for the initial distribution were tested. For each figure the first three panels show snapshots of the Monte Carlo simulation at the beginning, halfway through and at the end.

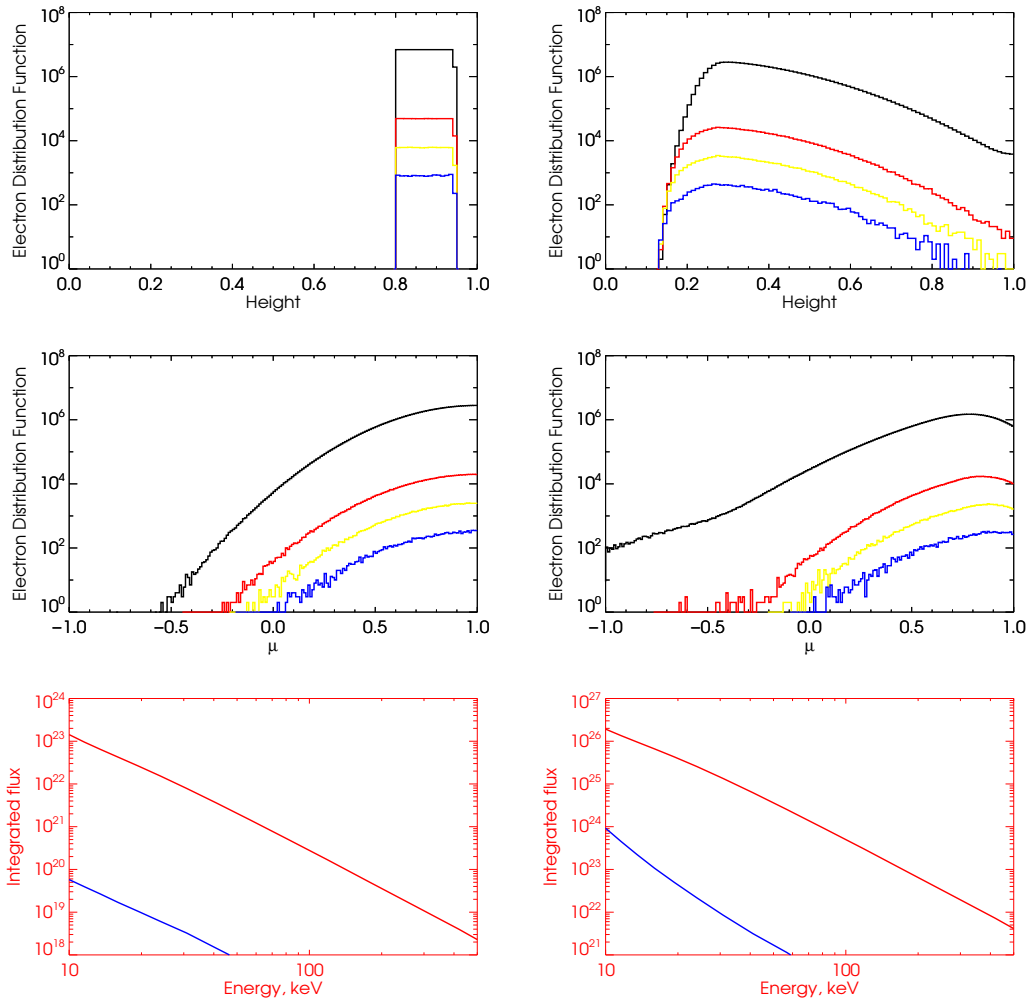

Figure 5.9: Electron distribution for an initial beamed distribution with $\Delta\mu = 0.4$. Top: Initial distribution in height, for several energy bands 10-50 keV (black), 50 - 100 keV (red), 100- 200 keV (yellow), 200 - 500 keV (blue). Middle: Initial distribution in pitch angle (μ) using the same colour codes. Bottom: electron flux spectrum $\overline{F}_d$ (red) $\overline{F}_u$ (blue) Left: initial distribution Right: distribution after 2000 iterations).

5.4 Comparison with observations

The stochastic simulations show that the effects of particle transport will have the effect of reducing the anisotropy for a strongly beamed distribution. However

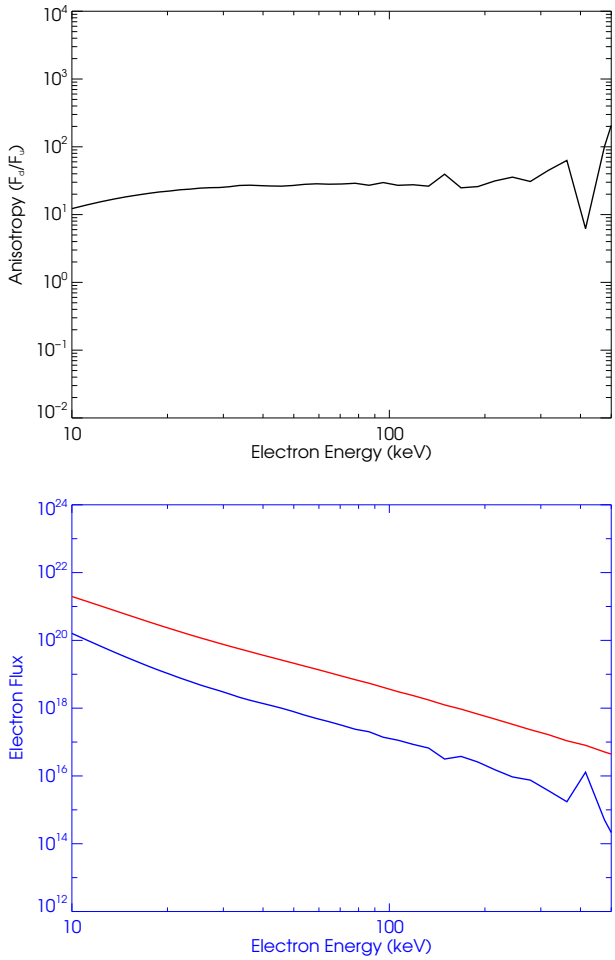

Figure 5.10: As Figure 5.6 for an initial beamed distribution with $\Delta\mu = 0.4$

for the standard thick target configuration where the electrons are injected with $H(\mu) = \delta(1 - \mu)$ and the energy loss and pitch angle scattering is by Coulomb collisions the effect is not strong enough to be consistent with the observations conducted in Chapter 4 (Figures 5.5 and 5.6).

For intermediate levels of anisotropy such as the beamed distributions considered in Chapter 2 there is also a spread in pitch angle distribution due to Coulomb collisions as the particles propagate (Figures 5.7 - 5.11). It is, however, not possible to determine an initial level of anisotropy which is consistent with the observations detailed in Chapter 4 when the boundary conditions at the top of

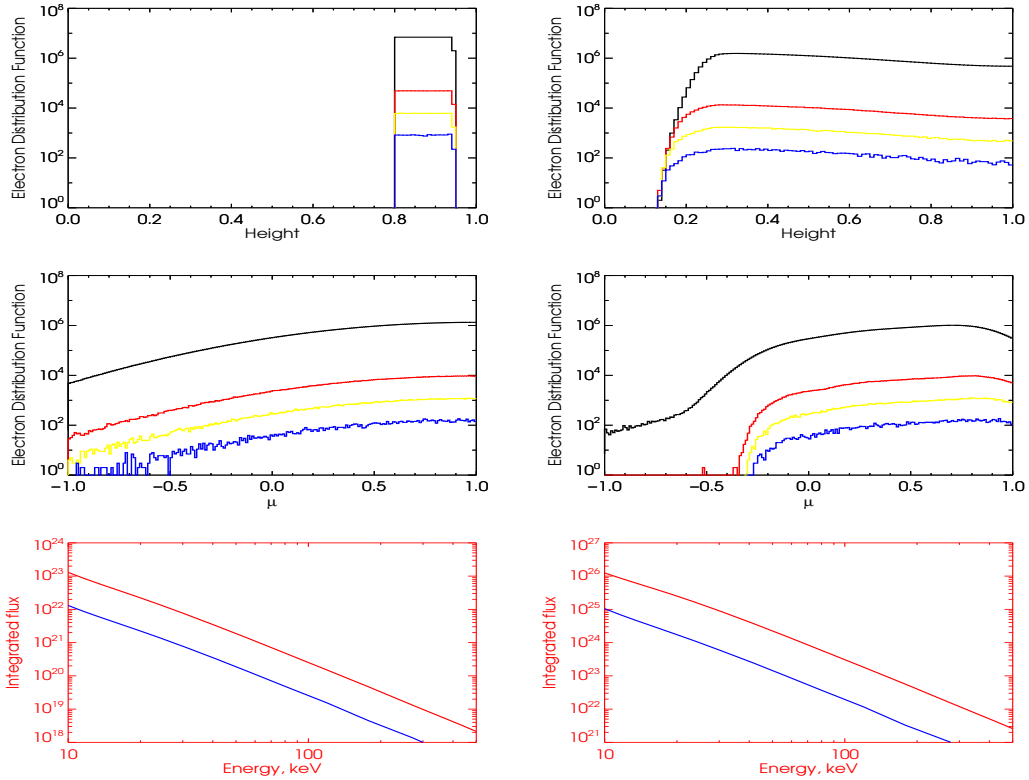

Figure 5.11: Electron distribution for an initial beamed distribution with an anisotropy of ~ 10 ($\Delta\mu = 0.85$). Top: Initial distribution in height, for several energy bands 10-50 keV (black), 50 - 100 keV (red), 100- 200 keV (yellow), 200 - 500 keV (blue). Middle: Initial distribution in pitch angle (μ) using the same colour codes. Bottom: electron flux spectrum $\overline{F}_d$ (red) $\overline{F}_u$ (blue) Left: initial distribution Right: distribution after 2000 iterations).

the loop are reflective. An isotropic distribution in initial pitch angle results in an anisotropy of the mean electron flux spectrum of ~ 4 (Figures 5.12 and 5.13). However if the reflective boundary condition is removed and electrons are allowed to escape from the top of the "loop" (Figures 5.15 and 5.16) the anisotropy in the final mean electron flux spectrum is reduced and weak anisotropy at a level $\sim 5:1$ is consistent with the measurements made in Chapter 4.

One commonly considered effect not included here is magnetic mirroring due to the convergence of the magnetic field at the loop footpoints, which could have

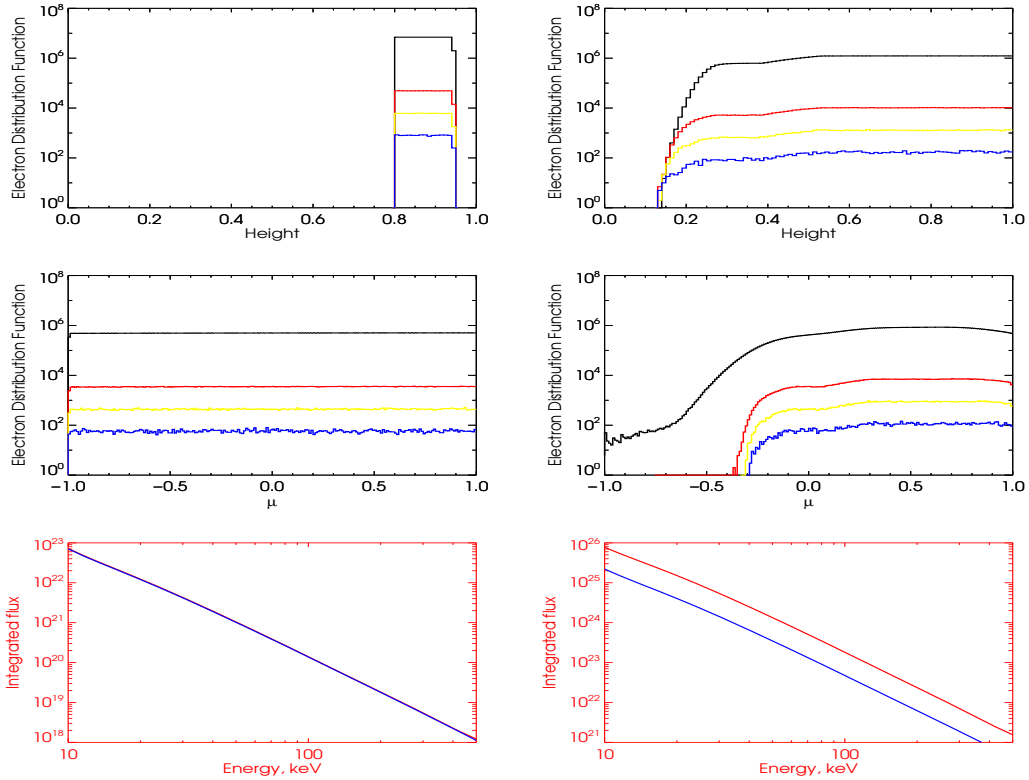

Figure 5.12: Electron distribution for an initial isotropic pitch angle distribution ($\Delta\mu = 10$). Top: Initial distribution in height, for several energy bands 10-50 keV (black), 50 - 100 keV (red), 100- 200 keV (yellow), 200 - 500 keV (blue). Middle: Initial distribution in pitch angle (μ) using the same colour codes. Bottom: electron flux spectrum $\overline{F}_d$ (red) $\overline{F}_u$ (blue) Left: initial distribution Right: distribution after 2000 iterations).

a significant effect on the pitch angle distribution of the beam, particularly for the high energy electrons which are likely to travel further down the loop before losing energy. In this case a model of magnetic field strength throughout the loop is needed. The magnetic mirroring does not alter the particle energy so can be included with the addition of the term

$$D_\mu = -\frac{1}{2}(1-\mu^2)\frac{d\ln B}{ds} \tag{5.24}$$

to the pitch angle advection component. While this is not part of the standard thick target model it has the potential to have an effect of a similar order to

collisional pitch angle scattering for reasonable estimates of the magnetic field in a coronal loop. In addition, wave-particle interactions due to plasma turbulence will also have an effect on the energy and pitch angle distributions.

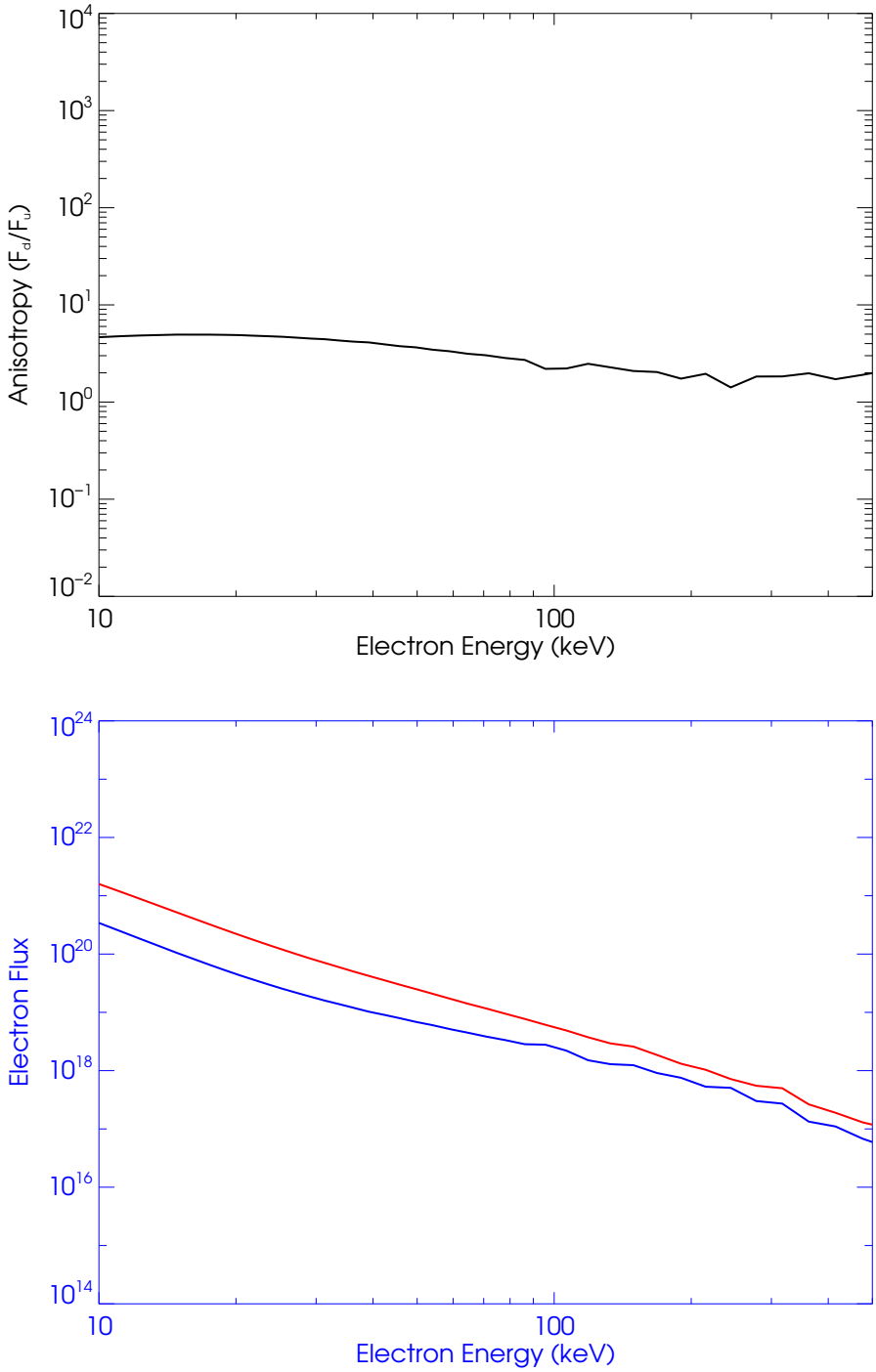

Figure 5.13: As Figure 5.6 for an initial beamed distribution with $\Delta\mu = 0.85$.

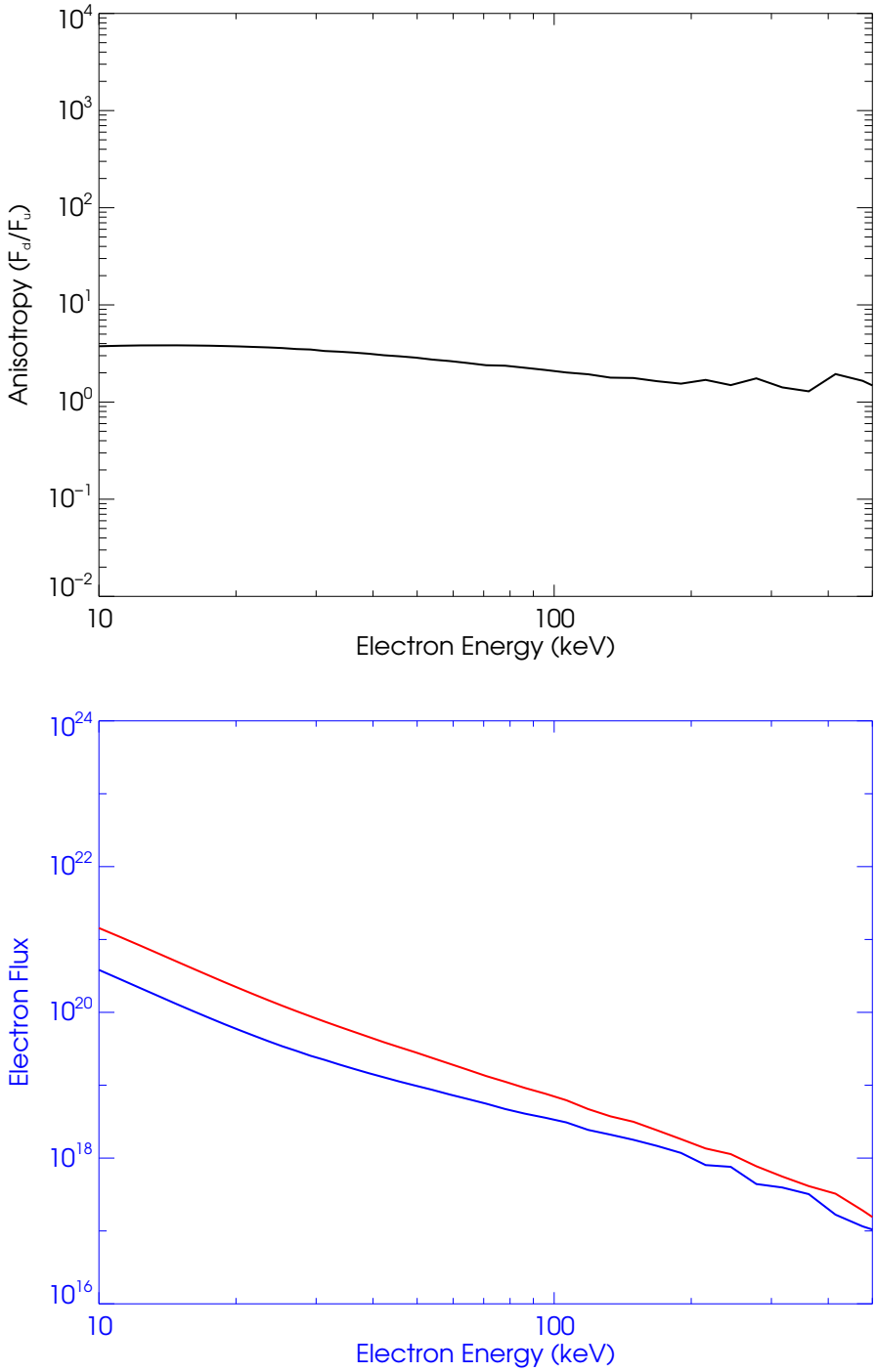

Figure 5.14: As Figure 5.6 for an initial isotropic pitch angle distribution

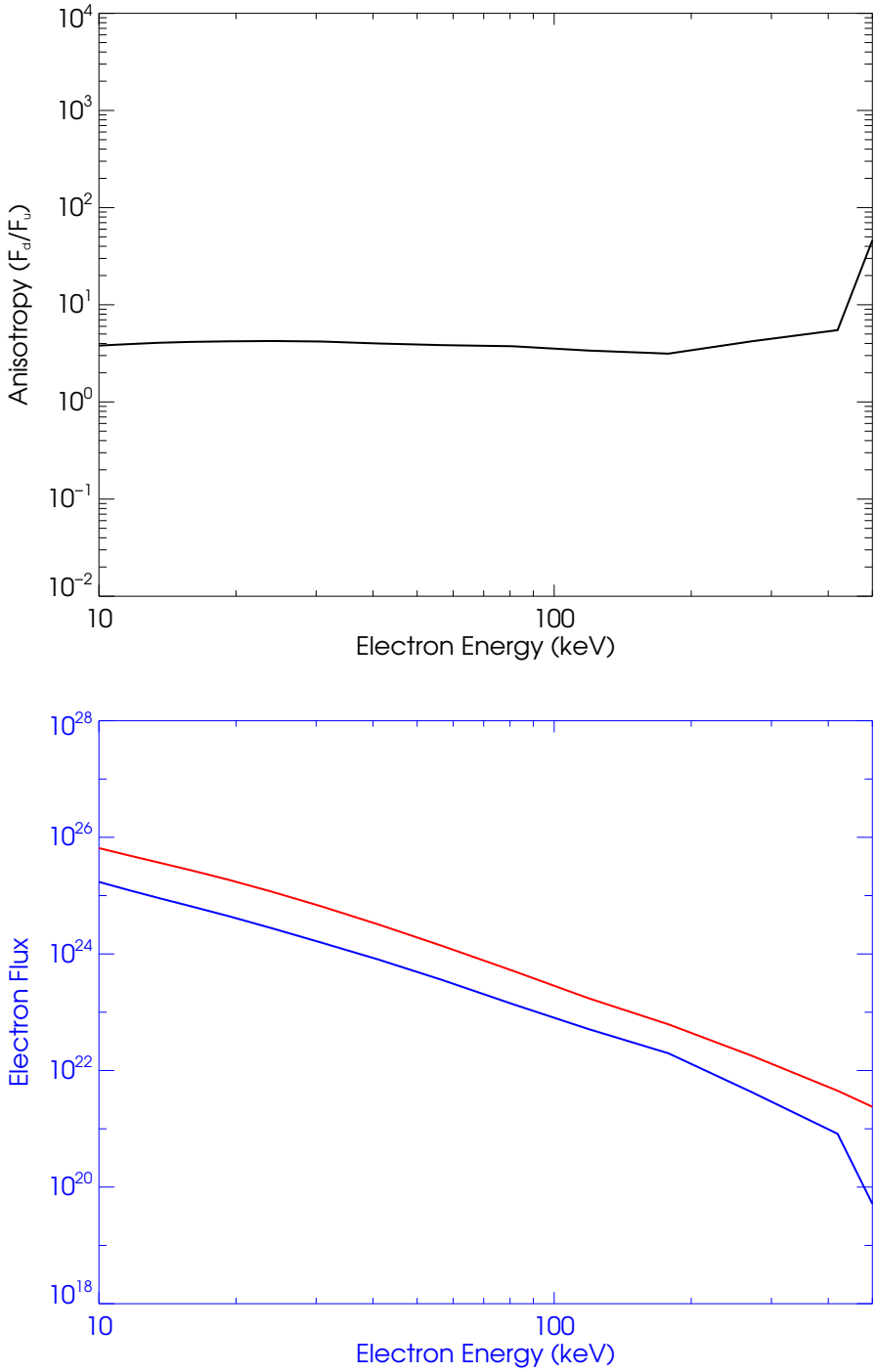

Figure 5.15: As Figure 5.6 for an initial beamed distribution with $\Delta\mu = 0.85$ and no reflection at the top of the loop.

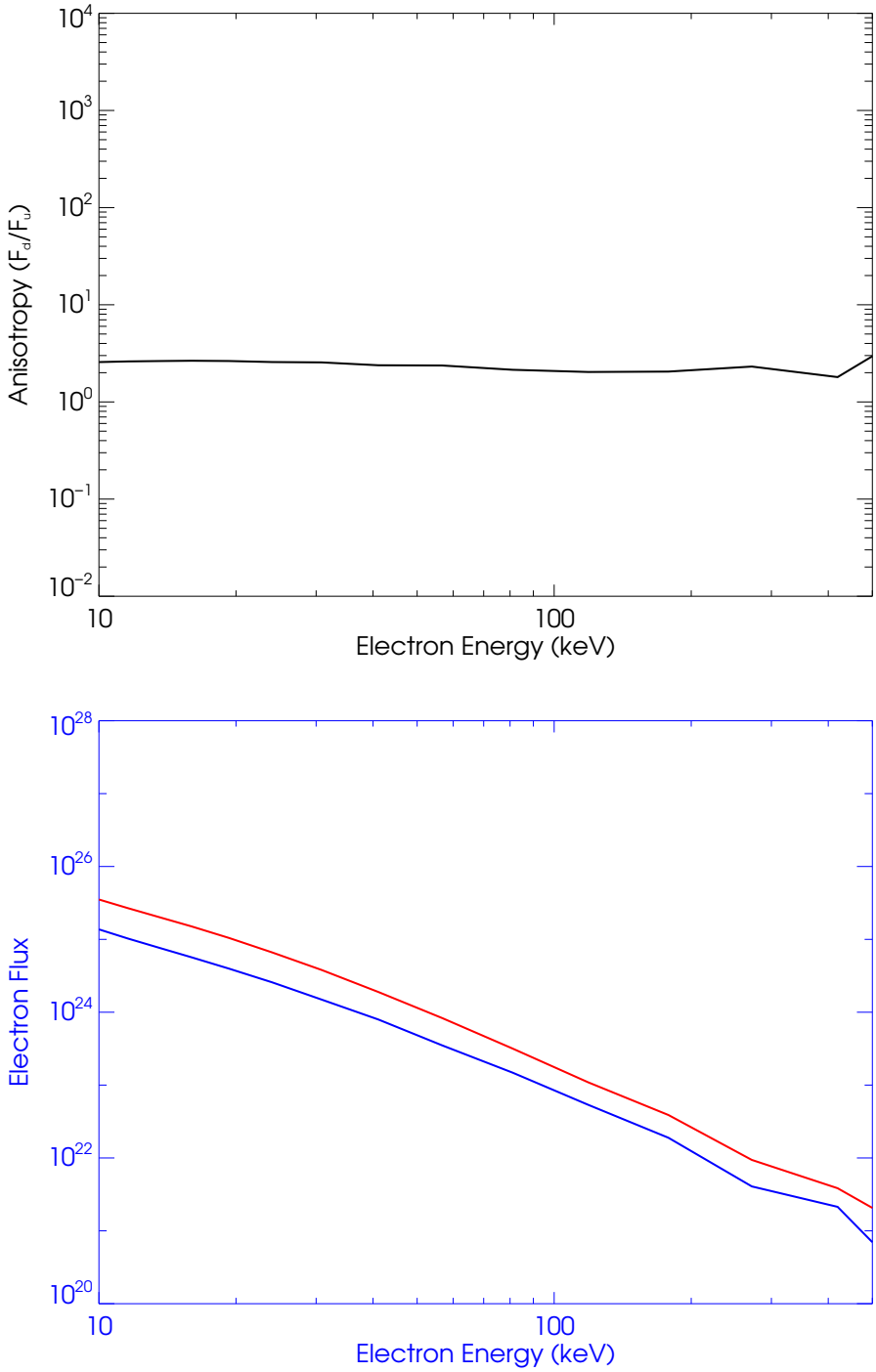

Figure 5.16: As Figure 5.6 for an initial isotropic pitch angle distribution and no reflection at the top of the loop.

6

Conclusions and Future Work

6.1 Conclusions

The aim of this thesis was to investigate the effect of Compton backscattered hard X-rays (also known as the photospheric albedo) on the observed photon spectrum at Earth and to determine what implications it has for inference of the parent electron distribution. In particular, looking at how measurements of the low energy cutoff of the non-thermal electrons and the directivity of the electron distribution are affected by albedo. I have used regularised inversion of RHESSI X-ray data to determine the electron energy distribution, both in terms of the angle averaged spectrum $\overline{F}(E)$, and a bi-directional approximation of the angular dependent electron distribution with downward and upward directed components. I have also conducted stochastic simulations to examine how this distribution is altered by particle transport in the solar atmosphere.

Chapter 2 deals with the effect directivity has on the observed photon spectrum, which is the combination of the components of both the primary, directly emitted, photon spectrum and the Compton backscattered X-ray flux, directed towards the observer. Simple commonly used functional forms were used to estimate the effects of different distributions in pitch angle of electrons in solar flares on the emitted photon spectrum. This was extended to include the contribution of photospheric albedo on the observed X-ray spectrum implemented, using the Green's

Matrix method of Kontar *et al.* (2006). The forward modelling shows that when there is strong downward-directed beaming in the emitting electron population, this will result in a very strong albedo emission. The characteristics of this reflected component can be very different from the directly emitted component, so the observed photon flux may show a clear signature of electron distribution anisotropy. For cases with substantial beaming, particularly for events which occur close to the disk centre, the albedo component can dominate over the primary component. Here the spectral index of the photon flux increases rapidly above 100 keV for flares close to the disk centre.

Chapter 3 considers the effect albedo has on inversions of the observed photon spectrum. The technique of regularised inversion was applied to the problem of inferring solar flare electron distributions from the observed RHESSI photons. In particular, we aimed to determine if the data showed evidence for a low energy cutoff, in the non-thermal electron spectrum. When regularised inversion is applied to simulated spectra with a low energy cutoff it is often seen as a dip in the recovered mean electron flux spectrum. This analysis was first performed neglecting the influence of albedo, and showed 17 flares with a clear dip in the electron distribution. However, this represents only a small proportion of the 177 events studied. Flares with a low value of γ_0 are very likely to exhibit a dip, as are flares located close to the disk centre and this is consistent with the appearance of these dips being due to the failure to take account of albedo. When a correction for albedo was applied to the observed photon spectrum, the presence of the dip in the electron spectrum was removed for all flares. The energies of the dip minima are concentrated near 15 keV, the energy which is expected from an isotropic albedo model. This work was published as Kontar, Dickson, and Kašparová (2008).

Chapter 4 ties the expected change in photon spectra with increasing directivity, modelled in Chapter 2, with the regularisation techniques introduced in Chapter 3. The inversion method was extended for the bi-directional problem of estimating the electron fluxes going downwards towards the photosphere, $\overline{F}_d$, and directed towards the observer $\overline{F}_u$. This method is most suitable when the albedo contribution is large; thus, flares close to the disk centre, with above background

counts at energies greater than 300 keV, were selected for analysis. The bivariate code was applied to the full impulsive phase for the eight flares studied, and the anisotropy in the electron spectrum determined. This analysis shows consistently that for almost all flares studied, the recovered $\overline{F}_d/\overline{F}_u$ is consistent, within the confidence intervals, with an isotropic pitch angle distribution. For almost every flare, downward beaming of a ratio greater than $\sim 3:1$ is ruled out to 3σ confidence below ~ 150 keV. Inversions of shorter time intervals (4 - 32 seconds) during the impulsive phase of the flares studied were also performed, to attempt to determine if there was any variation throughout the impulsive phase. These results are consistent with previously published results which showed little evidence of directivity at these energies and seem to rule out strong beaming of the sort usually expected in the basic collisional thick target model. However, the observations are consistent with a range of possible pitch angle distributions. The results of the inversions are model independent and can therefore be interpreted in terms of a variety of models, including those considered in Chapter 2. This work has been published as Dickson and Kontar (2012).

Chapter 5 considered the effect of particle transport through the solar atmosphere on the electron distribution. The Fokker-Plank formulation was used to estimate the change in the electron distribution due to Coulomb collisions. This was solved using stochastic simulations, as a Fokker-Planck equation can be written as a mathematically equivalent set of stochastic differential equations. The code was tested against the analytical results for several reduced cases and found to be in good agreement. The test was first run for a beam with all electrons initially directed downward. The simulations show that the effects of energy loss and pitch angle scattering by Coulomb collisions will reduce the anisotropy of a downward beamed distribution. However, the effect of Coulomb collisions alone is not strong enough to isotropise very strongly beamed distributions such that they are consistent with the RHESSI observations conducted in Chapter 4. For lower levels of initial anisotropy, it is possible to determine what level of anisotropy in the injected distribution would be needed to produce an emitting population consistent with the observations detailed in Chapter 4. These simulations suggest

that either the initially injected distribution is not strongly beamed or other mechanisms of energy loss and pitch angle scattering are significant.

6.2 Future Work

6.2.1 Electron-Electron Bremsstrahlung

The principal mechanism for X-ray production in the regime of RHESSI observations is ion-electron bremsstrahlung. However, there are several other mechanisms which will also be responsible for some of the X-ray emission in this energy, and while these are either never likely to be dominant or will only become significant under extreme conditions, their influence can have a large effect on the electron spectra inferred from the combined photon spectra, using techniques such as regularised inversion.

In particular the electron-electron bremsstrahlung might have an influence at high energies ($>$ 300 keV). The cross-section of electron-electron bremsstrahlung is quadrupole (Figure 6.1) whereas the ion-electron bremsstrahlung cross-section is dipole, therefore the inclusion of e-e bremsstrahlung could have an effect on the observed X-ray spectra for different levels of anisotropy.

The effect of electron-electron bremsstrahlung on inversion of RHESSI data was examined for the angle averaged case by Kontar *et al.* (2007). It was found that while this component was always much smaller than the usual e-i bremsstrahlung component, its inclusion could influence the inferred electron spectra, removing the need for an upward break in spectral index at high energies for one flare studied.

6.2.2 Further Observations

The spectral modelling in Chapter 2 suggests that there is a large amount of information on the directivity provided by the reflected albedo component. While

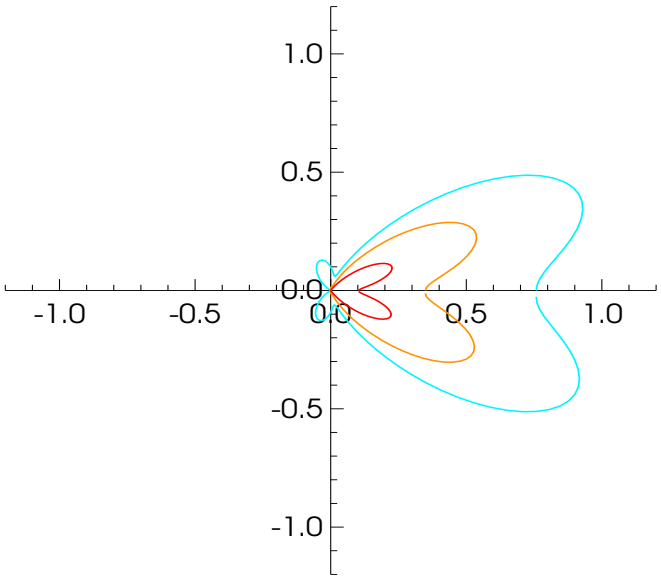

Figure 6.1: Polar diagram of electron-electron bremsstrahlung cross-section for an electron of energy 100 keV emitting a photon of 35 keV (blue) 45 keV (yellow) 55 keV (red) c.f. Massone *et al.* (2004), Figure 2.2.

this is most significant for the case of strong downwards anisotropy, other distributions including those with $\overline{F}_d = \overline{F}_u$ do show signatures of their angular distribution, at least for simple power-law distributions in electron energy.

As the drop off of albedo reflectivity is strongest at several hundred keV high quality observations in this regime are important. RHESSI is equipped to provide measurements in this regime with good energy resolution, however as the level of counts is close to the background at these energies in practice measurements are only possible for the strongest flares.

6.2.3 Stochastic Simulations

One of the advantages of using stochastic simulations to model the transport effects in solar flares is the flexibility they afford. Many physical interactions which affect energy loss and pitch angle scattering can be included by adding the

relevant terms to the stochastic equations. While Coulomb collisions are expected to be the major source of energy loss and pitch angle scattering, there are many other processes which will also affect the beam distribution.

In particular, magnetic mirroring due to the convergence of the magnetic field at the loop footpoints could have a significant effect on the pitch angle distribution of the beam, particularly for the high energy electrons which are likely to travel further down the loop before losing energy. The magnetic mirroring does not alter the particle energy, so can be included with the addition of the term $-\frac{1}{2}(1-\mu^2)\frac{d\ln B}{ds}$ to the pitch angle advection component D_μ. While this is not part of the standard thick target model, it has the potential to have a significant effect for real flares. For strong magnetic fields the effect of gyrosynchrotron emission on energy loss and pitch angle change can also become significant (Petrosian, 1985). As with magnetic mirroring this can be straightforwardly included by adding $D_E = -\frac{2}{3}(1-\mu^2)\frac{e^4\gamma^2\beta B^2}{m_e^2c^4}$ to the the energy loss and $D_\mu = -\frac{2}{3}\mu(1-\mu^2)\frac{e^4\beta B^2}{m_e^3c^6\gamma\beta^2}$ to the pitch angle advection terms. As synchrotron emission is optically thin there is no additional associated diffusion.

With more realistic conditions and the addition of the other effects these simulations will allow us to make more detailed comparisons between theoretical models and the electron spectra inferred using regularised inversion methods. This will allow us greater insight into the acceleration processes of solar flares.

References

Aki, K.: 1980, *Quantitative seismology : theory and methods.* **2**, Freeman, San Francisco. ISBN 0716710595. 70

Ambastha, A.: 2003, The Active and Explosive Sun. In: Antia, H.M., Bhatnagar, A., Ulmschneider, P. (eds.) *Lectures on Solar Physics*, *Lecture Notes in Physics, Berlin Springer Verlag* **619**, 127. 9

Anderson, K.A., Kane, S.R., Primbsch, J.H., Weitzmann, R.H., Evans, W.D., Klebesadel, R.W., Aiello, W.P.: 1978, X-ray spectrometer experiment aboard the ISEE-C /Heliocentric/ spacecraft. *IEEE Transactions on Geoscience Electronics* **16**, 157 – 159. 22

Aschwanden, M.J.: 1996, Electron versus Proton Timing Delays in Solar Flares. *Astrophys. J. Lett.* **470**, L69. doi:10.1086/310294. 21

Aschwanden, M.J.: 2004, *Physics of the Solar Corona. An Introduction*, Praxis Publishing Ltd. x, 22

Bai, T.: 1988, Directionality of continuum gamma rays from solar flares. *Astrophys. J.* **334**, 1049 – 1053. doi:10.1086/166897. 90

Bai, T., Ramaty, R.: 1978, Backscatter, anisotropy, and polarization of solar hard X-rays. *Astrophys. J.* **219**, 705 – 726. doi:10.1086/155830. x, 25, 26, 27, 41, 92

Battaglia, M., Kontar, E.P.: 2011, Hard X-Ray Footpoint Sizes and Positions as Diagnostics of Flare Accelerated Energetic Electrons in the Low Solar Atmosphere. *Astrophys. J.* **735**, 42. doi:10.1088/0004-637X/735/1/42. 13, 131

Battaglia, M., Kontar, E.P., Fletcher, L., MacKinnon, A.L.: 2012, Numerical Simulations of Chromospheric Hard X-Ray Source Sizes in Solar Flares. *Astrophys. J.* **752**, 4. doi:10.1088/0004-637X/752/1/4. 131

Benz, A.O.: 2008, Flare Observations. *Living Reviews in Solar Physics* **5**, 1. 10

Bertero, M., Demol, C., Pike, E.: 1985, Linear Inverse Problems With Discrete-data .1. General Formulation And Singular System-analysis. *Inverse Problems* **1**(4), 301 – 330. doi:10.1088/0266-5611/1/4/004. 68

Bertero, M., Mol, C.D., Pike, E.R.: 1988, Linear inverse problems with discrete data: Ii. stability and regularisation. *Inverse Problems* **4**(3), 573. http://stacks.iop.org/0266-5611/4/i=3/a=004. 75

Bevington, P.R., Robinson, D.K.: 1992, *Data reduction and error analysis for the physical sciences*, *Mcgraw-Hill International editions: Physics series*, McGraw-Hill. ISBN 9780079112439. 134

Bogovalov, S.V., Kotov, Y.D., Zenchenko, V.M., Vedrenne, G., Niel, M., Barat, C., Chambon, G., Talon, R.: 1985, Directionality of Solar Flare Hard X-Rays - VENERA:13 Observations. *Soviet Astronomy Letters* **11**, 322 – +. 90

Brodrick, D., Tingay, S., Wieringa, M.: 2005, X-ray magnitude of the 4 November 2003 solar flare inferred from the ionospheric attenuation of the galactic radio background. *Journal of Geophysical Research (Space Physics)* **110**, 9. doi:10.1029/2004JA010960. 11

Brown, J.C.: 1971, The Deduction of Energy Spectra of Non-Thermal Electrons in Flares from the Observed Dynamic Spectra of Hard X-Ray Bursts. *Solar Phys.* **18**, 489 – 502. doi:10.1007/BF00149070. 18, 19, 75, 79

Brown, J.C.: 1972, The Directivity and Polarisation of Thick Target X-Ray Bremsstrahlung from Solar Flares. *Solar Phys.* **26**, 441 – 459. doi:10.1007/BF00165286. 35, 127

Brown, J.C., Emslie, A.G.: 1988, Analytic limits on the forms of spectra possible from optically thin collisional bremsstrahlung source models. *Astrophys. J.* **331**, 554 – 564. doi:10.1086/166581. 32, 76

Brown, J.C., Mallik, P.C.V.: 2008, Non-thermal recombination - a neglected source of flare hard X-rays and fast electron diagnostic. *Astron. Astrophys.* **481**, 507 – 518. doi:10.1051/0004-6361:20078103. 20

Brown, J.C., Mallik, P.C.V.: 2009, Flare Hard X-Ray Sources Dominated by Nonthermal Recombination. *Astrophys. J. Lett.* **697**, L6 – L9. doi:10.1088/0004-637X/697/1/L6. 20

Brown, J.C., Emslie, A.G., Kontar, E.P.: 2003, The Determination and Use of Mean Electron Flux Spectra in Solar Flares. *Astrophys. J. Lett.* **595**, L115 – L117. doi:10.1086/378169. 29

Brown, J.C., Mallik, P.C.V., Badnell, N.R.: 2010, Non-thermal recombination - a neglected source of flare hard X-rays and fast electron diagnostics (Corrigendum). *Astron. Astrophys.* **515**, C1. doi:10.1051/0004-6361:20078103e. 20

Brown, J.C., Emslie, A.G., Holman, G.D., Johns-Krull, C.M., Kontar, E.P., Lin, R.P., Massone, A.M., Piana, M.: 2006, Evaluation of Algorithms for Reconstructing Electron Spectra from Their Bremsstrahlung Hard X-Ray Spectra. *Astrophys. J.* **643**, 523 – 531. doi:10.1086/501497. xvii, 77, 78, 93

Brown, J.C., Kašparová, J., Massone, A.M., Piana, M.: 2008, Fast spectral fitting of hard X-ray bremsstrahlung from truncated power-law electron spectra. *Astron. Astrophys.* **486**, 1023 – 1029. doi:10.1051/0004-6361:200809496. 31

Brown, J.C., Turkmani, R., Kontar, E.P., MacKinnon, A.L., Vlahos, L.: 2009, Local re-acceleration and a modified thick target model of solar flare electrons. *Astron. Astrophys.* **508**, 993 – 1000. doi:10.1051/0004-6361/200913145. 125

Carmichael, H.: 1964, A Process for Flares. *NASA Special Publication* **50**, 451. 13

Carrington, R.C.: 1859, Description of a Singular Appearance seen in the Sun on September 1, 1859. *Mon. Not. Roy. Astron. Soc.* **20**, 13 – 15. 8

Catalano, C.P., van Allen, J.A.: 1973, Height Distribution and Directionality of 2-12 a X-Ray Flare Emission in the Solar Atmosphere. *Astrophys. J.* **185**, 335 – 350. doi:10.1086/152420. 91

Christensen-Dalsgaard, J., Hansen, P.C., Thompson, M.J.: 1993, Generalized Singular Value Decomposition Analysis of Helioseismic Inversions. *Mon. Not. Roy. Astron. Soc.* **264**, 541. 71

Cliver, E.W., Svalgaard, L.: 2004, The 1859 Solar-Terrestrial Disturbance And the Current Limits of Extreme Space Weather Activity. *Solar Phys.* **224**, 407 – 422. doi:10.1007/s11207-005-4980-z. 9

Cliver, E.W., Dennis, B.R., Kiplinger, A.L., Kane, S.R., Neidig, D.F., Sheeley, N.R. Jr., Koomen, M.J.: 1986, Solar gradual hard X-ray bursts and associated phenomena. *Astrophys. J.* **305**, 920 – 935. doi:10.1086/164306. x, 12

Compton, A.H.: 1923, A Quantum Theory of the Scattering of X-rays by Light Elements. *Physical Review* **21**, 483 – 502. doi:10.1103/PhysRev.21.483. 25

Conway, A.J., Brown, J.C., Eves, B.A.C., Kontar, E.: 2003, Implications of solar flare hard X-ray "knee" spectra observed by RHESSI. *Astron. Astrophys.* **407**, 725 – 734. doi:10.1051/0004-6361:20030897. 32

Cox, A.N.: 2000, *Allen's astrophysical quantities*. 1

Craig, I.J.D., Brown, J.C.: 1986, *Inverse problems in astronomy: A guide to inversion strategies for remotely sensed data*. ISBN 0852743696. 68, 75

Crosby, N.B., Aschwanden, M.J., Dennis, B.R.: 1993, Frequency distributions and correlations of solar X-ray flare parameters. *Solar Phys.* **143**, 275 – 299. doi:10.1007/BF00646488. 7

Datlowe, D.W., Elcan, M.J., Hudson, H.S.: 1974, OSO-7 observations of solar X-rays in the energy range 10-100 keV. *Solar Phys.* **39**, 155 – 174. doi:10.1007/BF00154978. 90

Dennis, B.R.: 1985, Solar hard X-ray bursts. *Solar Phys.* **100**, 465 – 490. doi:10.1007/BF00158441. 30

Dennis, B.R.: 1988, Solar flare hard X-ray observations. *Solar Phys.* **118**, 49 – 94. doi:10.1007/BF00148588. 90

Dickson, E.C.M., Kontar, E.P.: 2012, Measurements of Electron Anisotropy in Solar Flares Using Albedo with RHESSI X-Ray Data. *Solar Phys.*, 301. doi:10.1007/s11207-012-0178-3. 154

Doschek, G.A., Feldman, U.: 2010, TOPICAL REVIEW The solar UV-x-ray spectrum from 1.5 to 2000 Å. *Journal of Physics B Atomic Molecular Physics* **43**(23), 232001. doi:10.1088/0953-4075/43/23/232001. 10

Dreicer, H.: 1959, Electron and Ion Runaway in a Fully Ionized Gas. I. *Physical Review* **115**, 238 – 249. doi:10.1103/PhysRev.115.238. 15

Dulk, G.A., Kiplinger, A.L., Winglee, R.M.: 1992, Characteristics of hard X-ray spectra of impulsive solar flares. *Astrophys. J.* **389**, 756 – 763. doi:10.1086/171248. 31

Elwert, G.: 1939, Verschärfte Berechnung von Intensität und Polarisation im kontinuierlichen Röntgenspektrum1. *Annalen der Physik* **426**, 178 – 208. doi:10.1002/andp.19394260206. 32, 33

Emslie, A.G.: 1978, The collisional interaction of a beam of charged particles with a hydrogen target of arbitrary ionization level. *Astrophys. J.* **224**, 241 – 246. doi:10.1086/156371. 19, 130

Emslie, A.G., Brown, J.C.: 1985, Hard X-ray bremsstrahlung production in solar flares by high-energy proton beams. *Astrophys. J.* **295**, 648 – 653. doi:10.1086/163408. 21

Emslie, A.G., Bradsher, H.L., McConnell, M.L.: 2008, Hard X-Ray Polarization from Non-vertical Solar Flare Loops. *Astrophys. J.* **674**, 570 – 575. doi:10.1086/524983. 92

Emslie, A.G., Kucharek, H., Dennis, B.R., Gopalswamy, N., Holman, G.D., Share, G.H., Vourlidas, A., Forbes, T.G., Gallagher, P.T., Mason, G.M., Metcalf, T.R., Mewaldt, R.A., Murphy, R.J., Schwartz, R.A., Zurbuchen, T.H.: 2004, Energy partition in two solar flare/CME events. *Journal of Geophysical Research (Space Physics)* **109**(18), 10104. doi:10.1029/2004JA010571. 16

Emslie, A.G., Dennis, B.R., Holman, G.D., Hudson, H.S.: 2005, Refinements to flare energy estimates: A followup to "Energy partition in two solar flare/CME events" by A. G. Emslie et al. *Journal of Geophysical Research (Space Physics)* **110**(9), 11103. doi:10.1029/2005JA011305. 16

Farnik, F., Hudson, H., Watanabe, T.: 1997, YOHKOH observations of flares with flat hard X-ray spectra. *Astron. Astrophys.* **320**, 620 – 630. 89

Fireman, E.L.: 1974, Interstellar Absorption of X-Rays. *Astrophys. J.* **187**, 57 – 60. doi:10.1086/152588. 26

Fishman, G.J., Meegan, C.A., Wilson, R.B., Parnell, T.A., Paciesas, W.S., Pendleton, G.N., Hudson, H.S., Matteson, J.L., Peterson, L.E., Cline, T.L., Teegarden, B.J., Schaefer, B.E.: 1989, The BATSE Experiment for the GRO - Solar Flare Hard X-Ray and Gamma-Ray Capabilities. In: *Bulletin of the American Astronomical Society*, *Bulletin of the American Astronomical Society* **21**, 860. 23

Fivian, M., Hemmeck, R., McHedlishvili, A., Zehnder, A.: 2002, RHESSI Aspect Reconstruction. *Solar Phys.* **210**, 87 – 99. doi:10.1023/A:1022448632344. 23

Fleishman, G.D., Kuznetsov, A.A.: 2010, Fast Gyrosynchrotron Codes. *Astrophys. J.* **721**, 1127 – 1141. doi:10.1088/0004-637X/721/2/1127. 52

Fleishman, G.D., Melnikov, V.F.: 2003, Gyrosynchrotron Emission from Anisotropic Electron Distributions. *Astrophys. J.* **587**, 823 – 835. doi:10.1086/368252. 56

Fletcher, L.: 1996, The height distribution of non-thermal X-ray sources in impulsive solar flares. *Astron. Astrophys.* **310**, 661 – 671. 130

Fletcher, L., Hudson, H.S.: 2008, Impulsive Phase Flare Energy Transport by Large-Scale Alfvén Waves and the Electron Acceleration Problem. *Astrophys. J.* **675**, 1645 – 1655. doi:10.1086/527044. 125

Fletcher, L., Martens, P.C.H.: 1998, A Model for Hard X-Ray Emission from the Top of Flaring Loops. *Astrophys. J.* **505**, 418 – 431. doi:10.1086/306137. 130

Gardiner, C.W.: 1985, *Handbook of stochastic methods for physics, chemistry, and the natural sciences*, *Springer series in synergetics*, Springer, Heildelberg. ISBN 9783540113577. 130

Gilliland, R.L., Dupree, A.K.: 1996, First Image of the Surface of a Star with the Hubble Space Telescope. *Astrophys. J. Lett.* **463**, L29. doi:10.1086/310043. 2

Golub, L., Pasachoff, J.M.: 2009, *The solar corona*, *The Solar Corona*, Cambridge University Press. ISBN 9780521882019. http://books.google.co.uk/books?id=XaRH1ZxEWu4C. 6

Groetsch, C.W.: 1984, *The theory of tikhonov regularization for fredholm equations of the first kind / c.w. groetsch.*, *Research Notes in Mathematics*, Pitman Advanced Pub. Program. ISBN 0273086421. 68

Grotian, W.: 1939, Zur frage der deutung der linien im spektrum der sonnenkorona. *Naturwissenschaften* **27**, 214 – 214. 10.1007/BF01488890. http://dx.doi.org/10.1007/BF01488890. 6

Hamilton, R.J., Lu, E.T., Petrosian, V.: 1990, Numerical solution of the time-dependent kinetic equation for electrons in magnetized plasma. *Astrophys. J.* **354**, 726 – 734. doi:10.1086/168729. 129

Hannah, I.G., Kontar, E.P.: 2012, Differential emission measures from the regularized inversion of Hinode and SDO data. *Astron. Astrophys.* **539**, A146. doi:10.1051/0004-6361/201117576. 71

Hannah, I.G., Hudson, H.S., Battaglia, M., Christe, S., Kašparová, J., Krucker, S., Kundu, M.R., Veronig, A.: 2011, Microflares and the Statistics of X-ray Flares. *Space Sci. Rev.* **159**, 263 – 300. doi:10.1007/s11214-010-9705-4. 7

Hansen, C.J., Kawaler, S.D.: 1994, *Stellar Interiors. Physical Principles, Structure, and Evolution.*. 3

Hansen, P.: 1989, Regularization, GSVD And Truncated GSVD. *BIT* **29**(3), 491 – 504. doi:10.1007/bf02219234. 70

Hansen, P.: 1992, Numerical Tools For Analysis And Solution Of Fredholm Integral-equations Of The 1st Kind. *Inverse Problems* **8**(6), 849 – 872. doi:10.1088/0266-5611/8/6/005. 68, 70

Hansen, P.C.: 2010, *Discrete inverse problems: Insight and algorithms*, *Fundamentals of Algorithms*, Society for Industrial and Applied Mathematics, Philadelphia. ISBN 9780898716962. 67

Haug, E.: 1997, On the use of nonrelativistic bremsstrahlung cross sections in astrophysics. *Astron. Astrophys.* **326**, 417 – 418. 18, 32, 76

Heitler, W.: 1954, *The quantum theory of radiation*, *International series of monographs on physics*, Clarendon Press, London. 18

Hey, J.S., Parsons, S.J., Phillips, J.W.: 1948, Some Characteristics of Solar Radio Emissions. *Mon. Not. Roy. Astron. Soc.* **108**, 354. 10

Hirayama, T.: 1974, Theoretical Model of Flares and Prominences. I: Evaporating Flare Model. *Solar Phys.* **34**, 323 – 338. doi:10.1007/BF00153671. 13

Hodgson, R.: 1859, On a curious Appearance seen in the Sun. *Mon. Not. Roy. Astron. Soc.* **20**, 15 – 16. 8

Holman, G.D.: 2003, The Effects of Low- and High-Energy Cutoffs on Solar Flare Microwave and Hard X-Ray Spectra. *Astrophys. J.* **586**, 606 – 616. doi:10.1086/367554. 30, 80

Holman, G.D., Sui, L., Schwartz, R.A., Emslie, A.G.: 2003, Electron Bremsstrahlung Hard X-Ray Spectra, Electron Distributions, and Energetics in the 2002 July 23 Solar Flare. *Astrophys. J. Lett.* **595**, L97 – L101. doi:10.1086/378488. 76, 77, 82

Holman, G.D., Aschwanden, M.J., Aurass, H., Battaglia, M., Grigis, P.C., Kontar, E.P., Liu, W., Saint-Hilaire, P., Zharkova, V.V.: 2011, Implications of X-ray Observations for Electron Acceleration and Propagation in Solar Flares. *Space Sci. Rev.* **159**, 107 – 166. doi:10.1007/s11214-010-9680-9. 90, 127

Hubeny, V., Judge, P.G.: 1995, Solution to the Bivariate Integral Inversion Problem: The Determination of Emission Measures Differential in Temperature and Density. *Astrophys. J. Lett.* **448**, L61+. doi:10.1086/309594. 94

Hudson, H.S., Wolfson, C.J., Metcalf, T.R.: 2006, White-Light Flares: A TRACE/RHESSI Overview. *Solar Phys.* **234**, 79 – 93. doi:10.1007/s11207-006-0056-y. 9

Hurford, G.J., Schmahl, E.J., Schwartz, R.A., Conway, A.J., Aschwanden, M.J., Csillaghy, A., Dennis, B.R., Johns-Krull, C., Krucker, S., Lin, R.P., McTiernan, J., Metcalf, T.R., Sato, J., Smith, D.M.: 2002, The RHESSI Imaging Concept. *Solar Phys.* **210**, 61 – 86. doi:10.1023/A:1022436213688. x, 23, 24

Hurford, G.J., Schwartz, R.A., Krucker, S., Lin, R.P., Smith, D.M., Vilmer, N.: 2003, First Gamma-Ray Images of a Solar Flare. *Astrophys. J. Lett.* **595**, L77 – L80. doi:10.1086/378179. 12

Hurford, G.J., Krucker, S., Lin, R.P., Schwartz, R.A., Share, G.H., Smith, D.M.: 2006, Gamma-Ray Imaging of the 2003 October/November Solar Flares. *Astrophys. J. Lett.* **644**, L93 – L96. doi:10.1086/505329. 12

Jess, D.B., Mathioudakis, M., Crockett, P.J., Keenan, F.P.: 2008, Do All Flares Have White-Light Emission? *Astrophys. J. Lett.* **688**, L119 – L122. doi:10.1086/595588. 9

Johns, C.M., Lin, R.P.: 1992, The derivation of parent electron spectra from bremsstrahlung hard X-ray spectra. *Solar Phys.* **137**, 121 – 140. doi:10.1007/BF00146579. 77

Kane, S.R., Hurley, K., McTiernan, J.M., Boer, M., Niel, M., Kosugi, T., Yoshimori, M.: 1998, Stereoscopic Observations of Solar Hard X-Ray Flares Made by ULYSSES and YOHKOH. *Astrophys. J.* **500**, 1003 – +. doi:10.1086/305738. 91

Karlický, M., Kosugi, T.: 2004, Acceleration and heating processes in a collapsing magnetic trap. *Astron. Astrophys.* **419**, 1159 – 1168. doi:10.1051/0004-6361:20034323. 47

Karlický, M., Brown, J.C., Conway, A.J., Penny, G.: 2000, Flare hard X-rays from neutral beams. *Astron. Astrophys.* **353**, 729 – 740. 21

Kašparová, J., Kontar, E.P., Brown, J.C.: 2007, Hard X-ray spectra and positions of solar flares observed by RHESSI: photospheric albedo, directivity and electron spectra. *Astron. Astrophys.* **466**, 705 – 712. doi:10.1051/0004-6361:20066689. xviii, 80, 81, 82, 87, 88, 90, 91, 99, 126

Kašparová, J., Karlický, M., Kontar, E.P., Schwartz, R.A., Dennis, B.R.: 2005, Multi-Wavelength Analysis of High-Energy Electrons in Solar Flares: A Case Study of the August 20, 2002 Flare. *Solar Phys.* **232**, 63 – 86. doi:10.1007/s11207-005-1581-9. 79, 80

Kirsch, A.: 1996, *An introduction to the mathematical theory of inverse problems*, *Applied Mathematical Sciences* **v. 120**, Springer, New York. ISBN 9780387945309. 66

Knight, J.W., Sturrock, P.A.: 1977, Reverse current in solar flares. *Astrophys. J.* **218**, 306 – 310. doi:10.1086/155683. 20

Koch, H.W., Motz, J.W.: 1959, Bremsstrahlung Cross-Section Formulas and Related Data. *Reviews of Modern Physics* **31**, 920 – 955. doi:10.1103/RevModPhys.31.920. 17, 31, 33

Kontar, E.P., Brown, J.C.: 2006a, Solar flare hard X-ray spectra possibly inconsistent with the collisional thick target model. *Advances in Space Research* **38**, 945 – 950. doi:10.1016/j.asr.2005.09.029. 79

Kontar, E.P., Brown, J.C.: 2006b, Stereoscopic Electron Spectroscopy of Solar Hard X-Ray Flares with a Single Spacecraft. *Astrophys. J.* **653**, L149 – L152. doi:10.1086/510586. 80, 92, 93

Kontar, E.P., Brown, J.C., McArthur, G.K.: 2002, X-ray observations with RHESSI and collisional thick target model with nonuniform target ionisation. In: Wilson, A. (ed.) *Solar Variability: From Core to Outer Frontiers*, *ESA Special Publication* **506**, 311 – 314. 31

Kontar, E.P., Dickson, E., Kašparová, J.: 2008, Low-Energy Cutoffs in Electron Spectra of Solar Flares: Statistical Survey. *Solar Phys.* **252**, 139 – 147. doi:10.1007/s11207-008-9249-x. 81, 153

Kontar, E.P., Piana, M., Massone, A.M., Emslie, A.G., Brown, J.C.: 2004, Generalized Regularization Techniques with Constraints for the Analysis of Solar Bremsstrahlung X-ray Spectra. *Solar Phys.* **225**, 293 – 309. doi:10.1007/s11207-004-4140-x. 70, 76, 80, 87

Kontar, E.P., Emslie, A.G., Piana, M., Massone, A.M., Brown, J.C.: 2005, Determination of Electron Flux Spectra in a Solar Flare with an Augmented Regularization Method: Application to Rhessi Data. *Solar Phys.* **226**, 317 – 325. doi:10.1007/s11207-005-7150-4. 93

Kontar, E.P., MacKinnon, A.L., Schwartz, R.A., Brown, J.C.: 2006, Compton backscattered and primary X-rays from solar flares: angle dependent Green's function correction for photospheric albedo. *Astron. Astrophys.* **446**, 1157 – 1163. doi:10.1051/0004-6361:20053672. xii, 42, 45, 87, 88, 93, 99, 101, 153

Kontar, E.P., Emslie, A.G., Massone, A.M., Piana, M., Brown, J.C., Prato, M.: 2007, Electron-Electron Bremsstrahlung Emission and the Inference of Electron Flux Spectra in Solar Flares. *Astrophys. J.* **670**, 857 – 861. doi:10.1086/521977. 155

Kontar, E.P., Brown, J.C., Emslie, A.G., Hajdas, W., Holman, G.D., Hurford, G.J., Kašparová, J., Mallik, P.C.V., Massone, A.M., McConnell, M.L., Piana, M., Prato, M., Schmahl, E.J., Suarez-Garcia, E.: 2011, Deducing Electron Properties from Hard X-ray Observations. *Space Sci. Rev.* **159**, 301 – 355. doi:10.1007/s11214-011-9804-x. 90

Kopp, R.A., Pneuman, G.W.: 1976, Magnetic reconnection in the corona and the loop prominence phenomenon. *Solar Phys.* **50**, 85 – 98. doi:10.1007/BF00206193. 13

Korchak, A.A.: 1967, Possible Mechanisms for Generating Hard X Rays in Solar Flares. *Sov. Astron.* **11**, 258. 16, 20

Kosugi, T., Makishima, K., Murakami, T., Sakao, T., Dotani, T., Inda, M., Kai, K., Masuda, S., Nakajima, H., Ogawara, Y., Sawa, M., Shibasaki, K.: 1991, The Hard X-ray Telescope (HXT) for the SOLAR-A Mission. *Solar Phys.* **136**, 17 – 36. doi:10.1007/BF00151693. 23

Kramers, H.: 1923, On the theory of X-ray absorption and of the continuous X-ray spectrum. *PHILOSOPHICAL MAGAZINE* **46**(275, 6TH SERIES), 836 – 871. 18

Krucker, S., Christe, S., Glesener, L., McBride, S., Turin, P., Glaser, D., Saint-Hilaire, P., Delory, G., Lin, R.P., Gubarev, M., Ramsey, B., Terada, Y., Ishikawa, S.-N., Kokubun, M., Saito, S., Takahashi, T., Watanabe, S., Nakazawa, K., Tajima, H., Masuda, S., Minoshima, T., Shomojo, M.: 2009, The Focusing Optics X-ray Solar Imager (FOXSI). In: *Society of Photo-Optical Instrumentation Engineers (SPIE) Conference Series*, *Society of Photo-Optical Instrumentation Engineers (SPIE) Conference Series* **7437**. doi:10.1117/12.827950. 22

Leach, J., Petrosian, V.: 1981, Impulsive phase of solar flares. I - Characteristics of high energy electrons. *Astrophys. J.* **251**, 781 – 791. doi:10.1086/159521. 127, 129

Leach, J., Petrosian, V.: 1983, The impulsive phase of solar flares. II - Characteristics of the hard X-rays. *Astrophys. J.* **269**, 715 – 727. doi:10.1086/161081. 35, 92

Li, P., Hurley, K., Barat, C., Niel, M., Talon, R., Kurt, V.: 1994, Directivity of 100-500 keV solar flare hard X-ray emission. *Astrophys. J.* **426**, 758 – 766. doi:10.1086/174112. 91

Lin, R.P., Dennis, B.R., Hurford, G.J., Smith, D.M., Zehnder, A., Harvey, P.R., Curtis, D.W., Pankow, D., Turin, P., Bester, M., Csillaghy, A., Lewis, M., Madden, N., van Beek, H.F., Appleby, M., Raudorf, T., McTiernan, J., Ramaty, R., Schmahl, E., Schwartz, R., Krucker, S., Abiad, R., Quinn, T., Berg, P., Hashii, M., Sterling, R., Jackson, R., Pratt, R., Campbell, R.D., Malone, D., Landis, D., Barrington-Leigh, C.P., Slassi-Sennou, S., Cork, C., Clark, D.,

Amato, D., Orwig, L., Boyle, R., Banks, I.S., Shirey, K., Tolbert, A.K., Zarro, D., Snow, F., Thomsen, K., Henneck, R., McHedlishvili, A., Ming, P., Fivian, M., Jordan, J., Wanner, R., Crubb, J., Preble, J., Matranga, M., Benz, A., Hudson, H., Canfield, R.C., Holman, G.D., Crannell, C., Kosugi, T., Emslie, A.G., Vilmer, N., Brown, J.C., Johns-Krull, C., Aschwanden, M., Metcalf, T., Conway, A.: 2002, The Reuven Ramaty High-Energy Solar Spectroscopic Imager (RHESSI). *Solar Phys.* **210**, 3 – 32. doi:10.1023/A:1022428818870. 23, 79, 90

Lu, E.T., Petrosian, V.: 1988, Rapid temporal evolution of radiation from nonthermal electrons in solar flares. *Astrophys. J.* **327**, 405 – 416. doi:10.1086/166203. 135

MacKinnon, A.L., Craig, I.J.D.: 1991, Stochastic simulation of fast particle diffusive transport. *Astron. Astrophys.* **251**, 693 – 699. 127, 130, 135

Magdziarz, P., Zdziarski, A.A.: 1995, Angle-dependent Compton reflection of X-rays and gamma-rays. *Mon. Not. Roy. Astron. Soc.* **273**, 837 – 848. 41, 42

Massone, A.M., Emslie, A.G., Kontar, E.P., Piana, M., Prato, M., Brown, J.C.: 2004, Anisotropic Bremsstrahlung Emission and the Form of Regularized Electron Flux Spectra in Solar Flares. *Astrophys. J.* **613**, 1233 – 1240. doi:10.1086/423127. xi, xxiv, 35, 36, 156

Masuda, S., Kosugi, T., Hara, H., Tsuneta, S., Ogawara, Y.: 1994, A loop-top hard X-ray source in a compact solar flare as evidence for magnetic reconnection. *Nature* **371**, 495 – 497. doi:10.1038/371495a0. 13

McConnell, M.L., Ryan, J.M., Smith, D.M., Lin, R.P., Emslie, A.G.: 2002, RHESSI as a Hard X-Ray Polarimeter. *Solar Phys.* **210**, 125 – 142. doi:10.1023/A:1022413708738. 92

McTiernan, J.M., Petrosian, V.: 1991, Center-to-limb variations of characteristics of solar flare hard X-ray and gamma-ray emission. *Astrophys. J.* **379**, 381 – 391. doi:10.1086/170513. 90, 126

Mel'Nik, V.N., Lapshin, V., Kontar, E.: 1999, Propagation of a Monoenergetic Electron Beam in the Solar Corona. *Solar Phys.* **184**, 353 – 362. 79

Miller, J.A., Cargill, P.J., Emslie, A.G., Holman, G.D., Dennis, B.R., LaRosa, T.N., Winglee, R.M., Benka, S.G., Tsuneta, S.: 1997, Critical issues for understanding particle acceleration in impulsive solar flares. *J. Geophys. Res.* **102**, 14631 – 14660. doi:10.1029/97JA00976. 15

Morozov, V.A.: 1967, Choice Of Parameter In Solving Functional Equations By Regularization Method. *Doklady Akademii NAUK SSSR* **175**(6), 1225 – &. 68

Nakel, W.: 1994, The elementary process of bremsstrahlung. *Phys. Rep.* **243**, 317 – 353. doi:10.1016/0370-1573(94)00068-9. x, 17

Nitta, N., Dennis, B.R., Kiplinger, A.L.: 1990, X-ray observations of two short but intense solar flares. *Astrophys. J.* **353**, 313 – 322. doi:10.1086/168618. 89

Parker, E.N.: 1957, Sweet's Mechanism for Merging Magnetic Fields in Conducting Fluids. *J. Geophys. Res.* **62**, 509 – 520. doi:10.1029/JZ062i004p00509. 14

Peterson, L., Winckler, J.R.: 1958, Short γ-Ray Burst from a Solar Flare. *Physical Review Letters* **1**, 205 – 206. doi:10.1103/PhysRevLett.1.205. 21

Petrosian, V.: 1985, Directivity of bremsstrahlung radiation from relativistic beams and the gamma rays from solar flares. *Astrophys. J.* **299**, 987 – 993. doi:10.1086/163765. 157

Petrosian, V., Donaghy, T.Q.: 1999, On the Spatial Distribution of Hard X-Rays from Solar Flare Loops. *Astrophys. J.* **527**, 945 – 957. doi:10.1086/308133. 47

Petschek, H.E.: 1964, Magnetic Field Annihilation. *NASA Special Publication* **50**, 425. 14

Phillips, K.J.H.: 2004, The Solar Flare 3.8-10 keV X-Ray Spectrum. *Astrophys. J.* **605**, 921 – 930. doi:10.1086/382523. 21

Piana, M.: 1994, Inversion of bremsstrahlung spectra emitted by solar plasma. *Astron. Astrophys.* **288**, 949 – 959. 18, 75

Piana, M., Massone, A.M., Kontar, E.P., Emslie, A.G., Brown, J.C., Schwartz, R.A.: 2003, Regularized Electron Flux Spectra in the 2002 July 23 Solar Flare. *Astrophys. J. Lett.* **595**, L127 – L130. doi:10.1086/378171. 75, 80

Pizzichini, G., Spizzichino, A., Vespignani, G.R.: 1974, On Anisotropy of Solar Hard X-Ray Emission. *Solar Phys.* **35**, 431 – 439. doi:10.1007/BF00151966. 90

Poutanen, J., Nagendra, K.N., Svensson, R.: 1996, Green's matrix for Compton reflection of polarized radiation from cold matter. *Mon. Not. Roy. Astron. Soc.* **283**, 892 – 904. 41

Priest, E.R.: 1984, *Solar magneto-hydrodynamics*, *Geophysics and Astrophysics Monographs*, D. Reidel Publishing Company, Dordrecht. ISBN 9789027718334. x, 8, 15

Santangelo, N., Horstman, H., Horstman-Moretti, E.: 1973, The Solar Albedo of HARD X-Ray Flares. *Solar Phys.* **29**, 143 – 148. doi:10.1007/BF00153445. 27

Schwartz, R.A., Csillaghy, A., Tolbert, A.K., Hurford, G.J., McTiernan, J., Zarro, D.: 2002, RHESSI Data Analysis Software: Rationale and Methods. *Solar Phys.* **210**, 165 – 191. doi:10.1023/A:1022444531435. 73, 82, 98

Shih, A.Y., Lin, R.P., Hurford, G.J., Boggs, S.E., Zoglauer, A.C., Wunderer, C.B., Sample, J.G., Turin, P., McBride, S., Smith, D.M., Tajima, H., Luke, P.N., Amman, M.S.: 2009, The Gamma-Ray Imager/Polarimeter For Solar Flares (GRIPS). In: *AAS/Solar Physics Division Meeting #40*, *AAS/Solar Physics Division Meeting* **40**, 18.10. 22

Smith, D.M., Lin, R.P., Turin, P., Curtis, D.W., Primbsch, J.H., Campbell, R.D., Abiad, R., Schroeder, P., Cork, C.P., Hull, E.L., Landis, D.A., Madden, N.W., Malone, D., Pehl, R.H., Raudorf, T., Sangsingkeow, P., Boyle, R., Banks, I.S., Shirey, K., Schwartz, R.: 2002, The RHESSI Spectrometer. *Solar Phys.* **210**, 33 – 60. doi:10.1023/A:1022400716414. 72, 82, 98

Stewart, B.: 1861, On the Great Magnetic Disturbance Which Extended from August 28 to September 7, 1859, as Recorded by Photography at the Kew Observatory. *Royal Society of London Philosophical Transactions Series I* **151**, 423 – 430. 9

Sturrock, P.A.: 1966, Model of the High-Energy Phase of Solar Flares. *Nature* **211**, 695 – 697. doi:10.1038/211695a0. 13

Suarez-Garcia, E., Hajdas, W., Wigger, C., Arzner, K., Güdel, M., Zehnder, A., Grigis, P.: 2006, X-Ray Polarization of Solar Flares Measured with Rhessi. *Solar Phys.* **239**, 149 – 172. doi:10.1007/s11207-006-0268-1. 92

Sui, L., Holman, G.D., Dennis, B.R.: 2007, Nonthermal X-Ray Spectral Flattening toward Low Energies in Early Impulsive Flares. *Astrophys. J.* **670**, 862 – 871. doi:10.1086/522198. 80, 82

Sweet, P.A.: 1958, The Neutral Point Theory of Solar Flares. In: Lehnert, B. (ed.) *Electromagnetic Phenomena in Cosmical Physics*, *IAU Symposium* **6**, 123. 14

Tanaka, Y.: 1983, Introduction to HINOTORI. *Solar Phys.* **86**, 3 – 6. doi:10.1007/BF00157168. 22

Tandberg-Hanssen, E., Emslie, A.G.: 1988, *The physics of solar flares.* 18

Tikhonov, A.N.: 1963, Regularization Of Incorrectly Posed Problems. *Doklady Akademii NAUK SSSR* **153**(1), 49 – &. 68

Tomblin, F.F.: 1972, Compton Backscattering of Solar X-Ray Emission. *Astrophys. J.* **171**, 377 – +. doi:10.1086/151288. 27

Tsuneta, S., Masuda, S., Kosugi, T., Sato, J.: 1997, Hot and Superhot Plasmas above an Impulsive Flare Loop. *Astrophys. J.* **478**, 787. doi:10.1086/303812. 13

van Beek, H.F., Hoyng, P., Lafleur, B., Simnett, G.M.: 1980, The Hard X-ray Imaging Spectrometer /HXIS/. *Solar Phys.* **65**, 39 – 52. doi:10.1007/BF00151383. 22

Vernazza, J.E., Avrett, E.H., Loeser, R.: 1981, Structure of the solar chromosphere. III - Models of the EUV brightness components of the quiet-sun. *Astrophys. J. Supp.* **45**, 635 – 725. doi:10.1086/190731. 132

Vestrand, W.T., Forrest, D.J., Rieger, E.: 1991, New Measurements of the Anisotropy of Solar Flare Gamma-Rays. In: *International Cosmic Ray Conference*, *International Cosmic Ray Conference* **3**, 69. 90

Vestrand, W.T., Forrest, D.J., Chupp, E.L., Rieger, E., Share, G.H.: 1987, The directivity of high-energy emission from solar flares - Solar Maximum Mission observations. *Astrophys. J.* **322**, 1010 – 1022. doi:10.1086/165796. 90

Vilmer, N.: 1994, Solar hard X-ray and gamma-ray observations from GRANAT. *Astrophys. J. Supp.* **90**, 611 – 621. doi:10.1086/191882. 90

Vilmer, N., MacKinnon, A.L., Hurford, G.J.: 2011, Properties of Energetic Ions in the Solar Atmosphere from γ-Ray and Neutron Observations. *Space Sci. Rev.* **159**, 167 – 224. doi:10.1007/s11214-010-9728-x. 11, 12

Zharkova, V.V., Gordovskyy, M.: 2005, The kinetic effects of electron beam precipitation and resulting hard X-ray intensity in solar flares. *Astron. Astrophys.* **432**, 1033 – 1047. doi:10.1051/0004-6361:20041102. 131

Zharkova, V.V., Gordovskyy, M.: 2006, The Effect of the Electric Field Induced by Precipitating Electron Beams on Hard X-Ray Photon and Mean Electron Spectra. *Astrophys. J.* **651**, 553 – 565. doi:10.1086/506423. 31

Zhitnik, I.A., Logachev, Y.I., Bogomolov, A.V., Denisov, Y.I., Kavanosyan, S.S., Kuznetsov, S.N., Morozov, O.V., Myagkova, I.N., Svertilov, S.I., Ignat'ev, A.P., Oparin, S.N., Pertsov, A.A., Tindo, I.P.: 2006, Polarization, temporal, and spectral parameters of solar flare hard X-rays as measured by the SPR-N instrument onboard the CORONAS-F satellite. *Solar System Research* **40**, 93 – 103. doi:10.1134/S003809460602002X. 92

Zirin, H.: 1988, *Astrophysics of the sun*, Cambridge University Press, Cambridge. 4, 9